Structure, Properties and Chemistry of Layered Oxypnictides

Alex J. Corkett

A thesis submitted in part fulfilment of the requirements for the degree of Doctor of Philosophy at the University of Oxford

Trinity College
University of Oxford
May 2012

The work described in this thesis was carried out in the Inorganic Chemistry Laboratory, South Parks Road, Oxford from October 2008 to May 2012 under the supervision of Dr Simon J. Clarke. All the work described hereafter is my own unless stated to the contrary, and has not been submitted for any degree at this or any other university.

Alex Corkett

May 2012

Abstract

Structure, Properties and Chemistry of Layered Oxypnictides

Alex Corkett Trinity College

D.Phil Thesis Trinity 2012

This thesis reports the synthesis and characterisation of the layered oxypnictides Sr_2MO_3FeAs (M = Sc, V and Cr) and CeOMnAs. In these materials the choice of transition metal cation at the tetrahedral site in the arsenide layer chiefly dictates the physical properties that are observed.

The bulk of this work has focussed on the development of a new family of iron arsenide superconductor with the general formula Sr_2MO_3FeAs (M = Sc, V, Cr). This structure is comprised of anti-PbO-type $[FeAs]^-$ layers which alternate with insulating $[Sr_2MO_3]^+$ oxide fragments that resemble a portion of the K_2NiF_4 structure. In contrast to other FeAs parent materials, no member of the Sr_2MO_3FeAs family exhibits any strong evidence for long range Fe order or a tetragonal to orthorhombic distortion upon cooling. Attempts to electron and hole dope Sr_2ScO_3FeAs into the superconducting regime have as yet been unsuccessful.

Although Sr_2CrO_3FeAs shows no evidence for Fe ordering, a checkerboard arrangement of Cr^{3+} spins in the *ab*-plane is observed below 40 K ($\boldsymbol{k}$ = (½, ½, 0)) analogous to that seen in Pr_2CuO_4. The partial substitution of Fe^{2+} (d^6) by Co^{2+} (d^7) in $Sr_2CrO_3Fe_{1-x}Co_xAs$ has been shown to be a fruitful strategy for electron-doping this material into the superconducting regime with T_c maximised at 18 K in $Sr_2CrO_3Fe_{0.92}Co_{0.08}As$. It is also established that this substitution influences the ordering on the Cr sub-lattice with a doubling in the size of the magnetic cell along the *c* axis ($\boldsymbol{k}$ = (½, ½, ½)).

Sr_2VO_3FeAs, a rare example of an "undoped" superconductor (T_c = 25 K), is shown to be electron-doped by mixed valence vanadium +3.13(5). Magnetometry measurements also reveal a series of magnetic transitions in Sr_2VO_3FeAs, however μSR and powder neutron diffraction studies suggest that this system is some way from commensurate long range order.

In contrast to Sr_2CrO_3FeAs, electron-doping strategies in Sr_2VO_3FeAs have the effect of decreasing T_c and ultimately suppressing superconductivity entirely as $Sr_2V_{1-x}Ti_xO_3FeAs$ and $Sr_2VO_3Fe_{1-x}Co_xAs$ materials are over electron-doped. $Sr_2V_{1-x}Mg_xO_3FeAs$ samples were also prepared, but rather than this strategy hole-doping the FeAs layer it preferentially oxidises vanadium towards V^{4+}. This substitution also has a considerable effect on the superconducting critical temperature (T_c) which is raised as high as 31 K in $Sr_2V_{0.775}Mg_{0.225}O_3FeAs$. The isovalent substitution of Sr^{2+} by Ca^{2+} in $Sr_{2-x}Ca_xVO_3FeAs$ has been shown to strongly influence the superconducting properties of this material and a clear correlation between the evolution of T_c and the shape of the $FeAs_4$ tetrahedron has been established. These results demonstrate that superconductivity in iron-based superconductors is extremely sensitive to both electron count and the crystal structure.

Finally, investigations into the manganese oxide arsenide CeOMnAs reveal room temperature ordering of Mn^{2+} spins and a spin reorientation transition of Mn moments at 36 K. This transition is concomitant with Ce ordering and an apparent weak structural distortion, demonstrating that *f* electrons are able to dictate the orientation of Mn moments.

Acknowledgements

Firstly I would like to thank my supervisor Dr Simon Clarke who has been a fantastic mentor and a constant source of enthusiasm and ideas throughout this project. I am also grateful to the group of Dr Julien Bobroff from the LPS in Orsay for performing NMR measurements and the group of Prof Steve Blundell from the Oxford Physics Department for their μSR expertise.

I would also like to thank members of "Team Clarke" past and present who have been great fun to work with. Specifically thanks must go to my fellow DPhils: Seb you have taught me the dimensions of a badger; Paul from you I have learnt that GSAS is my friend and is not to be feared; Mike you have made my LiFe-As a DPhil painfully pun-filled; Jack and Alice you are well on your way to becoming chemists; and Simon I expect your cat like goalkeeping talents to bring the catalyst cup back to Intercalate Milan next year.

Throughout my time in Oxford I have had the pleasure of pestering a number of excellent postdocs: Dinah and Raquel you have been great company on many a late night neutron diffraction experiment and Dave and Stefan I cannot thank you enough for bringing to the group the gift of TOPAS and cricket banter/schoko-bons, respectively.

I have also received a great amount of assistance throughout this project from a number of instrument scientists, namely: Dr K. Knight and Dr A. Daoud-Aladine (HRPD), Dr R. Smith (POLARIS), Dr F. Demmel (OSIRIS), Dr P. Manuel (WISH) from ISIS; Dr E. Suard (D2B) from the ILL; Dr S. Ramos (B18); Dr C. Tang, Dr J. Parker and Dr S. Thompson (I11) from Diamond and Dr A. Fitch and Dr C. Curfs (ID31) from the ESRF. I am also very grateful to the staff of the ICL, especially Dr P. Wiseman for the maintenance of the diffractometers and magnetometers.

I cannot fail to acknowledge my housemates Nick, Lawrence, Fred and Matt for their delightful company and patience with my inability to follow a very simple cleaning rota. Finally I would like to thank my family, friends and Julia, without whose support this project would not have been possible.

Contents

1 Introduction

1.1 Solid state chemistry

The origins of solid state chemistry can be traced back to the development of X-ray crystallography as a characterisation tool by M. von Laue and W.L./W.H. Bragg in the early part of the 20th century. This powerful technique has since become the cornerstone of structural analysis in crystalline materials, facilitating the establishment of crucial structure-property relationships.

The huge variety of interesting chemical and physical properties expressed in solid state materials has brought about considerable technological advances in recent times and continues to drive research in the field. The synthesis of new solid state materials and the tuning of the physical and electronic properties of those already known, continue to yield useful and often surprising discoveries. Perhaps most famously, the Nobel Prize for Physics was awarded to J. G. Bednorz and K. A. Müller in 1987 for the discovery of high temperature superconductivity in a layered perovskite-based cuprate, subsequently shown to be $Ba_xLa_{5-x}Cu_5O_{5(3-y)}$ (LBCO T_c = 35 K).[1] This stimulated tremendous synthetic activity towards new cuprate superconductors and within a few months T_c was raised above the boiling point of liquid nitrogen in $YBa_2Cu_3O_{7-\delta}$ (YBCO T_c = 89 K).[2] The prospect of cooling superconductors with liquid nitrogen, rather than helium, would present a considerable saving in the cost of cryogens. However, the replacement of conventional He-cooled superconductors like Nb_3Sn (T_c = 18 K) with high T_c superconductors in their commercial application as generators of large magnetic fields in scientific (SQUID magnetometers) and medical instruments (MRI scanners), will not prove possible until considerable processing challenges are overcome.[3]

In the area of rechargeable batteries, $LiCoO_2$ has found huge practical use as a cathode material in millions of electronic devices owing to its ability to reversibly intercalate Li ions in a high-voltage redox process.[4] The intercalation and deintercalation of simple inorganic anions, organic anions and even complex biological molecules such as DNA into layered double hydroxides ($[M^{II}_{(1-x)}M^{III}_x(OH)_2]A^{n-}_{x/n}\cdot mH_2O$) has also found application in the selective separation of isomeric mixtures and drug delivery systems.[5,6] More extended three dimensional porous framework materials such as zeolites, aluminophosphates and

metal-organic framework materials or MOFs are another important class of materials which are exploited for their adsorption properties and heterogeneous catalytic activity.[7-9]

Many solid state materials also possess interesting physical properties that are employed in the electronics industry. γ-Fe_2O_3 and CoPtCr are ferromagnetic and both find use in data storage, whilst dielectric materials such as $BaTiO_3$ and $PbTiO_3$ exhibit very low conductivity and function as capacitors.[10,11] More exotic physical phenomena like the colossal magnetoresistance in manganese-based perovskite oxides, in which the electrical resistance drops by a large amount upon the application of a magnetic field, have yet to find a use but show promise in the emerging field of spintronics.[12] The optical properties of TiO_2 are exploited for a huge range of applications from sunscreen to solar Grätzel cells, owing to its very high refractive index and brightness.[13]

Traditionally solid state chemistry has focused on oxide materials, which are the most thermodynamically stable products when traditional high temperature ceramic synthesis techniques are employed in our oxidising atmosphere. Oxides are known for virtually all elements and can adopt a huge array of structures. In synthesising non-oxide and mixed-anion materials precautions must be taken to exclude atmospheric moisture and oxygen to avoid the hydrolysis and/or oxidation of the reagents and target materials. Advances in air-sensitive techniques and equipment, such as inert gas dry boxes, have facilitated the synthesis of many novel and useful non-oxide materials. The simple ionic binary material MgB_2 was discovered to be a high temperature superconductor with T_c = 39 K, the highest T_c of any conventional superconductor, and now finds application in M.R.I. scanners.[14] GaN with the wurtzite structure is another commercially useful material, which thanks to its wide direct bandgap (3.4 eV) semiconductor properties is used in blue lasers and LEDs.[15] More recently researchers who were originally looking to synthesise transparent *p*-type semiconductors made the unexpected discovery of high T_c superconductivity (up to 26 K) in $LaO_{1-x}F_xFeAs$ (x = 0.05-0.12).[16] This finding has stimulated a tremendous amount of research and also been the inspiration for much of this thesis.

1.2 Layered pnictides, oxypnictides, and oxychalcogenides

Following this initial innovation in $LaO_{1-x}F_xFeAs$ it was quickly established that it is the FeAs anti-PbO-type layers which support superconductivity. Huge efforts were therefore directed towards the synthesis and characterisation of materials with FeP, FeAs, FeS and

FeSe anti-PbO-type layers. The PbO structure-type can be viewed as a fragment of fluorite, a ubiquitous building block from which a huge number of structure types may grow.

1.2.1 Fluorite and antifluorite layers

CaF_2 exhibits the archetypal fluorite structure (Figure 1.1), one of the most prevalent crystalline forms found in nature.[17] Cubic fluorite with *Fm*-3*m* symmetry is well described as a face centred packing of cations, with anions in all of the tetrahedral holes. Another helpful visual construct of CaF_2 is to consider the unit cell as being built from a three-dimensional edge-sharing network of tetrahedra, with cations at the corners and anions in the centres. The fluorite structure is adopted by oxides of large quadrivalent cations and fluorides of divalent cations, which are typically fairly ionic in nature.

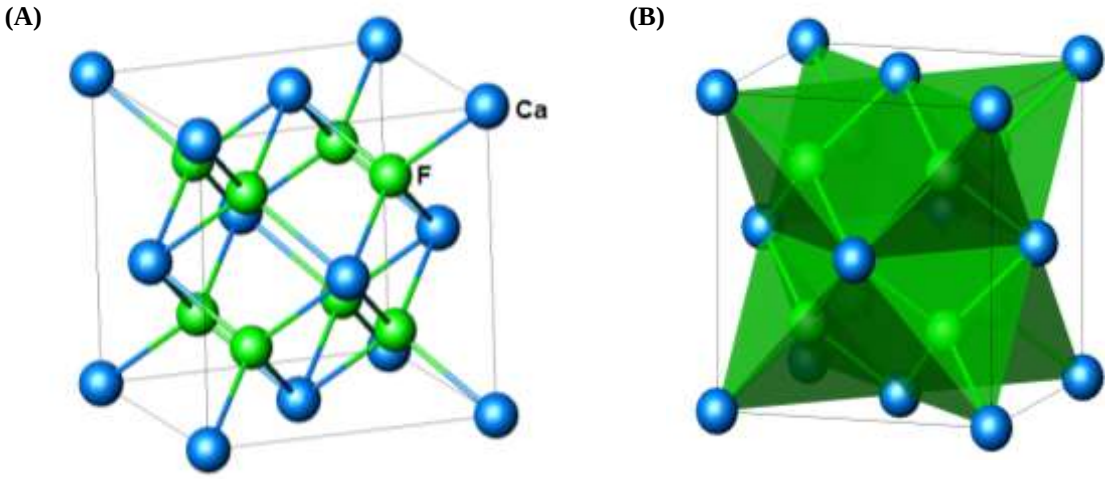

Figure 1.1 (A) Fluorite structure of CaF_2, (B) Fluorite structure showing edge-sharing anion tetrahedra.

The anti-fluorite structure has cations and anions exchanged, and is adopted by the oxides and chalcogenides of monovalent cations. α-Ag_2Te is one of several binary chalcogenides (α-Ag_2Te, α-Ag_2Te and α-Cu_2S) to display this structure that exhibit highly mobile cations, which move between tetrahedral sites through empty octahedral interstices.[18,19]

1.2.2 Defect fluorite and antifluorite structures

The partial occupancy of the tetrahedral sites in fluorite and anti-fluorite structure types opens the door to a range of common defect structures. ZnS (Zinc blende) is a derivative of anti-fluorite with vacancies at half of the tetrahedral sites located at the opposing corners. This yields a structural motif that is equivalent for both anions and cations, which are both tetrahedrally coordinated (Figure 1.2).[20] The layered lead oxide (PbO) structure type may

also be considered as a defect version of the fluorite structure, in which half of the oxygen sites are vacant from between every other layer of lead atoms.[21] This generates a distinctly two-dimensional structure of PbO layers with the lone pairs on Pb forming a van der Waals layer that holds adjacent lead oxide sheets together (Figure 1.2).[22]

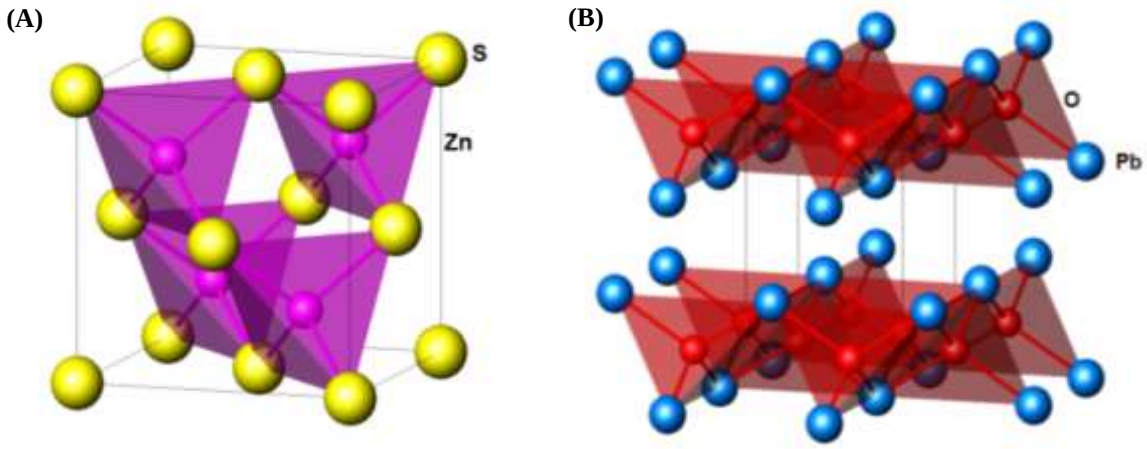

Figure 1.2 Crystal structures of (A) ZnS and (B) PbO

The anti-type of the PbO structure also exists in the beta polymorph of FeSe. This was first reported in 1933,[23] and crystallises in a tetragonal unit cell with the *P*4/*nmm* space group. However, after the discovery of superconductivity in $LaO_{1-x}F_xFeAs$ with isostructural anti-PbO-type formally $[FeAs]^-$ layers, β-FeSe was quickly recognised as a potential candidate for high temperature superconductivity and soon reported to have T_c = 8 K.[24] It has since been shown that T_c may be increased to 27 K by the application of pressure and much attention has been rightly devoted to β-FeSe as it offers the most fundamentally simple example of this family of Fe-based superconductor.[25]

1.2.3 Ternary pnictides and chalcogenides

The most basic way of decreasing the dimensionality of materials containing anti-PbO-type layers is to introduce a formal negative charge on the anti-PbO-type layer with charge balancing interstitial cations. Ternary pnictides typically adopt such layered motifs and the two most common crystal structures encountered are described below.

The $ThCr_2Si_2$ structure is a popular playground for studies of ternary pnictides and is also commonly adopted by silicides and germanides with over 600 known examples of this structure type.[26,27] Materials adopting this structure typically contain two different types of cation: a large group 1, group 2 or rare-earth metal and a smaller transition metal. The transition metal here occupies the tetrahedral site in the anti-PbO-type layer and the larger metal cation occupies a square prismatic 8-coordinate interlayer site. The coordination

requirements of the large interstitial metal cation require a translation of adjacent anti-PbO-type layers of $x + ½$, $y + ½$ relative to one another, resulting in a tetragonal body-centered unit cell with space group *I*4/*mmm* (Figure 1.3).

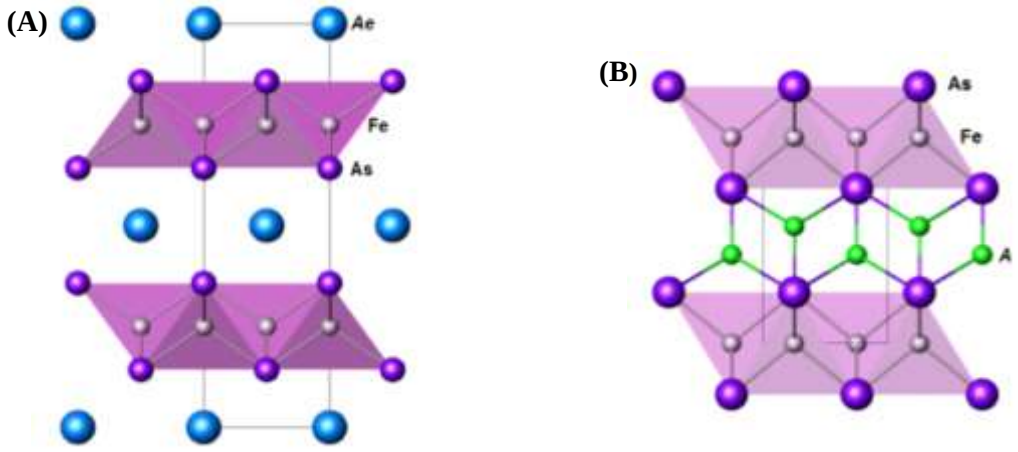

Figure 1.3 Crystal structures of the layered ternary iron pnictides (A) *Ae*Fe_2As_2 (*Ae* = Ca^{2+}, Sr^{2+}, Ba^{2+}, Eu^{2+}) and (B) *A*FeAs (A = Li^+, Na^+)

The simplicity of the $ThCr_2Si_2$ structure belies the wealth of interesting physical properties expressed by this structure type. $BaMn_2As_2$ is a collinear *G*-type antiferromagnet with a high Neel temperature T_N = 675 K,[28] whilst $EuCo_2P_2$ is ferromagnetic.[29] However most intriguing of all is the discovery of superconductivity in substituted *Ae*Fe_2Pn_2 materials (*Ae* = Ca^{2+}, Sr^{2+}, Ba^{2+}, Eu^{2+}), as seen in $Ba_{1-x}K_xFe_2As_2$ which through the hole doping of FeAs layers exhibits bulk superconductivity below 37 K.[30-32] More recently cation-deficient $K_{1-x}Fe_{2-2x}Ch_2$ (*Ch* = S, Se) materials have been synthesised and shown to adopt superstructures with ordered iron vacancies at room temperature.[33]The anti-type of this structure is somewhat less prevalent, with Nd_2O_2Te a rare example.[34]

The related PbFCl structure is also a common structure type and its anti-type is equally popular with over 200 known examples of both.[35] There exist both binary (Cu_2Sb) and ternary examples of this structure type whose character can range from being predominantly covalent (Cu_2As) to largely ionic in nature (BaFCl).[36,37] PbFCl crystallises in a primitive tetragonal unit cell with space group *P*4/*nmm* and consists of PbO-type layers which are directly overlaid, but separated by interlayer anions that occupy a 5-coordinate square pyramidal site (Figure 1.3). An alternative visual construct of PbFCl is of a Pb face-centered-cubic-type array with Cl in all octahedral holes and F in the tetrahedral holes of alternate layers.

The ternary iron arsenides LiFeAs and NaFeAs take the anti-PbFCl structure and feature anti-PbO-type $[FeAs]^-$ layers with the alkali metal cation in the 5-coordinate square pyramidal site (Figure 1.3).[38,39] Curiously stoichiometric LiFeAs, unlike other Fe*Pn*-based superconductors which need to be doped with suitable charge carriers, has been shown to be a bulk superconductor with T_c = 16 K in its undoped form.[40] NaFeAs exhibits a 10 % superconducting volume fraction and long-range AFM order in its stoichiometric state, but may be electron doped through the partial substitution of Co or Ni on the Fe site to enhance superconductivity.[41] Both offer intriguing, but compositionally limited forums for exploring Fe-based superconductivity.

1.2.4 Quaternary oxypnictides and oxychalcogenides

In order to expand the range of materials with anti-PbO-type iron pnictide layers, one must begin to synthesise quaternary and higher order mixed-anion materials. However, in designing such materials it is crucial to preserve the Fe*Pn* layers that have been shown to support superconductivity.

Perhaps the most thoroughly studied families of mixed-anion compounds are oxynitiride and oxyhalide materials. Whilst anion ordering in these materials is known, especially in the case of oxyhalides, the comparable sizes and coordination requirements of these anions may result in a random distribution of halide/nitride and oxide over the anion sites as in Ba_3ZnN_2O.[42] The long range ordering of anions is however much more common in oxychalcogenide and oxypnictide materials which naturally assume distinct oxide and pnictide/chalcogenide layers due to the different size and bonding requirements of the anions (Figure 1.4).

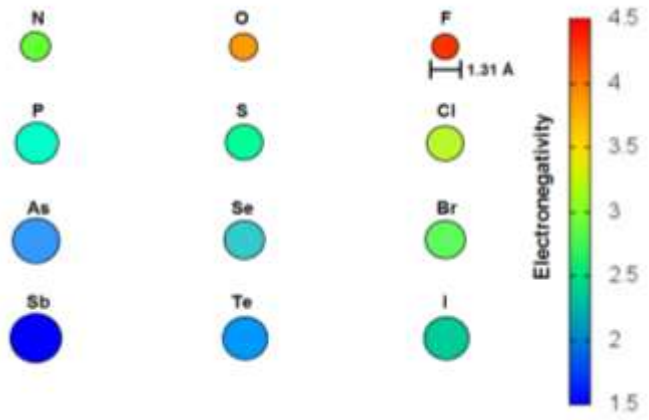

Figure 1.4 Pictorial representation of the variations in the electronegativity and ionic radius for group V, VI and VII anions.

In oxyarsenides for example the significantly larger ionic radii of As^{3-} (2.22 Å) compared to O^{2-} (1.31 Å) means that the two anions seldom occupy the same crystallographic site. Furthermore oxide is strongly electronegative and therefore preferentially coordinates to "hard" cations such as lanthanides and group 1 and 2 metals and early transition metals. Whereas chalcogenide and pnitcide anions are much more polarisable and favourably coordinate to "soft" cations with low-energy *d*-orbitals, such as late transition metals in low oxidation states.

1.2.4.1 ZrCuSiAs structure

The ZrCuSiAs structure is exemplified by a whole range of quaternary oxychalcogenides, oxypnictides and halide pnictides which adopt the ZrCuSiAs structure and crystallise in a tetragonal unit cells with the *P*4/*nmm* space group.[43] They may be viewed as an intergrowth of PbO-type layers alternating with anti-PbO-type layers and take the general formulae: *Ln*O*M*^{I}*Ch*, *Ln*O*M*^{II}*Pn* or *Ae*F*M*^{II}*Pn* (Figure 1.5).[44] Alternatively the ZrCuSiAs structure can be likened to that of PbFCl with all of the tetrahedral holes filled. In total there are over 150 representatives of the ZrCuSiAs this structure with the similarity in the basal dimensions of the two distinct layer types presumably facilitating their epitaxy.

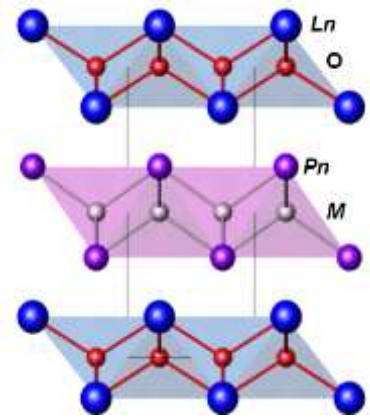

Figure 1.5 *Ln*O*MPn* structure

Given the structural flexibility of this family it is unsurprising that some of their number display interesting physical properties. LaOCuS has an optical band gap of 3.1 *eV* and exhibits *p*-type electrical conductivity, and therefore has potential application as a transparent *p*-type semiconductor, whilst the silver sulphide LaOAgS is a two-dimensional fast ion conductor.[45-47] Of particular interest to this thesis are a family of rare earth pnictide oxides with the electron precise formulae $Ln^{3+}O^{2-}M^{2+}Pn^{3-}$ many of which were originally synthesised by Jeitschko *et al*.[48] However, following the discovery of superconductivity in

$LaO_{1-x}F_xFeAs$, the ensuing research maelstrom has seen T_c optimised at 55 K in $SmO_{1-x}F_xFeAs$ and the range of *Ln*OFeAs materials extended through the use of high pressure synthesis techniques.[49] The isotructural *Ae*FFeAs (*Ae* = Ca, Sr, Eu) family has since been discovered, which also supports superconductivity when suitably carrier doped.[50,51]

1.2.5 Oxychalcogenides intergrowth structures

At the outset of this study in October 2008, the quaternary iron pnictides described in the previous section were the most complex known. In designing novel FeAs-based materials with more extended oxide layers, inspiration is well taken from a class of oxychalcogenide materials that all feature Cu*Ch* (*Ch* = S, Te) anti-PbO-type layers separated by oxide fragments. The $A_2MO_2Cu_2Ch_2$ family, where *A* is an electropositive metal, *M* is a transition metal and *Ch* is a chalcogen, can be seen as an intergrowth of cubic perovskite $SrTiO_3$ and the $ThCr_2Si_2$ structure as shown in Figure 1.6.[52] Here single MO_2 planes separate Cu*Ch* anti-PbO-type layers, with the oxide layer supporting a range of different transition metals.

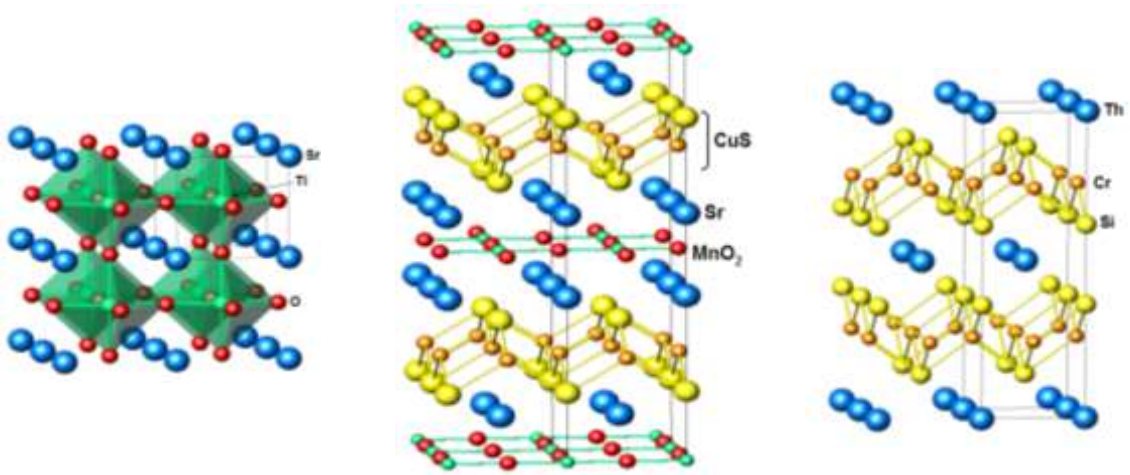

$SrTiO_3$ **$Sr_2MO_2Cu_2S_2$** **$ThCr_2Si_2$**

(***M*** = Mn, Co, Ni, Cu, Zn)

Figure 1.6 Intergrowth of perovskite $SrTiO_3$ and $ThCr_2Si_2$ in $Sr_2MO_2Cu_2S_2$

$Sr_2MnO_2Cu_{2-\delta}S_2$ ($\delta \approx 0.5$) exhibits an intriguing Cu deficiency facilitated by mixed valence Mn^{2+}/Mn^{3+} that order in zig-zag ferromagnetic chains on cooling.[53] Furthermore it is also possible to remove all of the Cu and replace it quasi-reversibly with Li via reductive topotactic ion exchange reactions, implying potential for $Sr_2MnO_2Cu_{2-\delta}S_2$ as an electrode material for use in rechargeable batteries.[54] Co, Ni, Cu and Zn analogues are also known and display varied and complex magnetic behaviour.[55-57]

1.2.5.1 The $A_{n+1}M_nO_{3n-1}Cu_2S_2$ homologous series

The $A_2MO_2Cu_2Ch_2$ materials discussed in the previous section are in fact part of a much larger family of oxychalcogenides. They take the general formula $A_{n+1}M_nO_{3n-1}Cu_2S_2$ and feature perovskite type oxide layers of variable thickness alternating with Cu*Ch* layers (Figure 1.7).[57]

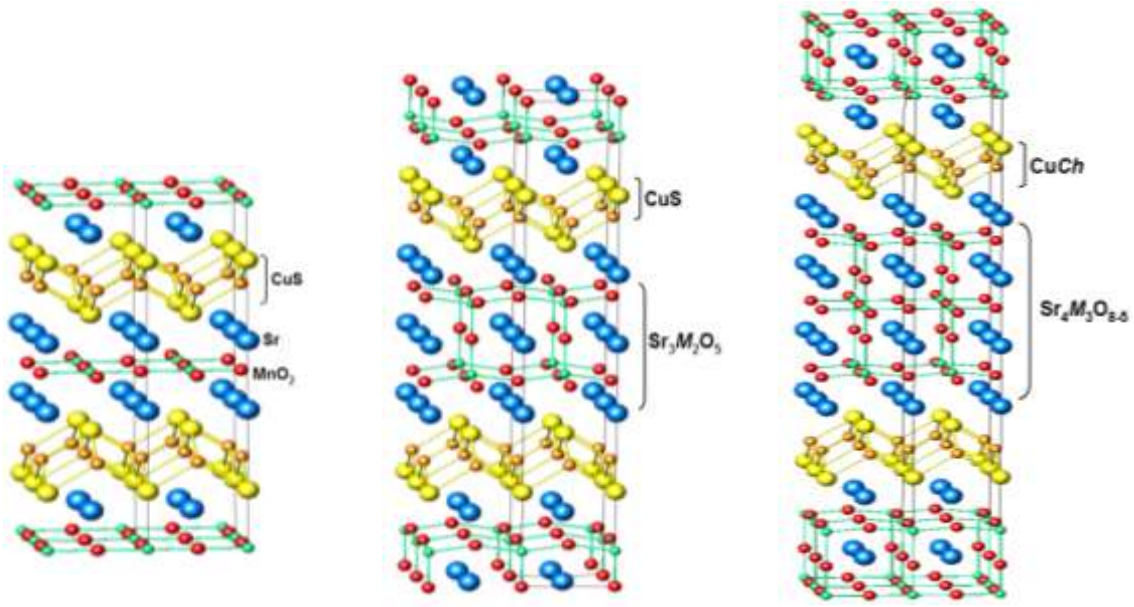

***n* = 1**	***n* = 2**	***n* = 3**
$Sr_2\boldsymbol{M}O_2Cu_2S_2$	$Sr_3\boldsymbol{M}_2O_5Cu_2S_2$	$Sr_4Mn_3O_{8-\delta}Cu_2\boldsymbol{Ch}_2$
(***M*** = Mn, Co, Ni, Cu, Zn)	(***M*** = Sc, Fe)	(***Ch*** = S, Se)

Figure 1.7 Crystal structures of the homologous $A_{n+1}M_nO_{3n-1}Cu_2S_2$ series

The $n = 2$ member with 'double thickness' oxide layers has *M* formally in the +3 oxidation state and are known for *M* = Sc and Fe.[58] The 'triple thickness' oxide layers in $Sr_4Mn_3O_{8-\delta}Cu_2Ch_2$ are found in the manganese sulphide and selenide and both exhibit oxygen vacancies ($\delta \approx 0.5$) in the central $MnO_{1.5}$ layer.[59] The anion content of this layer can in fact be tuned by topotactic oxidation (XeF_2) and reduction (NaH) reactions.[53]

1.2.5.2 Materials with K_2NiF_4 type oxide layers

The oxysulfide Sr_2GaO_3CuS crystallises in a tetragonal unit cell with the *P*4/*nmm* space group and has a structure related to that of the $n = 2$ members of the $A_{n+1}M_nO_{3n-1}Cu_2S_2$ perovskite type materials.[60] However, the oxide layer in this material resembles a portion of the K_2NiF_4 structure and may therefore be viewed as an intergrowth of the $ThCr_2Si_2$ and K_2NiF_4 structures as shown in Figure 1.8.

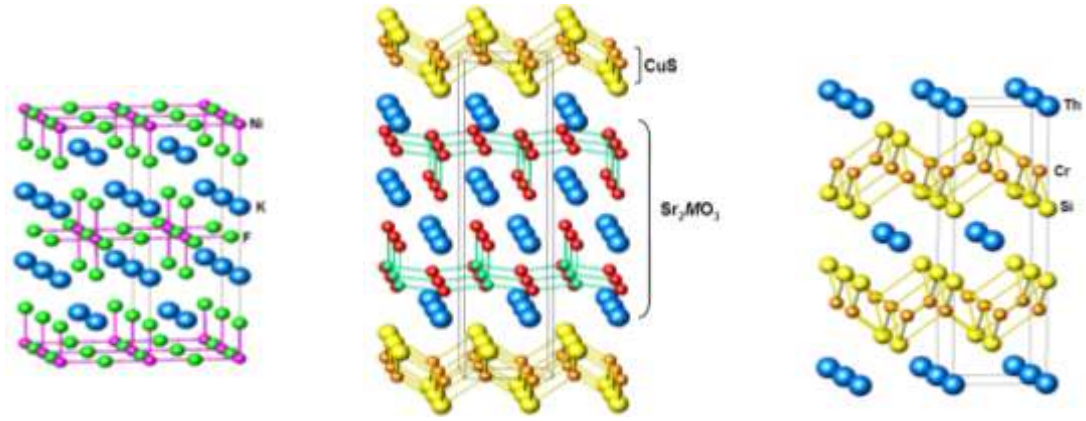

K_2NiF_4 **Sr_2MO_3CuS** **$ThCr_2Si_2$**

(***M*** = Cr, Mn, Fe, Ga and In)

Figure 1.8 Sr_2MO_3Cu*Ch* an intergrowth of K_2NiF_4 and $ThCr_2Si_2$

Here trivalent Ga is in an unusual square pyramidal coordination environment, the adoption of which is likely promoted by the favourable charge and geometrical compatibility of the two structural motifs. The range of oxychalcogenides with this Sr_2MO_3CuS structure type has since been extended to include analogues with *M* = Cr, Mn, Fe and In.[58,59]

1.2.5.3 $Bi_2LnO_4Cu_2Se_2$ oxychalcogenides

One final structure type to consider is that adopted by members of the $Bi_2LnO_4Cu_2Se_2$ family which crystallise in the *I*4/*mmm* space group (*Ln* = Y, Gd, Sm, Nd, La).[61] As shown in Figure 1.9 these materials have formally $[Bi_2LnO_4]^+$ 'triple fluorite' layers, also seen in the layered oxyhalides Bi_2LnO_4Cl (*Ln* = La, Nd, Y),[62] that are interspersed with the ubiquitous CuSe anti-PbO-type layers.

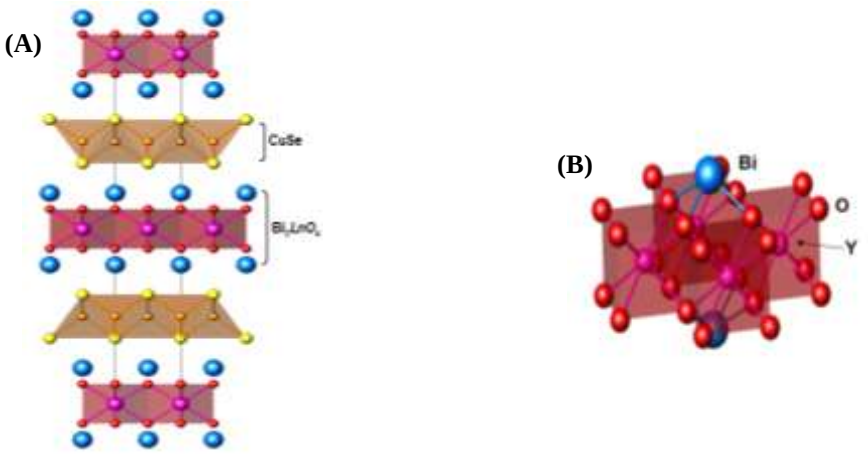

Figure 1.9 (A) $Bi_2LnO_4Cu_2Se_2$ crystal structure (B) $[Bi_2LnO_4]^+$ 'triple fluorite' layers

Interestingly though the formal charge on the $[Cu_2Se_2]^-$ layer means that there is necessarily one hole in the valence band for every Cu_2Se_2 unit. A study on related materials with $[Cu_2Ch_2]^-$ layers has shown the holes are Cu-*Ch* and Cu-Cu antibonding in nature, which would account for the considerable conductivity and relatively small *a* cell parameters seen in $Bi_2LnO_4Cu_2Se_2$ materials.[63]

1.2.6 Design considerations

In designing new Fe-based superconductors it is hoped that the similar size of isostructual $[Cu_2Se_2]^{2-}$ and $[Fe_2Pn_2]^{2-}$ layers should allow the former to be replaced with the latter in a number of the different structure types discussed above. Within such oxychalcogenides the highly chalcophilic nature of Cu ensures its uptake into the chalcogenide layer, affording oxides layers which support a whole range of transition metals. Since it has been established that it is the anti-PbO-type Fe*Pn* layers which support superconductivity, it is necessary to ensure a similar preference in Fe*Pn*-perovskite materials so that the iron enters the pnictide rather than the oxide layer. Hence by incorporating a very oxophilic metal into the oxide layer, competition for the tetrahedral sites within the pnictide layer can hopefully be avoided.

1.3 Superconductivity

1.3.1 Discovery and preliminary research

Superconductivity, the phenomena of zero electrical resistance and perfect diamagnetism below a characteristic critical temperature (T_c), was first reported over 100 years ago by Heike Kamerlingh Onnes in 1911. In studying the resistance of solid mercury at cryogenic temperatures, utilizing the newly condensed liquid helium, he observed that the resistance of mercury rapidly disappeared below 4.2 K.[64] The next breakthrough in the understanding of superconductivity came two decades later, in 1933, when Meissner and Ochsenfeld discovered that below the superconducting critical temperature all magnetic flux is expelled from a superconductor in a phenomenon now known as the Meissner-Ochsenfeld effect.[65]

1.3.2 BCS theory

These exotic physical properties are intrinsic to all superconductors, but at the time of their discovery could not be explained by contemporary theories. The first attempt to rationalise this behaviour came in 1950 with the phenomenological Ginzburg–Landau theory which

well describes the macroscopic properties of superconductors without offering an explanation for the underlying microscopic mechanism. In the same year Maxwell and Reynolds discovered a dependence of the superconducting critical temperature on the isotopic mass of the constituent elements – suggesting that electron-phonon interaction play an important role.[66,67] This eventually led to the formation of the Bardeen-Cooper-Schrieffer theory in 1957 which provided an explanation for the essential properties of all known superconductors at that time.[68]

In BCS theory phonons create a small attractive interaction between conduction electrons in the vicinity of the Fermi level which below T_c condense into so called 'Cooper pairs'. This has the effect of opening an energy gap at the Fermi level, stabilising the superconducting state over the normal state. The gap here corresponds to the energy required to break a Cooper pair and is related to the superconducting transition temperature T_c at a given temperature T by *eqn1.1*.

$$E = 3.52 k_B T_c \sqrt{1 - \frac{T}{T_c}} \qquad \textit{eqn1.1}$$

More fundamentally BCS theory predicts the superconducting transition temperature as a function of λ the electron-phonon coupling constant and the Debye energy E_D (the maximum phonon energy) *eqn1.2*.

$$k_B T_c = 1.13 E_D \exp(-1/\lambda) \qquad \textit{eqn1.2}$$

This shows that T_c is maximised in systems with strong electron coupling (high λ) and high frequency phonons. An important consequence of this theory is that it puts a physical limit on the maximum T_c accessible through electron-phonon coupling at ~ 40 K. Conventional superconductors are those which follow BCS theory and include elemental metals, alloys and as well as a number of more recently discovered compounds such as MgB_2 which exhibits a T_c of 39 K at about the upper limit of BCS superconductivity.[14] However a number of materials have been discovered which exhibit much higher superconducting transition temperatures and other properties inconsistent with BCS theory.

1.3.3 Cuprate superconductors

The 1986 discovery of superconductivity in $Ba_xLa_{5-x}Cu_5O_{5(3-y)}$ below 30 K was not only remarkable because of the record breaking critical temperature reported, but also for the

class of material in which the phenomena were observed,[1] since one would expect ceramic perovskite materials such as $Ba_xLa_{5-x}Cu_5O_{5(3-y)}$ to be insulators, rather than superconductors. This stimulated a flurry of research into related materials and reports of superconductivity at 38 K in $La_{2-x}Sr_xCuO_4$,[69] and other layered cuprates such as YBCO $YBa_2Cu_3O_{6+x}$ 85 K were soon reported.[2] Quinary cuprates quickly followed with the "2223" materials $Bi_2Sr_2Ca_2Cu_3O_{10}$ and $Tl_2Ba_2Ca_2Cu_3O_{10}$, which show impressively high critical temperatures of 110 K and 125 K, respectively.[70,71] However, the current record is held by $HgBa_2Ca_2Cu_3O_{8+\delta}$ with T_c = 135 K,[72] which may be enhanced to 164 K under pressure.[73]

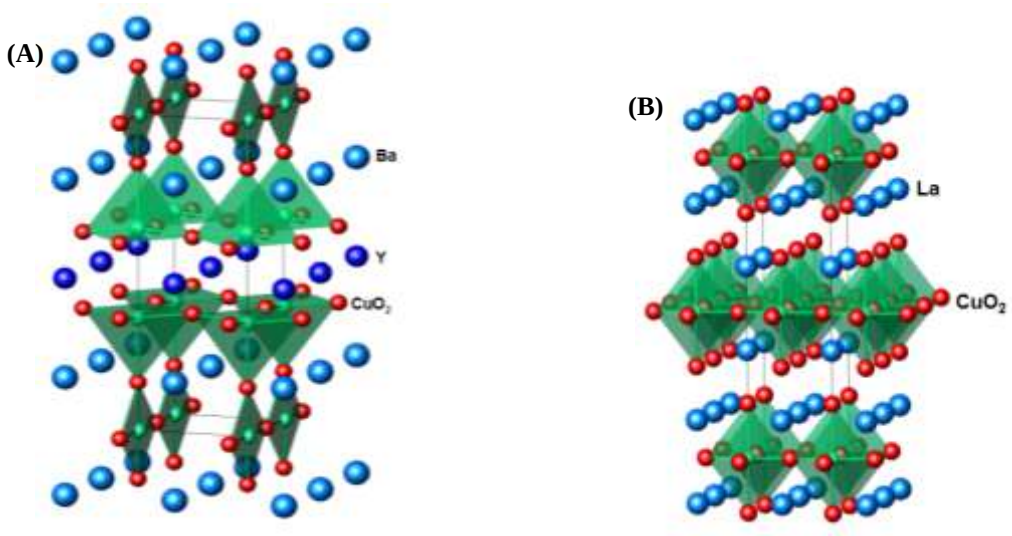

Figure 1.10 Crystal structures of (A) $YBa_2Cu_3O_7$ and (B) La_2CuO_4.

All of these cuprate superconductors adopt crystal structures related to that of perovskite and may be considered to be quasi-two-dimensional materials with a common feature of CuO_2 planes built from corner sharing square planar CuO_4 motifs, which are separated by blocking layers of varying thickness. The crystal structures of $YBa_2Cu_3O_7$ and La_2CuO_4 are shown in Figure 1.10.

The framework structure of cuprates means that they can often support variable occupancies on the oxide sites, as in YBCO. Aliovalent substitutions are also possible on a range of different crystallographic sites, permitting a considerable degree of compositional flexibility. In their undoped 'parent' state cuprates have Cu with a nominal valence of +2 and are Mott-Hubbard insulating antiferromagnets. Electron or hole doping these materials suppresses this behaviour to give metallic cuprates eventually bringing about superconductivity. The phase diagrams of $Nd_{2-x}Ce_xCuO_4$ and $La_{2-x}Sr_xCuO_4$ are shown in

Figure 1.11 and are typical examples of hole and electron doped cuprate superconductors, respectively.

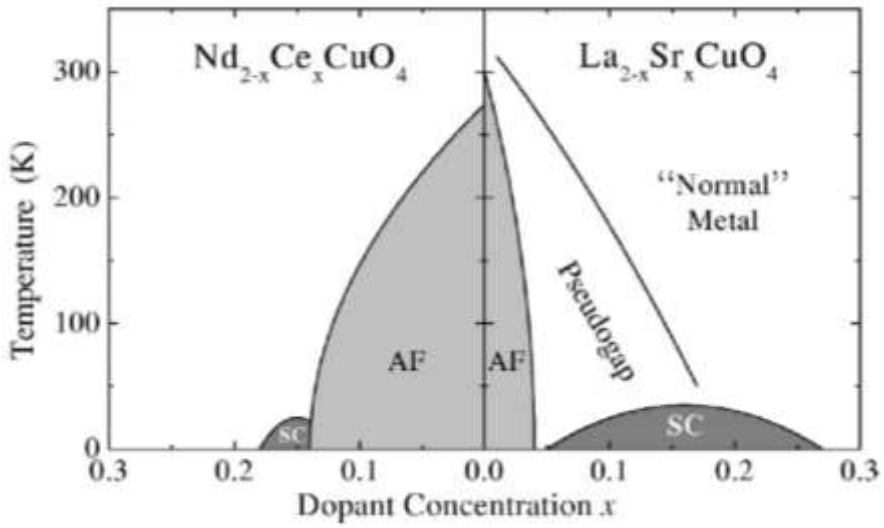

Figure 1.11 Phase diagram of *n*- and *p*-type cuprate superdconductors.[74]

The extremely high critical temperatures, as well as other properties of the superconducting state mean that the superconducting behaviour of cuprates cannot be rationalised by the electron-phonon interactions described in BCS theory. Instead it is proposed that in these unconventional superconductors the formation of Cooper pairs is facilitated by electronic correlations, whereby the role of phonons is replaced by "spin waves".[75] Despite the formidable critical temperatures exhibited by the cuprate superconductors, research into superconductivity began to wane in the latter part of the 20th century, due to the poor processing properties of these materials preventing the application of this lone class of high temperature superconductor. It was not until the breakthrough of high temperature superconductivity in a novel family of iron pnictide superconductors that a new gold, or should that be iron-rush began.

1.3.4 Iron pnictide superconductors

As previously stated, this impetus stemmed from the discovery of superconductivity in $LaO_{1-x}F_xFeAs$ below 26 K by Hosono *et al* in February 2008.[16] The synthesis of a whole series of isostructural *Ln*OFeAs (*Ln* = La-Dy) materials soon followed, and superconducting critical temperatures as high as 55 K have been reported in $SmO_{1-x}F_xFeAs$.[76-80] Such high superconducting critical temperatures are well above the predictions of the BCS theory for these compounds and even above the practical BCS

limit, an observation that immediately suggests unconventional superconductivity and a pairing mechanism mediated by electronic rather than electron-phonon interactions.

As described in section 1.2.4.1 *Ln*OFeAs superconductors crystallise with the ZrCuSiAs structure and feature anti-PbO-type FeAs layers. This prompted a concerted effort towards developing new, and characterising old, layered iron containing materials with anti-PbO-type Fe*Pn* (*Pn* = P, As), Fe*Ch* (*Ch* = S, Se, Te) layers. The so called 11, 111, 122 and 1111 families of iron pnictides/chalcogenides shown in Figure 1.12 are the result, which all crystallise in tetragonal unit cells with either the *P*4/*nmm* or *I*4/*mmm* space groups.

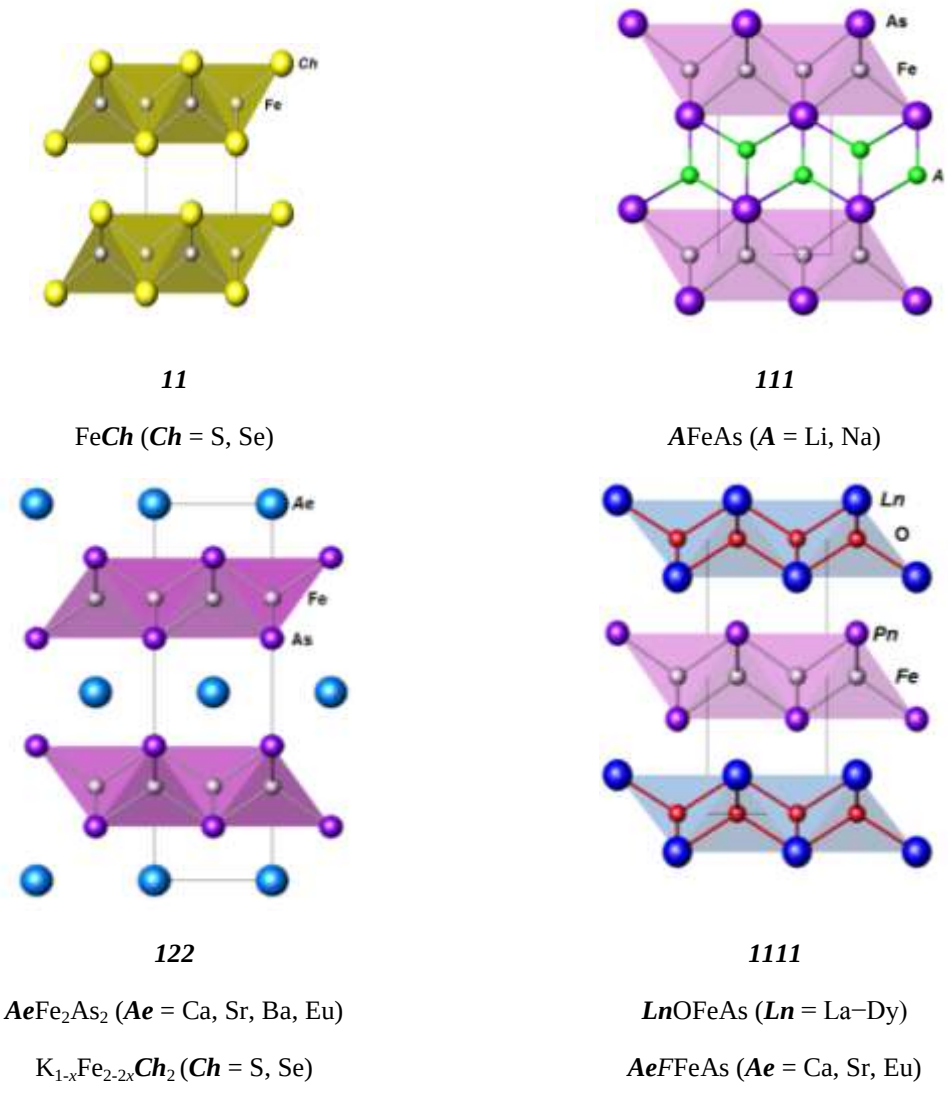

11

Fe***Ch*** (***Ch*** = S, Se)

111

AFeAs (***A*** = Li, Na)

122

AeFe_2As_2 (***Ae*** = Ca, Sr, Ba, Eu)

$K_{1-x}Fe_{2-2x}$***Ch***$_2$ (***Ch*** = S, Se)

1111

LnOFeAs (***Ln*** = La−Dy)

Ae*F*FeAs (***Ae*** = Ca, Sr, Eu)

Figure 1.12 Crystal structures adopted by Fe*Pn* and Fe*Ch*-based superconductors

In all of these undoped 'parent' materials iron is formally in the +2 oxidation state and the crystal structures typically undergo a structural distortion from tetragonal to orthorhombic symmetry upon cooling below T_S. Associated with this distortion is a transition to a striped

antiferromagnetically ordered state, below T_N, with small ordered moments on Fe (< 1μ_B). In this striped AFM ordered state the nearest-neighbour iron moments are aligned ferromagnetically along the shorter orthorhombic axis as shown in Figure 1.13. In 122 materials these transitions are concomitant whereas in 1111 materials $T_N < T_S$.[81] This observation suggests that the structural distortion is driven by nematic ordering and the difference between T_N and T_S increases as these compounds become more two dimensional.

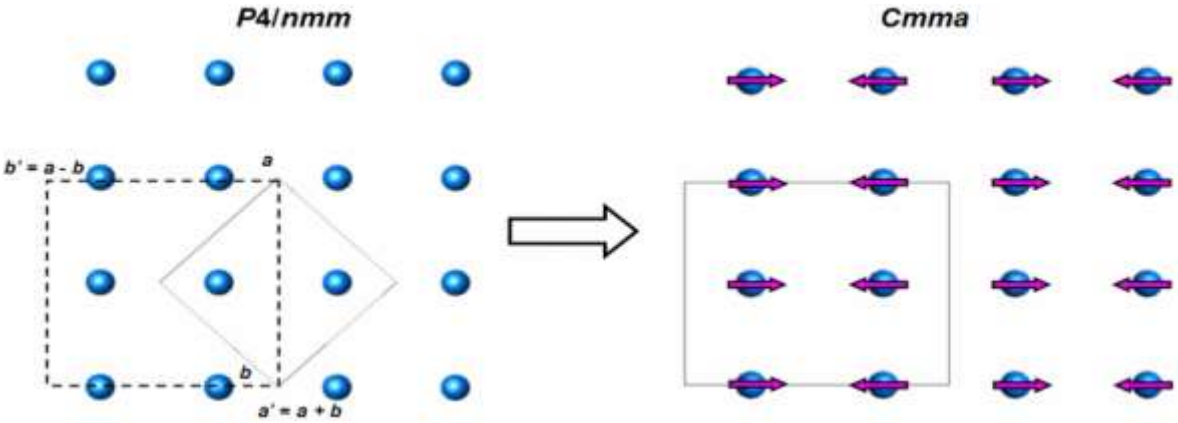

Figure 1.13 Schematic of the orthorhombic distortions and striped AFM magnetic order in an Fe-based superconductor.

Superconductivity may then be induced in Fe pnictides by aliovalent substitutions on a range of crystallographic sites; hole doping in $Ba_{1-x}K_xFe_2As_2$ and electron doping in $CaFFe_{1-x}Co_xAs$.[51,82] The latter strategy here is notable in that it creates disorder in the Fe planes that have been shown to support superconductivity; this is in strong contrast to the cuprate superconductors in which substitution on the Cu site leads to a rapid suppression of superconductivity.

The phase diagrams of $Ba(Fe_{1-x}Co_x)_2As_2$ and $Ba_{1-x}K_xFe_2As_2$ are shown in Figure 1.14 and are typical examples of electron and hole doped Fe pnictide superconductors, respectively.[83,84] It describes the suppression of both the magnitude of, and temperature at which, the orthorhombic distortion and striped AFM ordered occur, as well as a small doping region in which striped AFM order and superconductivity coexist. Exceptions to this general behaviour are seen in the 111 family which exhibit superconductivity in the stoichiometric 'undoped' state. However, the superconductivity is far from bulk in NaFeAs (~ 10 %) and long-range AFM order is seen in most of its volume.[85] Bulk superconductivity may be induced by electron doping through the partially substitution of

Co or Ni on the Fe crystallographic site.[41] LiFeAs is therefore conspicuous in that it exhibits bulk superconductivity without the need for carrier doping,[40] which in fact suppresses superconductivity.[86] As well as the electron count proving a crucial parameter in optimising the superconducting transition temperatures in Fe*Pn* superconductors, an empirical relationship has been established between T_c and the *Pn*-Fe-*Pn* bond angle, which appears to be maximised for regular FePn_4 geometries ($\alpha = \beta = 109.47$ °) .[87,88]

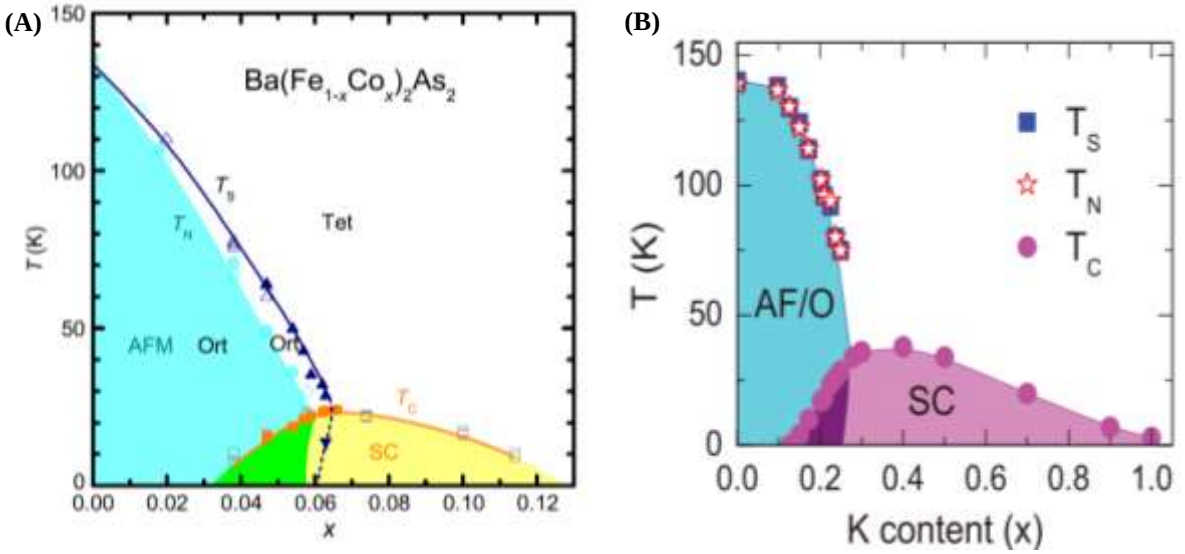

Figure 1.14 Phase diagrams of (A) $Ba(Fe_{1-x}Co_x)_2As_2$ and (B) $Ba_{1-x}K_xFe_2As_2$ taken from papers by Nandi *et al*[83] and Avci *et al*[84], respectively.

As already stated, the superconducting critical temperatures exhibited by a number of suitably doped Fe-pnictides well exceed the theoretical BCS limit. Furthermore the electron-phonon coupling constant in $LaO_{1-x}F_xFeAs$ has been shown to be too small to account for the observed critical temperature of 26 K.[89] Additionally comparison of the phase diagrams of cuprate and iron pnictide superconductors shows qualitatively the same behaviour in that superconductivity in both is proximate to a magnetically ordered state. It is now generally accepted that spin fluctuations generate Cooper pairs and that the superconducting order parameter has s ± symmetry.[90] However, the more that they are studied, the less iron-based superconductors look like cuprate superconductors. For one thing, undoped cuprates are Mott-Hubbard insulators, whilst iron-based superconductors are semi-metallic, and therefore have a qualitative resemblance to indirect band gap semiconductors, but with valence and conduction bands that overlap in energy but are separated in momentum space. As a consequence the charge carrier concentration is not as crucial to the emergence of superconductivity as it is in cuprate superconductors, and

superconductivity may be induced through isovalent substitutions or the application of pressure.[25,91-93] Furthermore, unlike in cuprates, iron pnictides exhibit significant overlap between the antiferromagnetic and superconducting domains, with microscopic co-existence of the two phenomena (i.e. all Fe atoms participate in both states).[94]

1.4 Magnetic order

As well as exhibiting perfect diamagnetism in the superconducting state a number of the oxypnictides discussed in this thesis display long range magnetic order. The most common types of magnetic behaviour found in the solid state are discussed below.

1.4.1 Paramagnetism and Diamagnetism

The magnetisation of a sample M is related to the applied magnetic field H by the dimensionless magnetic susceptibility χ_{vol} as shown in *eqn1.3*.

$$\chi_{vol} = \frac{M}{H} \qquad \textit{eqn1.3}$$

Depending on the response of a material's magnetic susceptibility to an applied external field diamagnetism or paramagnetism may be observed.

1.4.2 Diamagnetism

A degree of diamagnetism is encountered in all materials due to paired electrons which weakly repel an applied magnetic field. This is explained classically by the interaction of a magnetic field on the orbital motion of an electron, which induces a small current in the electron cloud which in turn generates an opposing magnetic field, as described by Lenz's law. However, the diamagnetic susceptibilities (10^{-5} emu mol^{-1}) are typically several orders of magnitude weaker than that of other types of magnetic phenomena and are therefore usually disregarded when considering materials with unpaired electrons. Diamagnetism is therefore most commonly observed in non-metallic compounds without unpaired valence electrons and is seen in a largely temperature independent negative magnetic susceptibility.

1.4.3 Paramagnetism

A material is said to express paramagnetism if it contains electrons with un-paired spins which tend to align parallel to an applied external field. Such materials will therefore be attracted to a magnetic field and display a positive magnetic susceptibility. Paramagnets

may be further categorised depending on whether the un-paired electrons are itinerant or localised.

1.4.3.1 Curie Paramagnetism

In a system of non-interacting spins between adjacent atoms or ions, spins will align to be parallel to an applied external field. However, the thermal energy (k_BT) of a system will tend to randomise the spins away from this alignment. Therefore in molecular paramagnets and extended solids with localised un-paired electrons and no interactions between spins there is an inverse relationship between paramagnetic susceptibility and temperature, as described by the Curie law (*eqn1.4*).

$$\chi = \frac{C}{T} \qquad \textit{eqn1.4}$$

Here C is the Curie constant, defined below in *eqn1.5*, where N_A is Avogadro's constant, μ_{eff} is the bohr magneton, μ_{eff} is the effective magnetic moment and k_B is the Boltzmann constant.

$$C = \frac{N_A \mu_{eff}^2 \mu_B^2}{3k_B} \qquad \textit{eqn1.5}$$

$$\mu_{eff} = 2.84\sqrt{C} \qquad \textit{eqn1.6}$$

From this it follows that the effective magnetic moment μ_{eff} may be calculated for a given paramagnetic material by extracting the Curie constant from a plot of $1/\chi$ against T, when measurements are made in low fields away from saturation, and substituting into *eqn1.6*.

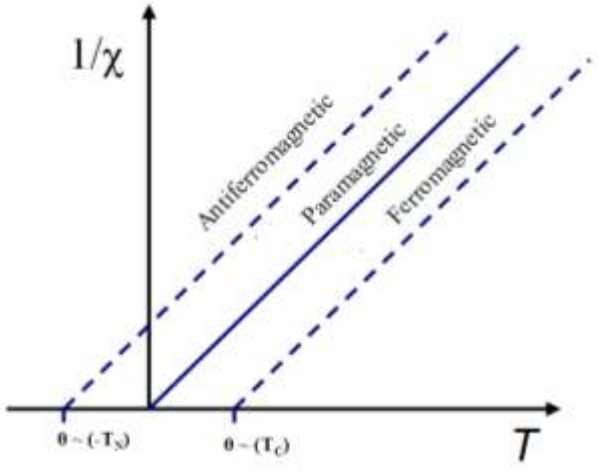

Figure 1.15 Plot of $1/\chi$ against T for Curie and Curie-Weiss paramagnets.

The Landé formula then relates the effective magnetic moment of a free transition metal ion to J (= L + S), the total angular momentum (*eqn1.7*), and the Landé g-factor (*eqn1.8*).

$$\mu_{eff} = g\sqrt{J(J+1)} \qquad \textit{eqn1.7}$$

$$g = 1 + \frac{J(J+1) + S(S+1) - L(L+1)}{2J(J+1)} \qquad \textit{eqn1.8}$$

In 1st row transition metals the orbital angular momentum contribution L is largely quenched by the presence of a ligand field which lifts the degeneracy of the 3*d* orbitals and permits the spin-only approximation to be made (L = 0 hence g =2 and S = J), such that:

$$\mu_{eff} = 2\sqrt{S(S+1)} \qquad \textit{eqn1.9}$$

It is thus possible to ascertain the number of unpaired electrons (2*S*) from a plot of $1/\chi$ against T for a Curie paramagnet. Values for the paramagnetic susceptibility at room temperature are typically of the order of 10^{-3} emu mol^{-1}.

1.4.3.2 Curie-Weiss Paramagnetism

As previously stated, the Curie Law assumes that there are no interactions between unpaired spins on adjacent atoms. More commonly interactions are present below a certain temperature, which tend to align the moments either parallel (ferromagnetic) or antiparallel (antiferromagnetic) to one another. In such cases the magnetic susceptibility deviates from the Curie Law and is often better described by the Curie-Weiss law (*eqn1.10* and Figure 1.15), in which θ is the Weiss constant.

$$\chi = \frac{C}{(T - \theta)} \qquad \textit{eqn1.10}$$

Here ($T - \theta$) is the effective temperature and the sign and magnitude of the Weiss constant θ give an indication of the nature and strength of the interactions. For materials with a positive Weiss constant these interactions are predominantly ferromagnetic and θ is anticipated to be close to the Curie temperature (T_C). Conversely in materials which exhibit a negative Weiss constant antiferromagnetic interactions are predominant and the modulus of θ is proximate to the Neel temperature (T_N). It should also be noted that if attempting to extract an accurate Curie constant for a Curie-Weiss paramagnet this should be done at temperatures well above $|\theta|$, at which the Curie-Weiss Law is valid.

1.4.3.3 Pauli Paramagnetism

Materials with itinerant electrons (metals) exhibit a temperature independent type of paramagnetic behaviour known as Pauli paramagnetism. The application of an external magnetic field means that the two possible spin arrangements of the itinerant electrons in the conduction band become non-degenerate. The energy levels corresponding to those whose spin is aligned with the field are therefore lowered and are preferentially filled in the ground state, generating a net magnetisation which is proportional to the density of states at the Fermi level $N(E_F)$, where μ_0 is the vacuum permeability (*eqn1.11*).

$$\chi = 2\mu_0\mu_B^2 N(E_F) \qquad \textit{eqn1.11}$$

This reveals the temperature independent nature of Pauli paramagnets, whose susceptibility is typically several orders of magnitude lower than that seen in Curie paramagnets. Determination of χ_{Pauli} will necessitate corrections for core diamagnetism and will be hampered by the presence of small amounts of ferromagnetic impurities.

1.4.4 Ferromagnetism

In ferromagnetic materials strong interactions between adjacent spins cause them to align parallel to one another in a domain structure below the characteristic Curie temperature (T_C), even in the absence of an external field. The application of an applied field may then be used to order these domains to be parallel to the applied field and give a net positive magnetisation (Figure 1.16). Ferromagnets therefore exhibit a rapid increase in their susceptibility below T_C which is saturated when all domains become co-aligned (Figure 1.17), with susceptibilities up to the order of 10^5 emu mol^{-1}. Above T_C the interaction between spins is disrupted by thermal energy and paramagnetism is observed.

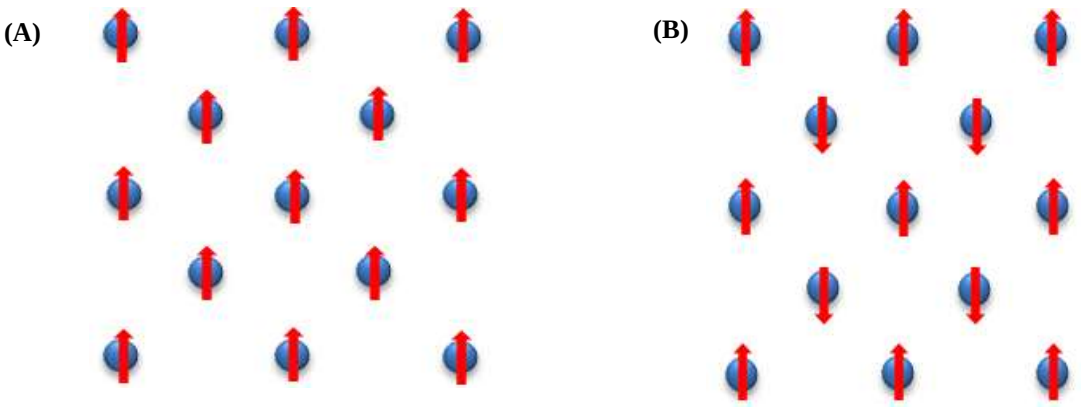

Figure 1.16 Schematic of (A) ferromagnetic and (B) antiferromagnetic ordering in 2D crystal.

Ferromagnetic order is often mediated by long range RKKY and double exchange interactions, which are described in appendix A. Electrical insulators may also exhibit ferromagnetism through superexchange interactions.

1.4.5 Antiferromagnetism

More frequently, exchange interactions result in long-range magnetic order in which the nearest neighbour spins are arranged anti-parallel to one another, below the critical Néel temperature T_N. As shown in (Figure 1.16), at very low temperatures, spins become locked in an anti-parallel alignment to give a net magnetisation that approaches zero, and which does not respond to an applied field. Increasing the temperature or thermal energy of an antiferromagnetic system causes some spins to break free and align with the applied field, increasing the net magnetisation. The magnetisation reaches a maximum at T_N, above which the thermal energy is sufficient to overcome the pairing interaction and paramagnetism is observed (Figure 1.17).

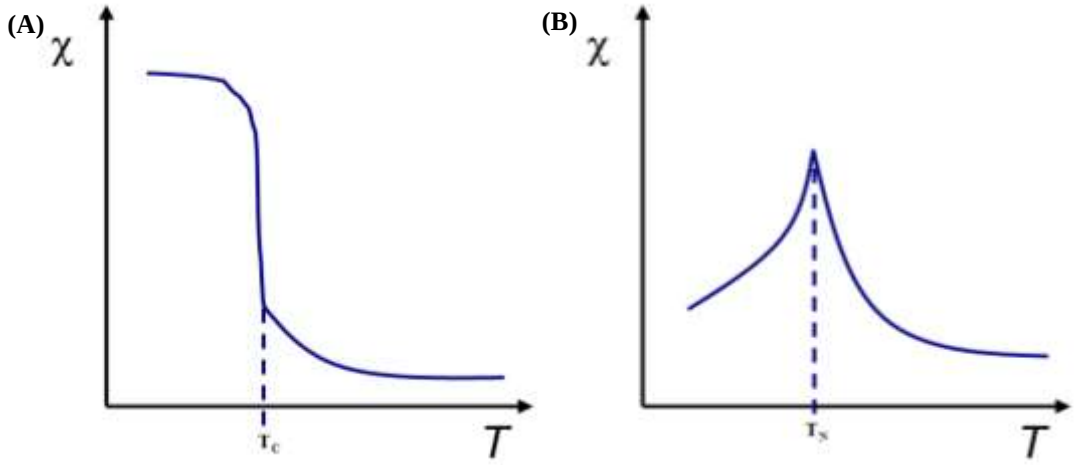

Figure 1.17 Schematic of the general behaviour of χ with *T* for (A) ferromagnetic and (B) antiferromagnetic materials.

The magnitude of the susceptibility for an antiferromagnet is thus considerably less than that of a paramagnet and the profile of the maximum in the susceptibility is instructive as to the dimensionality of the ordering. An abrupt maximum is seen in the susceptibility of materials that order antiferromagnetically in three dimensions, whereas a broad maximum is indicative of lower dimensional ordering. The majority of antiferromagnets only order at low temperatures (T_N < 293 K), though some transition metal compounds can order well above room temperature as in α-Fe_2O_3 (T_N = 953 K). α-Fe_2O_3 in fact exhibits a small

ferromagnetic moment at room temperature due to FM spin canting, a phenomena investigated in this thesis with respect to CeOMnAs in chapter 7.

1.4.6 Magnetic exchange mechanisms

The interactions between magnetic moments can proceed through a number of different mechanisms. Through space interactions are long range, displaying a r^{-3} dependence, but are generally too weak to account for the ordering of magnetic moments, being suppressed by the thermal energy even at very low temperatures.

Much stronger are through-bond exchange interactions which mediate long range order in the majority of magnetic materials. However, such direct exchange interactions are very short range (r^{-12} dependence) and are therefore only significant between the moments on nearest neighbour ions. In materials such as insulators, the neighbouring magnetic cations are separated from each other by some distance by anions necessitating an indirect superexchange pathway for exchange. The specifics of superexchange, direct exchange and RKKY interactions are discussed in further detail in appendix A.

1.4.7 Magnetic dimensionality

As well as the nature of the magnetic exchange interactions, the structural dimensionality of a material will also strongly dictate its magnetic properties. Structural motifs may have three-dimensional, plane or chain connectivity, as shown in section 1.2, leading to strong magnetic exchange in some directions but not in others.

The spin dimensionality of a material also influences its behaviour and three independent models are used to describe the characteristics of different systems. The Ising model has spins constrained to one dimension, so that they are orientated either spin “up” or “down” conventionally along the *z*-axis.[95] In the XY model, spins have the freedom to move in two-dimensions. Lastly in the Heisenberg model, the exchange is assumed to be fully isotropic and the spins have freedom in three-dimensions. Systems which express magnetic order may therefore be divided into different classes according to their lattice and spin dimensionality. Within a given class the critical exponent that describes the manner in which a system goes through a phase transition should be similar. As shown in *eqn1.12* the critical exponent for the magnetisation β relates the magnetisation M on an AFM sub-lattice to its temperature.

$$M = M_0\left(\left(T_N - T\right)T_N\right)^{\beta} \qquad \textit{eqn1.12}$$

Ideal values of the critical exponent β may be solved exactly for 3D lattices for all spin dimensionalities. In the case of a 2D lattice, which is of particular relevance in this thesis due to the layered nature of the structures adopted, the Ising model is the only class for which an exact result is available.[96] However, additional theoretical work has proposed that a 2D lattice with XY character would have a critical exponent of 0.23.[97]

1.4.8 Two-dimensional antiferromagnets

If a system is to be truly two dimensional with respect to its magnetic properties, then there should be no inter-layer exchange. This is essentially the case in materials which feature planes of magnetically coupled ions that are separated from one another by a non-magnetic layers, such that J_{inter} / J_{intra} ~ 10^{-3} – 10^{-6}. The intra-planar interactions are therefore much greater than those between the layers and long range ordered is driven through these in-plane ordering. That is to say that once a material is ordered in 2D, then 3D ordering will occur parasitically, since a very weak interaction between the planes will be amplified by a large number of in-plane spins.

In this thesis a number of different materials are discussed with oxide layers that resemble a portion of the K_2NiF_4 structure. It is therefore useful to consider the types of magnetic interaction that typically occur in these types of system. As discussed briefly in section 1.2, the K_2NiF_4 structure is related to that of the $KNiF_3$ perovskite, but with one extra KF plane separating and offsetting adjacent NiF_2 layers by x + ½, y + ½ relative to one another to give a Ni^{2+} body-centred unit cell (*I*4/*mmm*) as shown in Figure 1.18.

In perovskite $KNiF_3$ strong AFM superexchange interactions generate an antiparallel arrangement of Ni^{2+} spins with the *G*-type magnetic cell shown in Figure 1.18 with propagation vector $\boldsymbol{k}$ = (½, ½, ½). The same AFM superexchange interactions bring about a checkerboard arrangement of Ni^{2+} spins within the NiF_2 planes of K_2NiF_4. However, the separation of the NiF_2 planes in this structure means that the interplanar interactions are negligible. A further consideration is that the net interaction between Ni in one plane and the 4 nearest-Ni-neighbours in the adjacent layer is zero, such that the 3D magnetism with FM ordering between every other layer is driven by the in-plane order.

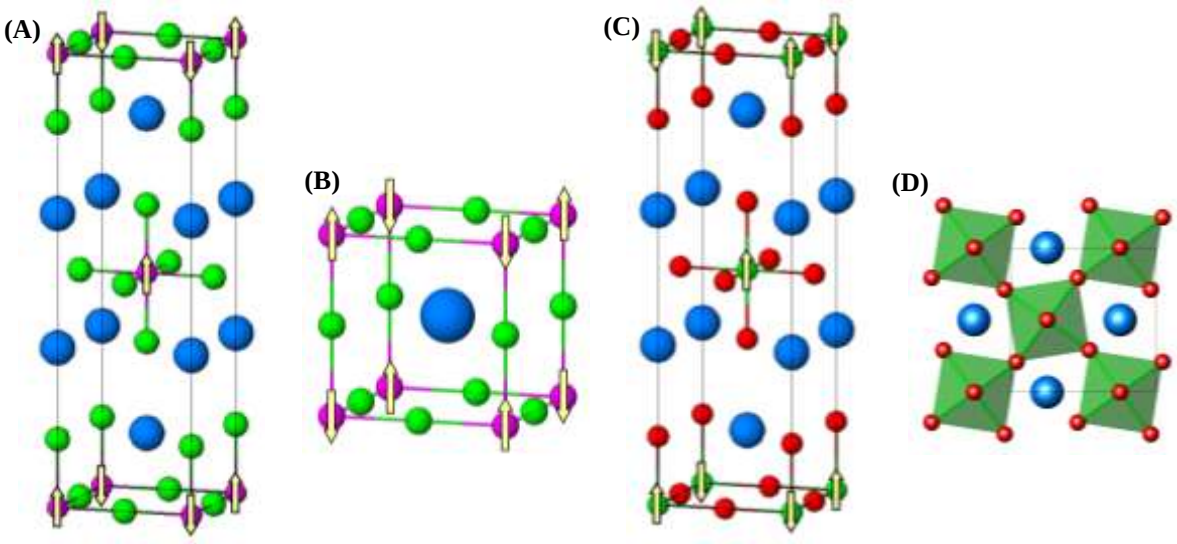

Figure 1.18 Crystallographic unit cells of (A) $KNiF_3$, (B) K_2NiF_4 and (C) Ca_2MnO_4 with spin orientations of transition metals overlaid. Disorder of MnO_6 octahedra is shown in (D).

Ca_2MnO_4, which was initially thought to be isostructural to K_2NiF_4 (*I*4/*mmm*),[98] though has more recently shown to adopt an *I*41/*acd* supercell due to oxygen disorder,[99] exhibits the same type of checkerboard spin arrangement in MnO_2 planes. However in Ca_2MnO_4 the antiferromagnetic coupling of the next-nearest-neighbour layers necessitates a doubling of the magnetic cell along *c* (note. For simplicity the magnetic cell is shown in Figure 1.18 with *I*4/*mmm* symmetry).[100] One further commonality between Ca_2MnO_4 and K_2NiF_4 is that the magnetic moments in both are aligned along the *c*-axis, however it is also possible to encounter 2D antiferromagnetism with spins orientated within the basal plane.

The two common magnetic structure types for three dimensionally ordered K_2NiF_4-type *xy* antiferromagnets are adopted by La_2NiO_4 and La_2CuO_4 (Figure 1.19).[101,102] Both assume non-collinear magnetic structures, described by the propagation vector ***k*** = (½, ½, 0), with the distinction between the two coming from consideration of the orientation of the moments relative to the (110) plane. In La_2CuO_4 there is a net ferromagnetic moment parallel to the (110), whereas in La_2NiO_4 the overall moment is perpendicular to the (110) plane. These magnetic structure types are discussed in more detail in Chapter 4 with respect to the difference between collinear and non-collinear spin arrangements.

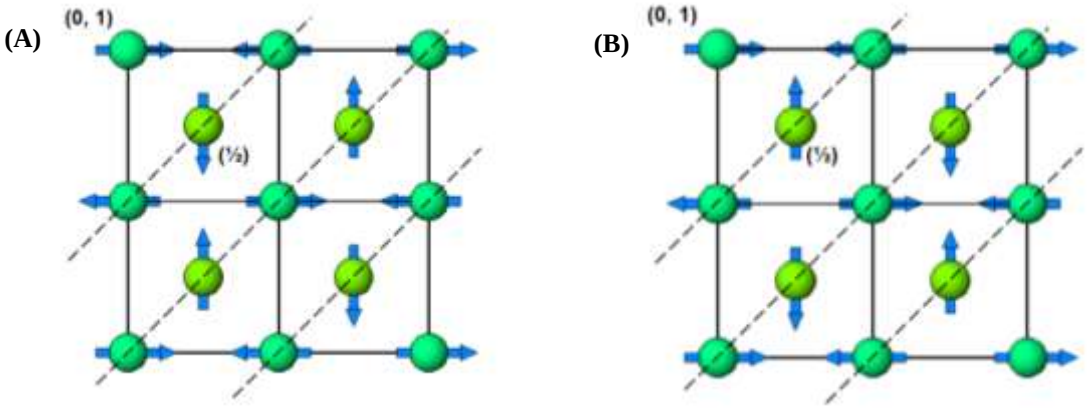

Figure 1.19 Projection along *z* of the magnetic structures of (A) La_2CuO_4 and (B) La_2NiO_4. The dotted black lines describe the (110) Bragg planes.

1.5 Aims of this thesis

The work described in this thesis focuses on the oxide arsenides CeOMnAs and Sr_2MO_3FeAs (*M* = Sc, V, Cr) which both feature anti-PbO-type *M*As layers. Despite the similarities in the crystal structures of these materials, their physical properties are radically different and are largely dictated by the choice of the transition metal *M* at the tetrahedral site in the arsenide layers.

In chapter 3 attempts are made to synthesise a new FeAs structure type. The structure, stoichiometry and properties of the novel oxide arsenide Sr_2ScO_3FeAs are then assessed by powder neutron diffraction, SQUID magnetometry and resistivity measurements. Efforts are then made to electron and hole dope this material into the superconducting regime by aliovalent substitutions on a variety of crystallographic sites.

In chapter 4 the range of materials with the Sr_2MO_3FeAs structure is extended to include a Cr analogue. The long range antiferromagnetic ordering of Cr^{3+} spins in this compound is then characterised by powder neutron diffraction measurements and compared with that of other materials with magnetic order on a K_2NiF_4 lattice. The effect of Co substitution in $Sr_2CrO_3Fe_{1-x}Co_xAs$ on the magnetic and superconducting properties of this material is then examined.

The report of superconductivity below 37 K in "undoped" Sr_2VO_3FeAs has provided the inspiration for chapter 5.[103] In this chapter the likely origins of superconductivity are investigated by assessing the crystal structure, stoichiometry and valence state of Fe and V in this material. Magnetic transitions on the V sublattice in Sr_2VO_3FeAs are then probed by

SQUID magnetometry, μSR and powder neutron diffraction measurements. Attempts to optimise the superconducting properties of Sr_2VO_3FeAs through aliovalent and isovalent substitutions on a variety of crystallographic sites are described in chapter 6. The structural and electronic changes imparted by these substitutions are then used to rationalise the observed changes in the magnetic and superconducting properties of these materials.

Finally in chapter 7, the manganese oxide arsenide CeOMnAs is considered. Materials with anti-PbO-type MnAs layers, like $BaMn_2As_2$ typically order antiferromagnetically with Mn moments orientated along the *c* axis.[28] However, recent PND studies on NdOMnAs reveal an intriguing spin-reorientation transition accompanied with AFM ordering of Nd moments.[104] In this chapter powder neutron diffraction studies are made to characterise the proposed spin reorientation transition in CeOMnAs.

References

(1) Bednorz, J. G.; Müller, K. A. *Zeitschrift für Physik B Condensed Matter* **1986**, *64*, 189-193.
(2) Wu, M. K.; Ashburn, J. R.; Torng, C. J.; Hor, P. H.; Meng, R. L.; Gao, L.; Huang, Z. J.; Wang, Y. Q.; Chu, C. W. *Physical Review Letters* **1987**, *58*, 908-910.
(3) Matthias, B. T.; Geballe, T. H.; Geller, S.; Corenzwit, E. *Physical Review* **1954**, *95*, 1435-1435.
(4) Bruce, P. G. *Chemical Communications* **1997**, 1817-1824.
(5) Williams, G. R.; Dunbar, T. G.; Beer, A. J.; Fogg, A. M.; O'Hare, D. *Journal of Materials Chemistry* **2006**, *16*, 1231-1237.
(6) Ambrogi, V.; Fardella, G.; Grandolini, G.; Perioli, L. *International Journal of Pharmaceutics* **2001**, *220*, 23-32.
(7) Saha, D.; Deng, S. *The Journal of Physical Chemistry Letters* **2009**, *1*, 73-78.
(8) Proch, S.; Herrmannsdörfer, J.; Kempe, R.; Kern, C.; Jess, A.; Seyfarth, L.; Senker, J. *Chemistry – A European Journal* **2008**, *14*, 8204-8212.
(9) Dams, M.; Drijkoningen, L.; Pauwels, B.; Van Tendeloo, G.; De Vos, D. E.; Jacobs, P. A. *Journal of Catalysis* **2002**, *209*, 225-236.
(10) Bate, G. *Journal of Magnetism and Magnetic Materials* **1991**, *100*, 413-424.
(11) Judy, J. H. *Journal of Magnetism and Magnetic Materials* **2005**, *287*, 16-26.
(12) Schiffer, P.; Ramirez, A. P.; Bao, W.; Cheong, S. W. *Physical Review Letters* **1995**, *75*, 3336-3339.
(13) Linsebigler, A. L.; Lu, G.; Yates, J. T. *Chemical Reviews* **1995**, *95*, 735-758.
(14) Nagamatsu, J.; Nakagawa, N.; Muranaka, T.; Zenitani, Y.; Akimitsu, J. *Nature* **2001**, *410*, 63-64.
(15) Yamane, H.; Shimada, M.; Clarke, S. J.; DiSalvo, F. J. *Chemistry of Materials* **1997**, *9*, 413-416.
(16) Kamihara, Y.; Watanabe, T.; Hirano, M.; Hosono, H. *Journal of the American Chemical Society* **2008**, *130*, 3296.
(17) Bragg, W. L. *Proceedings of the Royal Society of London, Series A: Mathematical and Physical Sciences* **1914**, *89*, 468-489.
(18) Sakuma, T.; Saitoh, S. *Journal of the Physical Society of Japan* **1985**, *54*, 3647-3648.
(19) Okazaki, H.; Tachibana, F. *Solid State Ionics* **1990**, *40, 1*, 171-174.
(20) Yeh, C.; Lu, Z. W.; Froyen, S.; Zunger, A. *Physical Review, Serie 3. B - Condensed Matter* **1992**, *46*, 10086-10097.
(21) Moore, W. J.; Pauling, L. *Journal of the American Chemical Society* **1941**, *63*, 1392-1394.
(22) Dickens, B. *Journal of Inorganic and Nuclear Chemistry* **1965**, *27*, 1503-1507.
(23) Haegg, G.; Kindstrom, A. L. *Zeitschrift fuer Physikalische Chemie, Abteilung B: Chemie der Elementarprozesse, Aufbau der Materie* **1933**, *22*, 453-464.
(24) Hsu, F. C.; Luo, J. Y.; Yeh, K. W.; Chen, T. K.; Huang, T. W.; Wu, P. M.; Lee, Y. C.; Huang, Y. L.; Chu, Y. Y.; Yan, D. C.; Wu, M. K. *Proceedings of the National Academy of Sciences of the United States of America* **2008**, *105*, 14262-14264.
(25) Mizuguchi, Y.; Tomioka, F.; Tsuda, S.; Yamaguchi, T.; Takano, Y. *Applied Physics Letters* **2008**, *93*, 3.
(26) Ban, Z.; Sikirica, M. *Acta Crystallographica* **1965**, *18*, 594-599.
(27) Just, G.; Paufler, P. *Journal of Alloys and Compounds* **1996**, *232*, 1-25.
(28) An, J.; Sefat, A. S.; Singh, D. J.; Du, M.-H. *Physical Review B* **2009**, *79*, 075120.
(29) Reehuis, M.; Jeitschko, W.; Moeller, M. H.; Brown, P. J. *Journal of Physics and Chemistry of Solids* **1992**, *53*, 687-690.

(30) Pfisterer, M.; Nagorsen, G. *Zeitschrift fuer Naturforschung, Teil B. Anorganische Chemie, Organische Chemie* **1980**, *35*, 703-704.
(31) Tegel, M.; Rotter, M.; Weiss, V.; Schappacher, F. M.; Poettgen, R.; Johrendt, D. *Journal of Physics: Condensed Matter* **2008**, *20*, 452201.
(32) Rotter, M.; Tegel, M.; Schellenberg, I.; Schappacher, F. M.; Pottgen, R.; Deisenhofer, J.; Gunther, A.; Schrettle, F.; Loidl, A.; Johrendt, D. *New Journal of Physics* **2009**, *11*, 18.
(33) Guo, J.; Jin, S.; Wang, G.; Wang, S.; Zhu, K.; Zhou, T.; He, M.; Chen, X. *Physical Review B* **2010**, *82*, 180520.
(34) Raccah, P. M.; Longo, J. M.; Eick, H. A. *Inorganic Chemistry* **1967**, *6*, 1471-1473.
(35) Nieuwenkamp, W.; Bijvoet, J. M. *Zeitschrift fuer Kristallographie, Kristallgeometrie, Kristallphysik, Kristallchemie* **1932**, *81*, 469-473.
(36) Pearson, W. B. *Canadian Journal of Physics* **1964**, *42*, 519-525.
(37) El haj Hassan, F.; Akbarzadeh, H.; Hashemifar, S. J.; Mokhtari, A. *Journal of Physics and Chemistry of Solids* **2004**, *65*, 1871-1878.
(38) Juza, R.; Langer, K. *Zeitschrift Fur Anorganische Und Allgemeine Chemie* **1968**, *361*, 58.
(39) Parker, D. R.; Pitcher, M. J.; Baker, P. J.; Franke, I.; Lancaster, T.; Blundell, S. J.; Clarke, S. J. *Chemical Communications* **2009**, *2009*, 2189-2191.
(40) Pitcher, M. J.; Parker, D. R.; Adamson, P.; Herkelrath, S. J. C.; Boothroyd, A. T.; Ibberson, R. M.; Brunelli, M.; Clarke, S. J. *Chemical Communications* **2008**, 5918-5920.
(41) Parker, D. R.; Smith, M. J. P.; Lancaster, T.; Steele, A. J.; Franke, I.; Baker, P. J.; Pratt, F. L.; Pitcher, M. J.; Blundell, S. J.; Clarke, S. J. *Physical Review Letters* **2010**, *104*, 057007.
(42) Yamane, H.; DiSalvo, F. J. *Journal of Alloys Compd.* **1996**, *234*, 203-206.
(43) Johnson, V.; Jeitschko, W. *Journal of Solid State Chemistry* **1974**, *11*, 161-166.
(44) Rainer Pöttgen, D. J. *Z. Naturforsch.* **2008**, *63b*.
(45) Palazzi, M. *Comptes Rendus Hebdomadaires des Seances de l'Academie des Sciences, Serie C, Sciences Chimiques* **1981**, *292*, 7899-7919.
(46) Palazzi, M.; Jaulmes, S. *Acta Crystallographica B* **1981**, *37*, 1337-1339.
(47) Wilmer, D.; Wuensch, B. J.; Jorgensen, J. D. *Materials Research Society Symposia Proceedings* **1999**, *548*, 455-460.
(48) Raffius, H.; Morsen, E.; Mosel, B. D.; Mueller-Warmuth, W.; Jeitschko, W.; Terbuchte, L.; Vomhof, T. *Journal of Physics and Chemistry of Solids* **1993**, *54*, 135-144.
(49) Ren, Z.-A.; Lu, W.; Yang, J.; Yi, W.; Shen, X.-L.; Zheng, C.; Che, G.-C.; Dong, X.-L.; Sun, L.-L.; Zhou, F.; Zhao, Z.-X. *Chinese Physics Letters* **2008**, *25*, 2215.
(50) Cheng, P.; Shen, B.; Mu, G.; Zhu, X. Y.; Han, F.; Zeng, B.; Wen, H. H. *European physics letters* **2009**, *85*, 4.
(51) Matsuishi, S.; Inoue, Y.; Nomura, T.; Yanagi, H.; Hirano, M.; Hosono, H. *Journal of the American Chemical Society* **2008**, *130*, 14428.
(52) Zhu, W. J.; Hor, P. H. *Journal of Solid State Chemistry* **1997**, *130*, 319-321.
(53) Hyett, G.; Barrier, N.; Clarke, S. J.; Hadermann, J. *Journal of the American Chemical Society* **2007**, *129*, 11192-11201.
(54) Rutt, O. J.; Williams, G. R.; Clarke, S. J. *Chemical Communications* **2006**, *2006*, 2869-2871.
(55) Clarke, S. J.; Adamson, P.; Herkelrath, S. J. C.; Rutt, O. J.; Parker, D. R.; Pitcher, M. J.; Smura, C. F. *Inorganic Chemistry* **2008**, *47*, 8473-8486.

(56) Smura, C. F.; Parker, D. R.; Zbiri, M.; Johnson, M. R.; Gal, Z. A.; Clarke, S. J. *Journal of the American Chemical Society* **2011**, *133*, 2691-2705.
(57) Otzschi, K.; Ogino, H.; Shimoyama, J. I.; Kishio, K. *Journal of Low Temperature Physics* **1999**, *117*, 729-733.
(58) Zhu, W. J.; Hor, P. H. *Journal of Solid State Chemistry* **1997**, *134*, 128-131.
(59) Zhu, W. J.; Hor, P. H. *Journal of Solid State Chemistry* **2000**, *153*, 26-29.
(60) Zhu, W. J.; Hor, P. H. *Inorganic Chemistry* **1997**, *36*, 3576-3577.
(61) Evans, J. S. O.; Brogden, E. R.; Thompson, A. L.; Cordiner, R. L. *Chemical Communications* **2002**, *2002*, 912-913.
(62) Milne, C. J.; Lightfoot, P.; Jorgensen, J. D.; Short, S. *Journal of Materials Chemistry* **1995**, *5*, 1419-1421.
(63) Zheng, C.; Hoffmann, R. *Journal of the American Chemical Society* **1986**, *108*, 3078-3088.
(64) Onnes, H. K. *Commun. Phys. Lab. Univ. Leiden* **1911**, *12*, 120.
(65) Ochsenfeld, W. M. a. R. *Naturwissenschaften* **1933**, *21*, 787.
(66) Maxwell, E. *Physical Review* **1950**, *78*, 477-477.
(67) Reynolds, C. A.; Serin, B.; Wright, W. H.; Nesbitt, L. B. *Physical Review* **1950**, *78*, 487-487.
(68) Bardeen, J.; Cooper, L. N.; Schrieffer, J. R. *Physical Review* **1957**, *108*, 1175-1204.
(69) Cava, R. J.; van Dover, R. B.; Batlogg, B.; Rietman, E. A. *Physical Review Letters* **1987**, *58*, 408-410.
(70) Hazen, R. M.; Prewitt, C. T.; Angel, R. J.; Ross, N. L.; Finger, L. W.; Hadidiacos, C. G.; Veblen, D. R.; Heaney, P. J.; Hor, P. H.; Meng, R. L.; Sun, Y. Y.; Wang, Y. Q.; Xue, Y. Y.; Huang, Z. J.; Gao, L.; Bechtold, J.; Chu, C. W. *Physical Review Letters* **1988**, *60*, 1174-1177.
(71) Torardi, C. C.; Subramanian, M. A.; Calabrese, J. C.; Gopalakrishnan, J.; Morrissey, K. J.; Askew, T. R.; Flippen, R. B.; Chowdhry, U.; Sleight, A. W. *Science* **1988**, *240*, 631-634.
(72) Schilling, A.; Cantoni, M.; Guo, J. D.; Ott, H. R. *Nature* **1993**, *363*, 56-58.
(73) Gao, L.; Xue, Y. Y.; Chen, F.; Xiong, Q.; Meng, R. L.; Ramirez, D.; Chu, C. W.; Eggert, J. H.; Mao, H. K. *Physical Review B* **1994**, *50*, 4260-4263.
(74) Damascelli, A.; Hussain, Z.; Shen, Z.-X. *Reviews of Modern Physics* **2003**, *75*, 473-541.
(75) Lee, P. A.; Nagaosa, N.; Wen, X.-G. *Reviews of Modern Physics* **2006**, *78*, 17-85.
(76) Ren, Z. A.; Lu, W.; Yang, J.; Yi, W.; Shen, X. L.; Li, Z. C.; Che, G. C.; Dong, X. L.; Sun, L. L.; Zhou, F.; Zhao, Z. X. *Chinese Physics Letters* **2008**, *25*, 2215-2216.
(77) Wang, C.; Li, Y. K.; Zhu, Z. W.; Jiang, S.; Lin, X.; Luo, Y. K.; Chi, S.; Li, L. J.; Ren, Z.; He, M.; Chen, H.; Wang, Y. T.; Tao, Q.; Cao, G. H.; Xu, Z. A. *Physical Review B* **2009**, *79*, 9.
(78) Xu, M.; Chen, F.; He, C.; Ou, H. W.; Zhao, L. F.; Feng, D. L. *Chemistry of Materials* **2008**, *20*, 7201-7203.
(79) Hunte, F.; Jaroszynski, J.; Gurevich, A.; Larbalestier, D. C.; Jin, R.; Sefat, A. S.; McGuire, M. A.; Sales, B. C.; Christen, D. K.; Mandrus, D. *Nature* **2008**, *453*, 903-905.
(80) Kasperkiewicz, K.; Bos, J. W. G.; Fitch, A. N.; Prassides, K.; Margadonna, S. *Chemical Communications* **2009**, 707-709.
(81) Baker, P. J.; Franke, I.; Lancaster, T.; Blundell, S. J.; Kerslake, L.; Clarke, S. J. *Physical Review B* **2009**, *79*, 4.
(82) Rotter, M.; Tegel, M.; Johrendt, D. *Physical Review Letters* **2008**, *101*, 107006.

(83) Nandi, S.; Kim, M. G.; Kreyssig, A.; Fernandes, R. M.; Pratt, D. K.; Thaler, A.; Ni, N.; Bud'ko, S. L.; Canfield, P. C.; Schmalian, J.; McQueeney, R. J.; Goldman, A. I. *Physical Review Letters* **2010**, *104*, 057006.
(84) Avci, S.; Chmaissem, O.; Chung, D. Y.; Rosenkranz, S.; Goremychkin, E. A.; Castellan, J. P.; Todorov, I. S.; Schlueter, J. A.; Claus, H.; Daoud-Aladine, A.; Khalyavin, D. D.; Kanatzidis, M. G.; Osborn, R. *Physical Review B* **2012**, *85*, 184507.
(85) Parker, D. R.; Pitcher, M. J.; Baker, P. J.; Franke, I.; Lancaster, T.; Blundell, S. J.; Clarke, S. J. *Chemical Communications* **2009**, 2189-2191.
(86) Pitcher, M. J.; Lancaster, T.; Wright, J. D.; Franke, I.; Steele, A. J.; Baker, P. J.; Pratt, F. L.; Thomas, W. T.; Parker, D. R.; Blundell, S. J.; Clarke, S. J. *Journal of the American Chemical Society* **2010**, *132*, 10467-10476.
(87) Lee, C.-H.; Iyo, A.; Eisaki, H.; Kito, H.; Fernandez-Diaz, M. T.; Ito, T.; Kihou, K.; Matsuhata, H.; Braden, M.; Yamada, K. *Journal of the Physical Society of Japan* **2008**, *77*, 083704.
(88) Johrendt, D.; Hosono, H.; Hoffmann, R.-D.; Poettgen, R. *Zeitschrift für Kristallographie* **2011**, *226*, 435-446.
(89) Boeri, L.; Dolgov, O. V.; Golubov, A. A. *Physical Review Letters* **2008**, *101*, 026403.
(90) Mazin, I. I. *Nature* **2010**, *464*, 183-186.
(91) Alireza, P. L.; Ko, Y. T. C.; Gillett, J.; Petrone, C. M.; Cole, J. M.; Lonzarich, G. G.; Sebastian, S. E. *Journal of Physics-Condensed Matter* **2009**, *21*, 4.
(92) Millican, J. N.; Phelan, D.; Thomas, E. L.; Leao, J. B.; Carpenter, E. *Solid State Communications* **2009**, *149*, 707-710.
(93) Iye, T.; Nakai, Y.; Kitagawa, S.; Ishida, K.; Kasahara, S.; Shibauchi, T.; Matsuda, Y.; Terashima, T. *Journal of the Physical Society of Japan* **2012**, *81*, 033701.
(94) Wiesenmayer, E.; Luetkens, H.; Pascua, G.; Khasanov, R.; Amato, A.; Potts, H.; Banusch, B.; Klauss, H.-H.; Johrendt, D. *Physical Review Letters* **2011**, *107*, 237001.
(95) Barry, A. C. *Am. Math. Monthly* **1987**, *94*, 937-959.
(96) Onsager, L. *Physical Review* **1944**, *65*, 117-149.
(97) Bramwell, S. T.; Holdsworth, P. C. W. *Physical Review B* **1994**, *49*, 8811-8814.
(98) Ruddlesden, S. N.; Popper, P. *Acta Crystallographica* **1957**, *10*, 538-539.
(99) Leonowicz, M. E.; Poeppelmeier, K. R.; Longo, J. M. *Journal of Solid State Chemistry* **1985**, *59*, 71-80.
(100) Cox, D. E.; Shirane, G.; Birgeneau, R. J.; MacChesney, J. B. *Physical Review* **1969**, *188*, 930-932.
(101) Aeppli, G.; Buttrey, D. J. *Physical Review Letters* **1988**, *61*, 203-206.
(102) Vaknin, D.; Sinha, S. K.; Moncton, D. E.; Johnston, D. C.; Newsam, J. M.; Safinya, C. R.; King, H. E., Jr. *Physical Review Letters* **1987**, *58*, 2802-2805.
(103) Zhu, X. Y.; Han, F.; Mu, G.; Cheng, P.; Shen, B.; Zeng, B.; Wen, H. H. *Physical Review B* **2009**, *79*, 4.
(104) Emery, N.; Wildman, E. J.; Skakle, J. M. S.; McLaughlin, A. C.; Smith, R. I.; Fitch, A. N. *Physical Review B* **2011**, *83*, 144429.

2 Experimental and Characterisation techniques

2.1 Synthetic methods

2.1.1 Solid state synthesis

Traditional solid state ceramic synthesis techniques involve the weighing out of stoichiometric quantities of reactants which are mixed together in an agate pestle and mortar. This grinding process reduces the size of the grains and homogenises the mixture to promote reaction. The mixture is then typically placed in an alumina crucible, chosen for its high melting point and inert nature, and heated to temperature for a period of anywhere from a couple of hours to a few weeks. The temperatures employed in such reactions range from 500 – 1400 ° C. At these temperatures the reactant ions may diffuse through the powder particles overcoming the kinetic barrier to reaction to give the most thermodynamically stable product. If any unreacted crystallites remain they are reintroduced at grain boundaries by a repeat process of grinding and annealing. To further encourage reaction, reagent mixtures are often pressed into pellets to maximise grain contact and enhance reaction rates. Annealing temperatures and times should be chosen carefully to avoid the favourable formation of side products, an issue that has proved particularly problematic in attempts to synthesise phase pure samples of the materials discussed in Chapter 6.

At the temperatures required for ceramic synthesis, the oxypnictides described in this thesis would be readily oxidised if treated in air. Additionally many of the reactants used are air and moisture sensitive. Therefore all stages in their preparation were carried out in an inert atmosphere. An argon-filled dry box was used for the storage, weighing and mixing of all of the reagents used in this thesis. In order to press a sample into a pellet, the homogenised reagent mixture is loaded into a 13 mm pellet die which is sealed inside two polythene bags. This ensemble is then removed from the glove-box, pressed into a pellet at a force of 3 tonnes, before being returned to the glove-box. The pellet is then positioned in an alumina crucible and placed in a silica tube that has been sealed at one end. Next an end-cap equipped with a Young's tap is fitted onto the end of the tube. The Young's tap is then closed and the ensemble removed from the glove box and attached to a vacuum line. The tube is then evacuated to a pressure of ~ 10^{-2} mbar and sealed under dynamic vacuum with a methane-oxygen blowtorch. All silica tubes are stored in a drying oven and

"flamed out", by heating for 5 minutes using a methane-oxygen torch under a dynamic vacuum, prior to use. This avoids the possibility of the hydrolysis of the reagents or target material by water absorbed to the inside of the silica tube.

In performing reactions involving volatile alkaline earth metals such as Sr, the use of an evacuated silica tube is not appropriate since the high vapour pressure which may be generated during a reaction presents an explosion hazard. Instead sealed ampoules of a suitably inert metal, in this case niobium, are used. Nb ampoules were prepared by crimping the end of an Nb tube and sealing under an Ar atmosphere using arc-welding apparatus. The metal ampoule itself is then sealed in an evacuated silica tube to avoid corrosion by atmospheric oxygen at the reaction temperatures.

2.1.2 Argon-filled dry box

To prevent aerial oxidation/H_2O adsorption of reagents and products, all samples described in this thesis were prepared and stored in a Glovebox technology argon-filled dry box, the atmosphere of which is continually circulated through a molecular sieve bed and a BASF copper catalyst to remove H_2O and O_2, respectively. An O_2 sensor is also employed to monitor the concentration of O_2, which should not rise above 1ppm under normal working conditions. To help maintain a clean atmosphere, all material brought into the dry box is dried in an oven prior to use.

2.1.3 Synthesis of starting materials

2.1.3.1 Preparation of SrO

SrO was used in the syntheses of Sr_2MO_3FeAs materials described in Chapters 3 - 6, and was prepared by the thermal decomposition of $SrCO_3$ (Alfa, 99.99 %,).[1] To do this approximately 5 g of $SrCO_3$ was loaded in an alumina boat and placed in a 25 mm silica tube sealed at one end. An O-ring fitted end cap with a three way tap was then attached to the open end of the tube, and the whole assembly positioned in a split tube furnace and attached to a vacuum line (Figure 2.1).

The tube was then evacuated to a pressure < 10^{-2} mbar and heated under dynamic vacuum at 10 °C min^{-1} to 850 °C and held for 18 h, before being ramped at 10 °C min^{-1} to 1100 C for a final 4 h firing. After allowing the tube to cool to room temperature, the three-way tap was closed and the ensemble taken into the argon dry box. Sample purity was then

analysed by X-ray powder diffraction. The highly air-sensitive nature of SrO necessitates the use of an air tight cell, to avoid absorption of H_2O and CO_2.

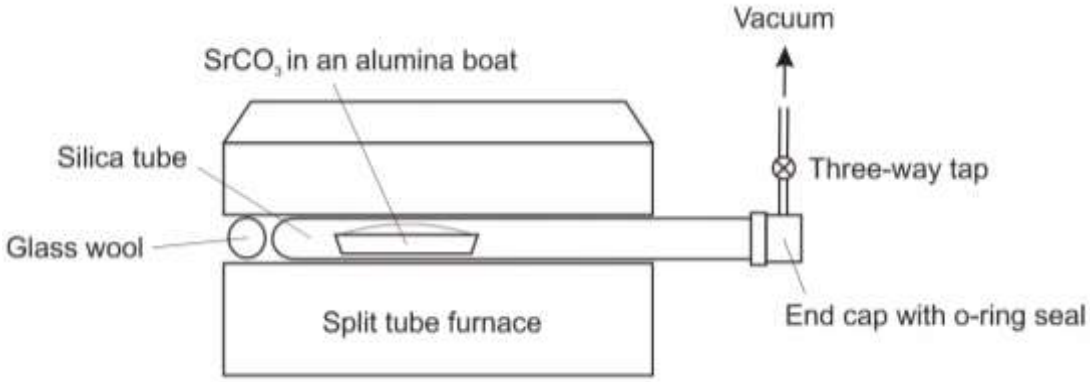

Figure 2.1 Experiment setup used for the thermal decomposition of $SrCO_3$ to SrO

2.1.3.2 Drying hygroscopic materials

To remove the presence of any absorbed moisture, hygroscopic CeO_2 (Alfa 99.99 %) was loaded into an alumina crucible and dried at 800 °C for 24 h. Sample purity was then assessed by X-ray powder diffraction.

2.1.3.3 Synthesis of CeAs, VAs and CrAs

CeAs, VAs and CrAs were prepared by a routine ceramic method, in which stoichiometric amounts of Cr (Alfa, 99.99 %) and V (Alfa, 99.5 %) metal powders, or metal filings in the case of Ce (Alfa, 99.8 %), were combined with pre-ground As powder (Alfa, 99.9999 %). These mixtures were loaded and sealed in silica ampoules, then heated slowly to temperature at 1 °C min^{-1}, this slow ramp rate was necessary so as to avoid the build up of high partial pressures due to the sublimation of As prior to reaction. The samples were then returned to the argon-filled dry box, opened and thoroughly ground.

2.1.3.4 Synthesis of SrAs

SrAs was prepared by combining stoichiometric amounts of pre-ground As powder (Alfa, 99.9999 %) with Sr (Alfa 99.95 %) pieces in a niobium tube, which was sealed under flowing argon (as described in section 2.1.1), then heated at 1 °C min^{-1} to 800 °C and held for 48 h. The highly air sensitive product was then placed in the argon dry box where it was ground and stored.

2.2 Characterisation techniques

2.2.1 Crystal systems

The vast majority of samples prepared in this thesis are crystalline in nature, with periodic atomic arrays. A crystalline solid is a space filling 3D crystal which is generated by the translational repetition of a structural motif. The lattice can be described by assigning points to generate a parallelepiped and define a unit cell, in which the edges of the cell (*a*, *b*, *c*) and angles between each pair of them (α, β, γ) are the unit cell parameters. In the case where only translational symmetry is present, $a \neq b \neq c$ and $\alpha \neq \beta \neq \gamma$ and such a system is termed "triclinic". The application of rotation and reflection symmetry elements generates a total of 7 different crystal classes.

A unit cell containing only a single lattice point is described as primitive and designated the space group symbol *P*. A unit cell containing more than one lattice point is described as being centred. The centring may be body-centred (*I*), in which there is an additional lattice point at the centre of the cell, faced-centred with lattice points at the centre of each face (*F*), or face-centred with lattice points at the centres of one pair of opposite faces (*A*, *B* or *C*). The combination these four types of lattice with the 7 possible crystal systems generates 14 permissible classes of Bravais lattice. The combination of the Bravais lattice type with all possible symmetry elements for the unit cell then define 230 unique space groups.

2.2.2 Diffraction

The periodic nature of the crystalline state makes structural characterisation by diffraction a very powerful tool. When a crystalline sample is illuminated by radiation with a wavelength comparable to that of the interatomic spacing (0.3 - 3 Å) each atom scatters radiation and acts as a secondary point source. If the radiation is scattered coherently, then constructive interference will occur and beams of diffracted intensity may be observed in certain allowed directions.

2.2.3 X-ray diffraction

A beam of X-rays incident to a crystal may interact with it in a number of different ways. In the process of fluorescence, photons are absorbed through the ionisation of core electrons and when the resulting ions relax back to their ground state secondary photons are emitted in random directions. This contributes to the background signal in an X-ray

diffraction experiment, but can be minimised by selecting X-rays of appropriate wavelength. X-rays may also be scattered by the Coulombic interaction of the oscillating electric field of an X-ray with an electron – which acts as a secondary point source. If the scattered radiation has the same wavelength as the incident photon the scattering is said to be elastic and it is this process which gives rise to X-ray diffraction. Max von Laue developed the first theory of the diffraction of X-rays by crystals in 1912, for which he received the 1914 Nobel Prize for Physics. He considered crystals to be a three dimensional network of atoms with a spacing of *a* along the *x*-axis, *b* along the *y*-axis and *c* along the *z*-axis. The theory can however be more simply illustrated by the hypothetical 1D row of atoms shown in Figure 2.2.

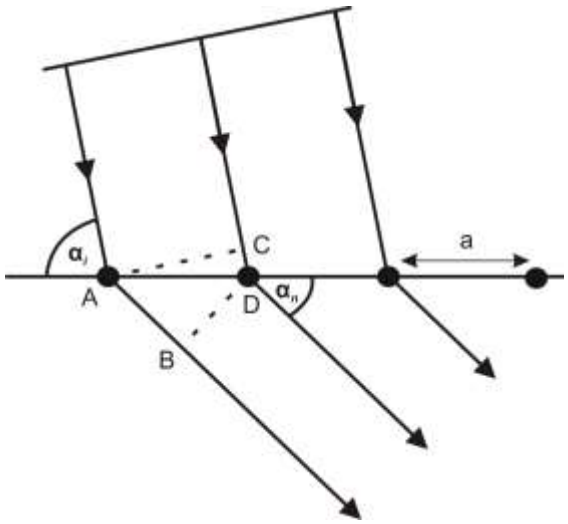

Figure 2.2 Diffraction of X-rays by a row of atoms

The condition for constructive interference from a row of atoms along the *x*-axis is then satisfied if the path length differs by an integer number (n) of wavelengths (λ):

$$AB - CD = a(\cos\alpha_n - \cos\alpha_i) = n\lambda \qquad \textit{eqn2.1}$$

Similar consideration of diffraction from rows of atoms along the *y* and *z* axes delivers the 2nd and 3rd Laue equations:

$$b(\cos\beta_n - \cos\beta_i) = n_y\lambda \qquad \textit{eqn2.2}$$

$$c(\cos\gamma_n - \cos\gamma_i) = n_z\lambda \qquad \textit{eqn2.3}$$

This is a mathematically rigorous approach, but requires the determination of up to 12 variables and their complexity limits their practical use in crystallography. Bragg's contribution took a different approach and considered diffraction as arising from the reflection of X-rays from planes of atoms within a crystal.

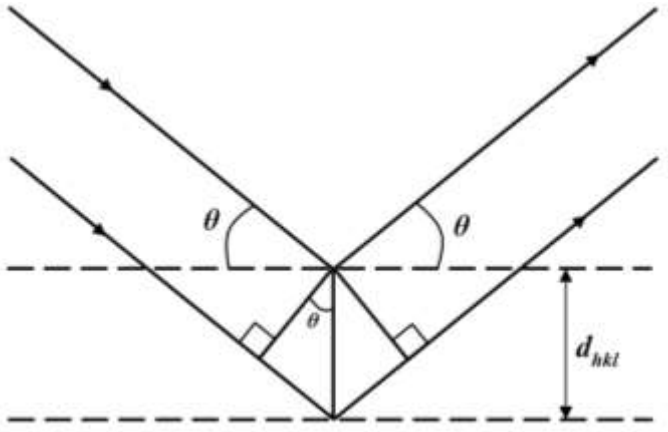

Figure 2.3 Bragg diffraction from lattice planes in a crystal.

These sets of planes are defined by the Miller indices *h k l* which intersect the unit cell edges at *a*/*h*, *b*/*k* and *c*/*l*, respectively. Constructive interference of reflected radiation will then occur when the path difference between scattered beams of X-rays is an integer number of wavelengths. It then follows from consideration of Figure 2.3 that the wavelength of the radiation (λ), the angle (θ) of the incident radiation to the planes and the distance between the planes (d_{hkl}) may be related by Bragg's Law:

$$n\lambda = 2d_{hkl}\sin\theta \qquad \textit{eqn2.4}$$

A routine X-ray diffraction experiment utilizes a monochromatic beam of incident X-ray radiation and a detector measures the intensity of the diffracted beams of radiation as a function of 2θ. An alternative assembly measures the diffracted intensity at a fixed value of θ and λ is used as a variable to obtain the same information. Assignment of *hkl* indices to the observed reflections, is known as indexing and allows the determination of the crystal system and cell parameters. Examination of the system absences, due to the presence of translational symmetry within the unit cell, then facilitates elucidation of the centring type and other translational symmetry operations and thus the Bravais lattice and space group may be determined. The intensity of a reflection I_{hkl} is dependent on the structure factor F_{hkl}, the Lorentz factor L (instrument geometry), a polarisation correction p and a scale factor s:

$$I_{hkl} = sLp\left|F_{hkl}\right|^2 \qquad \textit{eqn2.5}$$

The structure factor F_{hkl} dominates the equation and so we may write:

$$I_{hkl} \propto \left|F_{hkl}\right|^2 \qquad \textit{eqn2.6}$$

The structure factor F_{hkl} is a complex mathematical function that describes the phase and the amplitude of a wave diffracted from lattice planes with Miller indices *h k l* and is shown below:

$$F_{hkl} = \sum_{n=1}^{N} f_n(\theta)\exp\left[2\pi i\left(hx_i + ky_n + lz_n\right)\right]\cdot q \qquad \textit{eqn2.7}$$

Or it may alternatively be represented as:

$$F_{hkl} = \left(\sum_{n=1}^{N} f_n(\theta)\left[\cos 2\pi\left(hx_i + ky_n + lz_n\right)\right] + i\sum_{n=1}^{N} f_n(\theta)\left[\sin 2\pi\left(hx_i + ky_n + lz_n\right)\right]\right)\cdot q \qquad \textit{eqn2.8}$$

The sum is over all atoms in the unit cell, where the n^{th} atom has positional coordinates x_n, y_n, z_n, f_n is the scattering factor of the n^{th} atom and q is the Debye-Waller factor. However in the case of centrosymmetric unit cells, where identical atoms are present at +(x, y, z) and -(x, y, z), and given that sin(-x) = -sin(x), the structure factor reduces to a real number:

$$F_{hkl} = \sum_{n=1}^{N} f_n(\theta)\left[\cos 2\pi\left(hx_i + ky_n + lz_n\right)\right]\cdot q \qquad \textit{eqn2.9}$$

The atomic form factor for X-rays is determined by summing the contributions from all of its electrons.

$$f_n(\theta) = \frac{1}{2}\left(1+\cos 2\theta\right)\frac{e^2}{mc^2}\int \psi\psi * e^{ikr}\,dT \qquad \textit{eqn2.10}$$

To put it more simply, this means that the scattering amplitude is dependent on Z, the atomic number, and θ.

$$f_n(\theta) \propto \frac{Z}{2}\left(1+\cos 2\theta\right) \qquad \textit{eqn2.11}$$

The proportionality between Z and f_n has two important consequences which should be considered when analysing a sample by X-ray diffraction. Firstly, since heavier atoms, with a greater number of electrons, scatter X-rays more strongly they will dominate the diffraction pattern making it difficult to yield information about lighter atoms. The second important consideration is that atoms with similar atomic numbers will be difficult to distinguish between with X-rays, this is particularly relevant to this thesis in the investigation of doping on shared Co/Fe crystallographic sites in chapters 3-6.

The angular dependence on the atomic scattering factor for strontium, vanadium and oxygen are shown Figure 2.4 and both describe a fall off of intensity with θ. This is

because of the finite size of the electron cloud relative to wavelengths used, X-ray beam scattered from slightly different regions of electron cloud cause different path lengths bringing about destructive interference and a fall of intensity, which increases with θ.

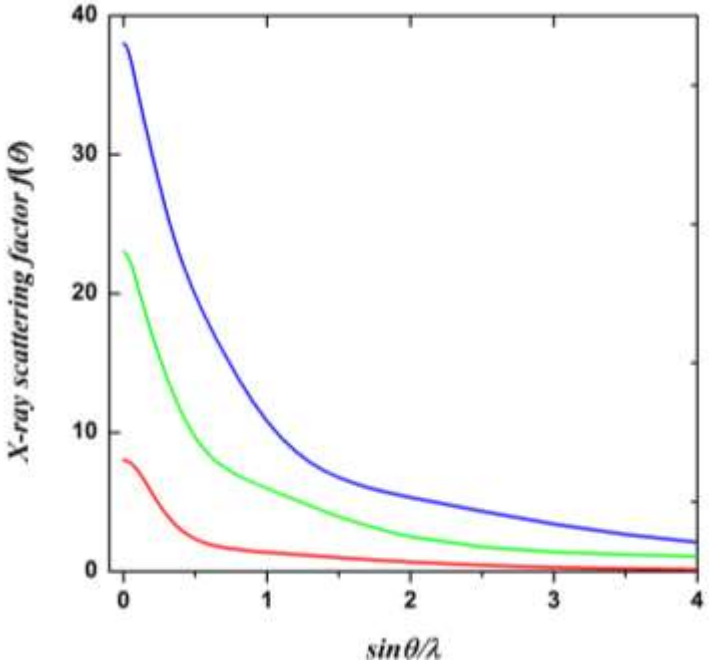

Figure 2.4 Plot showing the dependence of the X-ray scattering factor $f_n(\theta)$ on θ and Z. Values taken form International Tables for X-ray Crystallography.[2]

The Debye-Waller factor q also contributes to the structure factor. U_{iso} and B_{iso} are isotropic temperature factors and reflect the fact that atoms are not stationary at finite temperatures. This atomic vibration leads to a dispersion of electron density which results in a fall off of intensity with θ, as destructive interference increases due to greater phase difference between scattered waves. The effect increases with temperature, reflecting an increase in atomic vibrations. The Debye-Waller factor may also be used to model static or dynamic positional disorder of atoms which causes a smearing out of the electron density.

$$q_{iso} = \exp\left[-2\pi^2 U_{iso} r^{*2}\right] \qquad \textit{eqn2.12}$$

$$q_{iso} = \exp\left[-\frac{B_{iso}\sin^2\theta}{\lambda^2}\right] \qquad \textit{eqn2.13}$$

2.2.4 Powder diffraction

Polycrystalline samples contain a large number of randomly orientated small crystallites, typically less than 10 μm in diameter. When a beam of X-rays is incident to a powder sample all Miller planes are illuminated at the same time and therefore simultaneously

diffract at all angles, to generate Debye-Scherrer cones of diffracted intensity (Figure 2.5). A typical powder diffraction experiment involves intercepting these cones and measuring the diffracted intensity as a function of the scattering angle, 2θ.

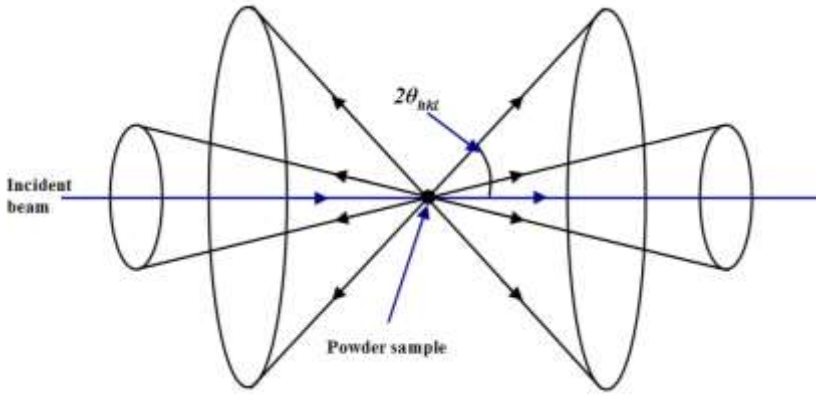

Figure 2.5 Debye-Scherrer cones of diffracted intensity.

The output is a 1-dimensional pattern, in which reflections with the same *d*-spacing are coincident. This results in a loss of information, as reflections with the same *d*-spacings, but different (*hkl*) values will contribute intensity to the same peak; for example in a cubic system the (110), (101) and (011) reflections will all be coincident. Further complexity is encountered due to the finite peak width of scattered reflections which often cause considerable overlap of peaks with similar *d*-spacings, making it very difficult to assign intensity to an individual reflection. These problems encountered by the convolution of overlapping reflections are more problematic in systems with low crystal symmetry, so powder diffraction is primarily used in the investigation of high symmetry extended solids, like those discussed in this thesis.

The combination of peak overlap along with the phase problem, make structure solution from powder diffraction data a considerable challenge. Powder diffraction is therefore more commonly used as a fingerprinting tool, in which sample purity is assessed by comparison of the collected pattern with one from the ICDD database. However, this is by no means the only use of powder diffraction and when data of a suitable quality are available, the application of the Rietveld method to this data affords the refinement and accurate determination of various structural parameters.

2.2.5 Neutron diffraction

The idea of wave-particle duality is expressed in the de Broglie equation, which relates the momentum of a particle to its wavelength.

$$\lambda = \frac{h}{mv} \qquad eqn2.14$$

This means that neutrons of a suitable energy can be diffracted by a crystal lattice. Whilst the diffraction conditions are the same for neutrons as they are for X-rays, the scattering mechanism is quite different. Neutrons are scattered directly by the nucleus of an atom via the nuclear force which acts at a range of 10^{-15} m. Since this interaction is over a considerably shorter distance than that of the typical incident neutron wavelengths (10^{-10} m), atomic form factors are independent of the incident angle (θ) because the scattering points are so small. This also means that neutrons interact relatively weakly with matter and as a consequence much larger samples (3 - 5 g) are required for neutron powder diffraction experiments if data collections are to be kept to reasonable times.

Another useful difference between X-ray and neutron diffraction is that the neutron scattering factor is not proportional to the electron count. Instead each isotope has its own coherent scattering length, so that the scattering amplitude shows a "saw-tooth" variation with atomic number and coherent scattering lengths in the range ~ -5 fm to ~ 16 fm. This has a number of important and useful implications. Firstly it can allow atoms with very similar electron counts but different coherent scattering lengths to be distinguished (i.e. Co and Fe). It can also be the case that light (low *Z*) atoms, which do not contribute strongly to diffracted X-ray intensity, possess considerable neutron scattering lengths (e.g. Li) and are therefore 'visible' with neutrons. The complementary use of both X-ray and neutron diffraction studies, often through joint refinements, can therefore allow further structural information to be gleaned, which would not be accessible with one technique alone. The coherent neutron scattering lengths of the elements used in this thesis are given in Table 2.1.

Element	*Z* (atomic number)	Neutron scattering length (fm)
O	8	5.803
Ca	20	4.70
Sc	21	12.29
V	23	-0.382
Cr	24	3.635
Mn	25	-3.73
Fe	26	9.45
Co	27	2.49
As	33	6.58
Sr	38	7.02
Ce	58	4.84

Table 2.1 Coherent neutron scattering lengths for atoms in this thesis.[3]

A further notable characteristic of neutrons is that they are spin-½ particles. This means that neutrons can be diffracted by an ordered array of magnetic moments, such as those in ferromagnets and antiferromagnets. The intensity of the diffracted beam of neutrons is proportional to the square of the magnetic scattering factor, which is in turn proportional to the magnitude of the ordered moment. It is fortuitous that the diffracted intensity arising from magnetic scattering is of the same order of magnitude of that resulting from nuclear scattering, such that one does not dominate the other. Thus when a beam of neutrons is incident on a magnetically ordered crystal or crystalline powder sample, two superimposed diffraction patterns will result, one structural and one magnetic. The solution of magnetic structures from neutron diffraction data was first demonstrated by Shull *et al.* in 1951.[4]

If all of the moments in a material are arranged parallel to one another, i.e. ferromagnetically, one would observe an increase in the intensity of the Bragg reflections to which the magnetic ion contributes. However if the moments are arranged antiferromagnetically extra peaks may be observed in the neutron diffraction pattern. These magnetic reflections can be indexed by assigning a propagation vector to give a magnetic unit cell that may or may not have the same size and symmetry as the nuclear cell. Further analysis and ultimately the refinement of a magnetic structure, using the SARAh program discussed in appendix C, allows the orientation and magnitude of ordered magnetic moments to be determined. A final point with regard to magnetic scattering comes from the consideration that since neutrons are scattered by electrons localised in the outermost atomic orbitals, magnetic form factors show a strong θ-dependence (greater than in X-ray diffraction), such that magnetic Bragg peaks are generally only visible at low scattering angles.

2.2.6 Laboratory X-ray diffractometers

Initial characterisation of all samples described in this work was undertaken using two laboratory X-ray diffractometers. X-ray generation in both of these instruments, involves the heating of a tungsten filament that produces electrons, which are then accelerated through a voltage of 40 *kV* towards a metal target. A Cu target is utilized in both diffractometers described hereafter in which the incident electrons are of sufficient energy to ionise core 1*s* (*K*-shell) electrons. An electron from a higher energy orbital then falls to fill this vacancy, with an accompanied emission of an X-ray photon of characteristic λ, with the $2p \rightarrow 1s$ transition termed K_α and the $3p \rightarrow 1s$ transition K_β. The K_α transition is in fact a doublet owing to spin orbit coupling, as the 2*p* electron can lead to either a $^2P_{3/2}$ or a

$^2P_{1/2}$ state. This gives rise to $K_{\alpha1}$ and $K_{\alpha2}$ radiation in a 2 : 1 intensity ratio with discrete wavelengths of 1.54051 Å and 1.54433 Å, respectively. A monochromator may then be used to select one specific wavelength of radiation.

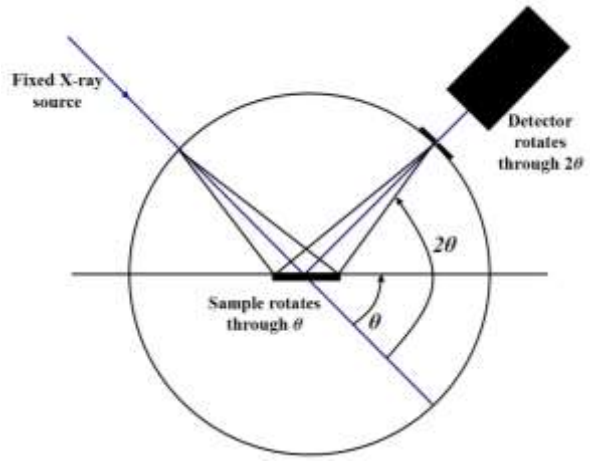

Figure 2.6 Schematic of a Bragg-Brentano geometry.

2.2.6.1 Philips PW1710

This low-resolution instrument is used primarily to assess the purity of starting materials. It utilises a Bragg-Brentano geometry with a fixed X-ray source and a detector on the 2θ axis. The incident X-ray beam is not monochromated and therefore contains both $K_{\alpha1}$ and $K_{\alpha2}$ radiation. Although the instrument is relatively low intensity and resolution, the presence of a diffracted beam monochromator makes it particularly useful for studying materials containing late 1st row transition metals, which fluoresce in K_α radiation. Air sensitive samples, such as SrO, were prepared in the argon-filled dry box by mounting a powder covered greased slide inside an air-tight cell fitted with a rubber O-ring and a Mylar window.

2.2.6.2 PANalytical X'pert Diffractometer

The PANalytical X'pert diffractometer is a high resolution and high intensity instrument that is used to collect high quality data suitable for Rietveld refinement. A Bragg-Brentano geometry is utilised and a germanium (111) monochromator on the incident beam exclusively selects Cu $K_{\alpha1}$ radiation, the effect of this is to improve the resolution and peak shape at the expense of some intensity. The majority of the samples produced in this thesis are air stable, at least on the time scale of a diffraction experiment. Samples were therefore mounted on greased silicon wafers, that are cut along the (110) direction to give no Bragg reflections. The sample was also mounted on a spinner plate, which rotates the sample at

60 *rpm* to improve the powder average. The CRL PANalytical X'pert diffractometer is a similar instrument but does not feature an incident beam monochromator, so both Cu $K_{\alpha 1}$ and $K_{\alpha 2}$ radiation are observed.

2.2.7 Synchrotron XRPD

Synchrotrons are a source of very intense beams of electromagnetic radiation. A synchrotron is comprised of 5 main components: an electron gun, a linac, a booster synchrotron, a storage ring and the beam lines. The electron gun produces a beam of electrons, by heating a high voltage cathode under vacuum, from which electrons with sufficient thermal energy (*keV*) may escape by a process known as thermionic emission. The linac then accelerates the electrons to relativistic energies (~100 *MeV*) using radio frequency cavities, before they enter the booster synchrotron which further accelerates X-rays to *GeV* range on an "athletics track" shaped trajectory, with bending magnets on the corners and RF voltage source on the straight sections. From here electrons are transferred to the storage ring which consists of a series of straight sections angled together to form a closed loop. Large electromagnets are used to curve the electron beam so it circulates in a ring, from which synchrotron 'light' is generated.

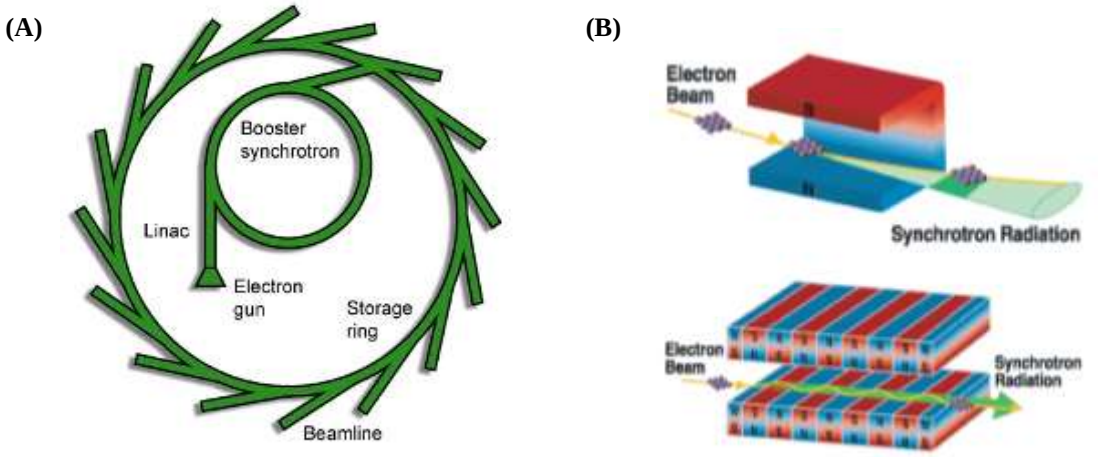

Figure 2.7 Schematic of a synchrotron (A).[5] Schematic of bending magnets (top) and insertion device (bottom) (B).[6]

The storage ring is maintained under a very high vacuum (< 10^{-10} *Torr*) in order to minimise the loss of electrons through scattering by air molecules. In order to maintain the radiation flux, the ring is "topped up" at regular intervals. Synchrotron radiation is generated in the storage ring by the interaction of electrons with two types of magnets: bending magnets and insertion devices. The effect of both of these devices is to accelerate

electrons causing the emission of radiation. When an electron is accelerated by a bending magnet it emits a fan of horizontally polarised radiation tangentially to the ring which is then extracted to the experimental beamlines. Tuneable magnetic insertion devices force electrons on an undulating path and are capable of generating a high flux of radiation. Beamlines are located at tangents to the storage ring and feature optics hutches upstream of the experimental stations which help to filter and focus the incident beam.

The use of synchrotron X-ray radiation for diffraction studies has several significant advantages over that generated in conventional laboratory sources. Firstly the radiation is several orders of magnitude more intense, which allows for rapid data collection and affords a sacrifice of intensity to be made to help maximise resolution. The continuous spectrum of radiation available also allows suitable wavelengths to be selected for the study intended. Alternatively measurements can be made in an energy-dispersive mode, in which a detector at a fixed scattering angle measures a white beam of X-rays.

2.2.7.1 ID31 (E.S.R.F.)

The ID31 diffractometer at the ESRF in Grenoble operates in the 5-60 *keV* energy range and diffraction patterns are typically measured using X-ray radiation in the range 0.3 - 0.9 Å. A white beam of radiation is produced by an undulator source and a single wavelength of X-ray radiation selected by a cryogenically cooled double-crystal Si (111) monochromator. The instrument operates in a Debye-Scherrer geometry and the detector bank is comprised of nine scintillation detectors which are preceded by Si (111) analyser crystals, they are arranged 2 ° apart and measure diffracted intensity as function of 2θ. The principal advantage of ID31 over I11 is that the incident beam contains a high flux of shorter wavelength X-rays which enable accurate determination of atomic coordinates i.e. measurements out to high values of $\sin\theta/\lambda$. In this work a wavelength of 0.4 Å was used for all measurements and samples were loaded into 0.7 mm capillaries which were mounted on the axis of the diffractometer and spun, to help reduce preferred-orientation effects.

2.2.7.2 I11 (DIAMOND)

I11 is a high resolution powder diffraction beamline at the diamond light source.[7] The instrument is similar in principle to ID31 with photons generated by an undulator which produces the highest beam flux at 11 - 20 *keV* or 0.6 - 1.1 Å. The white X-ray beam is then monochromated by a liquid nitrogen cooled Si(111) double crystal monochromator after

which harmonic rejection mirrors reflect the incident beam to remove any higher energy harmonic photons.

The instrument typically operates in a Debye-Scherrer geometry and features MAC detectors which are preceded by Si(111) analyser crystals that reduce background and improve resolution. The ensemble is composed of 45 individual detectors arranged on 5 separate arms at 30 ° intervals that are able to collect a full pattern with a 2θ range from 5 - 145 °. Each detector bank therefore need only scan through an angle of 30 °, before the patterns are merged to generate a single diffraction pattern. Alternatively the lower resolution Mythen position sensitive detector (PSD) can be used. The 90 ° aperture allows a full resolution diffraction pattern to be captured in a matter of seconds. For all measurements samples were contained in 0.5 mm borosilicate capillaries, which were rotated during data collection.

2.2.8 Neutron powder diffraction

Accelerator-based and steady-state reactor neutron sources were both used to undertake the neutron diffraction experiments described in this thesis. At the accelerator-based "spallation" neutron source ISIS, Rutherford Appleton Laboratory, Didcot, UK, 4 different diffractometers were used (POLARIS, HRPD, WISH and OSIRIS). Further measurements were made at the Institut Laue-Langevin (ILL) reactor source on the D2B instrument. These two methods of neutron generation, as well as the specifics of individual diffractometers will now be discussed.

Reactor sources produce neutrons by the fission of ^{235}U nuclei. The neutrons are then equilibrated in a heavy-water moderator, as they undergo inelastic collisions with low mass H/D nuclei. This slows down the neutrons, so that the fission process may be maintained and also generates a thermal beam with maximum flux at 1.2 Å, a wavelength suitable for diffraction studies. This white neutron beam covers a broad range of wavelengths and is typically monochromated before being extracted to the experimental beamlines, where the scattered monochromatic neutron radiation is measured as a function of the scattering angle. The flux generated at reactor sources is high in cold and thermal neutrons, but somewhat lower in those at higher epithermal energies. The implications of this will be discussed in due course.

At accelerator based sources, pulses of neutrons are produced by the high energy collision of charged particles with a heavy metal target, in a process known as spallation. The ISIS

facility utilizes a synchrotron, which provides a pulsed beam of protons with an energy of 800 MeV that are bombarded against a tungsten target with a frequency of 50 Hz. These collisions knock off neutrons from the nuclei of the target atoms, to give intense pulses of high-energy neutrons. Suitable moderators are then used to slow down the neutrons to a useful distribution of wavelengths for diffraction studies. The white neutron beam then illuminates a sample with regular discrete pulses and time of flight (ToF) diffraction experiments are performed in an energy dispersive mode, with detectors at fixed scattering angles (θ). In a ToF diffraction experiment the neutrons travel a known distance (L) from their source via the sample to the detector, which measures the arrival times of neutrons, or their time of flight (t). The de Broglie equation relates the wavelength of a neutron to its momentum.

$$\lambda = \frac{h}{mv} = \frac{ht}{mL} \qquad \textit{eqn2.15}$$

It is then trivial to calculate the d-spacings of the diffracted beams of neutrons by combining the de Broglie formula with Bragg's Law.

$$n\lambda = \frac{nht}{mL} = 2d_{hkl}\sin\theta \qquad \textit{eqn2.16}$$

The substitution of values for the neutron mass (m) and Planck's constant (h) then gives:

$$t = 505.56L\sin\theta d_{hkl} \qquad \textit{eqn2.17}$$

It can be seen from *eqn2.17* that the position of the detector relative to the sample and incident beam will dictate the range of d-spacings that may be observed. ToF diffractometers typically group large numbers of detectors into a series of "banks", which have their own characteristic d-ranges and resolutions. The longest d-spacings are observable in the low angle detector banks ($\sin\theta \rightarrow 0$), whilst the back scattered banks ($\sin\theta \rightarrow 1$) access much shorter d-spacings.

2.2.8.1 Comparison of ToF and Constant Wavelength PND

The intensity of neutron Bragg reflections are not strongly 2θ dependent and therefore the minimum useable d-spacings are determined by other factors. The lower limit (d_{min}) in a constant wavelength experiment is encountered when $\sin\theta = 1$ (i.e. when $2\theta = 180$ º) , which by rearrangement of Bragg's law gives $d_{min} = \lambda/2$. The d-spacings accessible at a pulsed neutron source are obviously dictated by the energy of the neutrons that are produced, which is in turn determined by the moderators. In order to retain the pulsed time

structure of the neutron beam, neutrons are "under-moderated" which leads to a high flux of neutrons with short wavelengths, facilitating the measurement of reflections at very short *d*-spacings. This makes the pulsed neutron source at ISIS very powerful for measurements at short *d*-spacings which get much stronger signals than those seen at the ILL reactor source or on synchrotron X-ray powder diffractometer with their associated form factors.

The resolution of a ToF diffractometer is dependent on three factors, namely a timing uncertainty Δt, a flight-path uncertainty ΔL and an uncertainty in the diffracted angle $\Delta\theta$.[8]

$$\frac{\Delta d}{d} = \left(\left(\frac{\Delta t}{t} \right)^2 + \left(\frac{\Delta L}{L} \right)^2 + (\Delta\theta \cot\theta)^2 \right)^{1/2} \qquad \textit{eqn2.18}$$

The greatest contributor to the timing uncertainty Δt comes from moderator source broadening and is constant for a given moderator. The flight-path uncertainty arises primarily from the finite thickness of the moderator, as well as to a lesser extent from finite detector and sample sizes. The uncertainty in both *t* and *L* may be reduced by increasing the flight path, as this also increases the neutron time of flight. The uncertainty in the scattering angle is a product of the finite angular widths of the moderator, sample and detector which allow a range of wavelengths to satisfy the Bragg condition for a given reflection. This term dominates at low angles as $\cot^2\theta$ is maximised but becomes vanishingly small as $2\theta \rightarrow 180$ ° and $\cot^2\theta \rightarrow 0$. A detector bank at $2\theta = 180$ ° would however interfere with the incident neutron beam, so the back scattered detector banks are orientated at slightly lower angles. A diffractometer with a long path length and a high angle detector bank will therefore afford the highest resolution, thus the HRPD instrument at ISIS with a path length of 100 m and a back scattering detector bank at 168 ° affords excellent resolution. Detector banks at low-angles are used to access reflections at much higher *d*-spacings, especially magnetic peaks and superstructure reflections. Intermediate detector banks offer a balance between resolution and *d*-spacings and help to improve statistics. The arrangement of detector banks at the ISIS pulsed neutron source means that $\Delta d/d$ is constant across a single detector bank, which results in Bragg peaks which get narrower at low *d*-spacings, minimising peak overlap.

The resolution of a constant wavelength diffractometer is θ-dependent and may be described as the variation of the full width at half maximum (FWHM) by a Caglioti function.[9]

$$\sigma^2 = \frac{FWHM^2}{8\log_e 2} = U\tan^2\theta + V\tan\theta + W \qquad eqn2.19$$

Here σ is proportional to the FWHM of the peak and the *U*, *V* and *W* parameters have both sample and instrumental contributions. The form of the Caglioti function dictates that after reaching a minimum, the width of reflections will increase with decreasing *d*-spacings. A plot illustrating the resolution of several powder neutron diffractometers at the ISIS and the ILL as a function of *d*-spacings is given below.[10]

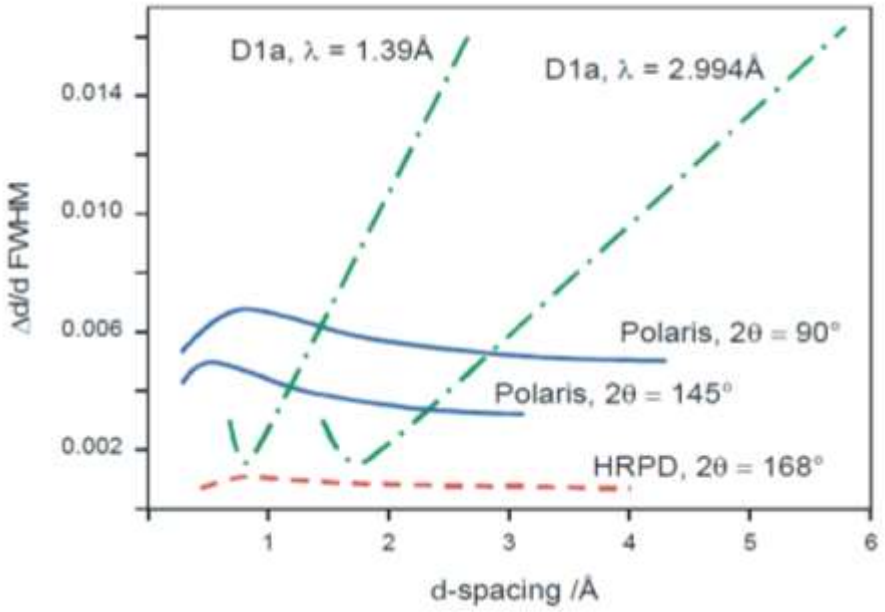

Figure 2.8 Resolution of a selection of ToF and constant λ powder neutron diffractometers. ISIS Neutron Training Course booklet 2009.[10]

A final consideration is that the peak shapes in diffraction patterns collected on pulsed and constant wavelength instruments are quite different. At a constant wavelength reactor source, peak shapes are symmetric except at very low and very high angles. However, at a pulsed neutron source the peak shape is clearly asymmetric, with a steep leading edge and a longer tail. The sharp leading edge is a result of the rapid build-up of neutron flux as the high energy proton beam strikes the target and the tail is a consequence of the slowing down process of the moderator.

In all powder neutron diffraction experiments, samples were contained in thin walled vanadium cylindrical cans. Vanadium is an ideal material for a sample container as it has a negligible coherent scattering length of -0.38 fm, so Bragg scattering from the can is minimized.

2.2.8.2 POLARIS (ISIS)

The POLARIS instrument in its pre-2011 configuration is a high intensity, medium resolution diffractometer and the incident neutron beam passes through an ambient H_2O moderator. The detectors are arranged in four banks positioned at 14, 35, 90 and 145 °, though data from the 14 ° bank was not of sufficient quality to warrant refinement against. The dimensions of the neutron beam at the sample, 40 × 20 mm are huge relative to those used in X-ray diffraction experiment, this allows greater sample volumes to be measured to help improve the scattered signal from weakly interacting neutrons. Typically samples were prepared on the 2.5 g scale, with collection times of the order of 2 - 4 hours depending on observed statistics.

2.2.8.3 HRPD (ISIS)

As the name suggests, HRPD is a high resolution powder diffractometer of medium intensity, with three banks of detectors at 168, 90 and 30 °. The high resolution is a consequence of the 100 m long flight-path, however this also limits the intensity of the incident beam.[11] The reduced intensity is, in part, a result of "lost" neutrons along the guide tube, though the presence of a Ni plated glass beam guide serves to minimise this loss. Another problem is that of "frame overlap" whereby the range of neutron velocities means that over such a long path length, high energy neutrons from one pulse catch up with low energy neutrons from the previous pulse. This issue is resolved by the use of only 1 in 5 pulses and two choppers situated at 6 and 9 m from the moderator which select a suitable range of neutron wavelengths. As a result of this reduced intensity larger samples and longer counting times were employed to achieve suitable statistics.

2.2.8.4 OSIRIS (ISIS)

OSIRIS is a long wavelength, high resolution diffractometer, with a neutron flight path of 34 m, intermediate between that of HRPD and POLARIS.[12] The presence of a 25 K liquid hydrogen moderator allows OSIRIS to access a high flux of long wavelength cold neutrons. The neutrons are delivered to the instrument by a curved supermirror neutron guide that significantly increases the flux which the sample is exposed to. This high intensity of long wavelength neutrons makes OSIRIS particularly suited for magnetic structure determination.

However, in contrast to HRPD and POLARIS, OSIRIS features only one detector bank that consists of 962 ZnS scintillation tubes covering back scattering angles between 150

and 171 °. With this limited detector coverage, access to suitable neutron energies and thus desired *d*-spacings ranges is achieved by adjusting the phases of two choppers situated at approximately 6 and 10 m from the moderator. Different chopper phases allow access to different *d*-ranges, so a series of measurements are performed with a range of chopper phases to give access to appropriate *d*-space coverage. The datasets from each measurement are then merged to generate a diffractogram which covers the entire range of interest. Due to the reduced neutron flux at higher wavelengths, count times were significantly increased at higher *d*-ranges.

2.2.8.5 WISH (ISIS)

WISH is a high-resolution long-wavelength diffractometer with a solid methane moderator giving access to incident wavelengths in the range 1.5 - 15 Å. The good resolution of the instrument at high *d*-spacings makes it particularly useful for the analysis of complex magnetic systems, in which peak overlap at high *d*-spacings is encountered.

2.2.8.6 D2B (ILL)

D2B is a high intensity constant wavelength diffractometer situated in the reactor hall of the ILL and operates in a Debye-Scherrer geometry.[13] A schematic of the instrument is given in Figure 2.9. The rotation of a Ge(115) monochromator relative to the white neutron beam illuminates different *h k l* planes to give discrete wavelengths of neutrons to be used for diffraction. The very high monochromator take-off angle of 135 º optimises monochromation, helping to eliminate wavelengths of radiation diffracted by *h k l* planes with different *d*-spacings. A wavelength of 1.59 Å was selected for all measurements in this thesis as this optimises intensity since this wavelength is close to the peak in the thermal beam and is suitable for structural as well as magnetic studies.

The scattered beam is detected by 128 ^{3}He tubes, set at 1.25 º intervals that are able to measure an angular range of 5 º $\leq 2\theta \leq$ 165 º and cover a *d*-range of 0.8 - 18 Å, using 1.59 Å neutrons. The height of the detector is 200 mm, however typically only the middle third of the collected data is used, to avoid peak asymmetry caused by the curvature of the Debye Scherrer cones. The dimensions of the beam at the sample position measure 2 × 5 cm, which allows large volume samples to be measured.

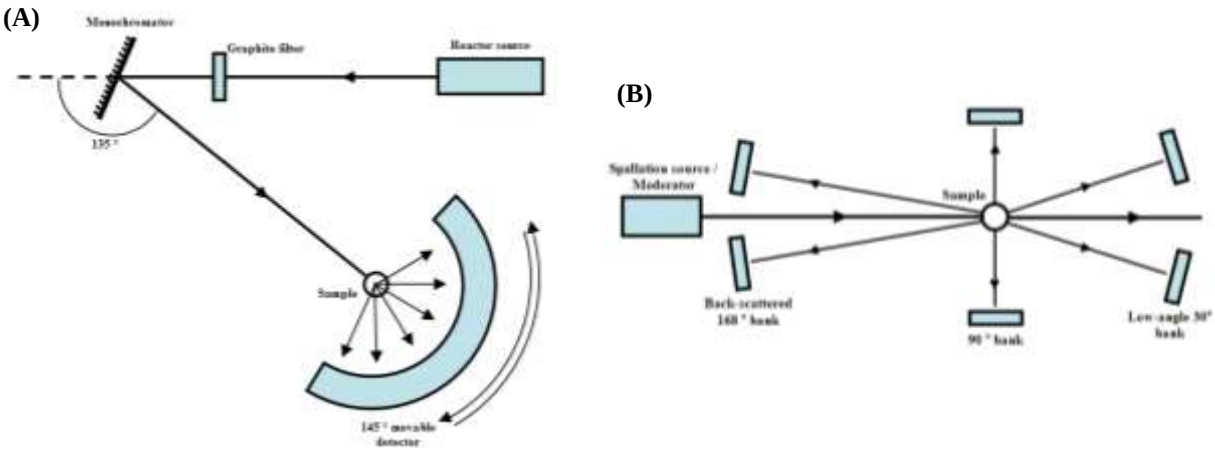

Figure 2.9 Schematic representation of (A) the constant λ neutron powder diffractometer D2B and (B) the HRPD ToF diffractometer.

2.2.8.7 Comparison of neutron powder diffractometers

A huge advantage of the ToF technique is that reflections are narrower at shorter *d*-spacings where the highest concentration of reflections are present. This makes the POLARIS and HRPD time of flight instruments at ISIS particularly powerful for structural studies. HRPD has the highest resolution at low *d*-spacings and is therefore particularly useful for investigating small structural distortions. POLARIS has a greater intensity and covers a wide range of *d*-spacings, this affords a good balance between structural and magnetic studies. The high flux also allows relatively small samples to be studied.

OSIRIS cannot access short *d*-spacings due to the curvature of the neutron guide, but offers higher resolution at long *d*-spacings and so is particularly useful in the determination of magnetic structures. It is however useful to "anchor" the refinement by supplying an accurate structural model from another source and applying an absorption correction, before accurate magnetic moments are extracted. The constant wavelength diffractometer D2B offers a higher flux at longer *d*-spacings than the POLARIS and HRPD instruments. The resolution on D2B is however poorer at higher *d*-spacings than that of OSIRIS, though its improved resolution at low *d*-spacings allows structural and magnetic investigations to be performed simultaneously.

2.2.9 Rietveld method

The Rietveld method was developed by H. M. Rietveld in the late 1960s.[14,15] It allows the refinement of a structural model against powder diffraction data sets, which afford useful structural information to be derived. However, the Rietveld method is not a technique of

structure solution and it relies on the availability of a good starting model, which is then used to calculate a theoretical diffraction pattern. This structural model is then refined to give a best fit to the observed diffraction data. In this work Rietveld refinements were undertaken using the Fullprof suite, the TOPAS academic package as well as the GSAS package with the EXPGUI graphical user.[16-18] The differences and relative advantages of these programs will be discussed in due course.

The manner in which the Rietveld method differed to previous attempts is that thanks to the improved computing power, he was able to treat each data point as an individual observation, rather than each peak, affording the treatment of overlapping reflections. In this treatment each data point y_i may have contributions from more than one Bragg reflection. The calculated intensity y_{ci} is then determined by summing all contributions of Bragg reflections for the structure factor F_{hkl}, for the proposed structural model, within a fixed range:

$$y_{ci} = y_{bi} + s\sum_{hkl} L_{hkl} P_{hkl} A \left|F_{hkl}\right|^2 \phi(2\theta_i - 2\theta_{hkl}) \qquad \textit{eqn2.20}$$

where y_{bi} is the background intensity (typically generated by a separate polynomial function), s is a scale factor, L_{hkl} is a combined Lorentz, polarisation and multiplicity term, P_{hkl} describes preferred orientation, A is an absorption term, φ is a reflection profile function that describes the peak shapes. The calculated intensity y_{ci} is then compared to the observed y_i to give the residual S_y.

$$S_y = \sum_i w_i (y_i - y_{ci})^2 \qquad \textit{eqn2.21}$$

in which w_i is a weighting factor equal to $1/y_i$ so that each point contributes equally to the residual. The best fit for a given set of refined parameters is then obtained by minimising the residual through a least-squares procedure. To achieve this, a normal matrix with elements M_{jk} is produced in which j and k are the parameters to be refined.

$$M_{jk} = -\sum_{i=1}^{n} 2w_i \left[(y_i - y_{ci}) \frac{\partial^2 y_{ci}}{\partial x_j \partial x_k} - \left(\frac{\partial y_{ci}}{\partial x_j} \right) \left(\frac{\partial y_{ci}}{\partial x_k} \right) \right] \qquad \textit{eqn2.22}$$

This may be simplified to:

$$M_{jk} = -\sum_{i=1}^{n} 2w_i \left[\left(\frac{\partial y_{ci}}{\partial x_j} \right) \left(\frac{\partial y_{ci}}{\partial x_k} \right) \right] \qquad \textit{eqn2.23}$$

since (y_i - y_{ci}) is assumed to be small enough to be ignored. This gives an $m \times m$ matrix, where m is the number of refined parameters. The matrix is then inverted and used in the least squares minimisation, which makes small shifts in the parameter x_k that is being refined.

$$\Delta x_k = \sum M^{-1}_{jk} \frac{\partial S_y}{\partial x_k} \qquad \textit{eqn2.24}$$

After the minimisation of each parameter, the new values for each parameter are reinserted into the model and the procedure is repeated until a stable solution, giving the best fit to the observed data for the refined variables is reached. However, the order in which parameters are refined is often critical if one is to reach the global refinement minimum for a given set of parameters. Firstly a close match should be obtained to the measured peak positions. This is achieved by refining the lattice parameters and a zero point correction. A polynominal function to describe the background intensity, along with scale factors is also refined at this stage. Parameters that control peak intensities are then introduced, namely fractional atomic coordinates, thermal displacement parameters and site occupancies, along with parameters that describe the peak profile and absorption factors.

After each stage of refinement the quality of the fit is examined by visual inspection of the calculated and observed patterns, as well as the difference between the two of them. A number of statistical outputs known as *R*-factors are also used to evaluate the quality of a refinement. The *R*-structure factor R_F is based on Bragg intensities close to those derived from the final model and is not sensitive to the full pattern. Unlike the weighted *R*-factor however, it not based directly on the observed y_i values, but extracted peak intensities which are biased by the structural model. It is therefore useful for looking at how good the structural model is for a single phase, without considering impurity phases. R_F is given by:

$$R_F = \left(\frac{\sum_K \left| I_{K_{obs}} - I_{K_{calc}} \right|}{\sum_K I_{K_{obs}}} \right)^{1/2} \qquad \textit{eqn2.25}$$

By contrast the profile *R* value, R_p, and the weighted profile *R*-value R_{wp} describe the quality of the fit to the full pattern, and take the form:

$$R_p = \frac{\sum_i \left| y_i - y_{ci} \right|}{\sum_i y_i} \qquad \textit{eqn2.26}$$

$$R_{wp} = \left(\frac{\sum_i w_i \left(y_i - y_{ci} \right)^2}{\sum_i w_i y_i^2} \right)^{1/2} = \left(\frac{S_y}{\sum_i w_i y_i} \right)^{1/2} \qquad \textit{eqn2.27}$$

R_{wp} is perhaps the most meaningful and mathematically robust R-factor as it relates directly to S_y, the quantity being minimised. However, unlike R_F, the weighted profile R_{wp} can be strongly affected by problems that are unrelated to the quality of the structural model, i.e. incorrect modelling of the background or the presence of impurity phases. That said, R_{wp} gives the best guide to the overall progress of the refinement and the final R_{wp} should approach R_{exp}, the statistically expected R value:

$$R_{\exp} = \left(\frac{N_{obs} - N_{\text{var}}}{\sum_i w_i y_i^2} \right)^{1/2} \qquad \textit{eqn2.28}$$

where N_{obs} is the number of observations and N_{var} the number of refined parameters. In a powder diffraction experiment N_{obs} ~ 2000, so typically N_{obs} is far greater than N_{var}. The goodness-of-fit (*gof*) or χ^2 is also commonly quoted and is the ratio of R_{wp} to R_{exp}:

$$\chi^2 = \left(\frac{R_{wp}}{R_{\exp}} \right)^2 \qquad \textit{eqn2.29}$$

In an idealised powder diffraction experiment the number of data points and counting times should be sufficient so that y_{ci} is not dominated by the background intensity y_{bi}. This combined with the refinement of an appropriate number of variables should yield a value of $\chi^2 < 2$, if a good structural model is employed. However, under certain conditions, misleadingly low values for χ^2 (sometimes less than 1) may be encountered if R_{exp} becomes too large, or R_{wp} too small. Specifically large values of R_{exp} can be due to the refinement of too many variables or insufficient counting times. Similarly a well fitted high background can lead to low values for R_{wp} and artificially low χ^2. Conversely anomalously high values of χ^2 may be encountered when R_{exp} becomes very small- a situation particularly evident when performing refinement against OSIRIS powder neutron diffraction data.

It is therefore crucial when assessing the quality of a structural model, to not only rely on the statistical R-factors, but also to examine the calculated pattern and compare it to the observed data. Such examination, especially of difference profile plots, typically allows problems such as a poorly modelled profile or the presence of a minor impurity phase to

identified and addressed. The refinement of a structural model is then considered to be acceptable if the fit to the data looks reasonable, the *R*-factors are appropriate and the model makes chemical sense.

2.2.9.1 Rietveld refinement software

Three different Rietveld refinement suites were used to analyse powder X-ray diffraction and powder neutron diffraction data in this thesis. The majority of refinements were performed using TOPAS Academic and GSAS (General Structure Analysis System) suites.[16,17] GSAS interfaced with SARAh refine was also used for magnetic structure determination and is discussed in more detail in the following section.[19] The FullProf Suite was also used for the profile fitting of incommensurate magnetic reflections. Magnetic structure determination is discussed in more detail in appendix C.

2.2.10 X-ray absorption spectroscopy (XAS)

In X-ray absorption spectroscopy, X-rays of sufficient energy are used to excite core electrons from an atom. Each core shell has a distinct binding energy and when the energy of incident X-rays is coincident with this, an abrupt increase in the absorption cross-section will be observed, giving rise to an absorption edge (Figure 2.10).

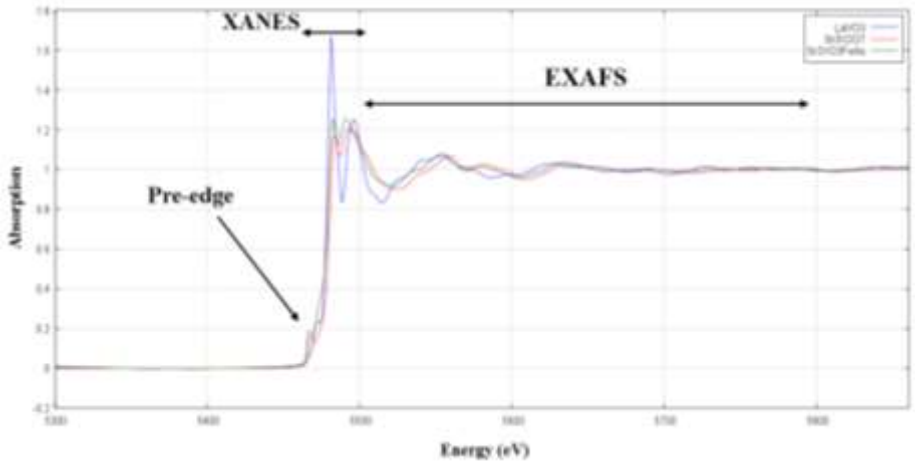

Figure 2.10 Typical XAS spectrum for transition metal *K*-edge

The different absorptions edges of an element are labelled according to the principal quantum number of the electron that has been promoted i.e. *K*-edge is $n = 1$, *L*-edge is $n = 2$ and so on. At a most basic level the presence of a characteristic absorption edge can serve to identify the presence of a particular elemental in a sample. However, a wealth of information is in fact contained within an XAS spectrum, which can generally be divided into 3 sections as shown in Figure 2.10.

Features in the pre-edge region of a spectrum ($E < E_0$) are a result of transitions of core level electron to higher vacant or half-filled orbitals. The X-ray absorption near edge structure or XANES region ($E = E_0 \pm 10$ eV) corresponds to the transition of a core electron to non-bound levels as seen in the abrupt rise of the absorption edge. The EXAFS region is the oscillating part of X-ray absorption spectrum that extends out up to 1000 eV beyond the absorption edge and is sensitive to the local environment of the excited atom.

In this study XANES measurements are primarily used to assess the oxidation states of 1st row transition metal elements. As the oxidation state of a given element increases the absorption edge shifts to higher energy, as described by Kunzl's law.[20] This observation can be rationalised simply by an electrostatic argument, in which atoms in a higher oxidation state require higher energy X-rays to excite core electrons since the nucleus is less shielded, so the core electron feels a higher effective charge. 1st row transition metals show weak pre-edge features prior to their characteristic *K*-edges which arise from 1*s* to 3*d* transition. This transition is dipole forbidden, but can be observed due to 3*d* / 4*p* orbital mixing. The intensity of the 1*s* to 3*d* transition increases as the geometry of the absorption site becomes less centrosymmetric and the 3*d* / 4*p* mixing increases.

XAS measurements may be performed in either transmission or fluorescence modes. In transmission measurements the X-ray beam is attenuated by the sample such that the intensity ratio of the incident and transmitted X-ray flux is proportional to the exponential of the absorption coefficient. In fluorescence measurements the intensity of the fluorescence X-rays is proportional to the absorption cross-section. XAS measurements are typically performed at synchrotrons, since the tuneability of the X-ray allows XAS spectra to be accessed for virtually all elements.

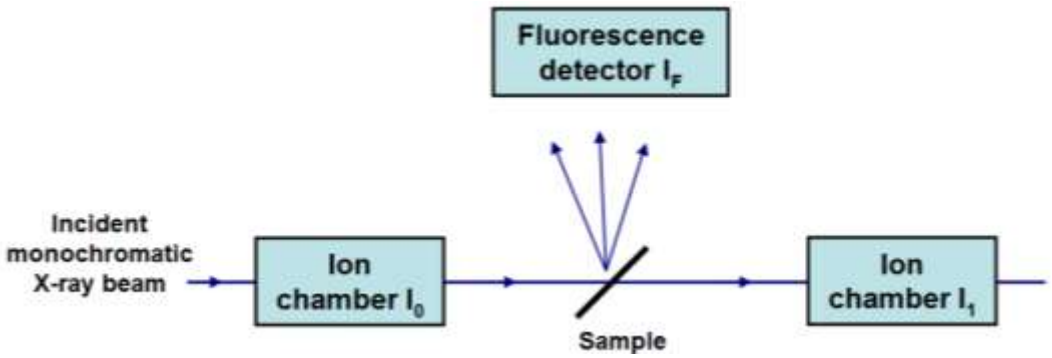

Transmission: $A = \ln\left(\frac{I_0}{I_1}\right)$ **Fluorescence:** $A = \left(\frac{I_F}{I_1}\right)$

Figure 2.11 Schematic experimental set-up for XAS in transmission an fluorescence modes

2.2.10.1 B18 (DIAMOND)

The beam source for the B18 beamline at Diamond comes from a bending magnet and allows access to X-rays in the 2.05-35 *keV* energy range.[21] The optics hutch on B18 contains four main elements: a collimating mirror, a water-cooled double Si(111)/(311) crystal monochromator, a focusing mirror and harmonic rejection mirrors. In the experimental hutch, there is first a vacuum section which can be used to collect low energy spectra (2-4 *keV*), this is followed by an open-air section for higher energy measurements (4-35 *keV*) where beam loss due to air absorption is less of a problem. For the high energy in-air measurements detectors can be utilised in both transmission and fluorescence modes. The majority of measurements in this thesis were carried out in fluorescence mode using a portable vortex detector. However samples were mixed with cellulose to an appropriate degree, so as to allow some transmission through the sample so that a reference foil downstream from the sample can be used to normalise the data.

2.2.11 DC SQUID Magnetometry

A Quantum Design MPMS SQUID magnetometer was used to perform magnetic susceptibility measurements on the materials described in this thesis. A Superconducting Quantum Interference Device, or SQUID,[22] forms the heart of the magnetometer and consists of a closed superconducting loop intersected by two thin strips of insulating material to form Josephson junctions. The application of a small current across the device causes Cooper pairs of electrons to tunnel through the insulating barrier with no resistance. However, if the applied current exceeds the critical current a voltage will be established across the junction and a finite resistivity will develop in the device. The presence of an external magnetic field affects the critical current and thus by monitoring changes in the voltage across the junction variations in the applied magnetic field may be measured. In order to function accurately, the SQUID must be protected from fluctuating external fields; this is achieved by a superconducting shield which insulates the SQUID from the instruments magnet. The sample to be measured is mounted on the end of a long stick which is held within an induction coil and is magnetised by a helium-cooled superconducting magnet which is capable of generating fields between +5 T and -5 T. The detector coil around the sample is a portion of superconducting wire wrapped around the centre of the superconducting magnet. Vertical translation of a magnetised sample through the detector coil induces a current. The detector coil is connected to an input coil by superconducting wires, which are in turn coupled to the SQUID such that an output

SQUID voltage is measured that is directly proportional to the magnetic moment of the sample. The magnetic contribution from the sample holder is minimised by loading samples inside gelatine capsules which are positioned within plastic drinking straws. The sample chamber is held under liquid helium and can be cooled from 330 K to 2 K. The magnetisation of a sample can therefore be measured as a function of both temperature and applied field.

2.2.11.1 Magnetic properties of superconducting materials

With the study of so many superconducting samples in this thesis, magnetic susceptibility measurements are crucial in understanding the bulk superconducting properties of these samples. Superconductivity is evidenced by the onset of strong diamagnetism below a critical temperature T_c. This strong diamagnetic signal is caused by the Meissner effect, which is the onset of perfect diamagnetism and the expulsion of all magnetic flux from the superconductor. The magnitude of the diamagnetic response may then be used to calculate the estimated superconducting volume fraction. In the normal (non-superconducting)-state the flux density inside a sample B_i is given by:

$$B_i = \mu_0(H + M) = B + \mu_0 M \qquad \textit{eqn2.30}$$

where $\mu_0 M$ is the contribution from the sample, B is the applied flux density. In the superconducting state all magnetic flux is expelled from the sample and the internal flux density $B_i = 0$, to give:

$$M = \frac{-B}{\mu_0} = -H \qquad \textit{eqn2.31}$$

This leads to the dimensionless quantity χ_{vol}:

$$\chi_{vol} = \frac{M}{H} = -1 \qquad \textit{eqn2.32}$$

However, the measured magnetic susceptibility χ_{meas} is characterised by μ_m, the magnetic moment of the sample, and the applied flux B:

$$\chi_{meas} = \frac{\mu_m \mu_0}{B} \qquad \textit{eqn2.33}$$

Since χ_{meas} has units of m^3, χ_{vol} may be calculated by dividing χ_{meas} by the sample volume, which is in turn approximated from the crystallographic density ρ and the sample mass m:

$$\chi_{vol} = \frac{\mu_m \mu_0 \rho}{Bm} \qquad eqn2.34$$

Values of χ_{vol} at 2 K are calculated for all superconducting samples in this thesis, and samples are considered to be bulk superconductors if χ_{vol} = -1. In samples where -1 < χ_{vol} < 0, superconducting volume fractions are reported, i.e. χ_{vol} = -0.5 corresponds to a superconducting volume fraction of 50 %. However, the value is very much an estimate, since it requires a number of assumptions to made, firstly it assumes the sample shape to be spherical, when in fact is crescent-like and it also neglects grain-boundary effects that can affect magnetisation. Whilst the absolute values of χ_{vol} are subject to these inaccuracies, the relative values for a given series of compounds should be quite robust, due to the similar shapes and packing densities.

In order to establish T_c, the superconducting transition temperature, the magnetisation of superconducting samples was measured as a function of temperature at short intervals in the region $2 \leq T$ (K) ≤ 50 in small applied fields (typically 5 - 50 Oe). The small applied fields in which all superconducting samples were measured are necessary due to the relatively low lower critical fields H_{C1} that these samples possess. Specific values of H_{C1} were estimated for a number of samples by *M* vs *H* measurements at 2 K. Magnetisation isotherms were also performed above T_c to investigate the possibility of ferromagnetic order in both the bulk and/or impurity phases.

The exact onset of superconductivity can be a difficult to define. A common approach is to take the temperature at which the sample first becomes diamagnetic, i.e. the intercept of the *x*-axis. However, since some of the samples that have been measured are magnetically ordered in the normal state here T_c is typically reported as the intercept between the extrapolation of normal state behaviour and that of the most rapidly changing ZFC susceptibility in the superconducting state.

References

(1) Brauer, G. *Handbook of Preparative Inorganic Chemistry* **1965**.

(2) Cromer, T.; Waber, J. T. *International Tables for X-ray Crystallography; vol IV* **1971**.

(3) Sears, V. F. *Neutron News* **1992**, *3*, 29.

(4) Shull, C. G.; Strauser, W. A.; Wollan, E. O. *Physical Review* **1951**, *83*, 333-345.

(5) *http://www.diamond.ac.uk/Home/About/Synchrotrons/Machine.html*.

(6) *http://www.spring8.or.jp/en/news_publications/publications/sp8_brochure/sr.html*.

(7) Thompson, S. P.; Parker, J. E.; Potter, J.; Hill, T. P.; Birt, A.; Cobb, T. M.; Yuan, F.; Tang, C. C. *Review of Scientific Instruments* **2009**, *80*, 9.

(8) Smith, R. I.; Hull, S. *User Guide for the POLARIS Diffractometer at ISIS*.

(9) Caglioti, G.; Paoletti, A.; Ricci, F. P. *Nuclear Instruments* **1958**, *3*, 223-228.

(10) *ISIS Neutron Training School Booklet* **2006**.

(11) Ibberson, R. M. D., W. I. F. Knight, K. S. *High resolution powder diffraction (HRPD) at ISIS. A user guide*.

(12) Telling, M. T.; Anderson, K. H. *The OSIRIS User Guide 3rd edition* **2008**.

(13) *The ILL Yellow Book* **2008**.

(14) Rietveld, H. *Acta Crystallographica* **1967**, *22*, 151-152.

(15) Rietveld, H. *Journal of Applied Crystallography* **1969**, *2*, 65-71.

(16) Larson, A. C.; Von Dreele, R. B. *General Structure Analysis System (GSAS); Los Alamos National Laboratory Report* **2004**, 86-784.

(17) Coelho, A. A. *TOPAS Academic; General profile and Structure Analysis Software for Powder Diffraction Data*, **2010**.

(18) Toby, B. H. *Journal of Applied Crystallography* **2001**, *34*, 210-221.

(19) Wills, A. S. *Physica B: Condensed Matter* **2000**, *276*, 680-681.

(20) Agarwal, B. K.; Verma, L. P. *Journal of Physics C: Solid State Physics* **1970**, *3*, 535.

(21) Dent, A. J.; Cibin, G.; Ramos, S.; Smith, A. D.; Scott, S. M.; Varandas, L.; Pearson, M. R.; Krumpa, N. A.; Jones, C. P.; Robbins, P. E. *Journal of Physics: Conference Series* **2009**, *190*, 012039.

(22) Clarke, J. *Scientific American* **1994**, 271.

3 Sr_2ScO_3FeAs

3.1 Introduction

As of October 2008 the thickest blocking layers found in FeAs based superconductors were the fluorite-type $(LnO)^+$ (*Ln* = La-Er) and $(AF)^+$ layers (*A* = Eu, Sr, Ba, Ca).[1-4] The development of further structure types featuring more extended layers will likely prove useful in establishing relationships between electronic dimensionality, magnetism and superconductivity in these systems. Oxypnictides are often layered owing to the different bonding requirements of oxide and pnictide ions. Oxide ions, being highly electronegative, preferentially coordinate 'hard' cations i.e. rare earths or early transition metals, whilst the more polarisable pnictide ions tend to bond with more covalent character to late transition metals. With this in mind, novel iron arsenide materials with extended oxide layers were targeted with inspiration taken from compounds containing Cu*Ch* (*Ch* = chalcogenide) anti-PbO-type layers.

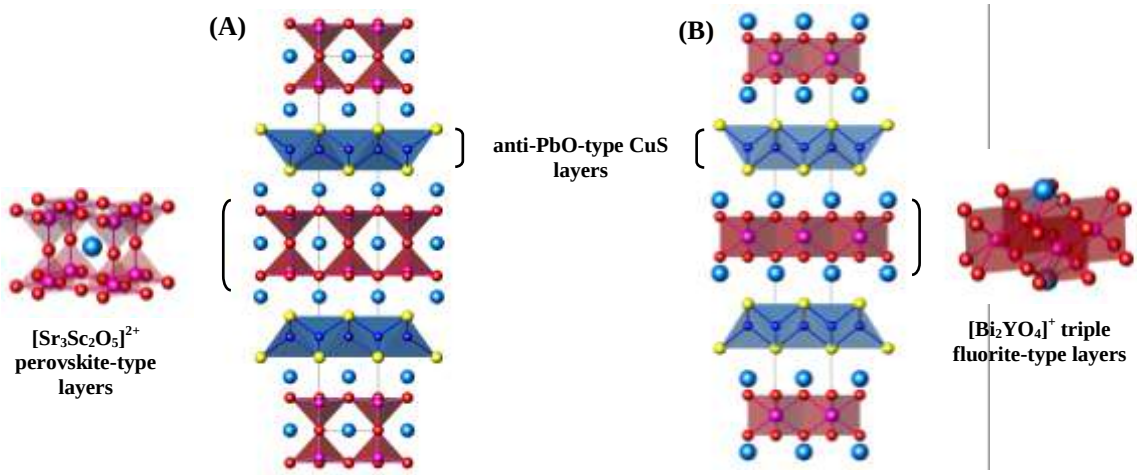

Figure 3.1 (A) Crystal structure of $Sr_3Sc_2O_5Cu_2S_2$. (B) Crystal structure of $Bi_2YO_4Cu_2Se_2$.

Early attempts focussed on preparing materials isostructural to $Bi_2Ln^{III}O_4Cu_2Se_2$ (*Ln* = Y, Gd, Sm, Nd, La), namely $Bi_2CeO_4Fe_2Pn_2$ (*Pn* = P, As), replacing the Ln^{III} metal cation with Ce^{4+} to preserve the formal charge on the iron pncitide layer $[FePn]^-$.[5] Unfortunately these attempts were unsuccessful. PXRD analysis reveals the presence of FeAs/FeP along with binary metal oxide phases. One possible explanation for the unwillingness of these materials to form may be that the Ce^{4+} cation is too small to occupy the 8-fold coordination site within the oxide layer. Thus replacing cerium with larger M^{IV} cations such thorium or uranium may produce stable materials, though attempts at their synthesis have yet to be made.

Further inspiration for new FeAs materials is found in a series of compounds containing CuS anti-PbO-type layers separated by perovskite-type oxide layers $(Sr_{n+1}M_nO_{3n+1})(Cu_2S_2)$.[6] Within such compounds the highly chalcophilic nature of Cu ensures its uptake into the chalcogenide layer, affording oxide layers which support a broad range of transition metals. Since it has been established that it is the FeAs layers which support superconductivity, it is necessary to ensure a similar preference in Fe*Pn* perovskite materials so that iron is coordinated by pncitide rather than oxide anions. Hence by incorporating a very oxophilic metal such as Sc into the oxide layer, competition for the tetrahedral sites within the pnictide layer can be avoided. $Sr_3Sc_2O_5Fe_2As_2$, a direct analogue of $Sr_3Sc_2O_5Cu_2S_2$ was therefore targeted. $Sr_3Sc_2O_5Cu_2S_2$ contains alternately stacked $(CuS)^-$ anti-PbO-type and $(Sr_3Sc_2O_5)^{2+}$ perovskite-type layers with Sc in a square-pyramidal coordination geometry (Figure 3.1).

3.2 Experimental

A synthetic route to $Sr_3Sc_2O_5Fe_2As_2$ was therefore designed according to *eqn.3.1* and a 1 g mixture was weighed out and loaded into a Nb tube and sealed under argon (procedure described in chapter 2). The Nb tube was sealed under a dynamic vacuum in a silica ampoule, then heated slowly at 1 °C / min to 500 °C for 12 h, before the temperature was increased to 800 °C for 24 h. This heating regime was employed to ensure that the volatile elemental arsenic reacts before it undergoes sublimation (615 °C).

$$Sc_2O_3 + 2\ SrO + Sr + 2\ Fe + 2\ As \rightarrow Sr_3Sc_2O_5Fe_2As_2 \qquad \textit{eqn.3.1}$$

A PXRD pattern collected on an X'pert pro diffractometer (AJC008) reveals a clear mixture of phases (Figure 3.2).

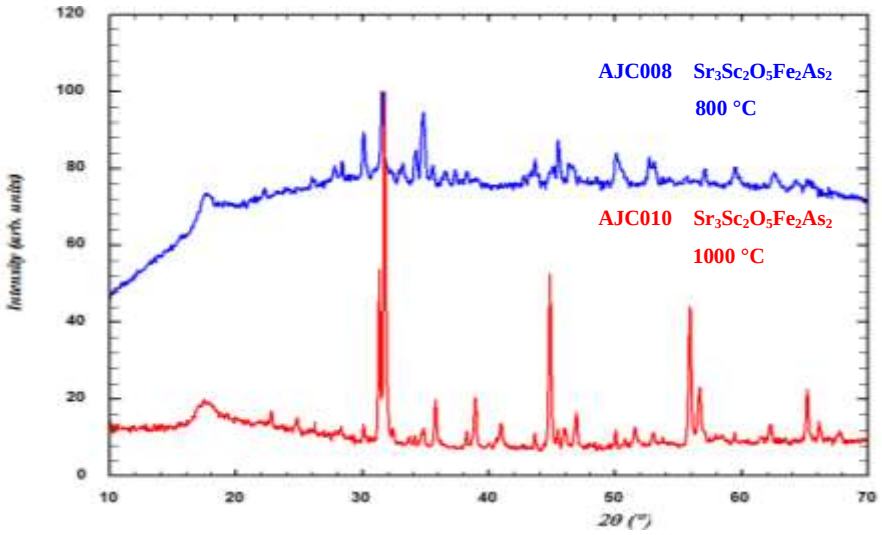

Figure 3.2 X-ray powder diffraction patterns for $Sr_3Sc_2O_5Fe_2As_2$

The sample was therefore ground, pressed into a 12 mm pellet at a force of 5 tonnes, placed in an alumina crucible, sealed in a silica tube and heated to 1000 °C at 1 °C min^{-1} and held at this temperature for 48 h, before being cooled to room temperature at 10 °C min^{-1}. The black polycrystalline product was stored in an argon dry box and a powder X-ray diffraction pattern was collected at room temperature using a PANalytical X'pert pro diffractometer (Figure 3.2). A search of the ICSD database indicates the presence of minor SrO, As and Sc_2O_3 phases, but the majority of reflections are attributed to an unknown phase.

A simulated model of $Sr_3Sc_2O_5Fe_2As_2$ was generated using a modified crystallographic information file of $Sr_3Sc_2O_5Cu_2S_2$ as a starting point (Figure 3.3), replacing Cu with Fe at the [4*d* (½, 0, ¼)] site and S with As at the [4*e* (0, 0, 0.195)] site. However, it was not possible to obtain a good fit to the observed data by refining the lattice parameters from this point, so an attempt was made to index individual reflections. The simulated pattern of $Sr_3Sc_2O_5Fe_2As_2$ predicts strong (110) and (200) reflections, which were assigned to Bragg intensity at 31.35 ° and 44.85 ° 2θ, respectively, to give an *a* cell parameter of 4.033 Å. The *c* cell parameter was then manually adjusted in an attempt to fit further reflections. A best fit to the data was realised with a *c* cell parameter of 27.60 Å. This modelled some further reflections well, however a good many more were predicted at *d*-spacings inconsistent with the observed data, including a strong (116) reflection.

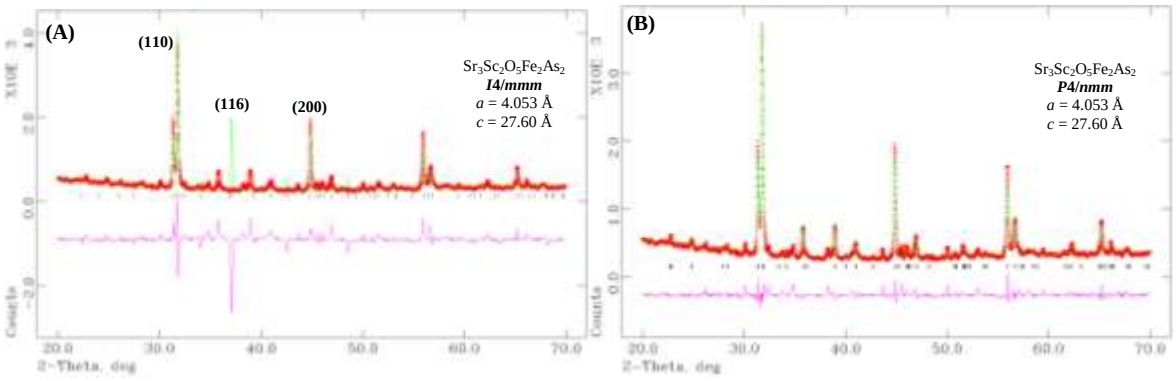

Figure 3.3 Rietveld fit to laboratory X-ray powder diffraction data (AJC010) with (A) $Sr_3Sc_2O_5Fe_2As_2$ and (B) Sr_2ScO_3FeAs structural models.

A re-evaluation of the likely unit cell was undertaken and based on the good fit of the (110) and (200) reflections, a tetragonal unit cell was proposed. The indexing program crystal cracker was then used with a primitive tetragonal cell and the *c* cell parameter was adjusted until a good fit to low angle peaks was achieved. The results of this analysis yield

a *c* cell parameter of 15.82 Å, a value a little over half the size of that expected for $Sr_3Sc_2O_5Fe_2As_2$.

To investigate if this is a known structure-type a search of the ICSD was made which revealed a series of Sr_2MO_3CuS (*M* = Cr, Mn, Fe, Ga and In) materials, originally synthesised and characterised by Zhu and Hor in 1997.[7,8,9] This family feature anti-PbO-type CuS layers separated by an oxide layer that resembles a portion of the K_2NiF_4 structure,[10] with the *M* metal cation in a square pyramidal geometry (Figure 3.4). All members of this family crystallise in the *P*4/*nmm* space group under the reflection condition $h + k = 2n$ for $h\ k\ 0$. The oxide layer in these Sr_2MO_3CuS materials are slightly thicker than those in $Sr_3M_2O_5Cu_2S_2$, but the absence of any cell centring means that the *c* cell parameter is slightly over half of that observed in $Sr_3M_2O_5Cu_2S_2$ (*I*4/*mmm*). This is consistent with the *c* cell parameter obtained from indexing, so a Rietveld fit of *P*4/*nmm* Sr_2ScO_3FeAs, isostructural to Sr_2MO_3CuS, was performed which shows a good agreement between the observed and calculated data (Figure 3.3).

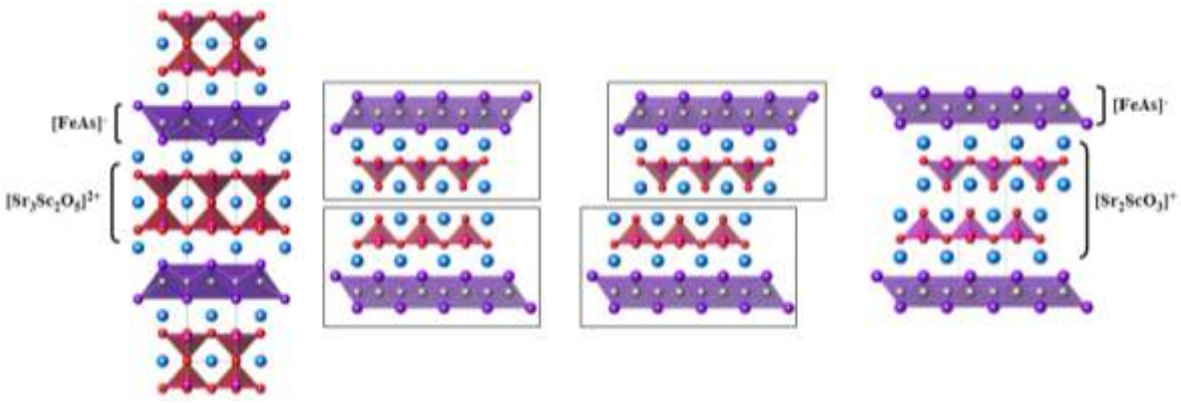

$Sr_3Sc_2O_5Fe_2As_2$ **Sr_2ScO_3FeAs**

Figure 3.4 Comparison of the crystal structures of $Sr_3Sc_2O_5Fe_2As_2$ and Sr_2ScO_3FeAs.

At the time of this discovery the original target material $Sr_3Sc_2O_5Fe_2As_2$ was reported by Wen *et al.*[11] It is therefore curious to note the preferential formation of Sr_2ScO_3FeAs over $Sr_3Sc_2O_5Fe_2As_2$ in the synthesis described above, given the ratio of starting materials used and the similar annealing profiles used here and by Wen *et al*. The observation would appear to imply that an excess of SrO is present among the reagents, since Sr_2ScO_3FeAs has one additional SrO per formula unit compared with $Sr_3Sc_2O_5Fe_2As_2$. The origin of such an excess is unclear, however in future syntheses precautions were taken to dry hygroscopic Sc_2O_3 in a furnace before use and bake silica tubes out in a furnace prior to use to eliminate any oxygen contamination.

Given the expeditious nature of the field, efforts were focussed on the refinement of a synthetic route to the novel iron oxide pnictide Sr_2ScO_3FeAs. In this refined synthetic procedure SrAs was prepared as a precursor to avoid the use of strontium metal. The synthesis of SrAs (AJC018) is detailed in chapter 2 and this highly air sensitive black polycrystalline powder was stored in an argon dry box. A 1 g sample of Sr_2ScO_3FeAs (AJC110) was synthesized by annealing stoichiometric mixtures of Sc_2O_3, SrO, SrAs, Fe and As in a 1 : 3 : 1 : 2 : 1 ratio. These reagents were thoroughly ground together in an agate pestle and mortar, pressed into a pellet, placed in an alumina crucible and sealed in a silica ampoule. The sample was heated to 500 °C at a rate of 1 °C / min, held at this temperature for 12 h, then heated to 800 °C for 24 h. The resultant black powder was reground, pressed into a pellet, sealed in a silica ampoule and annealed at 1100 °C for a further 48 h. Powder X-ray diffraction data on this air stable black sample was collected at room temperature using a PANalytical X'pert diffractometer.

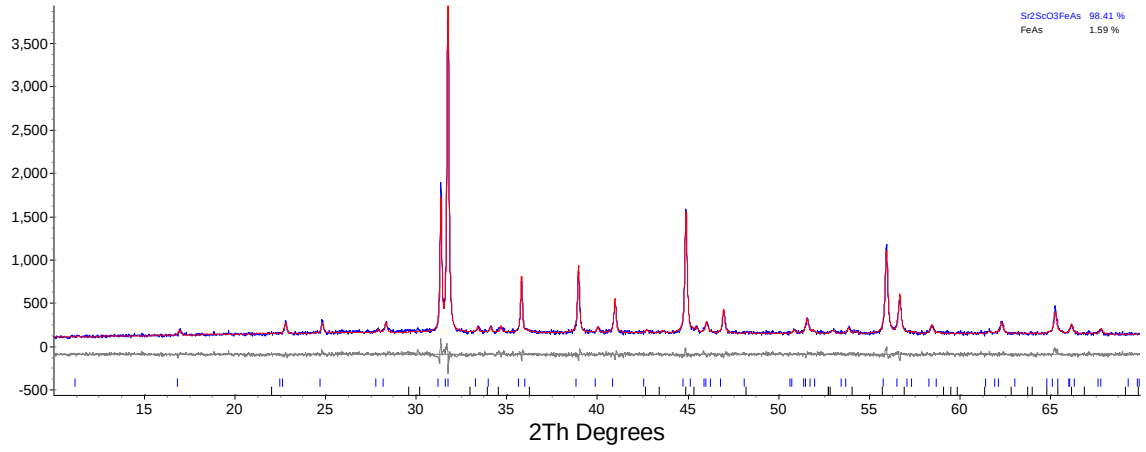

Figure 3.5 Rietveld fit to laboratory X-ray powder diffraction data for Sr_2ScO_3FeAs (AJC110)

The Rietveld fit of Sr_2ScO_3FeAs to this data is shown in Figure 3.5, which also includes a minor FeAs (1.59 wt %) impurity phase. The refined lattice parameters are a = 4.04969(7) Å and c = 15.8182(4) Å. Further discussion of the structure and stoichiometry is made in section 3.4.

3.3 SQUID Magnetometry and conductivity

The ZFC and FC magnetic susceptibilities of Sr_2ScO_3FeAs (AJC110) measured in an applied field of 1000 Oe between 2 and 300 K are shown in (Figure 3.6). The sample is paramagnetic at all temperatures and does not exhibit any signature of the ordering of Fe moments. The susceptibility is several orders of magnitude greater than that of a Pauli paramagnet and below 50 K at least exhibits a strong temperature dependence.

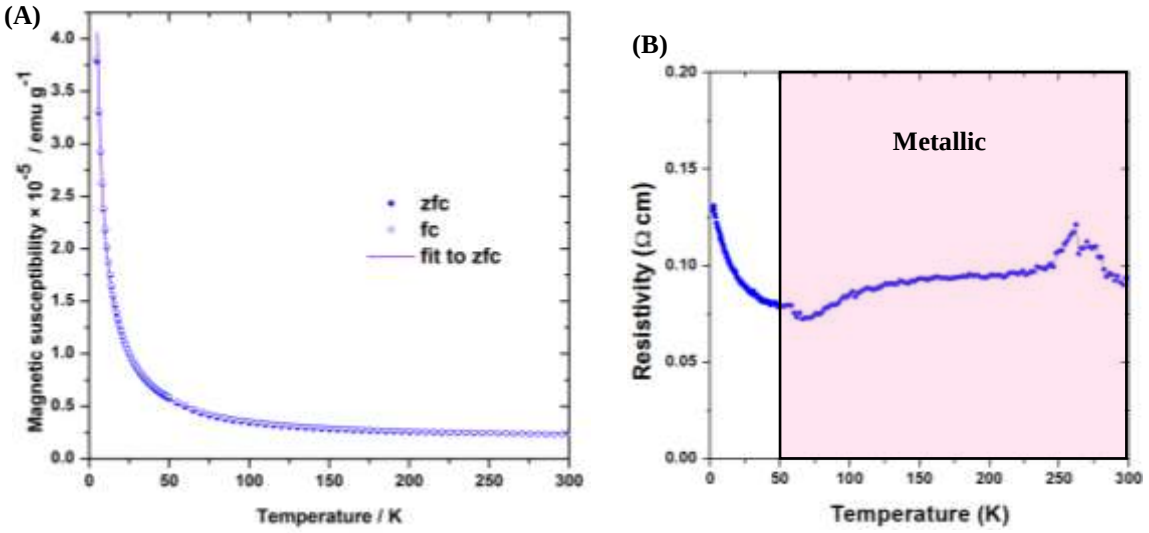

Figure 3.6 (A) Temperature dependence of magnetic susceptibility of Sr_2ScO_3FeAs (B) Temperature dependence of resistivity for Sr_2ScO_3FeAs.

The zero-field-cooled susceptibility is fitted here according to *eqn3.1*, from which a value for χ_0 the temperature-independent susceptibility is found to be 5.07(5) × 10^{-4} cm^3 mol^{-1}. From the Curie constant the effective moment is then deduced to be 0.79 μ_B, indicating that few iron spins are localised.

$$\chi = \chi_0 + C/T \qquad \textit{eqn3.1}$$

Resistivity measurements were carried out on a sintered pellet of Sr_2ScO_3FeAs cut into a bar with dimensions 4 × 2 × 1 mm^3. No superconducting transition was observed down to 2 K, instead poor metallic behaviour is seen above 70 K with a small upturn seen in the resistivity data below this temperature indicating weak semiconducting behaviour (Figure 3.6). Other anomalies in the resistivity data are accounted for by the low integrity of the sintered pellet and subsequent poor contact of electrodes. The low effective moment of Fe and the poor metallic behaviour point towards the itinerant nature of Sr_2ScO_3FeAs at least at high temperatures and show no evidence of the spin density wave anomaly seen in other undoped FeAs systems.

3.4 Variable Temperature Powder Neutron Diffraction (PND)

In order to more fully characterise Sr_2ScO_3FeAs powder neutron diffraction measurements were performed at room temperature and 5 K on the HRPD diffractometer at ISIS. The aim of these measurements was to confirm the stoichiometry of Sr_2ScO_3FeAs, investigate Sc/Fe mixing and examine the possibility of a low temperature structural distortion and/or magnetic Bragg reflections from ordered Fe moments.

A 3 g sample of Sr_2ScO_3FeAs (AJC012) was therefore prepared and preliminary characterisation made by X-ray powder diffraction using a PANalytical X'pert PRO instrument. The Rietveld fit to this data is shown in Figure 3.7 and refinement results reveal the sample to be largely phase pure with a small SrO impurity phase (2 wt %). The sample was loaded into a cylindrical vanadium can and sealed with indium wire in an argon-filled glove box. A room temperature data collection was then performed for a total integrated proton current of 100 μAh. The sample was then mounted on to the end of a sample stick, equipped with a temperature sensor and inserted into an Al-tailed orange cryostat with vanadium windows, which was subsequently cooled to 5 K. A further data collection was then made for a total integrated proton current of 100 μAh.

As described in chapter 2, HRPD features 3 detector banks placed about the sample at fixed angles of 168 ° (DIFC 48213 $\mu sec^{-1}Å^{-1}$), 90 ° (DIFC 34760 $\mu sec^{-1}Å^{-1}$) and 30 ° (DIFC 13150 $\mu sec^{-1}Å^{-1}$) with each bank having its own characteristic *d*-range coverage and resolution. A combined refinement of Sr_2ScO_3FeAs against both RT laboratory X-ray powder diffraction data and RT powder neutron diffraction data, using all three banks, was performed using the TOPAS academic suite including variables to describe instrumental and structural parameters. The refined values used to model the observed data include the structural parameters listed in table 3.1 and parameters to model background, 2θ zero error, absorption, scale factors and profile coefficients.

A SrO impurity phase was included in the refinement and found to be present at a level of 3 wt %. A weak reflection was also seen in the back scattered bank at 103,300 μsec. This was assigned to the (110) reflection of vanadium and likely arises due to weak Bragg scattering from the vanadium sample can. It was well modelled by a Pawley phase (*Im*-3*m* a = 3.027(2) Å) in the back scattered 168 ° bank, but was not resolved in the 90 ° bank and was therefore omitted. The Rietveld fits to PXRD data and for each of the HRPD bank are presented in Figure 3.7 and show good agreement between the observed and calculated data, confirming the tetragonal structure.

Refinement of the occupancies on individual atom sites was carried out to confirm the stoichiometry of Sr_2ScO_3FeAs. In doing this the possibility of Fe/Sc mixing on the Sc [2*c* (¼, ¼, *z*)] and/or Fe [2*a* (¼, ¾, 0)] crystallographic sites was investigated utilizing the modest contrast in the bound coherent scattering lengths of Sc (12.29 fm) and Fe (9.45 fm). Given that the refinement was performed against combined neutron diffraction data the only constraint applied was that the occupancy of any crystallographic site must not be

greater than 1. Fixing the occupancies of both Sr sites to 1 and allowing the occupancies of all other sites to refine gives the composition $Sr_2Sc_{0.96(2)}O_{2.90(1)}Fe_{1.00(1)}As_{1.000(6)}$. This result indicates that all crystallographic sites apart from the O [*4f* (¼, ¾, *z*)] site are fully occupied within error and also that there is no evidence for Sc/Fe mixing on either transition metal site. This is unsurprising as although the sizes of the two metals are not dissimilar, the strong preference of scandium for the +3 oxidation state along with its electropositive nature both mean that it prefers to coordinate to oxide ions rather than arsenide. It should however be noted that the e.s.d.'s generated by TOPAS are statistical errors for one single refinement and are typically smaller than the standard deviation one would find from the results of several measurements.

Temperature		(AJC012) 295 K	(AJC012) 5 K
	a / Å	4.0496(3)	4.0420(7)
	c / Å	15.804(1)	15.753(3)
	Cell volume / Å	259.18(4)	257.37(9)
	χ^2	19.61	4.239
	${}_wR_p$	6.589	3.067
Atomic parameters:			
Sc	[2*c* (¼, ¼, *z*)]	0.30638(4)	0.30589(6)
	U_{11}, U_{33} × 100 / Å^2	1.54(3), 1.79(4)	1.29(4), 1.93(6)
	occ	0.96(2)	0.96(4)
Fe	[2*a* (¼, ¾, 0)]		
	U_{11}, U_{33} × 100 / Å^2	2.01(5), 2.90(8)	1.43(6), 3.22(9)
	occ	1.00(1)	1.00(2)
Sr(1)	[2*c* (¾,¾, *z*)]	0.18751(9)	0.1865(1)
	U_{11}, U_{33} × 100 / Å^2	0.81(5), 5.91(9)	0.65(5), 6.8(1)
Sr(2)	[2*c* (¾,¾, *z*)]	0.41765(8)	0.41823(9)
	U_{11}, U_{33} × 100 / Å^2	0.81(5), 5.91(9)	0.36(5), 3.12(9)
As	[2*c* (¼, ¼, *z*)]	0.08295(8)	0.0832(1)
	U_{11}, U_{33} × 100 / Å^2	2.83(8), 1.71(9)	2.60(8), 0.00(8)
	occ	1.000(6)	1.000(6)
O(1)	[4*f* (¼, ¾, *z*)]	0.28560(5)	0.28512(6)
	U_{11}, U_{22}, U_{33} × 100 / Å^2	0.88(6), 0.36(5), 2.65(7)	0.86(7), 0.008(1), 1.63(8)
	occ	0.952(4)	0.94(1)
O(2)	[2*c* (¼, ¼, *z*)]	0.4331(1)	0.4338(1)
	U_{11}, U_{33} × 100 / Å^2	4.28(8), 4.7(1)	1.80(6), 4.6(1)
	occ	1.000(6)	4.3(1)
Bond lengths and angles:			
	Fe-Fe / Å	2.8635(2)	2.8581(5)
	Fe-As / Å	2.4143(7)	2.4092(9)
	Sc-$O_{(eq)}$ / Å	2.0513(2)	2.0474(2)
	Sc-$O_{(ax)}$ / Å	2.002(2)	2.019(2)
	α As-Fe-As / °	114.00(5)	114.04(6)
	β As-Fe-As / °	107.25(2)	107.24(3)

Table 3.1 Results of refinement against PND data for Sr_2ScO_3FeAs at room temperature and 5 K

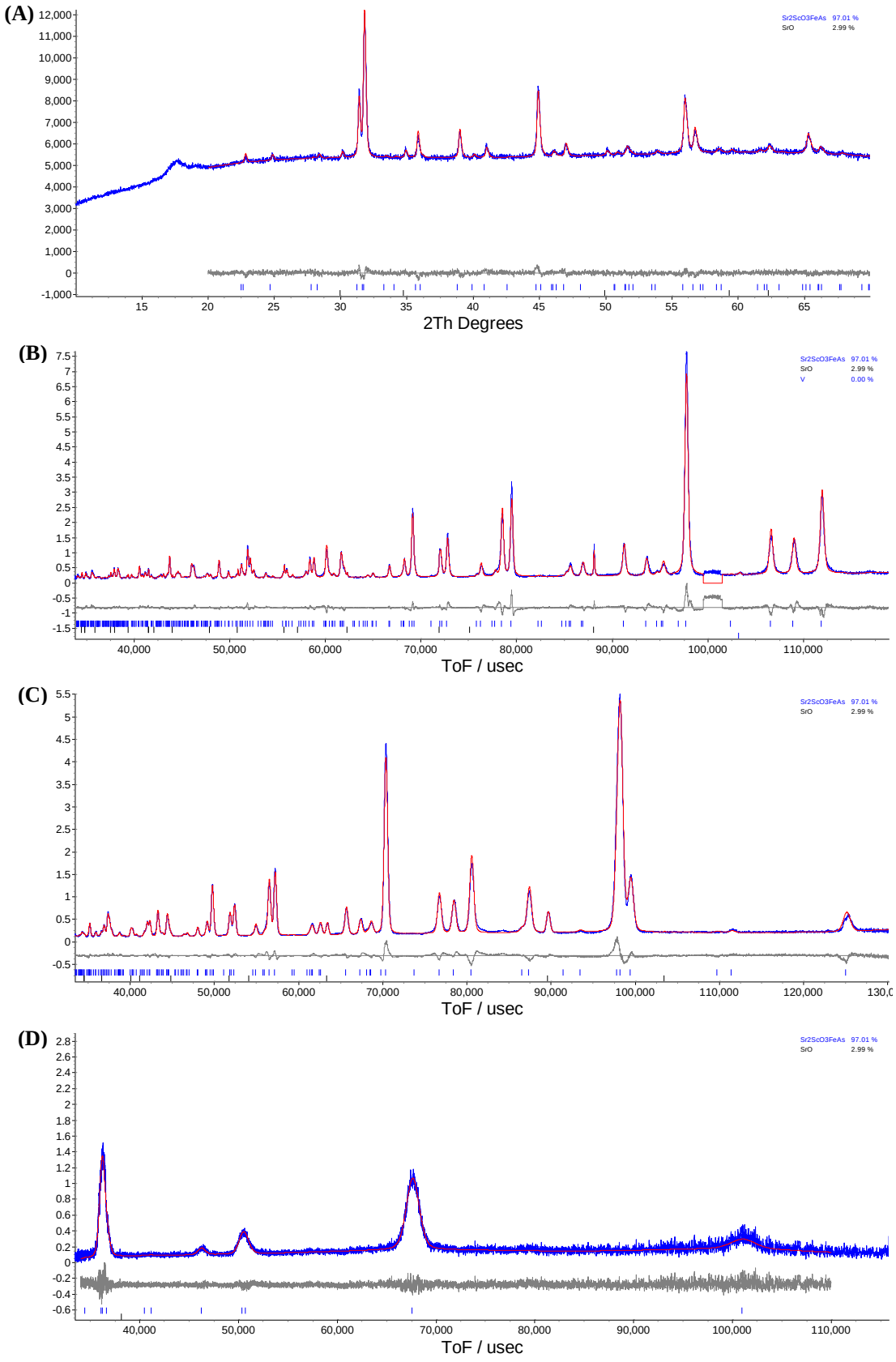

Figure 3.7 Rietveld fit for Sr_2ScO_3FeAs (AJC012) at room temperature to (A) Laboratory X-ray powder diffraction data, (B) HRPD backscattered 168° bank, (C) 90° bank, (D) 30° bank. Observed data = blue, calculated = red and difference = grey.

An analysis of the structure and geometry of Sr_2ScO_3FeAs is not complete without a comparison to other iron arsenide superconductors. Fe-Fe and Fe-As bond lengths for a selection of FeAs based superconductors are shown in Figure 3.8. The steric demands of the $[Sr_2ScO_3]^+$ layer mean that the Fe-Fe distance is greater than that seen in any ternary or quaternary iron arsenide materials. By contrast, the Fe-As bond length is intermediate between that of LaOFeAs and LiFeAs and thus the long Fe-Fe distance in Sr_2ScO_3FeAs results in $FeAs_4$ tetrahedra that are strongly compressed along the *c* axis (α = 114.00(5) °).

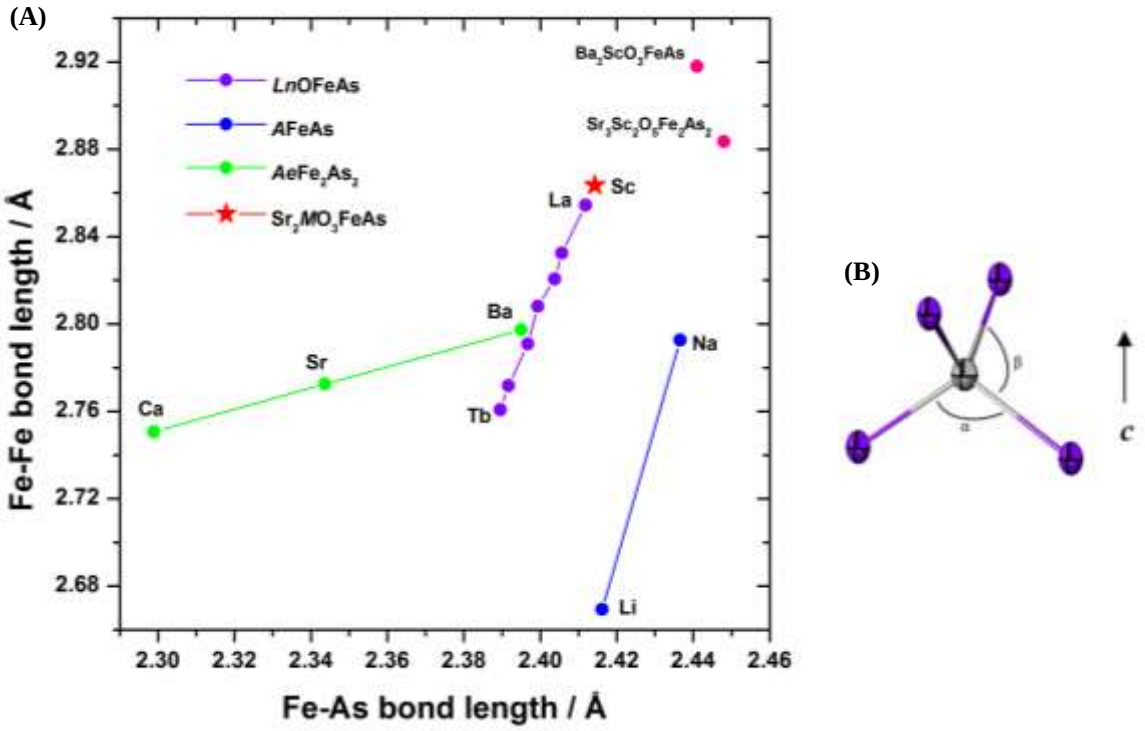

Figure 3.8 (A) Comparison of Fe-Fe and Fe-As bond lengths for selected iron arsenide superconductors. (B) Definition of α and β As-Fe-As bond angles.

The data collected at 5 K, exhibit a much higher background and lower signal to noise ratio than those collected at room temperature, despite the total integrated proton current being equal for both data sets (100 μAh). This is a result of the Al cryostat which is also responsible for the additional aluminium Bragg reflections observed at 98,000 and 69,300 μsec. As with the vanadium reflections in the room temperature data, this additional Bragg intensity was modelled by a Pawley phase (*Fm*-3*m* *a* = 4.0610(7) Å). The Rietveld fit to the 5 K data sets for all three detector banks are given in Figure 3.9 and all show good agreement between the observed and calculated data. Important structural parameters are summarised in table 3.1.

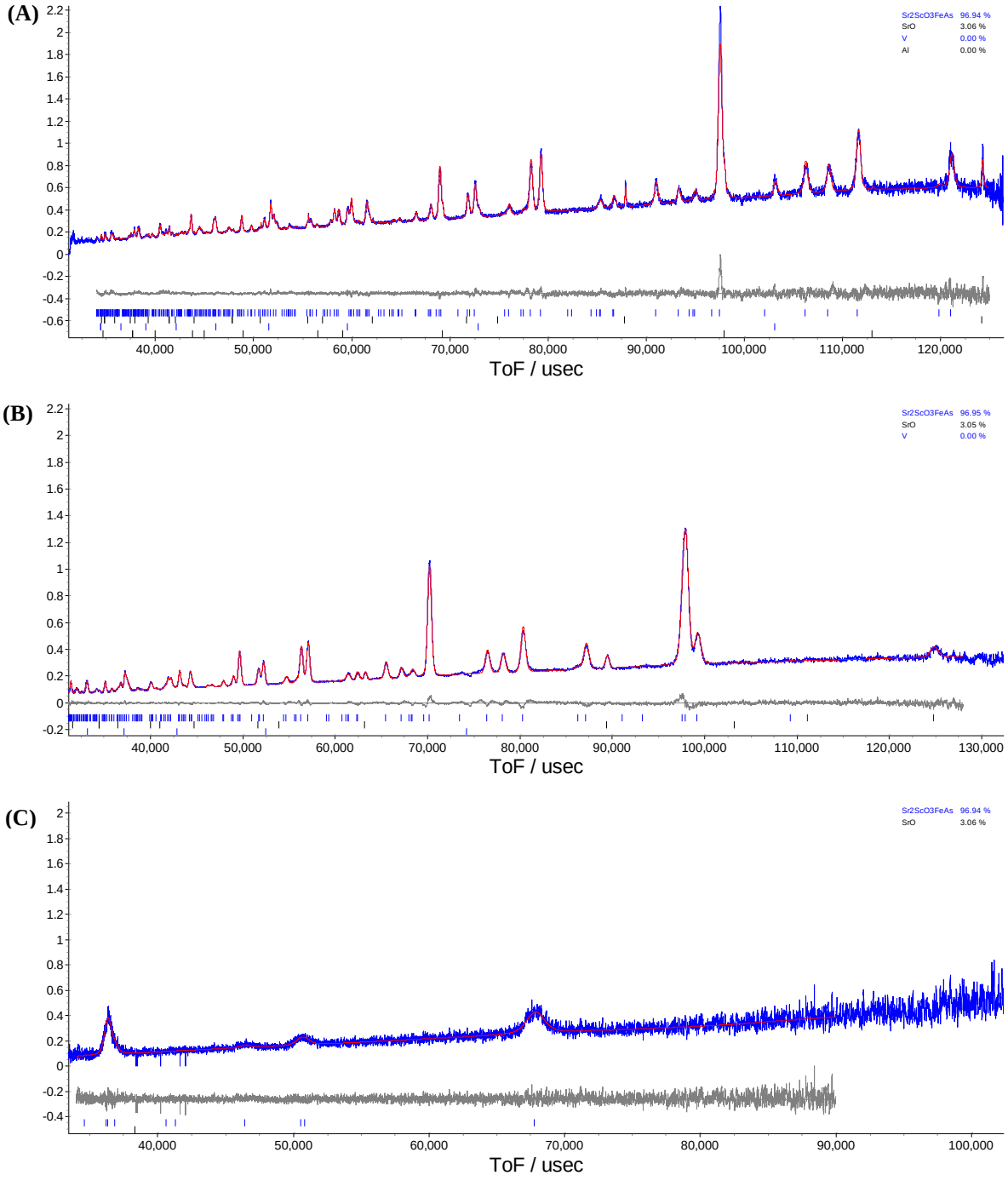

Figure 3.9 Rietveld fit for Sr_2ScO_3FeAs (AJC012) at 5 K to (A) HRPD backscattered 168 ° bank, (B) 90 ° bank, (C) 30 ° bank. Observed data = blue, calculated = red and difference = grey.

A small contraction is seen in the lattice parameters, but apart from this the tetragonal *P*4/*nmm* structural model for Sr_2ScO_3FeAs remains largely the same as that seen at room temperature. This is in contrast to other parent FeAs based superconductors i.e. 122, 1111 materials which undergo an orthorhombic distortion upon cooling.

To more rigorously assess the possibility of an orthorhombic distortion in Sr_2ScO_3FeAs, the full width at half maximum (FWHM) of the (200) reflection was scrutinised in the back

scattered bank at 295 K and 5 K. An increase in the FWHM of this peak would imply that the (200) and (020) reflections are no longer at the same position suggesting a degree of orthorhombicity. The FWHM of the (200) reflection was determined by a Pawley fit to this reflection in TOPAS over a short ToF range, from 96000 to 99000 μsec, with a single term to model the background. Also included in the 5 K data set is a Pawley fit to the Al(200) at 98,000 μsec. The Pawley fit to these reflections are shown in Figure 3.10 and the FWHM of the (200) at 295 and 5 K are 0.00381(2) and 0.00392(4) Å, respectively.

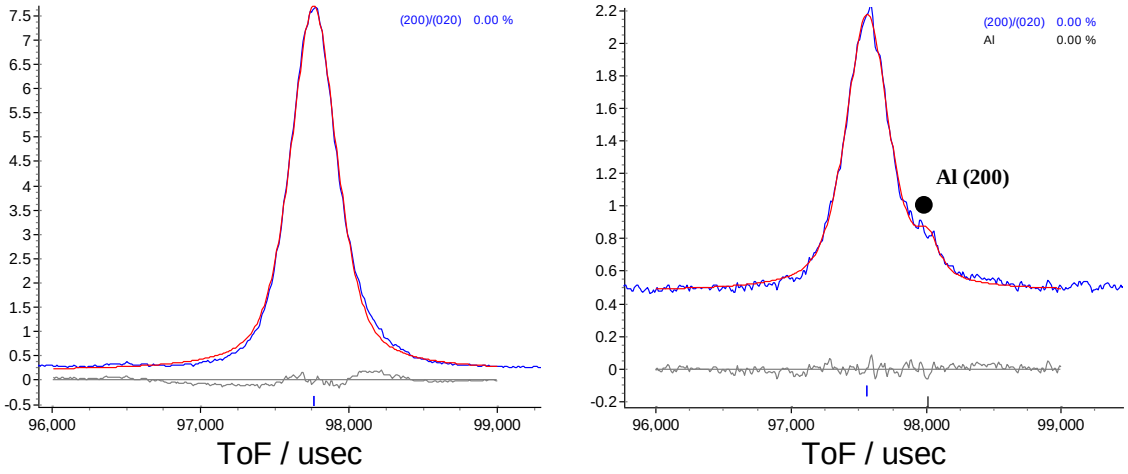

Figure 3.10 FWHM of the (200) reflection by a Pawley fit to PND data at (A) 295 and (B) 5 K.

Although the FWHM is slightly greater for the 5 K data, these values are equal within 3σ indicating that there is no strong evidence for an orthorhombic distortion in Sr_2ScO_3FeAs within the limits of this diffraction experiment. Furthermore no additional magnetic Bragg reflections are observed in the 5 K data. The absence of both an observable orthorhombic distortion and Fe magnetic Bragg reflections indicates that Sr_2ScO_3FeAs is somewhat different from other undoped FeAs materials.

3.5 Chemical substitutions

As in the case of the cuprate superconductors, the electron count in Fe-based superconductors appears to be a crucial parameter in determining whether a phase is superconducting and the magnitude of T_c. Many aliovalent substitutions on a range of crystallographic sites can be envisaged to attempt to tune the electron count of Sr_2ScO_3FeAs into the superconducting region.

3.5.1 $Sr_2ScO_3Fe_{1-x}Co_xAs$ electron doping

The partial substitution of Co^{2+} (d^7) on the Fe^{2+} (d^6) crystallographic site [2*a* (¼, ¾, 0)] is nominally e^- doping and has been shown to be a successful strategy for inducing

superconductivity in a variety of FeAs-based materials i.e. $LaOFe_{1-x}Co_xAs$,[12] $SrFe_{2-x}Co_xAs_2$,[13] and $CaFFe_{1-x}Co_xAs$.[14] This substitution also creates disorder in the Fe planes that have been shown to support superconductivity. This ability of the Co-substituted materials to support superconductivity is in strong contrast to the cuprate superconductors in which substitution on the Cu site leads to a rapid suppression of superconductivity. 1 g samples of $Sr_2ScO_3Fe_{1-x}Co_xAs$ in the compositional range $0 \leq x \leq 0.3$ were prepared according to *eqn.3.2*, using the experimental procedure detailed described for AJC110.

$$Sc_2O_3 + 3\ SrO + SrAs + (2 - 2x)\ Fe + 2x\ Co + As \rightarrow 2\ Sr_2ScO_3Fe_{1-x}Co_xAs \qquad \textit{eqn.3.2}$$

Samples of $Sr_2ScO_3Fe_{1-x}Co_xAs$ appear to be largely single phase according to laboratory PXRD measurements. However, small amounts of SrO and FeAs impurity phases are observed and could be accounted for quantitatively using Rietveld analysis, from which they were found to be present at levels of typically less than 5 wt %. All $Sr_2ScO_3Fe_{1-x}Co_xAs$ compositions crystallise at room temperature with the tetragonal Sr_2GaO_3CuS-type structure in the *P*4/*nmm* space group. Rietveld analysis was therefore performed using the TOPAS academic suite and Sr_2ScO_3FeAs as a starting model, including variables to describe instrumental and structural parameters. The Rietveld fit of $Sr_2ScO_3Fe_{0.8}Co_{0.2}As$ to laboratory PXRD data is shown in Figure 3.11.

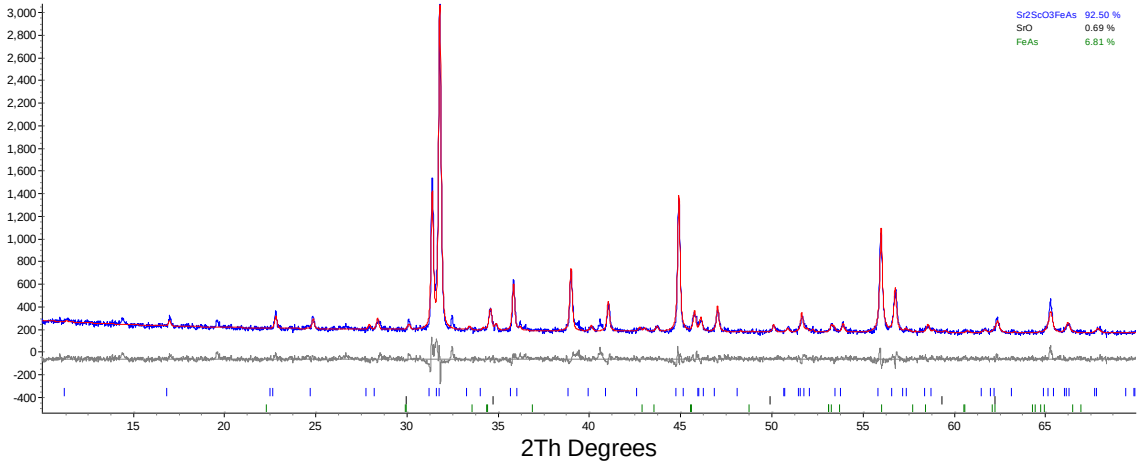

Figure 3.11 Rietveld fit of $Sr_2ScO_3Fe_{0.8}Co_{0.2}As$ to laboratory powder X-ray diffraction data

The variation of the lattice parameters with Co substitution from Rietveld analysis against laboratory PXRD data are shown in Figure 3.12. The *a* and *c* lattice parameters vary approximately linearly with *x* across the full compositional range synthesised, confirming the successful substitution of Co in Sr_2ScO_3FeAs. The basal lattice parameter *a* increases

as Co is introduced into the structure while the *c* lattice parameter perpendicular to the FeAs layers decreases. Overall this has the effect of decreasing the *c*/*a* ratio, compressing the structure along the *c* axis. The cell volume shows no strong trends with *x* as the contraction along the *c* axis compensates the increase in the basal cell parameter.

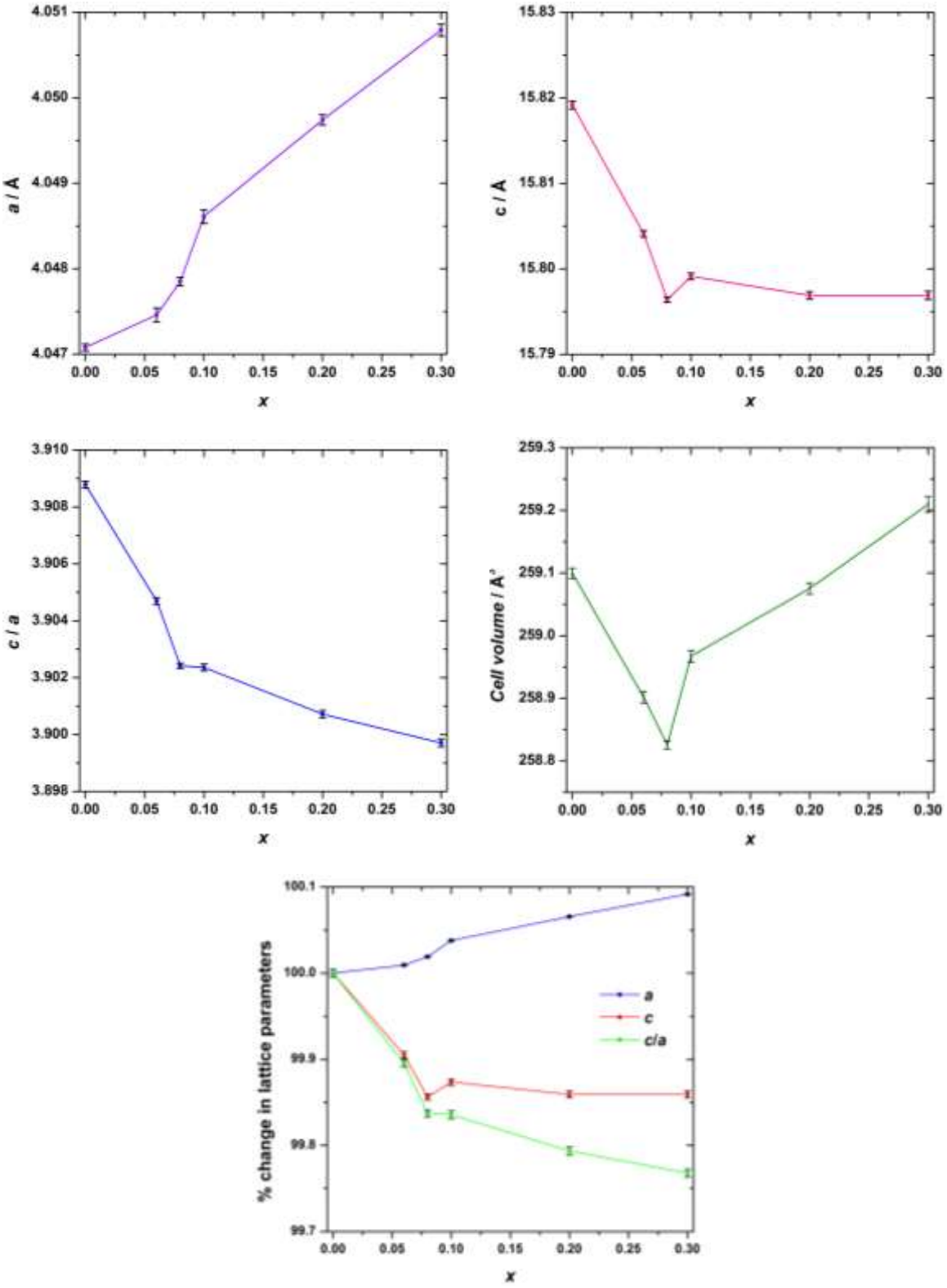

Figure 3.12 Variation in lattice parameters with *x* in $Sr_2ScO_3Fe_{1-x}Co_xAs$

The occupancy of Co^{2+} on the Fe^{2+} [2*a* (¼, ¾, 0)] site was not refined due to the lack of contrast between the X-ray scattering factors of iron and cobalt. The systematic trends in lattice parameters and absence of Co containing impurities in PXRD patterns are, however, strong evidence for the successful substitution of Co. The possibility of Co substitution on the Sc [2*c* (¼, ¼, *z*)] site is not considered likely as Co^{2+} is even less electropositive than Fe^{2+} and would therefore preferentially coordinate arsenide rather than oxide. Further evidence for the substitution of Co on the Fe site is seen in ^{57}Fe NMR measurements performed by collaborators at the LPS in Orsay. A clear cobalt induced broadening of the ^{57}Fe NMR signal is seen for $Sr_2ScO_3Fe_{1-x}Co_xAs$ samples with x = 0, 0.6 and 0.1 as the nominal Co content is increased (Figure 3.13).

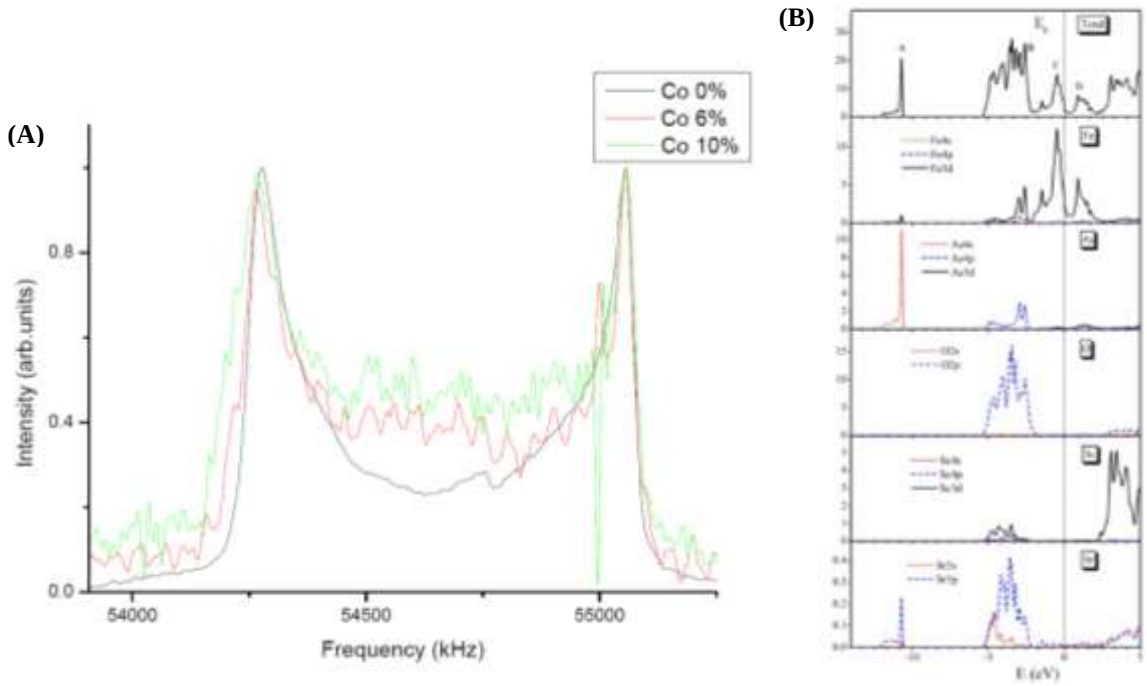

Figure 3.13 (A) ^{57}Fe NMR measurements on $Sr_2ScO_3Fe_{1-x}Co_xAs$ samples x = 0, 0.06 and 0.1. (B) Total and partial densities of states for Sr_2ScO_3FeAs from reference 6.[6]

The observed changes in the cell parameters with x cannot be rationalised by a simple geometric argument based on the size of the Co^{2+} (0.58 Å) and Fe^{2+} (0.63 Å) metal cations. Instead it is useful to consider the Fermi-surface topology and partial density of states of Sr_2ScO_3FeAs as calculated by Shein and Ivanovskii.[15] This study reveals that the bands in the proximity of the Fermi level are predominantly antibonding Fe 3*d* in character and similar to other FeAs parent materials (Figure 3.13). The nominal e^- doping by the substitution of Co^{2+} (d^7) for Fe^{2+} (d^6) therefore introduces electrons into the antibonding Fe 3*d* bands causing the antifluorite-type slabs to expand in the basal plane. This is seen in the

increase in the Fe(Co)-As bond length with *x*, which increases by 3 % over the range 0 - 0.3 $Sr_2ScO_3Fe_{0.7}Co_{0.3}As$. The trends in the Fe-Fe distance follow those in the basal lattice parameter because Fe-Fe = $a / \sqrt{2}$.

The As-Fe-As bond angles are two further parameters which exhibit significant changes upon Co doping. The two-fold α As-Fe-As bond angle, perpendicular to the *c* axis, decreases as Co is substituted while the four-fold β As-Fe-As bond angle increases. The $FeAs_4$ tetrahedra therefore change from being slightly compressed along the *c* axis in Sr_2ScO_3FeAs (α =114.5 °) to a geometry very close to that of a regular tetrahedron in $Sr_2ScO_3Fe_{0.7}Co_{0.3}As$ (α = 109.4 °). The increase in the regularity of the $FeAs_4$ tetrahedra upon Co substitution is perhaps unexpected when one considers the observed decrease in the *c*/*a* ratio. Thus the increase in the regularity of the $FeAs_4$ is driven by the increase in the Fe-As bond length which dominates over the compression in the basal plane.

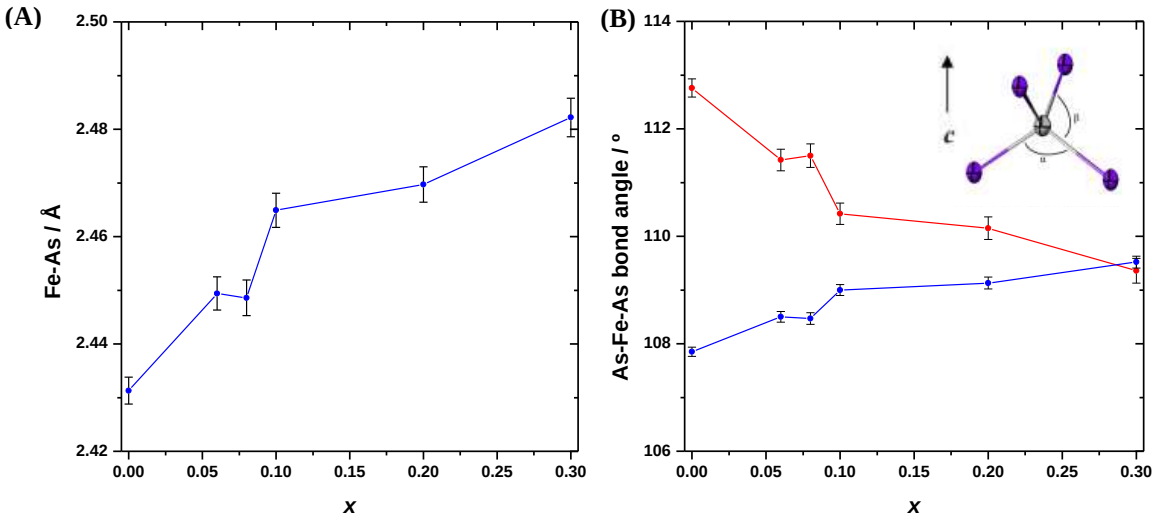

Figure 3.14 (A) Variation of Fe-As bond length and (B) As-Fe-As bond angles with *x* in $Sr_2ScO_3Fe_{1-x}Co_xAs$. Inset defines As-Fe-As bond angles.

The magnetic properties of $Sr_2ScO_3Fe_{1-x}Co_xAs$ materials were characterised by zero-field-cooled (ZFC) and field-cooled (FC) magnetisation measurements performed from 2 to 100 K in an applied field of 50 Oe using a SQUID magnetometer (Quantum Design, MPMS-XL). The magnetic susceptibilities of $Sr_2ScO_3Fe_{0.94}Co_{0.06}As$ and $Sr_2ScO_3Fe_{0.7}Co_{0.3}As$ are shown in Figure 3.15. No transition to diamagnetism was observed in any of the $Sr_2ScO_3Fe_{1-x}Co_xAs$ materials that have been synthesised. Instead $Sr_2ScO_3Fe_{1-x}Co_xAs$ materials are paramagnetic at all temperatures. The divergence of ZFC and FC susceptibilities in some samples suggests the presence of minor ferromagnetic impurities.

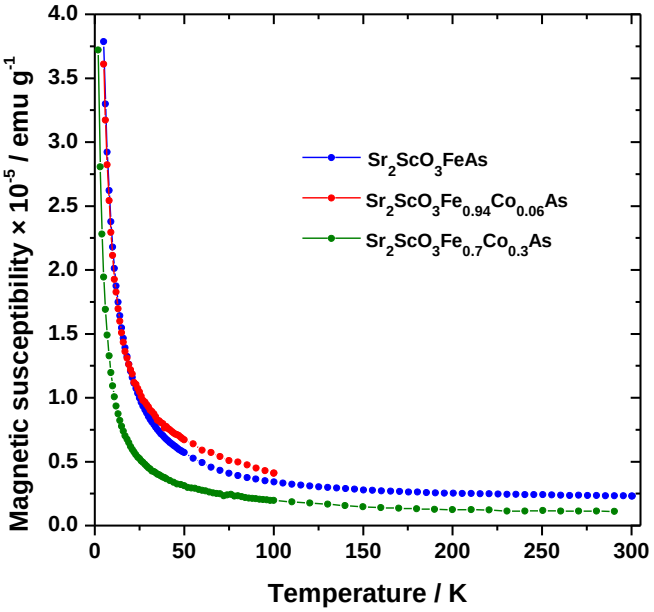

Figure 3.15 Comparison of the temperature dependence of the zero-field-cooled susceptibility of Sr_2ScO_3FeAs, $Sr_2ScO_3Fe_{0.94}Co_{0.06}As$ and $Sr_2ScO_3Fe_{0.7}Co_{0.3}As$

3.5.2 Further attempts to electron and hole doping strategies

Additional efforts were also made to electron dope Sr_2ScO_3FeAs into the superconducting state through the partial substitution of Sr^{2+} by La^{3+} in $Sr_{2-x}La_xScO_3FeAs$, whilst hole doping was realised in $Sr_2Sc_{1-x}Mg_xO_3FeAs$ samples. Doping levels of $\pm 0.1e^-$ / Fe atom were targeted, as this level has been shown to maximise T_c in other FeAs materials. Unfortunately, although these substitutions were in general successful, as evidenced by systematic changes in lattice parameters (appendix D), in no cases was a transition to diamagnetism observed above 2 K from magnetic susceptibilities measurements.

3.6 Discussion

In attempting to synthesise $Sr_3Sc_2O_5Fe_2As_2$, a competing and novel iron arsenide oxide Sr_2ScO_3FeAs has been discovered that crystallises in a tetragonal unit cell, in the *P*4/*nmm* space group with the Sr_2GaO_3CuS-type structure. At the time of its synthesis the separation of the Fe-Fe planes was the greatest seen in any FeAs structure type. Sr_2ScO_3FeAs is comprised of FeAs antifluorite type layers separated by insulating $[Sr_2ScO_3]^+$ oxide layers which resemble a portion of the K_2NiF_4 structure with Sc in a square pyramidal coordination of oxide anions.

Magnetic susceptibility measurements reveal that Sr_2ScO_3FeAs is paramagnetic down to 2 K and exhibits no anomaly indicative of long range Fe order. Room temperature powder neutron diffraction measurements confirm that, as anticipated, Sc occupies the

[2*c* (¼, ¼, 0.306)] site in the oxide layer and Fe occupies the [2*a* (¼, ¾, 0)] site in the arsenide layer. Refinement results not only reveal that Sr_2ScO_3FeAs features an anomalously large interplanar Fe-Fe distance, but also that the intraplanar Fe-Fe distance is larger than those observed in any ternary or quaternary iron pnictides, shorter only than those seen in isostructural Ba_2ScO_3FeAs, which was reported whilst this work was undertaken, and $Sr_3Sc_2O_5Fe_2As_2$.[11,16]

Powder neutron diffraction patterns collected at 5 K exhibit no additional magnetic Bragg reflections and no obvious splitting/broadening of the (200) Bragg reflection is observed. The absence of an observable antiferromagnetic ordering transition and an orthorhombic distortion is curious, and unexpected, given that band structure calculations on Sr_2ScO_3FeAs show features typical of iron arsenide superconductors. The Fe 3*d* band dominates in the vicinity of the Fermi level and these bands generate two hole-like cylinders around the Γ point and two electron-like cylinders at *M* linked by a (π, π) nesting vector. Therefore from an electronic view point the current calculations suggest that one would expect a SDW anomaly. This perhaps indicates that the decreased dimensionality of Sr_2ScO_3FeAs due to the introduction of thick oxide charge reservoirs is detrimental to the formation of a spin density wave. That said, a recent study of Sr_2ScO_3FeAs by Uemura *et al* has detected antiferromagnetic ordering of Fe moments below T_N = 35 K, with an ordered moment of ~0.1 μ_B at 2 K on each Fe, from ^{57}Fe Mössbauer and μSR measurements.[17] Such a small ordered moment would be very difficult to detect by powder neutron diffraction. Furthermore since the magnetic ordering is strongly coupled to the lattice an orthorhombic distortion associated with an ordered Fe moment of ~0.1 μ_B would likely be very small. Subsequent chapters will go on to investigate if the absence of an observed orthorhombic distortion and SDW, from the measurements reported here are a product of an increased intraplanar Fe-Fe distance, through the synthesis of isostructural materials with different transition metals at the [2*c* (¼, ¼, *z*)] site in the oxide layer.

The partial substitution of Co^{2+} (d^7) on the Fe^{2+} (d^6) crystallographic site has been successfully realised for $Sr_2ScO_3Fe_{1-x}Co_xAs$ in the compositional range $0 \leq x \leq 0.3$. This has a considerable effect on the Fe(Co)-As bond length and other structural parameters. These changes are rationalised by the introduction of additional electrons from Co into antibonding Fe 3*d* orbitals. Unfortunately it was not possible to induce superconductivity in these samples by this method of electron doping, or by any other hole/electron doping strategies attempted.

References

(1) Miyazawa, K.; Kihou, K.; Ishikado, M.; Shirage, P. M.; Lee, C. H.; Takeshita, N.; Eisaki, H.; Kito, H.; Iyo, A. *New Journal of Physics* **2009**, *11*, 9.

(2) Kamihara, Y.; Watanabe, T.; Hirano, M.; Hosono, H. *Journal of the American Chemical Society* **2008**, *130*, 3296.

(3) Han, F.; Zhu, X.; Mu, G.; Cheng, P.; Wen, H.-H. *Physical Review B* **2008**, *78*, 180503-4.

(4) Cheng, P.; Shen, B.; Mu, G.; Zhu, X. Y.; Han, F.; Zeng, B.; Wen, H. H. *European physics letters* **2009**, *85*, 4.

(5) Evans, J. S. O.; Brogden, E. R.; Thompson, A. L.; Cordiner, R. L. *Chemical Communications* **2002**, *2002*, 912-913.

(6) Otzschi, K.; Ogino, H.; Shimoyama, J.-i.; Kishio, K. *Journal of Low Temperature Physics* **1999**, *117*, 729-733.

(7) Zhu, W. J.; Hor, P. H. *Journal of Solid State Chemistry* **1997**, *134*, 128-131.

(8) Zhu, W. J.; Hor, P. H. *Inorganic Chemistry* **1997**, *36*, 3576-3577.

(9) Zhu, W. J.; Hor, P. H. *Journal of Solid State Chemistry* **2000**, *153*, 26-29.

(10) Ganguly, P.; Rao, C. N. R. *Journal of Solid State Chemistry* **1984**, *53*, 193-216.

(11) Zhu, X. Y.; Han, F.; Mu, G.; Zeng, B.; Cheng, P.; Shen, B.; Wen, H. H. *Physical Review B* **2009**, *79*, 5.

(12) Wang, C.; Li, Y. K.; Zhu, Z. W.; Jiang, S.; Lin, X.; Luo, Y. K.; Chi, S.; Li, L. J.; Ren, Z.; He, M.; Chen, H.; Wang, Y. T.; Tao, Q.; Cao, G. H.; Xu, Z. A. *Physical Review B* **2009**, *79*, 9.

(13) Leithe-Jasper, A.; Schnelle, W.; Geibel, C.; Rosner, H. *Physical Review Letters* **2008**, *101*, 207004.

(14) Matsuishi, S.; Inoue, Y.; Nomura, T.; Yanagi, H.; Hirano, M.; Hosono, H. *Journal of the American Chemical Society* **2008**, *130*, 14428.

(15) Shein, I. R.; Ivanovskii, A. L. *Physical Review B* **2009**, *79*, 245115.

(16) Tegel, M.; Hummel, F.; Lackner, S.; Schellenberg, I.; Pöttgen, R.; Johrendt, D. *Zeitschrift Fur Anorganische Und Allgemeine Chemie* **2009**, *635*, 2242-2248.

(17) Munevar, J.; Sánchez, D. R.; Alzamora, M.; Baggio-Saitovitch, E.; Carlo, J. P.; Goko, T.; Aczel, A. A.; Williams, T. J.; Luke, G. M.; Wen, H.-H.; Zhu, X.; Han, F.; Uemura, Y. J. *Physical Review B* **2011**, *84*, 024527.

4. Sr_2CrO_3FeAs

4.1 Introduction

In the previous chapter a new FeAs-structure type was realised in the form of Sr_2ScO_3FeAs. In this chapter the range of materials with this structure is extended to include a Cr analogue and the effect of partial substitution of Fe by Co is assessed with respect to the magnetic and superconducting properties of this material.

4.2 Synthesis

A 1 g sample of Sr_2CrO_3FeAs was synthesised by homogenising in an agate pestle and mortar stoichiometric amounts of SrO (prepared by thermal decomposition of $SrCO_3$ as described in chapter 2), Cr (Alfa 99.99 %), Fe_2O_3 (Alfa 99.998 %), Fe (Alfa 99.998 %) and As (Alfa 99.999 %) in a 2 : 1 : ⅓ : ⅓ : 1 ratio. This mixture was pressed into a 13 mm pellet at a force of 5 tonnes, placed in an alumina crucible and sealed in a silica ampoule. The sample was heated to 1100 °C at 1 °C / min, held at this temperature for 48 h and cooled to room temperature. The product was reground, pressed into a pellet and sintered again in a protective alumina crucible inside a sealed silica ampoule at 1100 °C for 48 h.

4.3 PXRD

Preliminary characterisation was made by PXRD measurements on a PANalytical X'Pert Pro diffractometer, which utilises Cu $K_{\alpha 1}$ radiation in a Bragg-Brentano geometry. The Rietveld fit to this data is shown in Figure 4.1 and the good agreement between the observed data and the calculated model confirm the synthesis of a phase pure sample of Sr_2CrO_3FeAs.

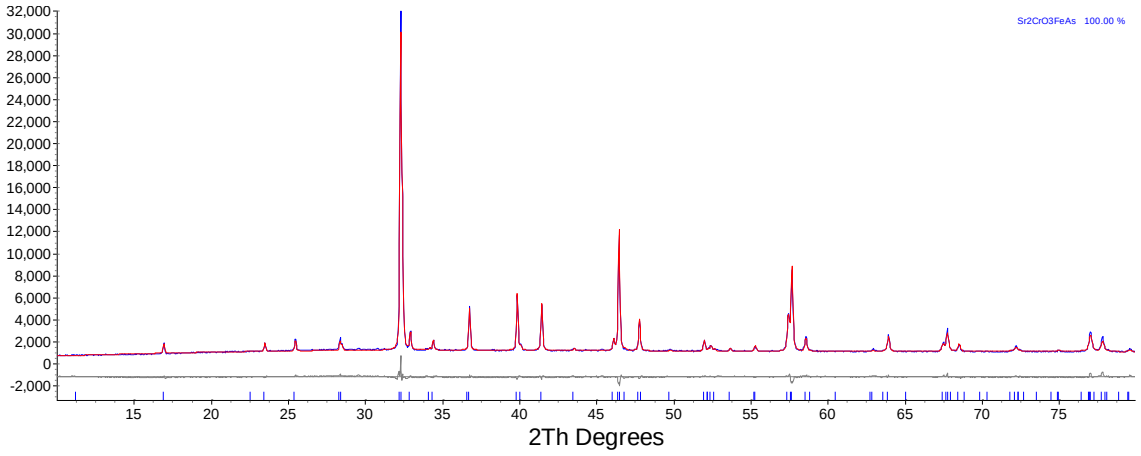

Figure 4.1 Rietveld fit of Sr_2CrO_3FeAs (AJC079) to laboratory powder X-ray diffraction data

The refinement was performed using the TOPAS academic suite and includes variables to describe instrumental and structural parameters. Important refined structural parameters for Sr_2CrO_3FeAs are summarised in Table4.1, along with those of Sr_2ScO_3FeAs for comparison. Additional parameters include terms to model background, 2θ zero error, absorption, scale factors and profile coefficients.

		Sr_2CrO_3FeAs (AJC079)	Sr_2ScO_3FeAs (AJC110)
		Space group *P4/nmm*: cell setting 2	
Cell parameters and global fitting parameters:			
a / Å		3.91492(3)	4.04962(7)
c / Å		15.7721(2)	15.8184(4)
Cell volume / Å^3		241.733(4)	259.41(1)
R_{wp}		3.685	6.717
χ^2		1.871	0.872
Atomic parameters:			
Sr1	[2*c* (¾, ¾, *z*)]	0.1950(1)	0.1899(2)
	b_{iso} / Å^2	4.91(8)	4.6(2)
Sr2	[2*c* (¾, ¾, *z*)]	0.4150(1)	0.4154(2)
	b_{iso} / Å^2	4.84(5)	5.2(1)
Sc/Cr	[2*c* (¼, ¼, *z*)]	0.3107(2)	0.3073(5)
	b_{iso} / Å^2	4.91(8)	4.6(2)
Fe	[2*a* (¼, ¾, 0)]	0	0
	b_{iso} / Å^2	5.82(8)	6.8(2)
As	[2*a* (¼, ¼, *z*)]	0.0899(2)	0.0846(2)
	b_{iso} / Å^2	4.78(7)	4.7(1)
O1	[4*f* (¼, ¾, *z*)]	0.2946(4)	0.2841(7)
	b_{iso} / Å^2	7.3(2)	6.1(4)
O2	[2*c* (¼, ¼, *z*)]	0.4257(5)	0.4275(9)
	b_{iso} / Å^2	6.5(3)	6.2(4)
Bond lengths and angles:			
	Fe-As / Å	2.417(1)	2.428(2)
	Fe-Fe / Å	2.76827(2)	2.86351(5)
	α As-Fe-As / °	108.14(9)	113.1(1)
	β As-Fe-As / °	110.14(5)	107.71(7)

Table4.1 Results of refinement against PXRD data for Sr_2CrO_3FeAs and Sr_2ScO_3FeAs

The replacement of Sc^{3+} (0.745 Å) with the smaller transition metal cation Cr^{3+} (0.615 Å) at the [2*c* (¼, ¼, *z*)] crystallographic site in the oxide layer causes a contraction in the *a* (3.32 %) and *c* (0.29 %) cell parameters (Figure 4.2).[1] This also generates a contraction in the Fe-Fe bond length of 3.32 % which follows that of the *a* cell parameter, since Fe-Fe = $a/\sqrt{2}$. By contrast the Fe-As bond length only decreases by 0.45 %. This is a reflection of the flexibility of the FeAs layer which affords dramatic changes in the geometry of the $FeAs_4$ tetrahedra, which go from being slightly compressed along the *c* axis in

Sr_2ScO_3FeAs (α = 113.1(1)°) to being slightly squashed in the *ab* plane in Sr_2CrO_3FeAs (α = 108.14(9)°), relative to a regular tetrahedron ($\alpha = \beta$ = 109.47°).

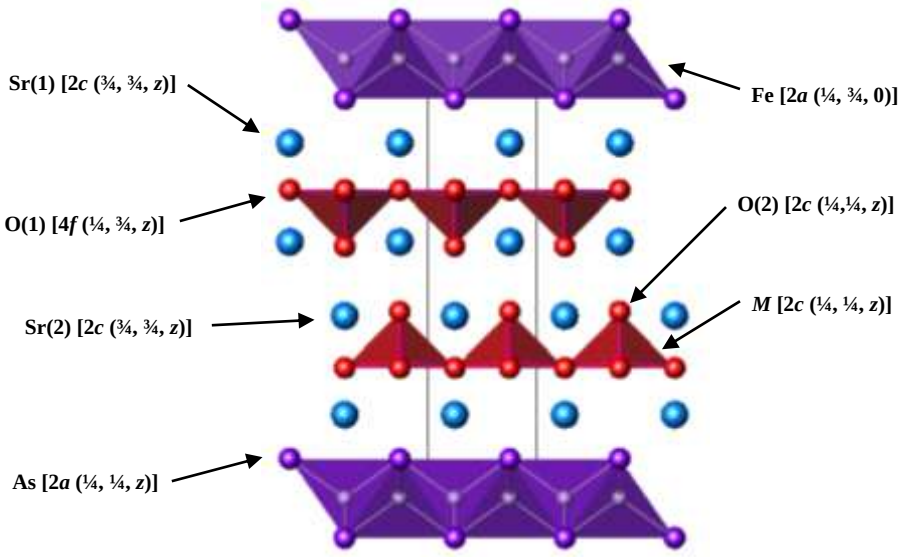

Figure 4.2 Crystal structure of Sr_2MO_3FeAs

4.4 SQUID Magnetometry

The magnetic susceptibility of Sr_2CrO_3FeAs (AJC079) measured in an applied field of 100 Oe between 2 and 300 K is shown in Figure 4.3. A broad maximum is observed at 40 K, analogous to that seen in Sr_2CrO_3CuS, indicative of the antiferromagnetic ordering of Cr^{3+} moments.[2] The absence of a transition to a diamagnetic superconducting state is typical for an undoped 'parent' Fe pnictide material.

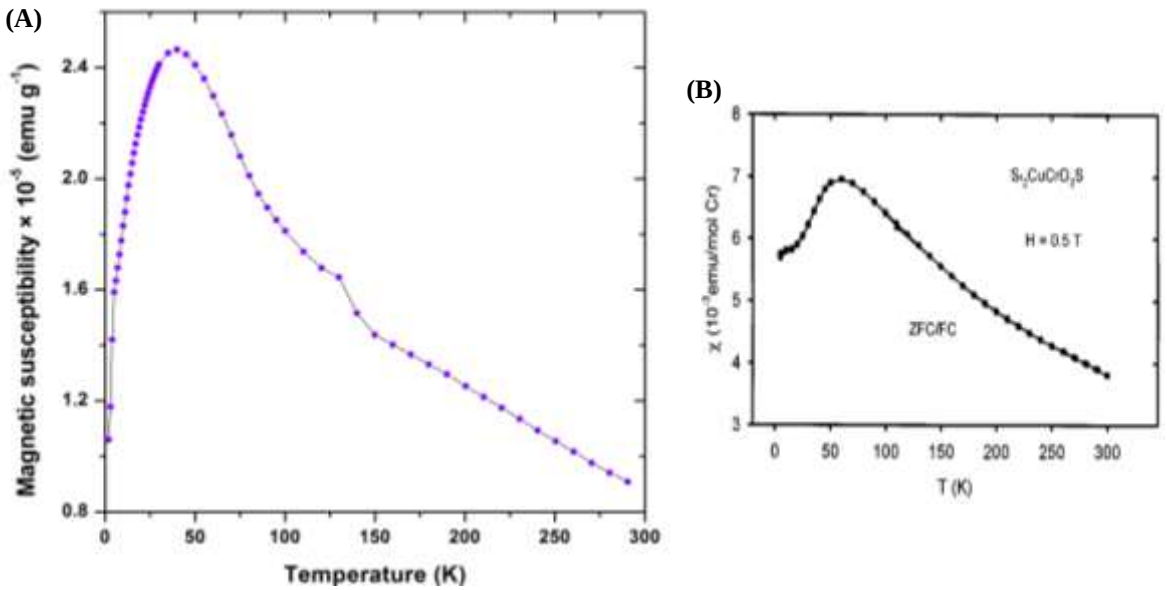

Figure 4.3 (A) ZFC magnetic susceptibility of Sr_2CrO_3FeAs measured in an applied field of 100 Oe between 2 and 300 K. (B) ZFC susceptibility of Sr_2CrO_3CuS from reference 2.[2]

4.5 Powder neutron diffraction studies

To investigate the stoichiometry, structure and magnetic properties of Sr_2CrO_3FeAs, powder neutron diffraction measurements were performed on the POLARIS and WISH time of flight diffractometers at ISIS. Preliminary measurements were carried out on a 2.5 g sample of Sr_2CrO_3FeAs (RM20) using the POLARIS instrument at room temperature (295 K) and 5 K. Investigations using the WISH instrument on a phase pure sample (AJC079) were made to confirm the magnetic structure and map out the transition to long range antiferromagnetic order.

4.5.1 POLARIS PND studies

Time-of-flight (ToF) neutron powder diffraction measurements were carried out at room temperature (295 K) and 5 K on a 2.5 g sample of Sr_2CrO_3FeAs (RM020) using the POLARIS diffractometer at the ISIS facility in its pre-2011 configuration. POLARIS is a high intensity, medium resolution powder diffractometer. The resolution of the back scattered detector bank on POLARIS ($\Delta d/d$ ~5×10^{-3}) is a factor of ten lower than that on HRPD ($\Delta d/d$ 4-5×10^{-4}). This means that there is a much greater degree of peak overlap at low *d*-spacings making the examination of any potential low temperature orthorhombic distortion difficult to probe. However, POLARIS benefits from a much higher neutron flux and covers a wide range of *d*-spacings, such that it offers a good balance between structural and magnetic studies. The instrument was reconfigured in 2012, but at the time of these measurements there were ^{3}He gas and ZnS scintillator detectors arranged in banks at 35°, 14°, 145° and 90° which are referred to as the A, B, C and E banks, respectively. The low angle B bank was excluded from refinements due to the poor signal to noise and resolution.

4.5.1.1 Room temperature POLARIS measurements

A refinement of Sr_2CrO_3FeAs (RM020) against room temperature powder neutron diffraction data, collected in the A, C and E detector banks, was performed using the GSAS software suite. Refined structural parameters are listed in Table 4.2 and instrumental parameters include those to model background, DIFA, scale factors and profile coefficients. FeAs and Cr impurity phases were included in the refinement and found to be present at levels of 3.91(4) and 3.41(6) wt %, respectively. The Rietveld fit of Sr_2CrO_3FeAs to room temperature PND data is depicted in Figure 4.4 and shows a good agreement between the calculated model and the observed data.

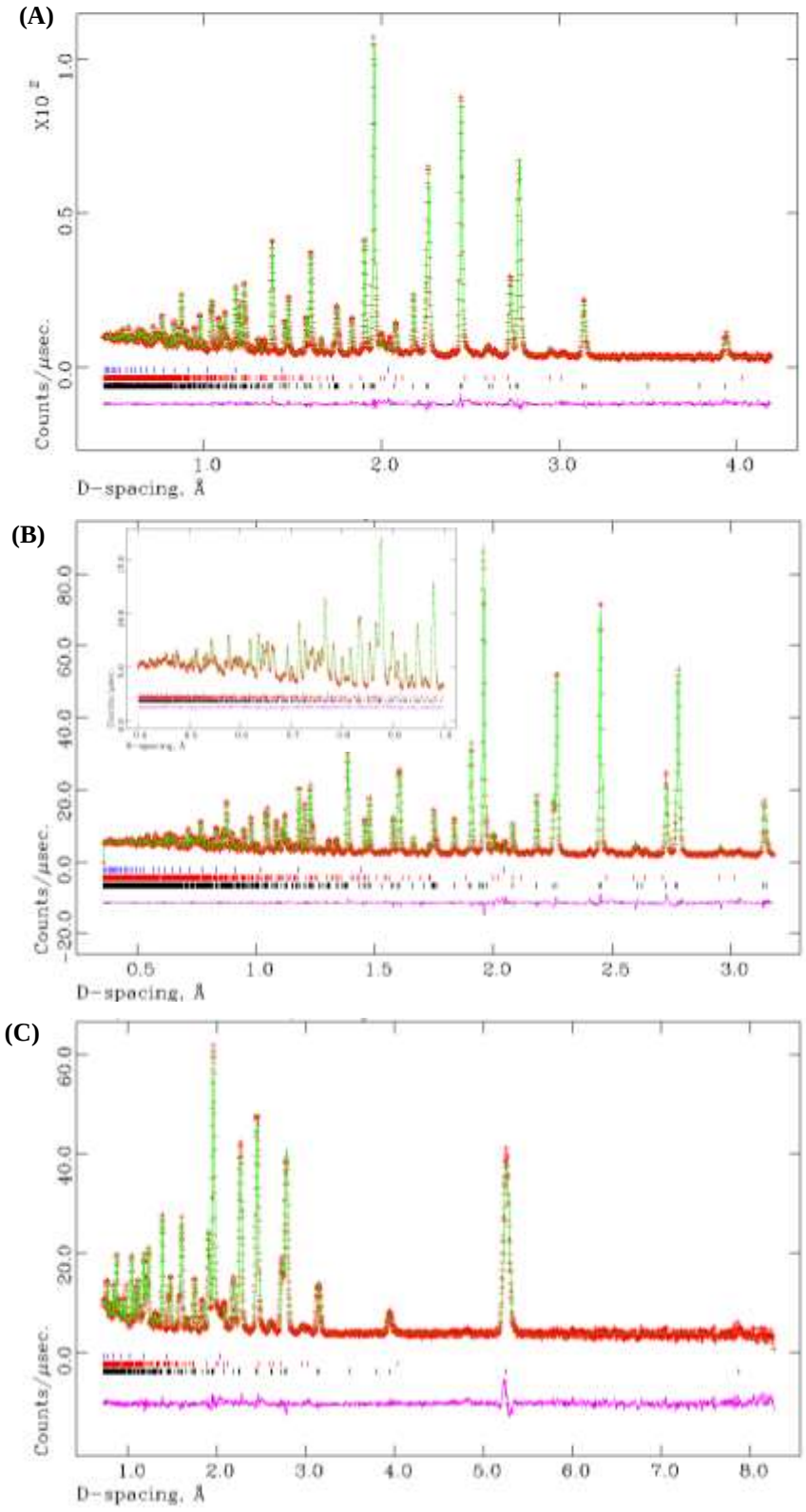

Figure 4.4 Rietveld fit to (A) 90 ° (B) 145 ° (C) 35 ° detector banks for room temperature Sr_2CrO_3FeAs powder neutron diffraction data

Temperature:		Sr_2CrO_3FeAs 295 K	Sr_2CrO_3FeAs (5 K)
		Space group *P*4/*nmm*: 2	
Cell parameters and global fitting parameters:			
a / Å		3.91334(3)	3.91043(1)
c / Å		15.7604(1)	15.6895(1)
Cell volume / Å^3		241.359(5)	239.916(2)
R_{wp} 90° bank		0.0298	0.0159
145° bank		0.0203	0.0072
30° bank		0.0506	0.0244
χ^2		2.041	1.776
Variables refined		76	77
Atomic parameters:			
Sr1	[2*c* (¾, ¾, *z*)]	0.19448(4)	0.19422(4)
	U_{11}, U_{33} × 100 / Å^2	0.44(1), 0.67(2)	0.197(5), 0.169(9)
Sr2	[2*c* (¾, ¾, *z*)]	0.41499(5)	0.41469(4)
	U_{11}, U_{33} × 100 / Å^2	0.59(2), 0.69(2)	0.203(5), 0.29(1)
Cr:Fe	[2*c* (¼, ¼, *z*)]	0.31080(7)	0.30945(7)
	U_{11}, U_{33} × 100 / Å^2	0.24(2), 0.41(4)	0.113(7)
	f_{occ}	1.00(2) : 0.00(2)	1.00(2) : 0.00(2)
	m_x / μ_B	0	1.76(4)
Fe:Cr	[2*a* (¼, ¾, 0)]		
	U_{11}, U_{33} × 100 / Å^2	0.48(1), 0.67(2)	0.176(3), 0.288(6)
	f_{occ}	0.977(2) : 0.023(2)	0.970(2) : 0.030(2)
As	[2*a* (¼, ¼, *z*)]	0.08951(5)	0.08900(4)
	U_{11}, U_{33} × 100 / Å^2	0.51(2), 0.80(3)	0.161(5), 0.40(1)
O1	[4*f* (¼, ¾, *z*)]	0.29460(3)	0.29432(3)
	U_{11}, U_{22}, U_{33} × 100 / Å^2	0.51(2), 0.24(2), 1.08(2)	0.255(8), 0.180(7), 0.62(1)
O2	[2*c* (¼, ¼, *z*)]	0.43019(5)	0.43017(5)
	U_{11}, U_{33} × 100 / Å^2	0.48(1), 0.67(2)	0.406(9), 0.45(2)
Bond lengths and angles:			
	Fe-As × (4) / Å	2.4122(5)	2.4022(4)
	Fe-Fe × (4) / Å	2.76715(2)	2.76510(1)
	Cr-$O_{(eq)}$ × (4) / Å	1.9733(2)	1.9695(2)
	Cr-$O_{(ax)}$ × (1) / Å	1.882(1)	1.894(1)
	α As-Fe-As / °	108.42(3)	108.96(3)
	β As-Fe-As / °	110.00(2)	109.73(1)
Impurity phases:			
	FeAs / wt %	3.91(4)	
	Cr / wt %	3.41(6)	

Table 4.2 Results of refinement against POLARIS data for Sr_2CrO_3FeAs at 295 and 5 K

The structural parameters from this refinement show fair agreement with those derived from refinement against X-ray powder diffraction data of a phase pure sample of Sr_2CrO_3FeAs (AJC079). However, the advantage of refinement against PND data is that the strong contrast between the neutron scattering lengths of Fe (9.45 fm) and Cr (3.635 fm) and the knowledge of the full occupancies of both sites from refinement against X-ray powder diffraction data permits the potential mixing of the two transition metals

sites to be assessed. Furthermore the possibility of correlation between the occupancies and displacement parameters of transition metals is minimised on POLARIS thanks to the large *d*-range accessible on this instrument.Rietveld refinement against PND data, employing a $f_{occ}Cr + f_{occ}Fe = 1$ constraint on both transition metal, results suggests a mixed occupancy of Fe 97.7(2) % and Cr 2.3(2) % on the iron [2*a* (¼, ¾, 0)] crystallographic site, but no such mixing on the chromium [2*c* (¼, ¼, 0.31)] site (. Such mixing introduces disorder into the Fe plane and is notably absent in isostructural Sr_2ScO_3FeAs, which contains the highly electropositive Sc^{3+} cation which coordinates exclusively to oxide. Similar results have since been reported by Johrendt *et al* and the significance of this result with respect to the emergence of superconductivity and spin density wave formation are discussed in section 4.8.[3]

4.5.1.2 Magnetic order in Sr_2CrO_3FeAs

As discussed in section 4.4 the magnetic susceptibility of Sr_2CrO_3FeAs exhibits a broad maximum at 40 K. A similar feature is also observed in isostructural Sr_2CrO_3CuS (T_N = 60 K) indicating low-dimensional antiferromagnetic ordering of Cr^{3+} moments, though the magnetic structure has not been studied in the oxysulfide. In an attempt to characterise this magnetic structure a data collection was made at 5 K using the POLARIS powder neutron diffractometer. In comparing the 35 ° bank at 295 and 5 K additional Bragg reflections are revealed in the low temperature data set (Figure 4.5).

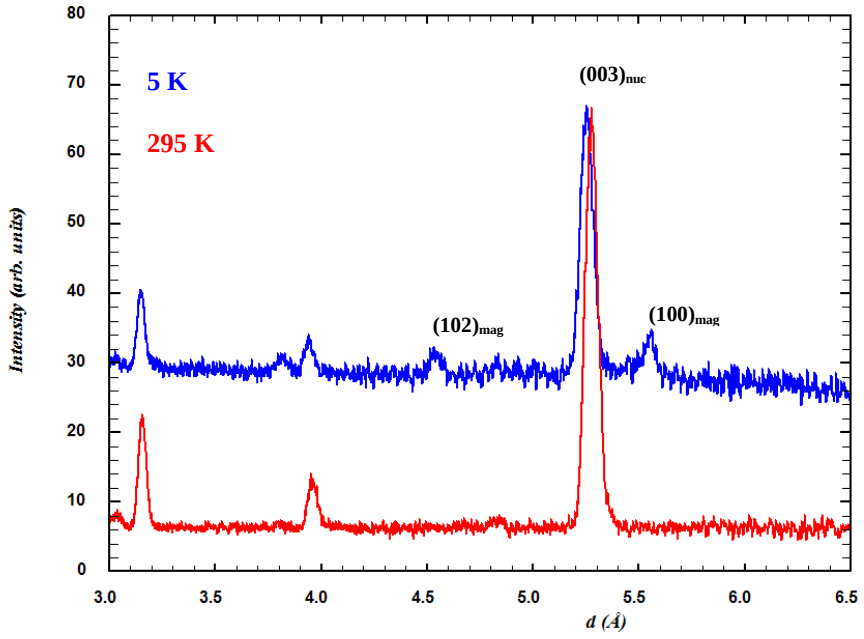

Figure 4.5 Comparison of powder neutron diffraction patterns of Sr_2CrO_3FeAs collected on the POLARIS ToF diffractometer at 295 and 5 K

The emergence of additional magnetic Bragg reflections is consistent with the antiferromagnetic character observed from susceptibility measurements and these additional magnetic reflections were indexed to a primitive tetragonal cell that is a $\sqrt{2}a \times \sqrt{2}a \times c$ expansion of the structural unit cell. A chequerboard arrangement of spins was therefore proposed, which afford the 3 different magnetic structures shown in Figure 4.6. In these magnetic structures the moments are either orientated along *a* as in those labelled Ψ^1 and Ψ^2, or along *c* as in Ψ^3. The spin arrangement between the Cr planes are then designated as being pseudo *C*-type or pseudo *G*-type depending on whether the spins in one layer can overlay those in adjacent layers by translation parallel to the orientation of the moment.

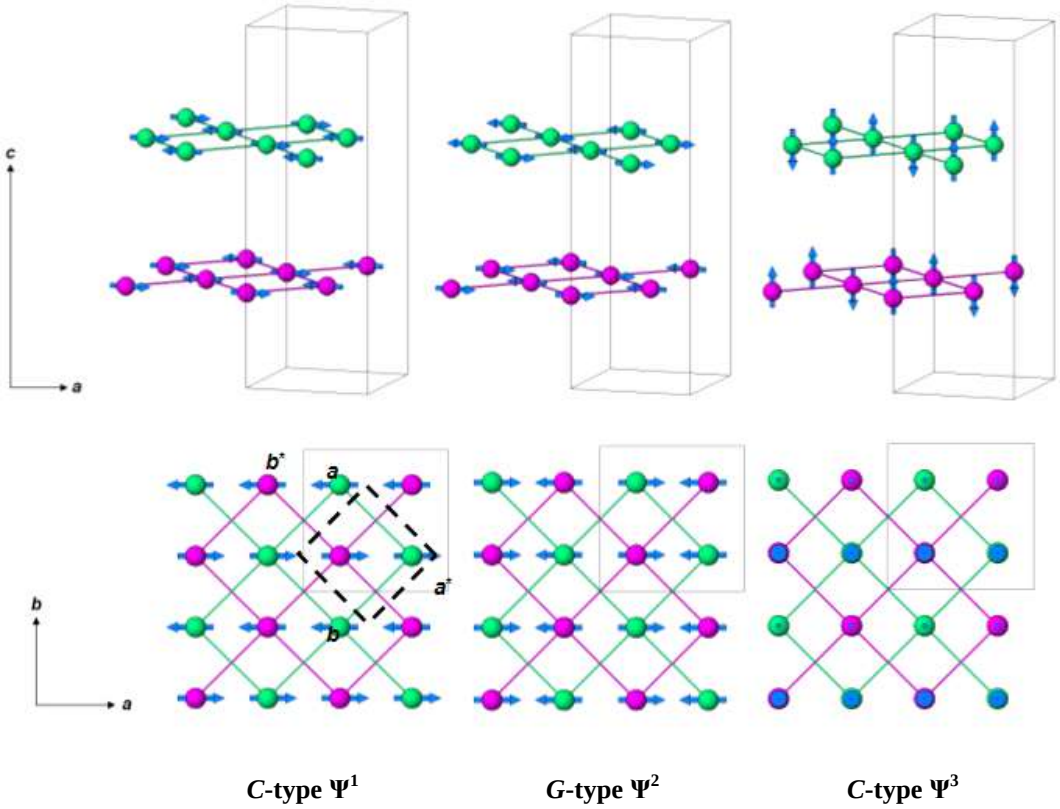

Figure 4.6 Possible magnetic structures for antiferromagnetic checkerboard arrangement of Cr spins in Sr_2CrO_3FeAs with a k = (½, ½, 0) propagation vector. a' = *a* + *b*, *b*' = *a* - *b*, *c*' = c

These magnetic structures were tested by introducing an additional phase into the GSAS refinement, in the *P*1 space group with lattice parameters constrained by reciprocal lattice tensors to be a $\sqrt{2}a \times \sqrt{2}a \times c$ relative to the nuclear Sr_2CrO_3FeAs phase. Cr atoms were then placed at the fractional coordinates (0.25, 0.25, *z*), (0.75, 0.75, *z*), (0.25, 0.75, (1 - *z*)) and (0.75, 0.25, (1 – *z*)) and the orientations of the Cr moments fixed to give the desired magnetic structure. The magnitude of the Cr moments were then allowed to refine, but

fixed to have the same value on all sites. The resultant Rietveld plots and fitting statistics are shown in Figure 4.7.

These refinement results indicate that a *C*-type magnetic structure is favoured over *G*-type, since the latter (Ψ^1) does not put any intensity at the position of the (100) magnetic Bragg reflection. In comparing the fits of the *C*-type Ψ^1 and Ψ^3 magnetic structures, a slightly improved goodness of fit is realised for Ψ^3 in which Cr^{3+} moments are aligned along *c*. By scrutinising the difference plots of these two models, one can see that the improved fit, is in part due to a magnetic contribution to the model at 5.2 Å. In the room temperature nuclear model the Bragg intensity at this position is solely a result of the (003) reflection, however this intensity is not well modelled (Figure 4.4). The improved fit for Ψ^3, relative to Ψ^1 may therefore be a result of the magnetic model of Sr_2CrO_3FeAs making up for inadequacies in that of the nuclear. Furthermore, the data are quite noisy, especially in the low angle (A) bank where magnetic Bragg peaks are most prominent, so it is not possible to definitely ascertain the orientation of the Cr^{3+} moments from these data.

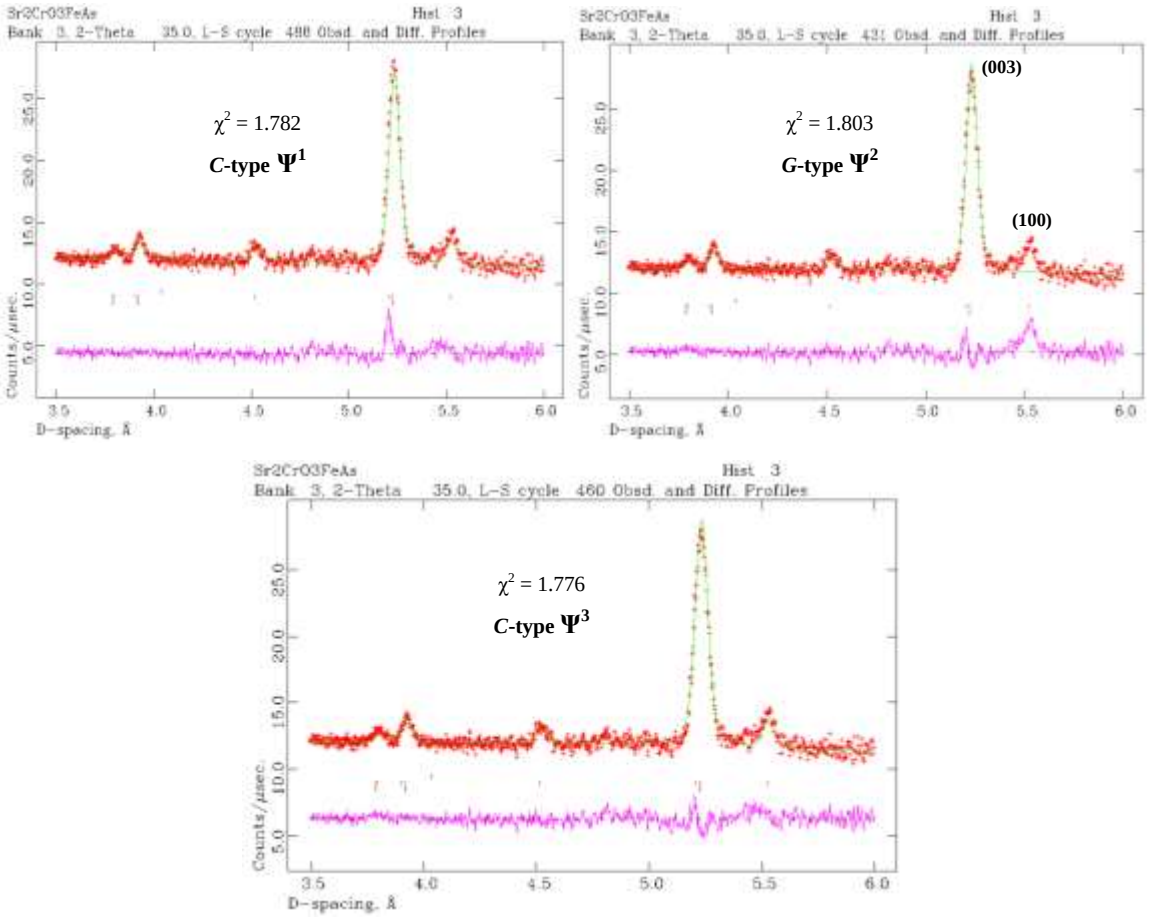

Figure 4.7 Rietveld fit of 5 K data PND data for Sr_2CrO_3FeAs nuclear and magnetic phases

The Rietveld fit of a Sr_2CrO_3FeAs nuclear and Ψ^3 magnetic phase to 5 K POLARIS data for the 35 ° detector bank is presented in Figure 4.8 (the 145 ° and 90 ° banks are presented in appendix E) and show good agreement between the observed and calculated data. Refined structural parameters are listed in table 4.2 and instrumental parameters include those to model background, DIFA, scale factors and profile coefficients. The cell volume of tetragonal Sr_2CrO_3FeAs contracts by 0.6 % upon cooling from room temperature to 5 K. This contraction is dominated by the *c* cell parameter which decreases by 0.6 % whilst the basal lattice parameter *a* decreases by 0.074 %. One would expect this compression in the basal plane (decrease in *c/a*) to result in an increase in the α As-Fe-As bond angle. Indeed this is what is observed as an increase in the *α* As-Fe-As bond angle from 108.42(3) ° to 108.96(3) ° is found upon cooling Sr_2CrO_3FeAs from room temperature to 5 K.

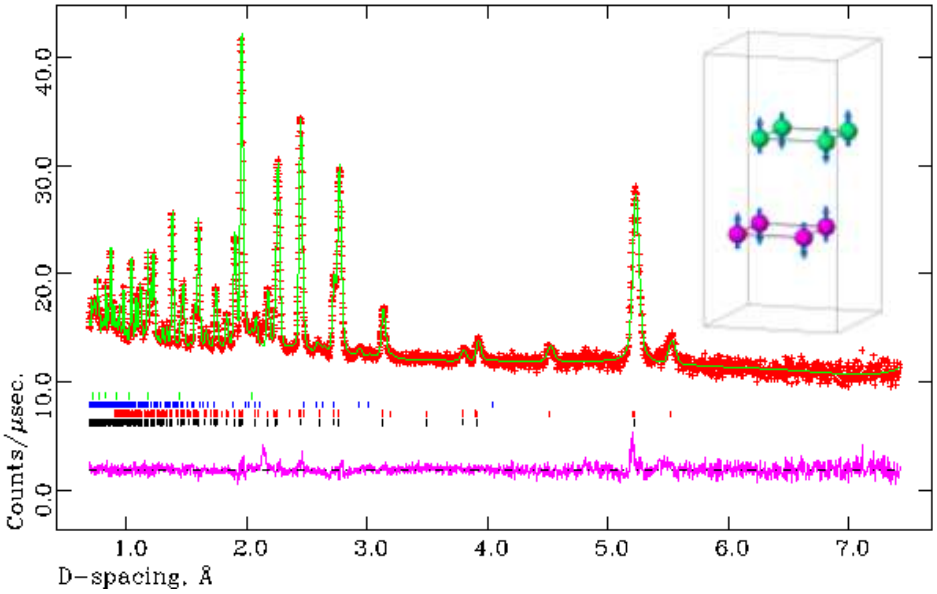

Figure 4.8 Rietveld fit to 35 ° detector banks for 5 K Sr_2CrO_3FeAs powder neutron diffraction data and magnetic structure of Sr_2CrO_3FeAs.

The refined value for the ordered moment of Cr at 5 K is 1.76(4) μ_B. This is significantly lower than the 3 μ_B expected for d^3 Cr^{3+}, and is likely reduced due to covalency and perhaps a lack of long range magnetic ordering between the layers.[4] However, a recent polarised neutron study, which separates nuclear and magnetic scattering, on Sr_2CrO_3FeAs by Tegel *et al* reports a significantly higher ordered moment of Cr^{3+} at 3.5 K of 2.75(5) μ_B.[3] The study also confirms the propagation vector $\boldsymbol{k}$ = (½, ½, 0) and *C*-type checkerboard arrangement of spins, but has the spins aligned in the *ab*-plane rather than along *c*. To confirm the magnetic structure of Sr_2CrO_3FeAs additional PND studies were performed on a phase pure sample of Sr_2CrO_3FeAs on the WISH ToF diffractometer (4.5.2).

4.5.1.3 Orthorhombic distortion

Although the Rietveld fit of the tetragonal nuclear and magnetic Sr_2CrO_3FeAs phases in Figure 4.8 shows good agreement between the observed and calculated data, the possibility of a small orthorhombic distortion, as seen in other parent FeAs-based superconductors, was also investigated. This is achieved by modelling the (200) reflection in the POLARIS backscattered 145 ° bank at 295 and 5 K by performing a Pawley fit in TOPAS in the ToF range 11900 to 12100 µsec, as shown in Figure 4.9. This allows the FWHM of the (200) reflection at 295 and 2 K to be determined as 0.00424(4) and 0.00452(6) Å, respectively. These values are equal within 3σ indicating that peak broadening suggestive of an orthorhombic distortion is not statistically significant.

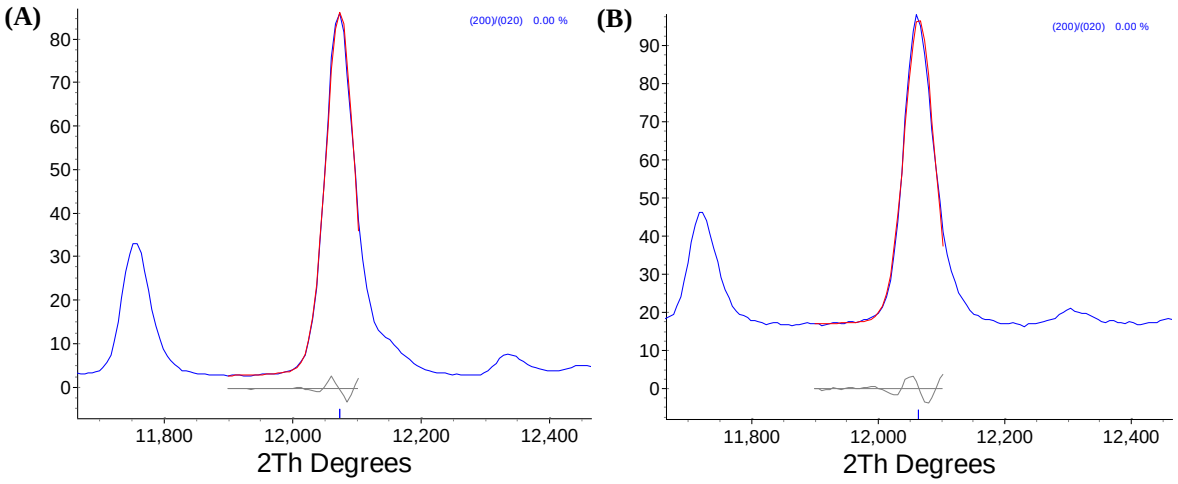

Figure 4.9 Modelling of the FWHM of the (200) reflection by a Pawley fit to PND data at (A) 295 and (B) 5 K.

4.5.2 WISH PND studies

WISH is a long-wavelength diffractometer which is optimised for high resolution powder neutron diffraction measurements at high *d*-spacings, due to a solid methane moderator. This makes it ideal for studying magnetic structures in which magnetic Bragg reflections can overlap at high *d*-spacing. The high count rate on WISH also permits very small samples to be measured with good statistics in reasonable time scales. Powder neutron diffraction measurements on a phase pure sample (AJC079) of Sr_2CrO_3FeAs (~ 0.5 g) were therefore performed at variable temperatures to map out the evolution of magnetic Bragg peaks and to confirm the magnetic structure. The sample was contained in an ultra thin walled cylindrical vanadium can and all measurements were performed in an Oxford Variox cryostat (vanadium tail).

The detector array on WISH covers a solid angle of 160 ° 2θ using a pixelated PSD. However, the data are typically separated into distinct histograms to aid in the modelling of peak profiles, whose form is not constant with the 2θ detector angle. With this in mind Rietveld refinements were performed against data collected in banks centred at 152.9 and 90 ° 2θ, which afford high resolution in the *d*-range 1.1 - 6.5 Å. Data collected in banks positioned at lower angles did not reveal any additional magnetic Bragg reflections at higher *d*-spacings and were therefore omitted from refinements. The asymmetry of Bragg reflections in the ToF PND data reported in this thesis is a product of the way in which neutrons are generated at ISIS. This is particularly pronounced on the WISH instrument (Figure 4.10) which makes use of a solid methane moderator, to access longer wavelength neutrons, and is modelled by a convolution of a pseudo-Voigt function with two back-to-back exponentials.

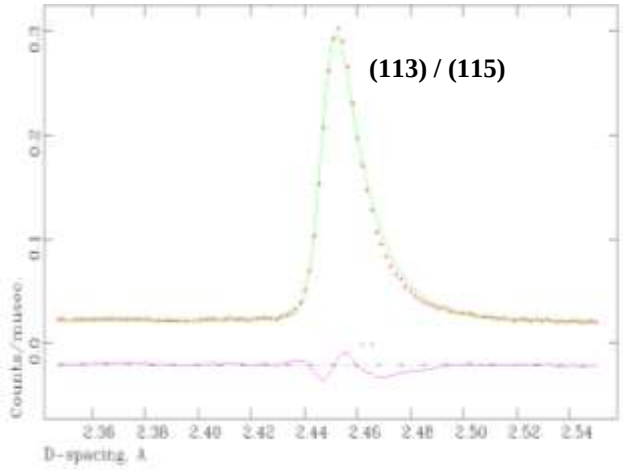

Figure 4.10 Asymmetric peak profile of the (113)/(115) reflection on the WISH instrument at ISIS

A preliminary data collection was performed on Sr_2CrO_3FeAs at 100 K, a temperature well above T_N. Refinement of a nuclear Sr_2CrO_3FeAs phase (AJC079) against 100 K powder neutron diffraction data, was performed using the GSAS software. Refined structural parameters are listed in table 4.2 and additional terms were included to model background, scaling and profile coefficients. The diffractometer constants DIFC, DIFA and zero, which relate the time of flight of a reflection to its *d*-spacing, as described in chapter 2, were refined for the lower resolution 90 ° histogram. For the back-scattered 152.9 ° detector bank only DIFA, the correction accounting for the wavelength dependence of the neutron absorption cross-section, was refined. The Rietveld fit to the 100 K WISH data is depicted in Figure 4.11 and shows good agreement between the calculated model and the observed data.

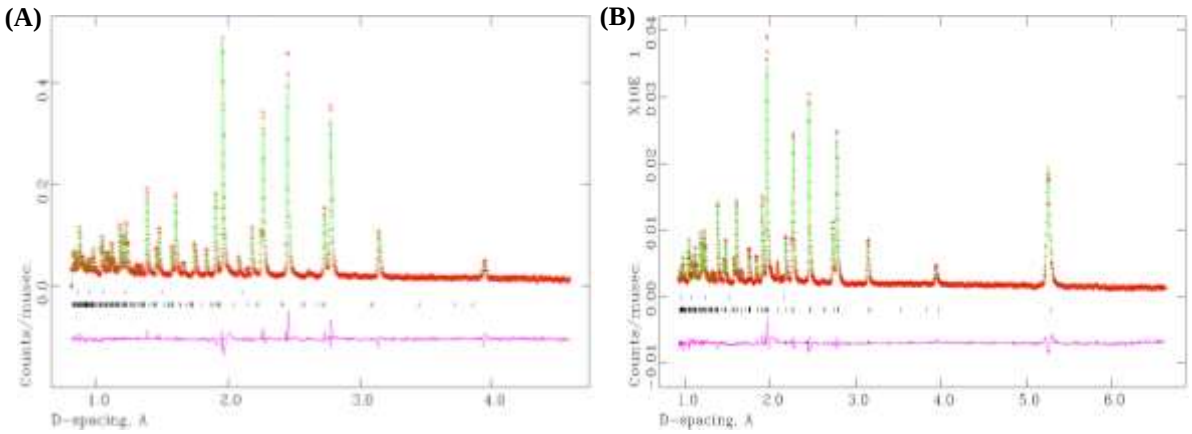

Figure 4.11 Rietveld fit of Sr_2CrO_3FeAs (black) and V (blue) to (A) 152.9° (B) 90 ° detector banks for 100 K WISH powder neutron diffraction data.

The slight discrepancies between the observed and calculated intensities are attributed to poor modelling of the exponential decay in the peak shape as shown in Figure 4.10, due to un-idealised calibration of the decay coefficients. As for refinements made against POLARIS PND data the possibility of Cr/Fe mixing was assessed by refining the chromium and iron occupancies, by introducing a $f_{occCr} + f_{occFe} = 1$ constraint on both transition metal sites. Once again refinement results do not indicate the presence of any Fe at the [2*c* (¼, ¼, 0.31)] position, but do suggest 2.5(1.1) % Cr at the [2*a* (¼, ¾, 0)] Fe site in the arsenide layer, consistent with refinements against POLARIS data. Tegel *et al* also report the occupancy of the iron 2*a* site to be (93 ± 1 % Fe : 7 ± 1 % Cr) from PND studies indicating that Cr doping of the Fe layer is an intrinsic property of Sr_2CrO_3FeAs.[3]

4.5.2.1 Re-examination of the Sr_2CrO_3FeAs magnetic structure

The sample (AJC079) was then cooled to 1.5 K and data were collected on warming at 4, 8, 12, 16, 20, 24, 28, 32, 35, 38, 41 and 45 K to map out the magnetic transition. In all refinements against WISH data described hereafter the diffractometer constants DIFA, DIFC and zero were fixed at the values obtained in the refinement against 100 K data, so as to avoid strong correlation with the lattice parameters influencing trends in structural parameters with temperature.

In comparing the 1.5 K and 100 K WISH data collected on Sr_2CrO_3FeAs (AJC079) it is clear from the additional reflections that the magnetic propagation vector $\boldsymbol{k}$ = (½, ½, 0) is the same as at that for the sample (RM020) measured on POLARIS. After refining a nuclear model of Sr_2CrO_3FeAs against the 1.5 K data, using that of the 100 K refinement as a starting point, a more rigorous analysis of the possible magnetic structure was

undertaken using the SARAh Representational analysis and SARAh refine software interfaced with GSAS (the use of which is described in appendix C).

Initially SARAh Rep. Analysis was used to determine the irreducible representations which are permitted for the Cr^{3+} magnetic atom, in the *P*4/*nmm* nuclear space group with propagation vector $\boldsymbol{k}$ = (½, ½, 0). In Sr_2CrO_3FeAs this generates 4 irreducible representations or irreps, but since two are degenerate, due to the tetragonal symmetry of the system, there are a total of 6 basis vectors, which are visualised in Figure 4.12.

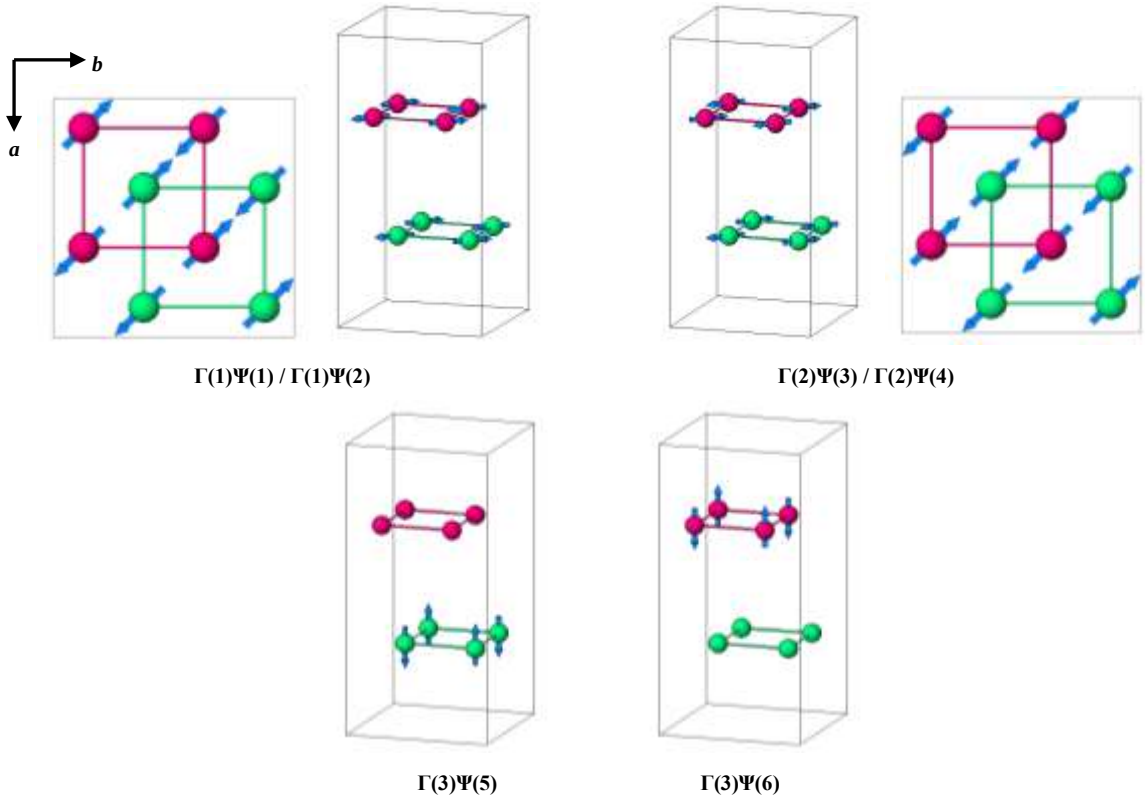

Figure 4.12 Basis vectors allowed for Cr ordering in Sr_2CrO_3FeAs

The most obvious feature of all of these basis vectors, is that they describe a antiferromagnetic checkerboard arrangement of Cr^{3+} moments, as is to be expected for a magnetic propagation vector $\boldsymbol{k}$ = (½, ½, 0). The Γ(1) basis vectors describe Cr^{3+} spins orientated in the *ab*-plane with the spins in alternate layers coupled ferromagnetically in an orientation perpendicular to that of the moment. Conversely the Γ(2) basis vectors display ferromagnetic interlayer coupling parallel to the orientation of the Cr^{3+} spins. The Γ(3) basis vectors represent a checkerboard arrangement of spins in a single Cr layer with the Cr^{3+} moments orientated along the *c* axis. A constraint was therefore applied in SARAh Refine for the Γ(3)Ψ(5) and Γ(3)Ψ(6) basis vectors such that the coefficient of the two basis vectors must be the same in all refinements, but the sign of the coefficient is

permitted to vary randomly. SARAh Refine interfaced with the GSAS software was then used to investigate which basis vector or combination of basis vectors best model the observed magnetic Bragg intensity. The power of SARAh Refine lies in its ability to mix different coefficients of all possible basis vectors to generate an extensive array of trial magnetic structures. Initially all six basis vectors were mixed, using Reverse Monte Carlo analysis with a total of 10000 refinement cycles, in an attempt to model the observed magnetic Bragg intensity. The results are displayed in Figure 4.13 in the form of contour plots, the generation of which is discussed in appendix C.

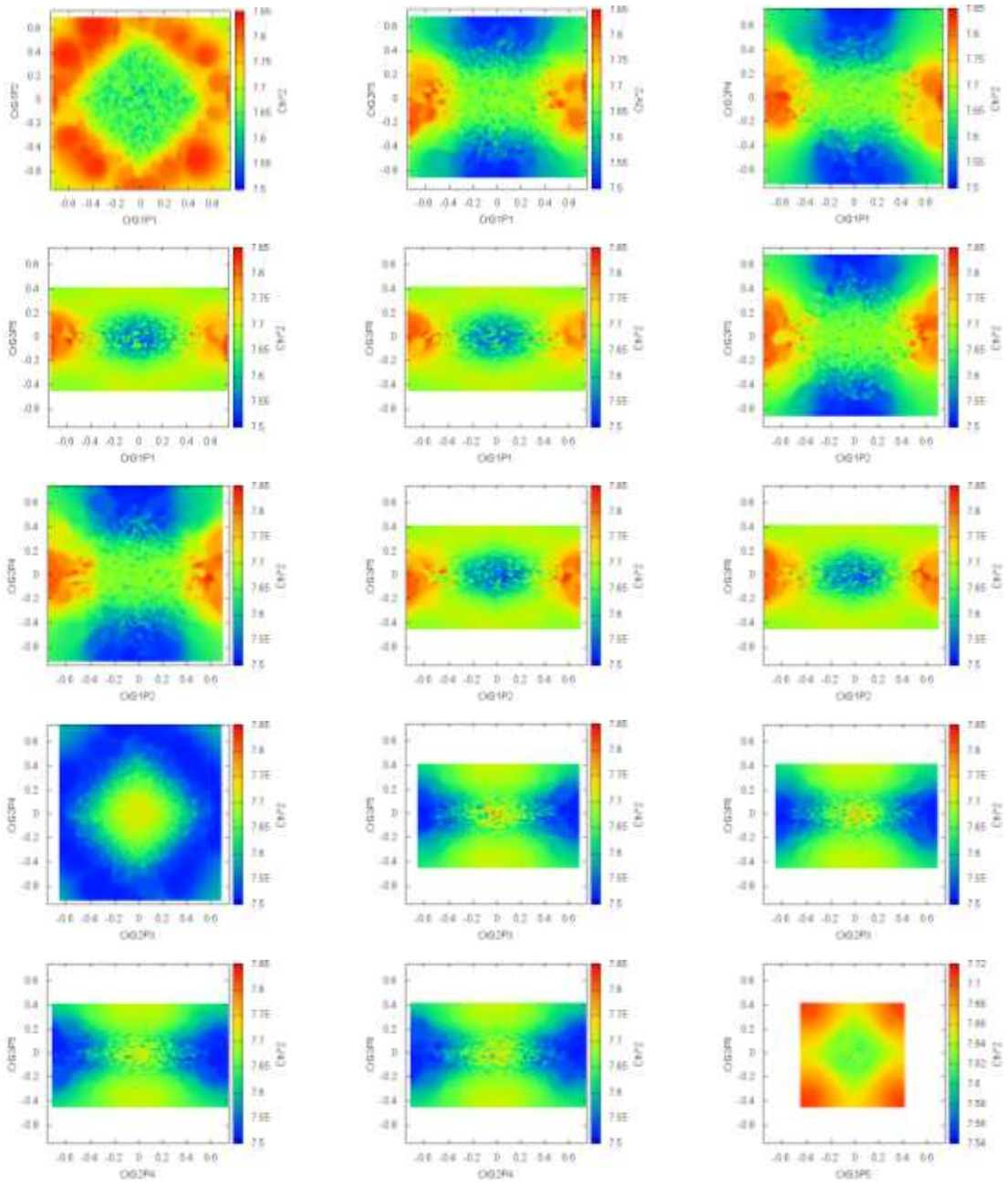

Figure 4.13 Results of Reverse Monte Carlo analysis of all 6 Cr basis vectors.

The results of this analysis clearly indicate that values of χ^2 are consistently higher (red) for refinements in which a high proportion of the Γ(1) basis vectors (Ψ(1) and Ψ(2)) are present. Equally it is evident that values of χ^2 are consistently lower for refinements that include a high proportion of the Γ(2) basis vectors (Ψ(3) and Ψ(4)), indicating that they describe the likely magnetic structure. Further analysis was therefore carried out excluding the Γ(1)Ψ(1), and Γ(1)Ψ(2) basis vectors, to confirm the magnetic structure and investigate the possibility of spin canting. The resulting contour plots are given in Figure 4.14.

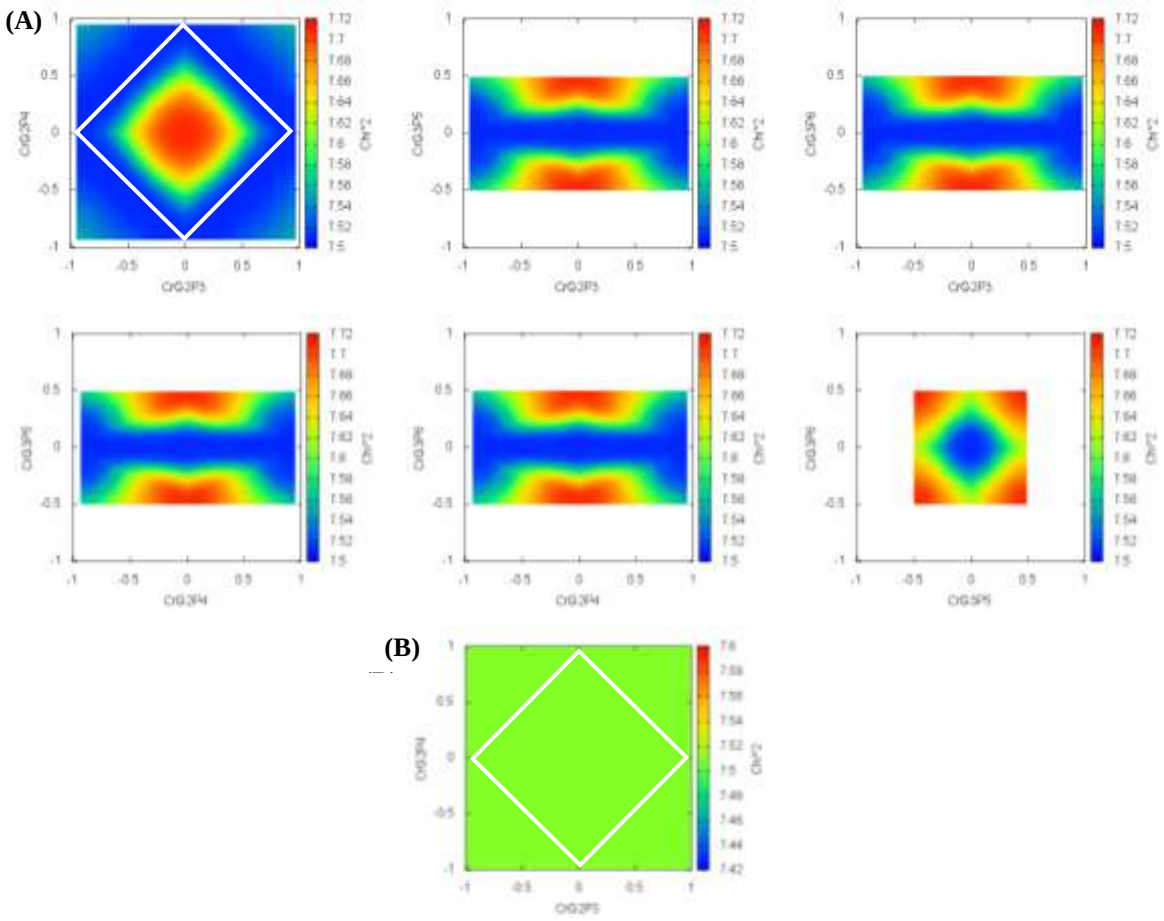

Figure 4.14 (A) Results of Reverse Monte Carlo analysis of the Γ(2) and Γ(3) Cr basis vectors. (B) Results of Reverse Monte Carlo analysis of the Γ(2) basis vectors. (nb. The overlaid white diamond emphasises the physical bounds of the contour plots)

The results of these refinements suggest that Sr_2CrO_3FeAs adopts a magnetic structure described by a combination of exclusively the Γ(2) basis vectors, with the Cr^{3+} moments orientated in the *ab*-plane. Reverse Monte Carlo analysis using solely the Γ(2) basis vectors confirms the degeneracy of the solution as shown in Figure 4.14(B). Furthermore there is no evidence for spin canting, as the addition of even a small proportion of the Γ(3) Cr basis vectors to refinements has an adverse effect on the fit. Examples of the degenerate

solutions with different relative spin orientations in adjacent planes that are permitted in this tetragonal system are depicted in Figure 4.15.

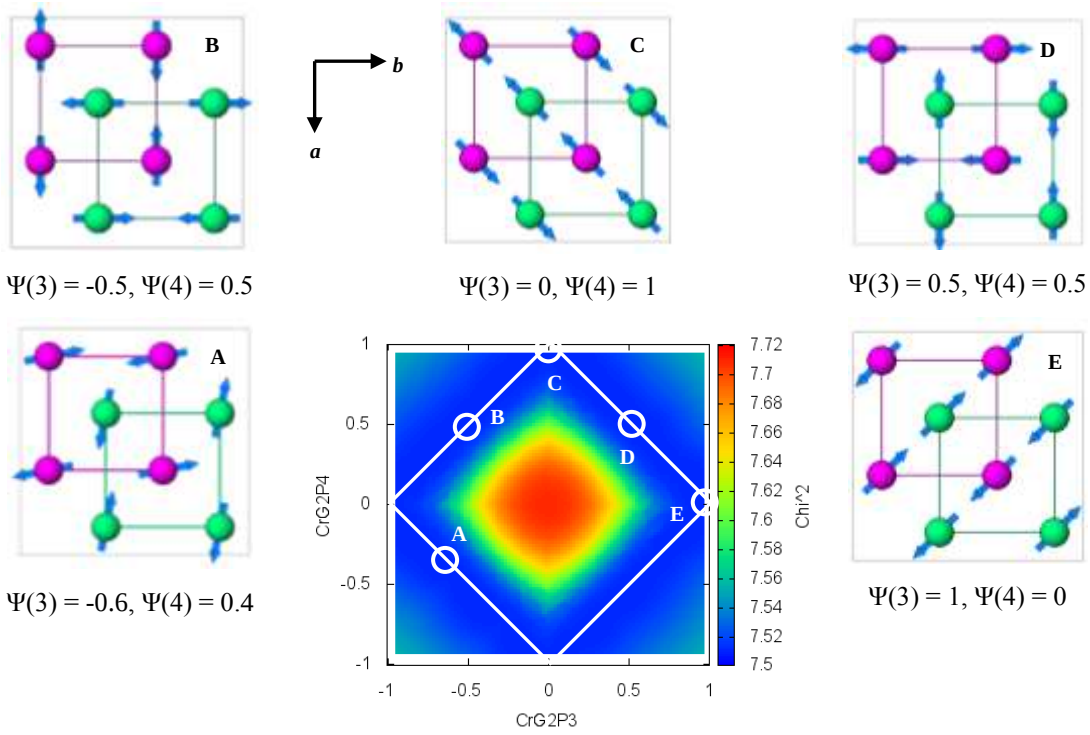

Figure 4.15 Degenerate solutions for the Sr_2CrO_3FeAs magnetic structure

This visualisation describes both collinear and non-collinear spin arrangements which all give identical magnetic Bragg scattering, since one cannot tell whether a magnetic Bragg reflection is the (101), the (011) or a combination of them both. The collinear structures (C and E) are generated by full contributions of either the Ψ(3) or the Ψ(4) basis vectors and have all of the spins directed either parallel or anti-parallel to the (110) direction. Alternatively the spins in adjacent layers may be orthogonal to one another in non-collinear arrangements.

In Chapter 1 the two common magnetic structure types for K_2NiF_4-type *xy* antiferromagnets; La_2CuO_4 and La_2NiO_4 are discussed.[5,6] Both are described by the $\boldsymbol{k}$ = (½, ½, 0) propagation vector and crystallise with a body-centered Cu^{2+} lattice, as a result of which there is no net interaction between Cu^{2+} ions in adjacent CuO_2 planes, assuming conventional isotropic exchange coupling. Sr_2CrO_3FeAs clearly takes a La_2CuO_4-type magnetic structure, but since Sr_2CrO_3FeAs does not undergo an orthorhombic distortion, as La_2CuO_4 does, it can more accurately be described as adopting the magnetic structure of the R_2CuO_4 (R = Sm $I4/mmm$).[7] In these materials the non-collinearity of the magnetic structures has been established unambiguously by neutron

scattering experiments performed in an applied magnetic field on single crystals. Sr_2CrO_3FeAs can therefore be described as a 2D dimensional antiferromagnet adopting the Sm_2CuO_4-type magnetic structure with XY spin character, and one would therefore expect the critical exponent of magnetisation (β) to be 0.23.[8] Full refinement results for the Sr_2CrO_3FeAs nuclear and magnetic phases can be found in appendix E and the Rietveld fit to data collected at 1.5 K in the 90 ° detector bank along with the magnetic structure of Sr_2CrO_3FeAs are shown in Figure 4.16.

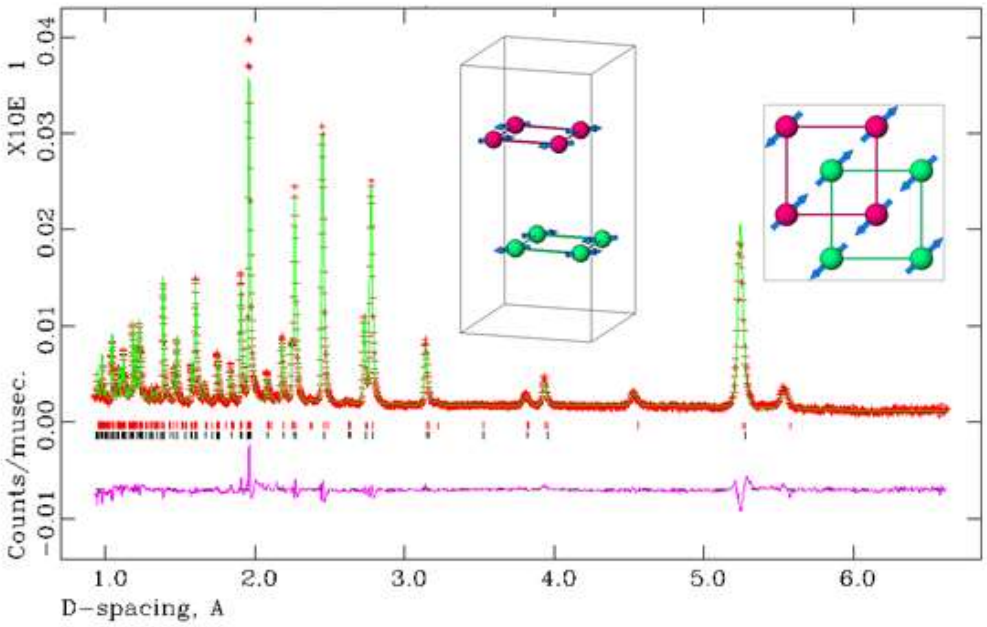

Figure 4.16 Rietveld fit to 90 ° detector bank for 100 K Sr_2CrO_3FeAs WISH powder neutron diffraction data.

This result is in agreement with the structure described by Tegel *et al*, as a best fit is realised when the Cr^{3+} moments are orientated in the *ab*-plane, but in contrast to those from refinement against POLARIS data which displays an improved fit when the Cr^{3+} moments are aligned along the *c*-axis. However, since the measurements made on WISH were performed on a phase pure sample of Sr_2CrO_3FeAs and given the enhanced resolution and signal to noise ratio of the observed data at high *d*-spacings, it is proposed that the Ψ^1 arrangement with Cr^{3+} moments orientated in the *ab* plane is the probable magnetic structure. The refined ordered Cr^{3+} moment of 1.95(7) μ_B at 1.5 K is slightly greater than that derived from refinement against 5 K POLARIS PND data, but significantly less than the 2.75(5) μ_B reported by Tegel *et al*.[3] This may possibly be as a result of not all of the Cr^{3+} spins contributing to long range order or the presence, in small amounts, of competing magnetic structures as is discussed in section 4.7.1.

4.5.2.2 Evolution of magnetic order in Sr_2CrO_3FeAs

To map out the transition of Sr_2CrO_3FeAs to an antiferromagnetically ordered state, additional data collections were performed on warming between 4 and 45 K. Figure 4.17 shows the evolution of magnetic Bragg intensity of the (102) reflection as a function of temperature relative to the nuclear (003) reflection in the 90 ° bank. The intensity of this reflection can be seen to decrease as the temperature is increased, until the 38 K data set in which no intensity is seen at the position (4.53 Å) of the (102) magnetic Bragg reflection.

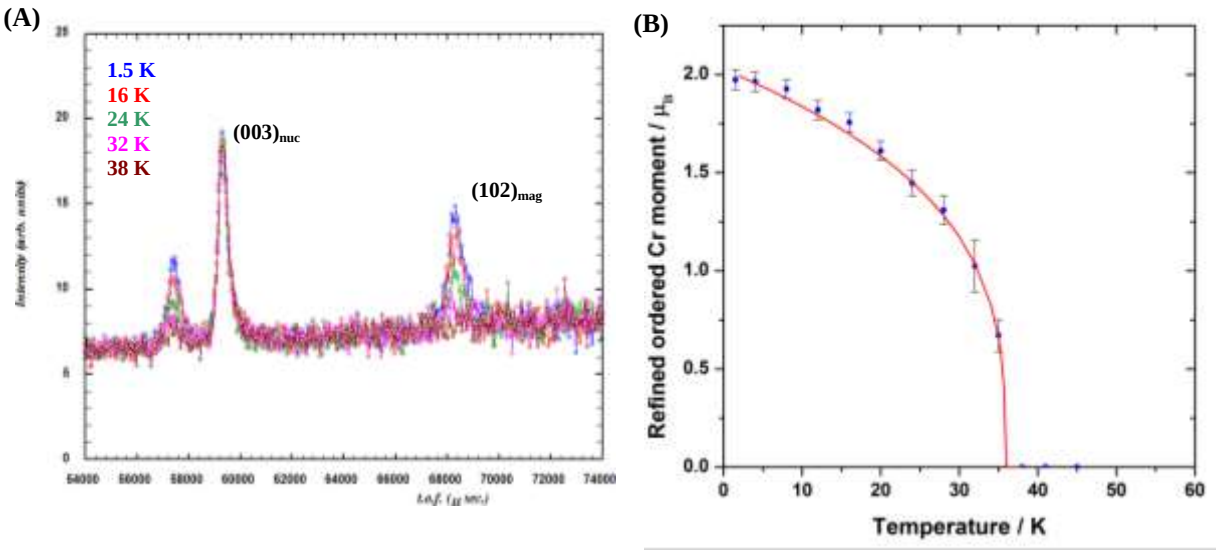

Figure 4.17 (A) Variation in the magnetic Bragg intensity of the (102) reflection as a function of temperature. (B) Refined ordered Cr moment as a function of temperature.

In order to more fully characterise this transition, Rietveld refinements were carried out against all PND data sets. In all of these refinements the diffractometer constants DIFA, DIFC and zero were fixed at the values obtained in the refinement against 100 K data, so as to avoid strong correlation with the lattice parameters influencing trends with temperature. With respect to the nuclear and magnetic phases of Sr_2CrO_3FeAs, the 1.5 K model was used as a starting point for all refinements, with a non-collinear arrangement of spins, but the magnitude of the ordered moment refined.

$$m_T = m_0\left(\frac{T_N - T}{T_N}\right)^{\beta} \qquad eqn4.1$$

Table 4.3 summarises the refined ordered Cr^{3+} moments and other selected structural parameters. The refined lattice parameters of Sr_2CrO_3FeAs show little variation with temperature below 32 K but positive thermal expansion above this temperature.

Temperature / K	*a* / Å	*c* / Å	*Cell volume* / Å^3	Cr moment / μ_B
1.5	3.91338(4)	15.7095(3)	240.585(5)	1.97(5)
4	3.91334(4)	15.7092(3)	240.575(5)	1.96(5)
8	3.91333(4)	15.7091(3)	240.571(5)	1.85(5)
12	3.91329(4)	15.7093(3)	240.570(5)	1.82(5)
16	3.91331(2)	15.7092(3)	240.570(5)	1.75(5)
20	3.91331(4)	15.7094(3)	240.573(5)	1.61(5)
24	3.91325(4)	15.7093(3)	240.565(5)	1.45(7)
28	3.91326(4)	15.7098(3)	240.573(5)	1.31(8)
32	3.91321(6)	15.7104(4)	240.578(7)	1.0(1)
35	3.91328(3)	15.7106(3)	240.589(5)	0.67(8)
38	3.91326(3)	15.7116(3)	240.601(5)	0
41	3.91323(3)	15.7124(3)	240.609(5)	0
45	3.91323(4)	15.7122(3)	240.616(6)	0
100	3.91416(4)	15.7357(3)	241.081(5)	0

Table 4.3 Results of refinement against powder neutron diffraction data for variable temperature measurements performed on the WISH diffractometer.

The temperature dependence of the magnitude of the ordered Cr^{3+} moment is shown in Figure 4.17 nd is well modelled by the power law described in *eqn4.1* in which $m_0 = 2.05(1)\ \mu_B$, $T_N = 35.9(1)$ K and $\beta = 0.302(9)$. The value of the critical exponent 0.302(9) is intermediate between that of a 2-D and 3-D system, though considerably closer to the latter. This is in strong contrast to the behaviour seen in the archetypal 2-D antiferromagnet K_2NiF_4 ($\beta \sim 0.15$), in which the transition from two-dimensional correlations to long-range magnetic order occurs within a 2 K temperature window about T_N.[9] In Sr_2CrO_3FeAs the more gradual transition to long-range order suggests that significant interlayer coupling exists, suggesting a more 3-D transition similar to that seen in the structurally related oxide chloride Sr_2CoO_3Cl ($\beta = 0.28(3)$).[10]

4.6 $Sr_2CrO_3Fe_{1-x}Co_xAs$ electron doping

The partial substitution of Co^{2+} (d^7) for Fe^{2+} (d^6) on the [2*a* (¼, ¾, 0)] crystallographic site has been shown to be a fruitful strategy for doping FeAs-based materials into the superconducting regime. $Sr_2ScO_3Fe_{1-x}Co_xAs$ samples were successfully synthesised in the compositional range ($0 \leq x \leq 0.3$), however none of these materials exhibit any evidence for a superconducting transition above 2 K. It was hoped that the reduced intraplanar Fe-Fe distance in Sr_2CrO_3FeAs would support superconductivity when suitably carrier doped. Preliminary work by R. Moor therefore went into synthesising samples of $Sr_2CrO_3Fe_{1-x}Co_xAs$ covering a wide compositional range ($0 \leq x \leq 0.3$) in coarse nominal doping steps.[11]

4.6.1 Experimental

$Sr_2CrO_3Fe_{1-x}Co_xAs$ ($0 < x < 0.3$) samples were synthesized on the 0.5 – 3 g scale by annealing stoichiometric mixtures of SrO (prepared by the thermal decomposition of $SrCO_3$), Cr (Alfa 99.988%), Fe_2O_3 (Alfa 99.998%), Fe (Alfa 99.998%), Co (Alfa 99.998%) and As (Alfa 99.999%) according to *eqn4.2*. These reagents were thoroughly ground together using an agate pestle and mortar, pressed into 13 mm diameter pellets at a force of 5 tonnes, placed in alumina crucibles and sealed in silica ampoules under dynamic vacuum. The samples were then heated to 1100 °C according to the procedure described in section 4.2. The resultant black crystalline products were stored in an argon-filled glove box.

$$2\ SrO + Cr + \tfrac{1}{3}\ Fe_2O_3 + (\tfrac{1}{3} - x)\ Fe + x\ Co \rightarrow Sr_2CrO_3Fe_{1-x}Co_xAs \qquad eqn4.2$$

4.6.2 PXRD

Initial characterisation of $Sr_2CrO_3Fe_{1-x}Co_xAs$ samples was carried out by X-ray powder diffraction (XRPD) using a PANalytical X'pert PRO instrument. The Rietveld fit to X-ray powder diffraction data for $Sr_2CrO_3Fe_{0.94}Co_{0.06}As$ is shown in Figure 4.18. The sample appears to be largely phase pure, however an additional reflection is observed at 29.5 ° 2θ which cannot be accounted for by the main phase. This impurity phase is present in the majority of $Sr_2CrO_3Fe_{1-x}Co_xAs$ materials synthesised, however since it is very broad in nature and no further unaccounted for Bragg reflections are seen, it was not possible to identify its origin. Additional FeAs and SrO impurity phases were observed in some $Sr_2CrO_3Fe_{1-x}Co_xAs$ samples, but typically present at a level of less than 5 wt %. No Co containing impurities were identified and the simulation of a PXRD pattern of the Fe-based

superconductor $SrFe_{2-x}Co_xAs_2$ shown in Figure 4.18 generates peak positions that are inconsistent with the unaccounted for Bragg intensity.

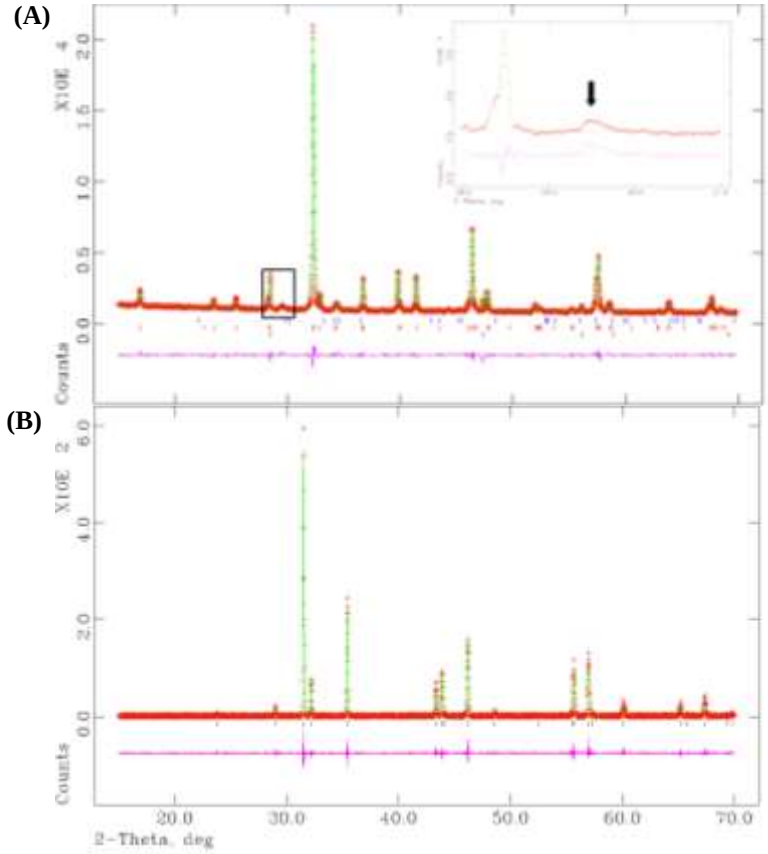

Figure 4.18 (A) Rietveld fit of $Sr_2CrO_3Fe_{0.94}Co_{0.06}As$ to laboratory powder X-ray diffraction data. Inset shows a magnification of the 28-31° 2θ region. (B) Simulated PXRD pattern of $SrFe_{1.8}Co_{0.2}As_2$ with lattice parameters taken from reference 12.[12]

The near identical X-ray scattering factors of Co, Fe and Cr mean that it is difficult to confirm the successful uptake of cobalt from X-ray powder diffraction data by the refinement of fractional occupancies. However, the successful substitution of Co in $Sr_2CrO_3Fe_{1-x}Co_xAs$ is implied in the approximately linear decrease in the *c* lattice parameter with *x*. In contrast to the changes in *c*, the *a* cell parameter shows no strong trends upon Co doping, this is made more clear when one plots the percentage change in *a* and *c* against *x*, as shown in Figure 4.19. These variations in the lattice parameters with *x* are typical for Co substitution in FeAs-based superconductors, as in $BaFe_{1-x}Co_xAs_2$ and $SrFe_{2-x}Co_xAs_2$ and $LaOFe_{1-x}Co_xAs$.[13-15]

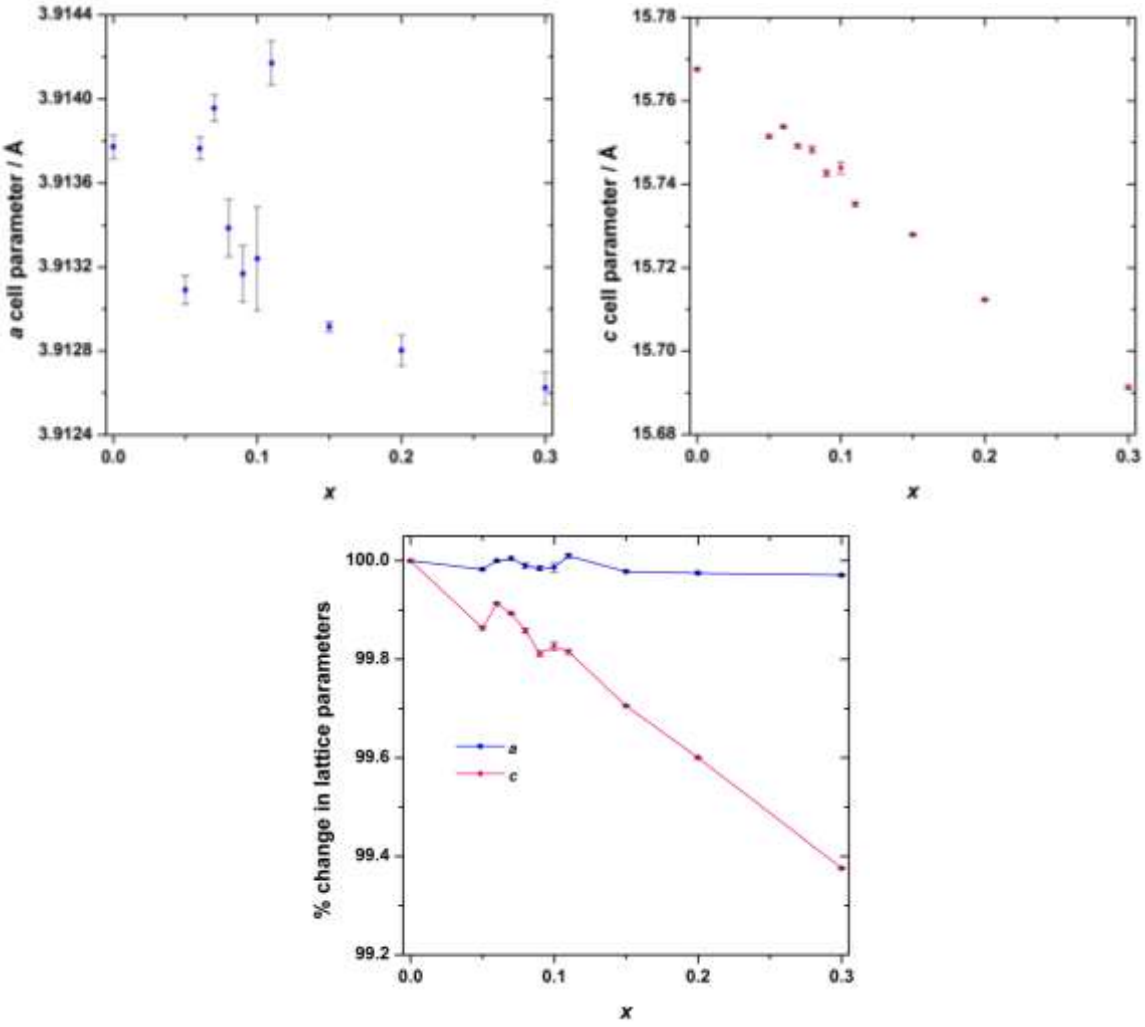

Figure 4.19 Variation of lattice parameters with *x* in $Sr_2CrO_3Fe_{1-x}Co_xAs$ materials.

4.6.3 SQUID Magnetometry

The magnetic properties of all $Sr_2CrO_3Fe_{1-x}Co_xAs$ samples were characterised by zero-field-cooled (ZFC) and field-cooled (FC) magnetisation measurements using 30-50 mg samples loaded into gelatine capsules on a Quantum Design MPMS-SL SQUID magnetometer. Preliminary measurements were made in an applied field of 50 Oe on $Sr_2CrO_3Fe_{1-x}Co_xAs$ samples with x = 0.05, 0.1, 0.15, 0.2 and 0.3 that were prepared by R. Moor.

The magnetic susceptibilities of $Sr_2CrO_3Fe_{1-x}Co_xAs$ with x = 0.05 and 0.1 are shown in Figure 4.20 and both exhibit broad transitions to diamagnetism at 8 and 12 K respectively. The superconducting volume fractions calculated from the susceptibility at 2 K are 1.7 % and 9.5 % for $Sr_2CrO_3Fe_{1-x}Co_xAs$ with x = 0.05 and 0.1 respectively. This would seem to indicate that the bulk of sample is not superconducting. Samples with nominal Co doping levels ≥ 15 % show no transition to diamagnetism above 2 K.

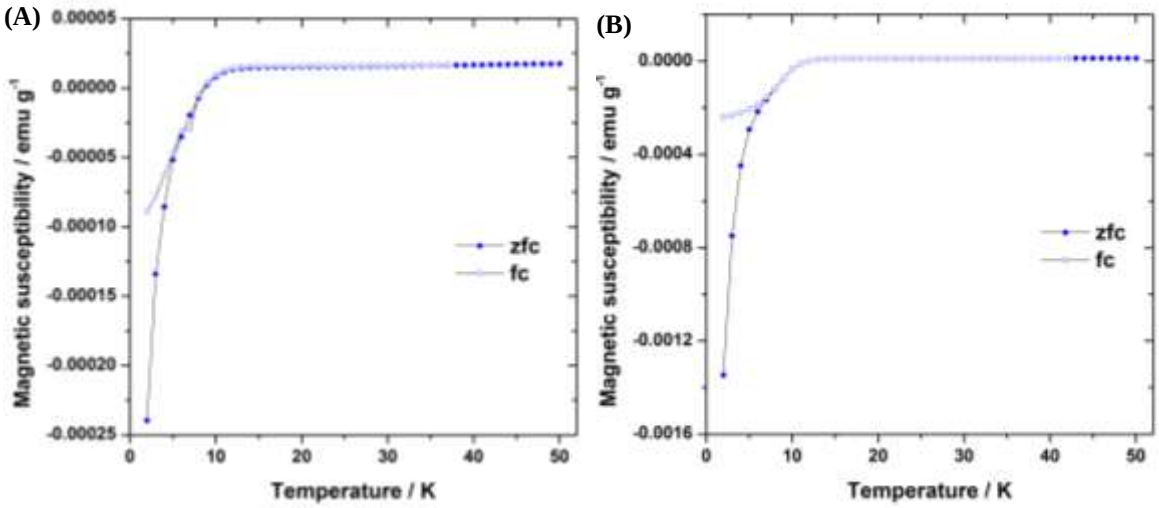

Figure 4.20 Plots of magnetisation against temperature measured in an applied field of 50 Oe for superconducting samples of $Sr_2CrO_3Fe_{1-x}Co_xAs$ with nominal x = 0.05 (A) and 0.1 (B).

Additional measurements were therefore performed on $Sr_2CrO_3Fe_{1-x}Co_xAs$ samples in the compositional range $0.04 < x < 0.15$. Given the relatively low superconducting volume fractions in those samples measured in an applied field of 50 Oe, a magnetisation isotherm was performed at 2 K on $Sr_2CrO_3Fe_{0.94}Co_{0.06}As$ to ascertain an estimate of the lower critical field H_{C1}, the point at which magnetic flux begins to enter the superconductor. The hysteresis loop of $Sr_2CrO_3Fe_{0.94}Co_{0.06}As$ measured at 2 K is shown in Figure 4.21 and is typical for that of a type II superconductor, with the minima in the hysteresis loop estimated at ~ 200 Oe. However, the increase in the strength of the diamagnetic signal as the applied field is increased from 0 to 200 Oe becomes non-linear some way before this point indicating that H_{C1} is very small (> 50 Oe). Therefore subsequent magnetic susceptibility measurements on superconducting $Sr_2CrO_3Fe_{1-x}Co_xAs$ samples were performed in a lower applied field of 5 Oe.

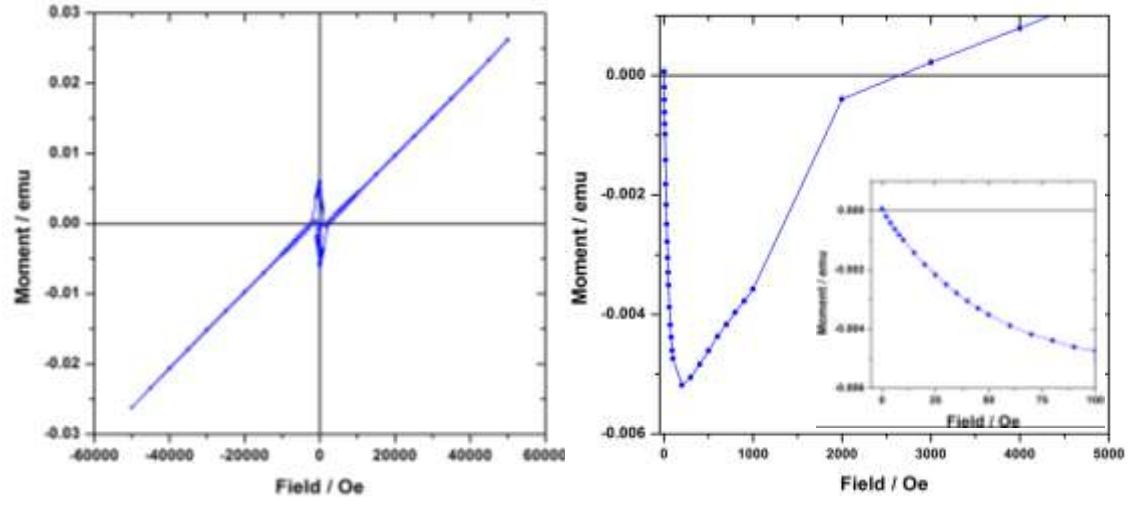

Figure 4.21 $Sr_2CrO_3Fe_{0.94}Co_{0.06}As$ (AJC048) hysteresis loop at 2 K

Given the modest applied fields it is crucial to account for the presence of any small residual fields (typically $H_{residual} \leq 2$ Oe) if accurate superconducting volume fractions are to be obtained. Therefore prior to each data collection a measurement was made at 300 K in a nominal applied field of 0 Oe and if a signal due to sample magnetisation was detected, then the applied field was varied until $H_{applied} = - H_{residual}$. The sample is then cooled to 2 K in this correct zero field, such that the net flux density about the sample is zero. The zero-field-cooled and field-cooled susceptibilities of $Sr_2CrO_3Fe_{0.94}Co_{0.06}As$ measured in an applied field of 5 Oe is shown in Figure 4.22 and is typical for $Sr_2CrO_3Fe_{1-x}Co_xAs$ samples in the range ($0.06 \leq x \leq 0.11$). The sample becomes diamagnetic at 16 K and the transition to maximum shielding is significantly less broad than in those measurements performed in a field of 50 Oe, showing 10 % maximum shielding at 14 K. The zero-field-cooled susceptibility at 2 K is -0.00342 emu which represents an 18 % superconducting volume fraction.

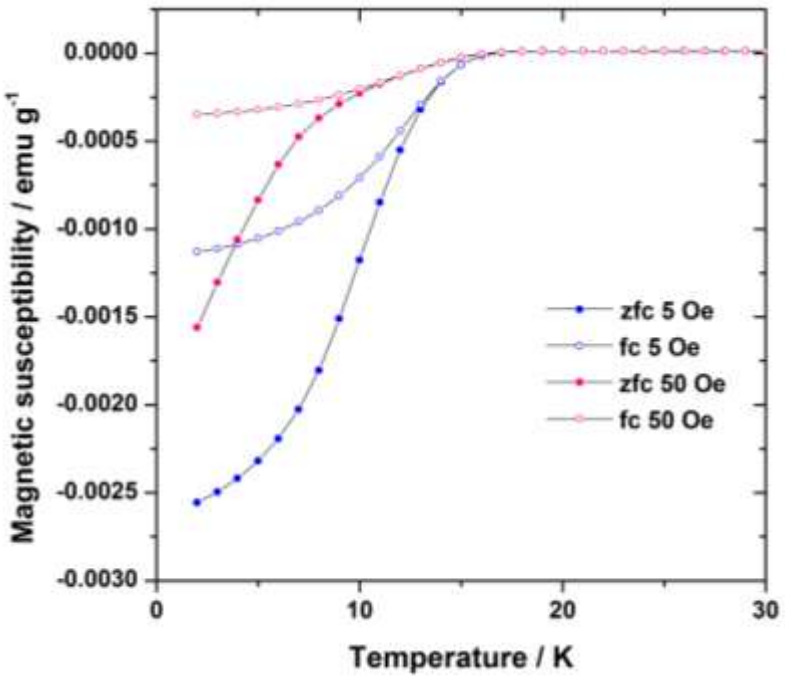

Figure 4.22 Comparison of ZFC and FC magnetisation measurements performed on $Sr_2CrO_3Fe_{0.94}Co_{0.06}As$ in applied fields of 5 Oe and 50 Oe.

Further measurements in applied fields of 5 Oe allow the superconducting phase diagram of $Sr_2CrO_3Fe_{1-x}Co_xAs$ to be mapped out (Figure 4.23). The onset of superconductivity is first seen in $Sr_2CrO_3Fe_{1-x}Co_xAs$ with a nominal composition $x = 0.05$. Further Co doping increases T_c which is maximised at 18 K in $Sr_2CrO_3Fe_{0.92}Co_{0.08}As$. Samples with Co

doping levels greater than 0.11 electrons per iron do not exhibit superconductivity. These observations are consistent with the electron doping of Sr_2CrO_3FeAs through the partial doping of Co^{2+} (d^7) on the Fe^{2+} (d^6) 2*a* site and the profile of the superconducting region shows striking similarities to the cobalt doping dependence of superconductivity in 122 and 1111 FeAs-based materials.[13,14,16] Superconducting volume fractions are also presented in Figure 4.23, estimated from the zero-field-cooled magnetisation at 2 K. In a similar manner to the variation of T_c with *x*, the superconducting volume shows a characteristic dome, maximised in $Sr_2CrO_3Fe_{0.91}Co_{0.09}As$ at 26 %.

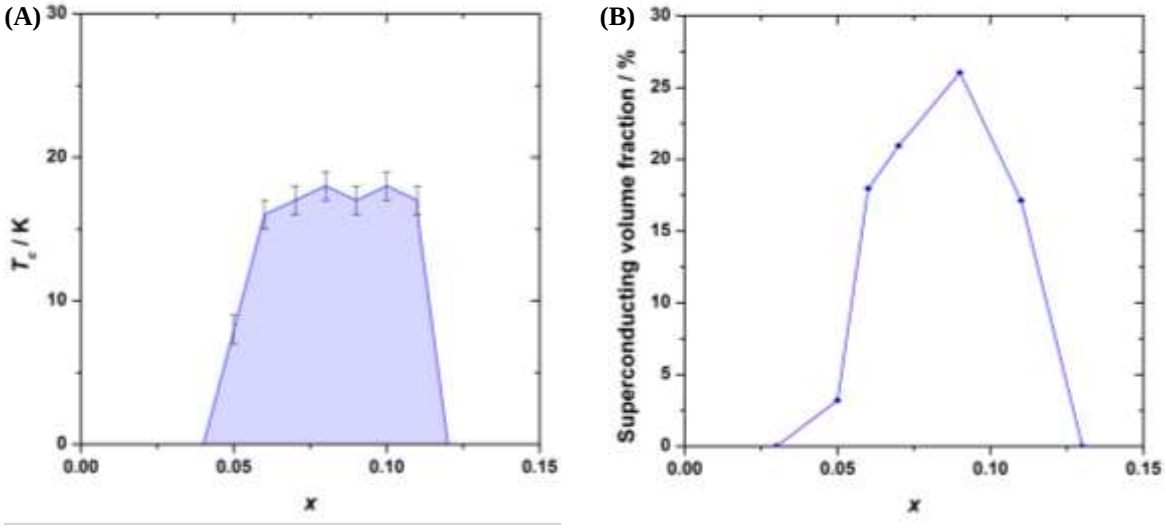

Figure 4.23 Evolution of (A) T_c and (B) superconducting volume fraction with *x* in $Sr_2CrO_3Fe_{1-x}Co_xAs$

One further point to address with respect to the magnetisation of $Sr_2CrO_3Fe_{1-x}Co_xAs$ samples is the effect which Co doping has on the antiferromagnetic ordering of Cr^{3+} moments in the oxide layer. Additional zero-field-cooled and field-cooled magnetisation measurements were therefore performed in an enhanced applied field of 1 kOe. The magnetic susceptibility of superconducting $Sr_2CrO_3Fe_{0.91}Co_{0.09}As$ (T_c = 17 K) measured in the range 2-300 K is shown in Figure 4.24. As in the undoped parent material Sr_2CrO_3FeAs a broad maximum is observed in the ZFC and FC susceptibilities, indicative of the AFM ordering of Cr^{3+}. The Neel temperature T_N is however enhanced from 40 K in Sr_2CrO_3FeAs to 80 K in $Sr_2CrO_3Fe_{0.91}Co_{0.09}As$ as Co is introduced into the FeAs layers. Similar measurements on $Sr_2CrO_3Fe_{1-x}Co_xAs$ samples with x = 0.06, 0.09, 0.12, 0.15, 0.2 and 0.3, spanning the full compositional range that support superconductivity, all show similar maxima with the Neel temperature in the temperature range $70 \leq T_N \leq 80$ K. This yields the magnetic phase diagram of $Sr_2CrO_3Fe_{1-x}Co_xAs$ depicted in Figure 4.25.

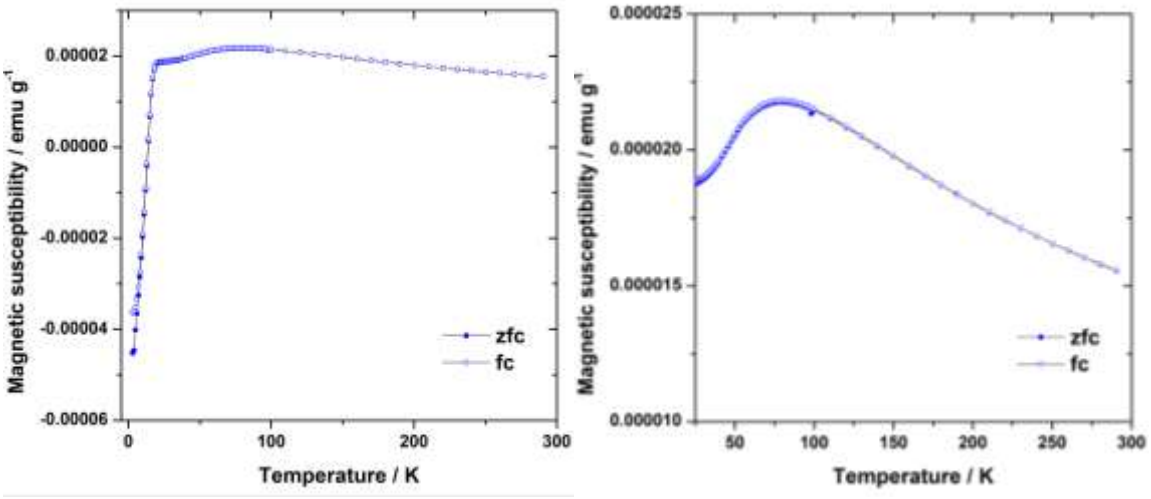

Figure 4.24 Field cooled and zero-field cooled magnetisation measurements performed on $Sr_2CrO_3Fe_{0.91}Co_{0.09}As$ in an applied field of 1000 Oe.

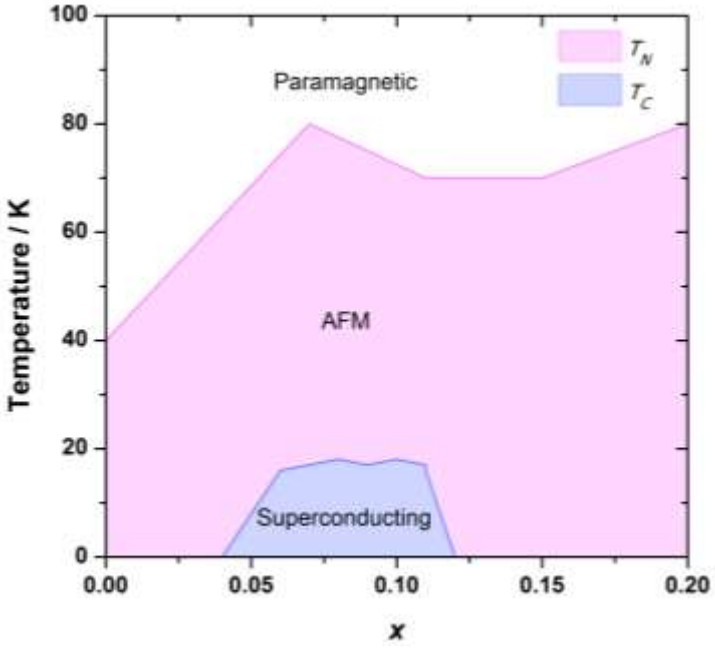

Figure 4.25 Phase diagram of $Sr_2CrO_3Fe_{1-x}Co_xAs$

4.6.4 D2B variable temperature PND measurements

In order to probe the structure, stoichiometry and antiferromagnetic order of superconducting $Sr_2CrO_3Fe_{1-x}Co_xAs$ materials, powder neutron diffraction measurements were performed on the D2B instrument at the ILL reactor source, Grenoble. Room temperature PND measurements were made on D2B using 1.59 Å neutrons on 3 g samples of $Sr_2CrO_3Fe_{1-x}Co_xAs$, with x = 0.07 and 0.09. These were loaded into 6 mm diameter cylindrical vanadium sample cans and measured in the range 5 ° ≤ 2θ ≤ 150 °, covering a

d-space range of 0.82 to 18 Å. Data was also collected at 2 K inside an Oxford Instruments cryostat.

Rietveld refinement against room temperature powder neutron diffraction data of samples with the nominal compositions $Sr_2CrO_3Fe_{0.93}Co_{0.07}As$ and $Sr_2CrO_3Fe_{0.91}Co_{0.09}As$ was performed using the GSAS software. Refined structural parameters are listed in Table 4.4 and instrumental parameters include those to model background, zero error and profile coefficients. FeAs, SrO and Fe impurity phases were also included in these refinements and found to be present at no greater than 4 wt %. The Rietveld fit of $Sr_2CrO_3Fe_{0.93}Co_{0.07}As$ and $Sr_2CrO_3Fe_{0.91}Co_{0.09}As$ to room temperature PND data are presented in Figure 4.26 and both show good agreement between the calculated model and the observed data.

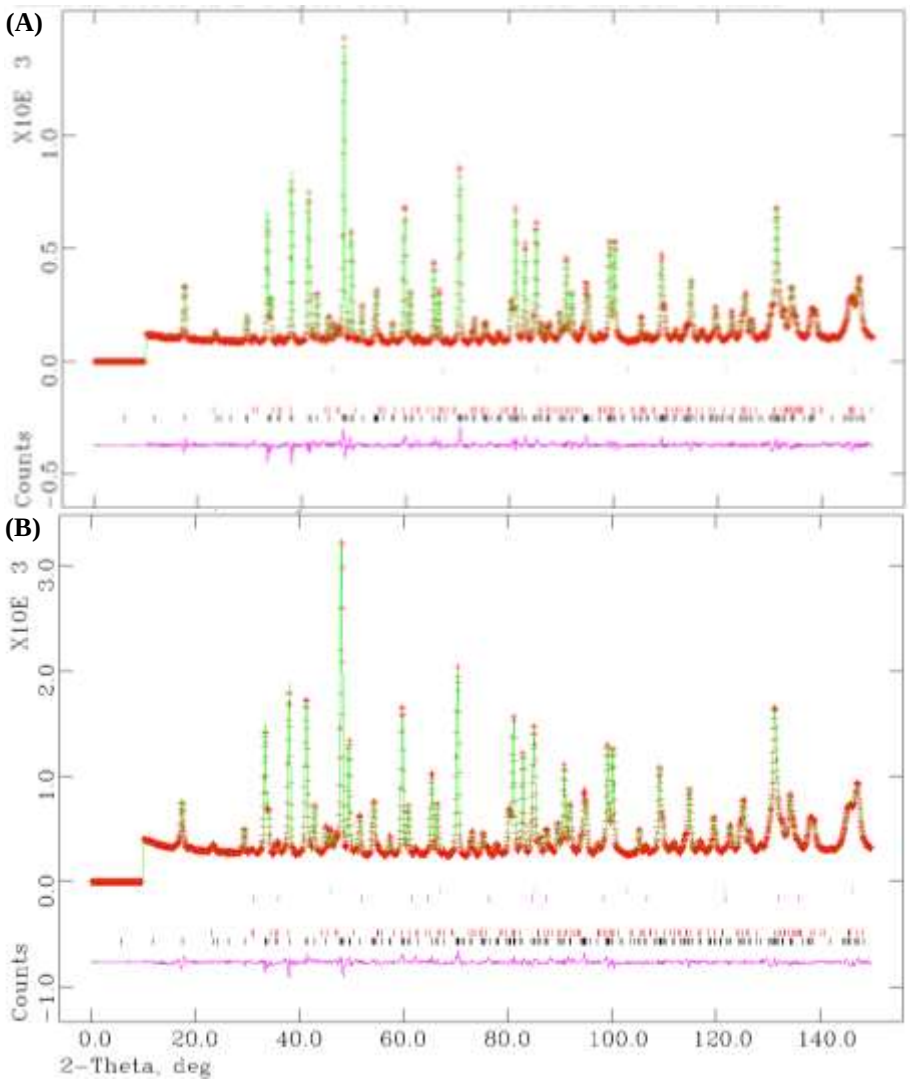

Figure 4.26 Rietveld fit of (A) $Sr_2CrO_3Fe_{0.93}Co_{0.07}As$ and (B) $Sr_2CrO_3Fe_{0.91}Co_{0.09}As$ to room temperature powder neutron diffraction data.

		AJC069 $Sr_2CrO_3Fe_{0.93}Co_{0.07}As$		AJC070 $Sr_2CrO_3Fe_{0.91}Co_{0.09}As$	
Temperature / K		293	5	293	5
a / Å		3.91382(4)	3.90889(4)	3.91455(3)	3.90898(5)
c / Å		15.7482(2)	15.6737(3)	15.7475(2)	15.6694(3)
Cell volume / Å^3		241.230(7)	239.486(6)	241.310(4)	239.430(8)
R_{wp}		0.0500	0.0542	0.0364	0.054
χ^2		4.053	5.023	5.874	4.800
Atomic parameters:					
Sr1	[2*c* (¾, ¾, *z*)]	0.1940(1)	0.1935(2)	0.19422(9)	0.1935(2)
	U_{iso} × 100 / Å^2	0.31(4)	0.39(4)	0.40(2)	0.24(6)
Sr2	[2*c* (¾, ¾, *z*)]	0.4143(2)	0.4148(2)	0.41434(9)	0.4147(2)
	U_{iso} × 100 / Å^2	0.2495)	0.63(6)	0.35(3)	0.44(7)
Cr	[2*c* (¼, ¼, *z*)]	0.31042(2)	0.3096(2)	0.3101(2)	0.3095(3)
	U_{iso} × 100 / Å^2	0.09(7)	0.9(8)	0.45(5)	0.2(1)
	Cr μ_B		2.27(5)		2.26(6)
Fe	[2*a* (¼, ¾, 0)]				
	U_{iso} × 100 / Å^2	0.13(4)	0.27(3)	0.28(2)	0.23(6)
	Cr_{occ}	0.025	0.025	0.025	0.025
	Fe_{occ}	0.903(8)	0.94(1)	0.885(3)	0.92(1)
	Co_{occ}	0.097(8)	0.06(1)	0.115	0.08(1)
As	[2*a* (¼, ¼, *z*)]	0.0879(2)	0.0879(2)	0.0879(1)	0.0876(2)
	U_{iso} × 100 / Å^2	0.51(5)	0.63(6)	0.76(3)	0.42(7)
O1	[4*f* (¼, ¾, *z*)]	0.29435(9)	0.29399(9)	0.29401(6)	0.2937(1)
	U_{iso} × 100 / Å^2	0.32(3)	0.46(4)	0.45(2)	0.40(5)
O2	[2*c* (¼, ¼, *z*)]	0.4301(2)	0.4300(2)	0.4301(1)	0.4296(2)
	U_{iso} × 100 / Å^2	0.72(6)	0.63(6)	1.05(4)	0.55(8)
Impurity phases:					
FeAs / wt %		3.1(1)		3.34(7)	
SrO / wt %				1.3(1)	
Fe / wt %		1.75(8)		2.48(4)	
Bond lengths and angles:					
	Fe-As / Å	2.398(2)	2.391(2)	2.398(1)	2.389(2)
	Fe-Fe / Å	2.76749(3)	2.76401(3)	2.76800(2)	2.76407(4)
	α As-Fe-As / °	109.4(1)	109.7(1)	109.44(7)	109.8(2)
	β As-Fe-As / °	109.50(5)	109.38(6)	109.48(3)	109.30(7)

Table 4.4 Results of refinement against powder neutron diffraction data for $Sr_2CrO_3Fe_{1-x}Co_xAs$ at room temperature (293 K) and 5 K.

The true stoichiometry of $Sr_2CrO_3Fe_{1-x}Co_xAs$ materials is somewhat difficult to determine. The similar electronegativities and ionic radii of Cr, Fe and Co present the mixing of all three transition metals on either the [2*c* (¼, ¼, 0.31)] site in the oxide layer or the [2*a* (¼, ¾, 0)] site in the arsenide layer as a distinct possibility. One could envisage being able to obtain a discrete solution to this problem by solving the 3 simultaneous equations shown below by refinement against combined X-ray powder diffraction and neutron

powder diffraction data, making the assumption that the transition metal site is fully occupied (*nb.* Here *Z* is used as a proxy for the atomic X-ray scattering factor).

$$(24)\ f_{Cr} + (26)\ f_{Fe} + (27)\ f_{Co} = \text{Total atomic X-ray scattering from } TM \text{ site} \qquad eqn4.3$$

$$(3.65\text{ fm})\ f_{Cr} + (9.45\text{ fm})\ f_{Fe} + (2.49\text{ fm})\ f_{Co} = \text{Total neutron scattering from } TM \text{ site} \qquad eqn4.4$$

$$f_{Cr} + f_{Fe} + f_{Co} = 1 \qquad eqn4.5$$

Practically the results of such refinements should be treated with caution, since the similarity in the atomic X-ray scattering factors of Cr, Fe and Co mean that a number of different values for f_{Cr}, f_{Fe} and f_{Co} can give very similar solutions to the above equations. An assumption is therefore made that the degree to which Fe and Cr mix on their respective sites in $Sr_2CrO_3Fe_{1-x}Co_xAs$ is the same as in the undoped 'parent' Sr_2CrO_3FeAs. That is to say that the [2*c* (¼, ¼, 0.31)] site is exclusively occupied by Cr, but the [2*a* (¼, ¾, 0)] site in the arsenide layer is 97.5 % Fe and 2.5 % Cr.

An estimate as to the occupancy of Co on the *TM* sites in $Sr_2CrO_3Fe_{1-x}Co_xAs$ materials is then made by Rietveld refinement against D2B data employing a $f_{Cr} + f_{Co} = 1$ constraint on the Cr site and a $f_{Fe} + f_{Co} = 0.975$ constraint on the Fe site. The results of these refinements suggest that no Co is present at the Cr crystallographic site in either $Sr_2CrO_3Fe_{0.93}Co_{0.07}As$ or $Sr_2CrO_3Fe_{0.91}Co_{0.09}As$, this is a chemically sensible result since Cr^{3+} is far more oxophilic than Co^{2+}. The fractional occupancies of Co (f_{Co}) in $Sr_2CrO_3Fe_{0.93}Co_{0.07}As$ and $Sr_2CrO_3Fe_{0.91}Co_{0.09}As$ are 7.5(8) % and 9.4(3) %, respectively. These results are consistent with the nominal Co doping levels and confirm the successful substitution of Co exclusively on the Fe site.

4.6.5 D2B PND measurements 2 K

A comparison of the PND patterns of $Sr_2CrO_3Fe_{0.93}Co_{0.07}As$ and $Sr_2CrO_3Fe_{0.91}Co_{0.09}As$ collected at room temperature (295 K) and 2 K on D2B reveal the presence of additional low angle reflections in the 2 K data sets, as shown in Figure 4.27. This observation of additional magnetic Bragg reflections is consistent with the antiferromagnetic character observed from susceptibility measurements (T_N ~ 80 K). However the positions of these reflections are inconsistent with the $\boldsymbol{k}$ = (½, ½, 0) propagation vector observed in Sr_2CrO_3FeAs (Figure 4.27).

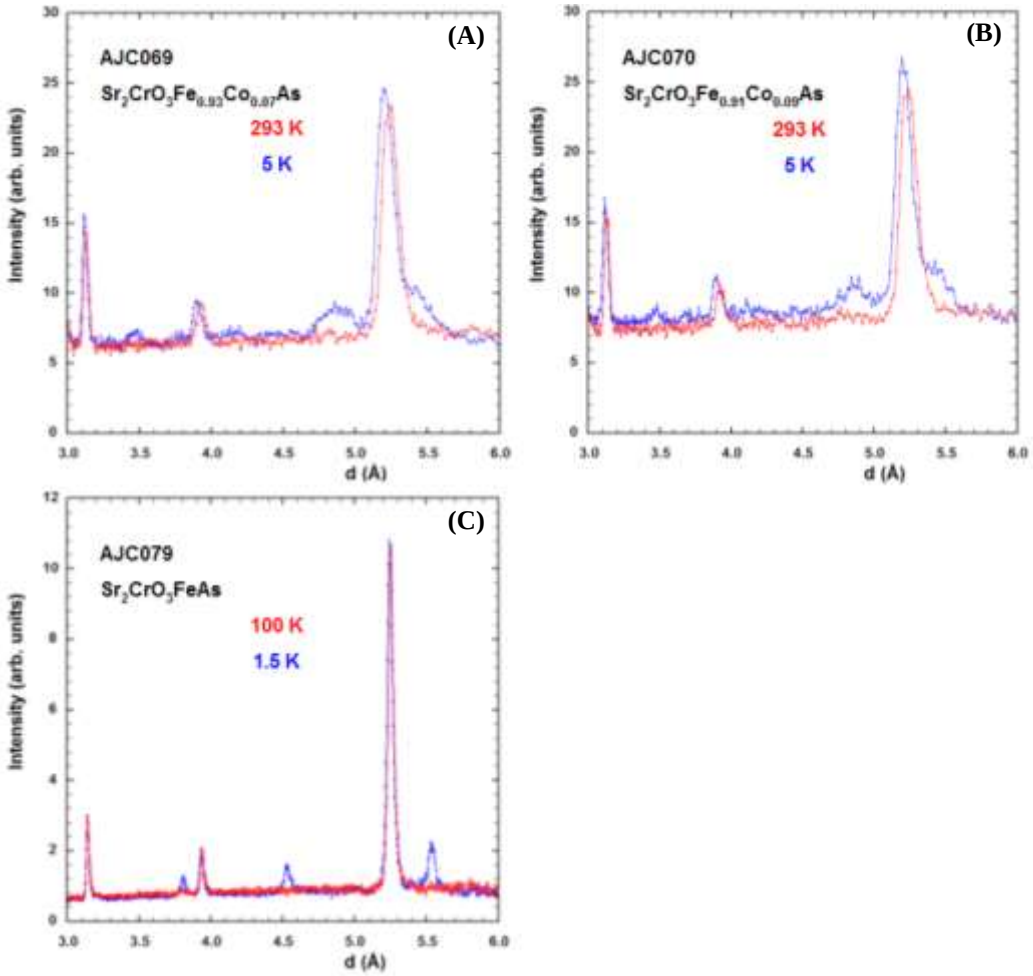

Figure 4.27 Comparison of low temperature magnetic reflections in (A) $Sr_2CrO_3Fe_{0.93}Co_{0.07}As$ and (B) $Sr_2CrO_3Fe_{0.91}Co_{0.09}As$ (collected on the constant λ D2B diffractometer) and (C) Sr_2CrO_3FeAs (collected on ToF WISH diffractometer).

Instead these reflections are indexed to a primitive tetragonal magnetic cell that is a $\sqrt{2}a \times \sqrt{2}a \times 2c$ expansion of the structural unit cell. This indicates a chequerboard arrangement of spins, similar to that seen in Sr_2CrO_3FeAs, but with the doubling along *c* implying AFM coupling of the spins between oxide slabs. This affords the 3 different magnetic structures described in Figure 4.28, in which the moments are either orientated in the basal plane as in those labelled Ψ^1 and Ψ^2, or along *c* as in Ψ^3. These magnetic structures were trialled by introducing an additional phase into the GSAS refinement, in the *P*1 space group with lattice parameters constrained by reciprocal lattice tensors to be $\sqrt{2}a \times \sqrt{2}a \times 2c$ relative to the nuclear $Sr_2CrO_3Fe_{1-x}Co_xAs$ phase. Cr atoms were then introduced at the fractional coordinates (0.25, 0.25, *z*/2), (0.75, 0.75, *z*/2), (0.25, 0.25, (1 - *z*)/2), (0.75, 0.75, (1 - *z*)/2), (0.25, 0.25, (1 - *z*)/2), (0.75, 0.75, ½ + (1 - *z*)/2), (0.25, 0.75, ½ + (1 – *z*/2)) and (0.75, 0.25, (1 – *z*/2)) and the orientations of the Cr moments fixed to give the desired magnetic structure. The Cr moments were then allowed to refine, but fixed to

have the same magnitude on all sites. The resultant Rietveld plots and fitting statistics for AJC069 with the nominal composition $Sr_2CrO_3Fe_{0.93}Co_{0.07}As$ are shown in Figure 4.28.

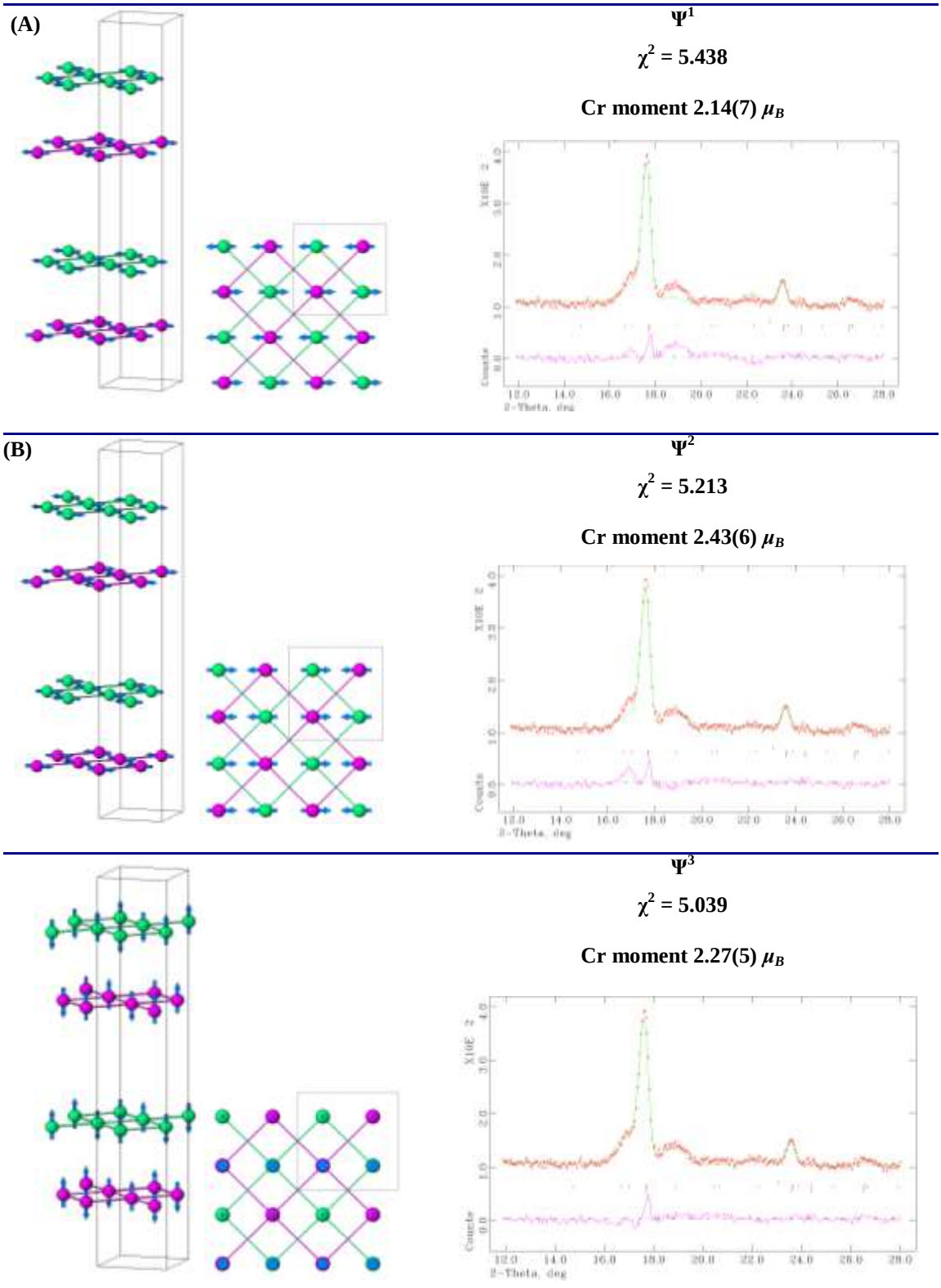

Figure 4.28 (A) Possible magnetic structures for antiferromagnetic checkerboard arrangement of Cr^{3+} spins in $Sr_2CrO_3Fe_{1-x}Co_xAs$ with a k = (½, ½, ½) propagation vector. (B) Rietveld fit to 1.5 K D2B PND data for the $Sr_2CrO_3Fe_{0.03}Co_{0.07}As$ (AJC069) nuclear and trial magnetic phases in the range 3.5 – 6.0 Å.

The results of these refinements against $Sr_2CrO_3Fe_{0.93}Co_{0.07}As$ data, and of those against $Sr_2CrO_3Fe_{0.91}Co_{0.09}As$, both show an improved fit with the Ψ^3 magnetic structure, in which Cr moments are orientated along the *c* axis. Full refinement results for the nuclear and magnetic phases of these two samples are presented in Table 4.4 and the refined ordered Cr moments are 2.27(5) μ_B and 2.26(6) μ_B for $Sr_2CrO_3Fe_{0.93}Co_{0.07}As$ and $Sr_2CrO_3Fe_{0.91}Co_{0.09}As$, respectively.

The Rietveld fit for $Sr_2CrO_3Fe_{0.93}Co_{0.07}As$ at 2 K is shown in Figure 4.29, along with a magnification of the region 18 – 28 ° 2θ. In this region a very broad peak is observed at 18.8 ° 2θ, which corresponds to the (103) magnetic Bragg reflection, as well as a much narrower (004) nuclear reflection at 23.6 ° 2θ. Assuming long range magnetic order and an absence of magnetic strain, the FWHM of reflections originating from both nuclear and magnetic Bragg scattering should be approximately equally. However, estimates for the FWHM of the reflections designated $(103)_{mag}$ and $(004)_{nuc}$ are 0.296 Å and 0.073 Å, respectively. This perhaps indicates that there is more than one reflection con tributing to the peak at 18.8 ° 2θ, but that the resolution on D2B at high *d*-spacings is not sufficient to resolve this. Alternatively the broadening of the magnetic signal could be a result of a short length scale to magnetic order. To investigate the origins of this apparent broadening further PND studies were conducted on the WISH ToF diffractometer.

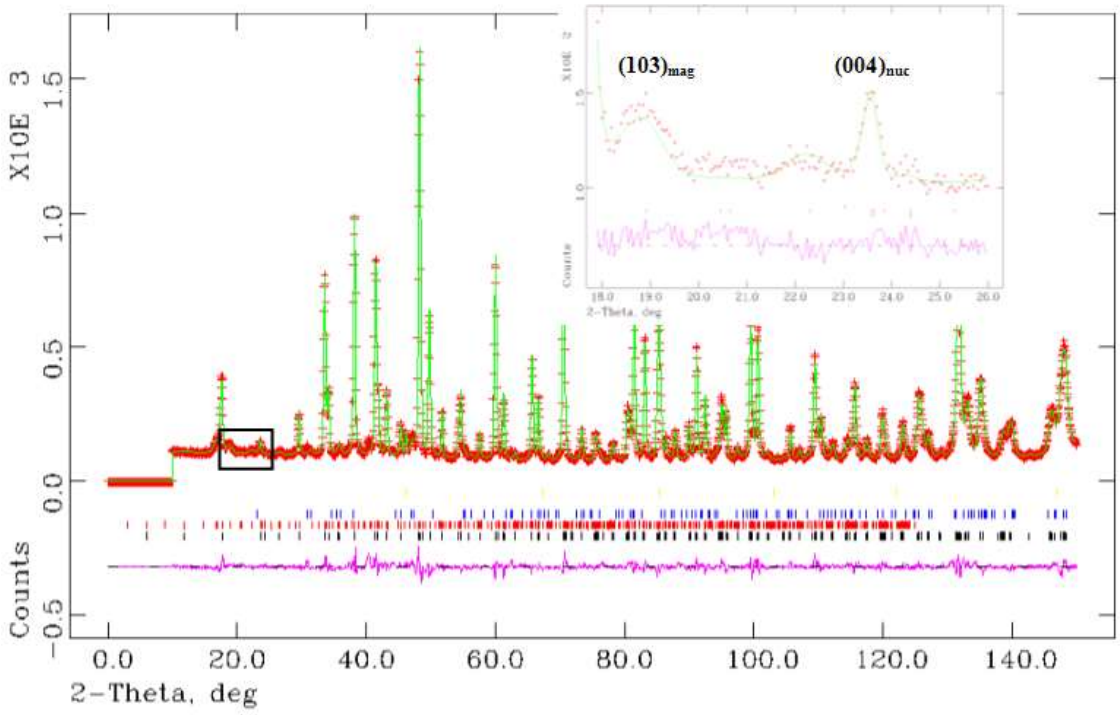

Figure 4.29 Rietveld fit of $Sr_2CrO_3Fe_{0.93}Co_{0.07}As$ to D2B data collected at 2 K. Inset shows a magnification of the 18 – 26 ° 2θ region.

4.7 WISH PND measurements on $Sr_2CrO_3Fe_{0.91}Co_{0.09}As$

As described in chapter 2, the WISH ToF diffractometer at ISIS is optimised for high resolution neutron powder diffraction measurements at high *d*-spacings. Since there appear to be overlapping magnetic Bragg reflections observed in D2B PND data on $Sr_2CrO_3Fe_{1-x}Co_xAs$ materials, additional measurements were performed at 100 K and 1.5 K on a sample with the nominal composition $Sr_2CrO_3Fe_{0.91}Co_{0.09}As$ (AJC069). WISH PND data collected on $Sr_2CrO_3Fe_{0.91}Co_{0.09}As$ at 1.5 K and 100 K are presented in Figure 4.30 along with data collected on Sr_2CrO_3FeAs for comparison.

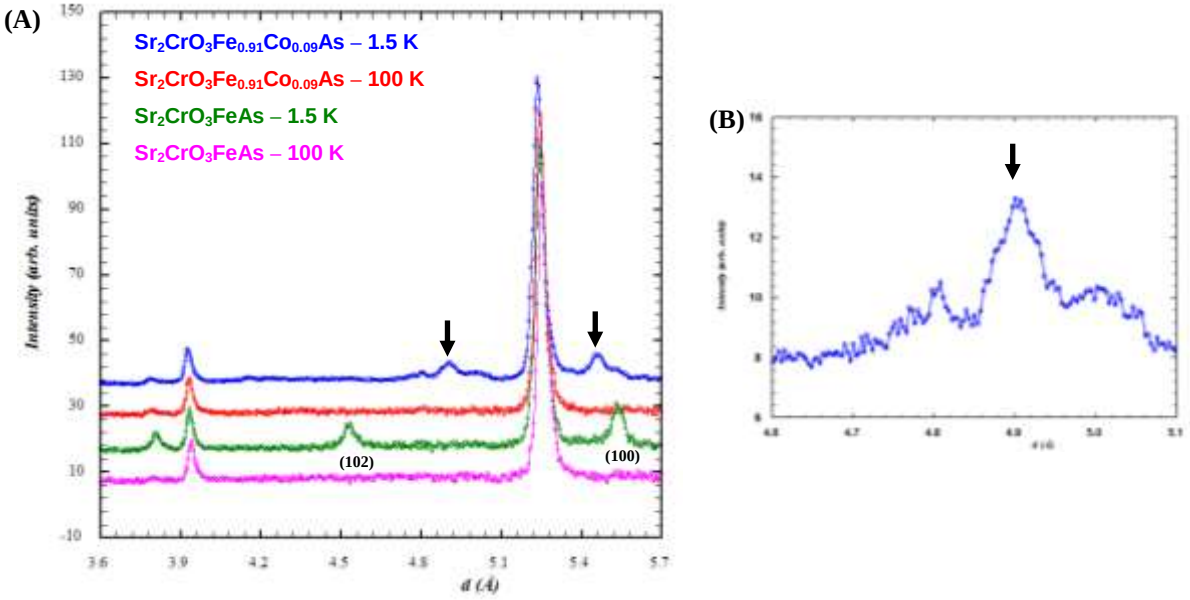

Figure 4.30 Comparison of the PND patterns of Sr_2CrO_3FeAs and $Sr_2CrO_3Fe_{0.91}Co_{0.09}As$ collected at 1.5 and 100 K. Inset shows magnification of 4.7 - 5.1 Å

This comparison clearly shows that the additional low temperature peaks in the $Sr_2CrO_3Fe_{0.91}Co_{0.09}As$ 1.5 K data set are present at *d*-spacings different to those in Sr_2CrO_3FeAs. Furthermore the improved resolution of WISH compared with D2B at high *d*-spacings allows the magnetic Bragg intensity between 4.73 and 5.09 Å to be resolved as 3 distinct peaks (Inset). The middle one of these reflections, along with the strong peak at 5.45 Å are well modelled in Figure 4.31 by a Le Bail fit in Fullprof with a propagation vector of $\boldsymbol{k}$ = (½, ½, ½). This result is consistent with the magnetic model obtained from refinement against D2B data for $Sr_2CrO_3Fe_{1-x}Co_xAs$ materials, however it does not account for the newly resolved magnetic Bragg reflections observed at 4.79 and 5.00 Å. By undertaking systematic Le Bail fits with a range of different $\boldsymbol{k}$-vectors, suggested for the *P*4/*nmm* space group,[17] it was found that a propagation vector of (0.530, ½, ½) well

modelled these two reflections along with another weak reflection at 4.15 Å. This indicates that as well as displaying commensurate magnetic order, $Sr_2CrO_3Fe_{1-x}Co_xAs$ materials also display incommensurate magnetic order with a small modulation in the basal plane, which may account for the large FWHM of magnetic Bragg reflections observed in low temperature D2B measurements.

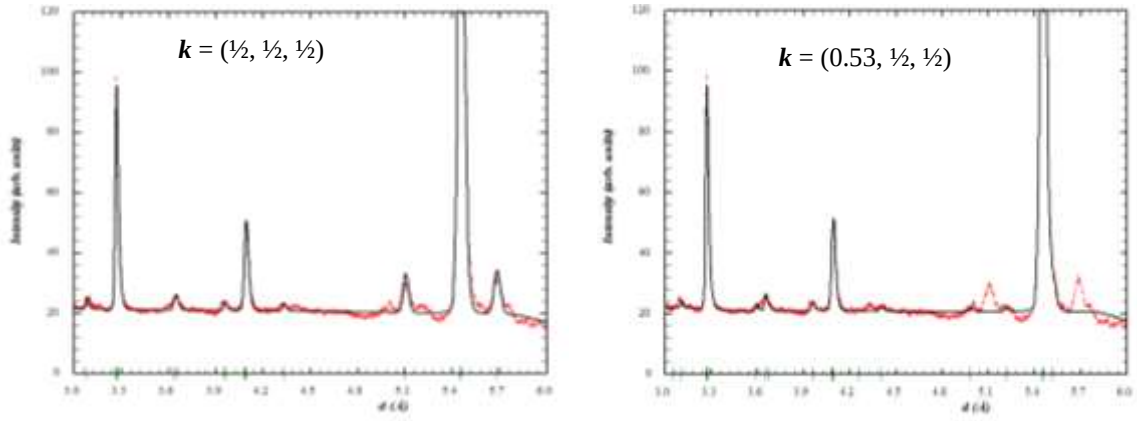

Figure 4.31 Magnetic Le Bail fits to 1.5 K WISH data of $Sr_2CrO_3Fe_{0.91}Co_{0.09}As$

4.7.1 Magnetic structure determination in $Sr_2CrO_3Fe_{0.91}Co_{0.09}As$

In a similar manner as was used to determine the magnetic structure of Sr_2CrO_3FeAs, SARAh Rep. analysis and SARAh refine software interfaced with GSAS were used to determine the likely spin orientations in the commensurately ordered component to magnetic order in $Sr_2CrO_3Fe_{0.91}Co_{0.09}As$. SARAh Rep. Analysis was used to determine the irreps for Cr^{3+}, in the *P*4/*nmm* nuclear space group with propagation vector $\boldsymbol{k}$ = (½, ½, ½). This generates the 6 basis vectors shown in Figure 4.32.

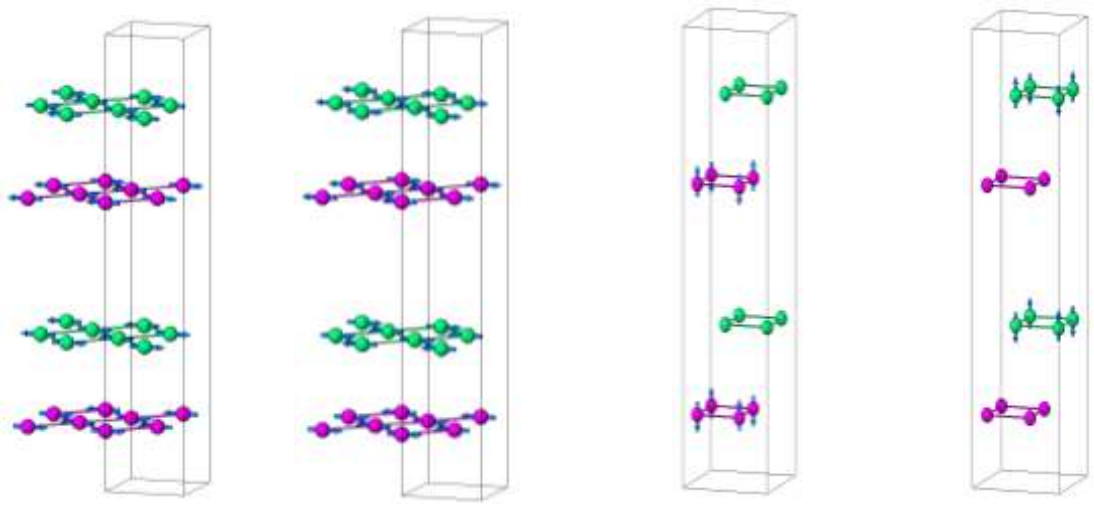

Γ(1)Ψ(1)/ Ψ(2) **Γ(2)Ψ(3)/ Ψ(4)** **Γ(3)Ψ(5)** **Γ(3)Ψ(6)**

Figure 4.32 Basis vectors allowed for Cr ordering in $Sr_2CrO_3Fe_{1-x}Co_xAs$

These basis vectors are similar to those described for Sr_2CrO_3FeAs (Figure 4.12), but the doubling along *c* means that the Cr moments in adjacent oxides layers are coupled antiferromagnetically. Once more, as with Sr_2CrO_3FeAs, a constraint was applied in SARAh Refine for the Γ(3)Ψ(5) and Γ(3)Ψ(6) basis vectors such that the coefficient of the two basis vectors must be the same in all refinements, but the sign of the coefficient is permitted to vary randomly. Initially all six basis vectors were mixed, using Reverse Monte Carlo analysis with a total of 10000 refinement cycles, in an attempt to model the observed magnetic Bragg intensity. The results are displayed in Figure 4.33 in the form of contour plots.

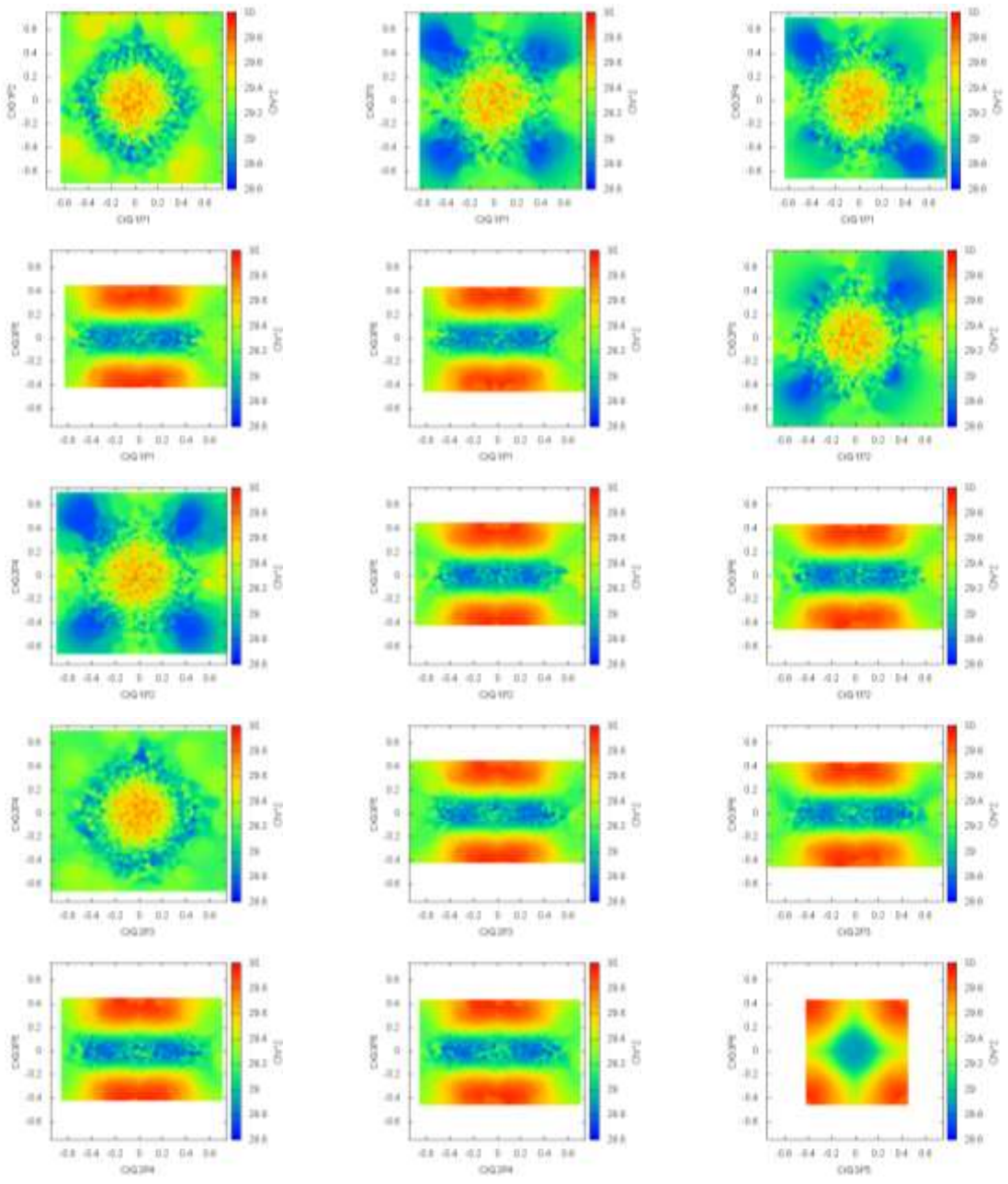

Figure 4.33 Results of Reverse Monte Carlo analysis of all 6 Cr basis vectors.

In contrast to the results obtained from refinement against D2B data, this analysis clearly indicates that values of χ^2 are consistently higher for refinements in which a high proportion of the Ψ(5) and Ψ(6) basis vectors are present. Further analysis was therefore carried out excluding the Γ(3)Ψ(5), and Γ(3)Ψ(6) basis vectors. The resulting contour plots are shown in Figure 4.34.

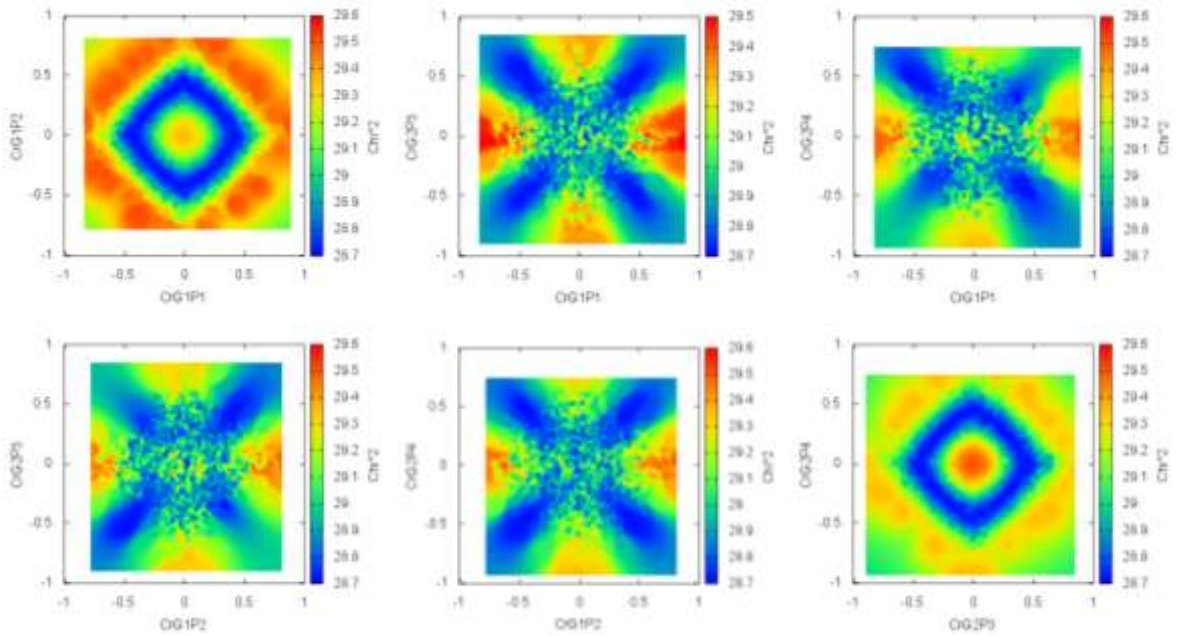

Figure 4.34 Results of Reverse Monte Carlo analysis of the Γ(1) and Γ(2) Cr basis vectors

The results from this analysis show that the global minima in χ^2 for these refinements are encountered when ½ of either of the two Γ(1) basis vectors are present with ½ of either of the two Γ(2) basis vectors. A final cycle of analysis was therefore undertaken using solely the Γ(1)Ψ(1) and Γ(2)Ψ(3) basis vectors to confirm the magnetic structure. The results of this investigation along with the visualisations of the degenerate solutions for the magnetic structure of the commensurate component of antiferromagnetism in $Sr_2CrO_3Fe_{0.91}Co_{0.09}As$ are shown in (Figure 4.35). This analysis yields 4 degenerate solutions which all describe a collinear arrangement of Cr spins directed along either the (100) or (010) directions, towards the nearest neighbour Cr. The refined ordered moment on Cr is 1.24(4) μ_B, a value somewhat lower than in Sr_2CrO_3FeAs and considerably lower than 3 μ_B. The probable explanation for this is attributed to the assumption made that all of the Cr in $Sr_2CrO_3Fe_{0.91}Co_{0.09}As$ is contributing to the commensurate Bragg reflections and hence the scale factor of the commensurate model was fixed at a level ⅛ of that of the nuclear phase. However, this is clearly not the case as additional peaks are observed which are proposed to be from an incommensurately ordered Cr phase. This model is evidently different from

that obtained by refinement against 2 K D2B data. However, this is unsuprisingly given that the magnetic model in D2B refinements has a very broad peak profile which was fitting additional intensity that is now ascribed to an incommesurate magnetic phase with ***k*** = (0.53, ½, ½). Further work is required to ascertain the nature of this incommensurate order and relate these magnetic and superconducting properties to the structure and stoichiometry of this intriguing family of materials.

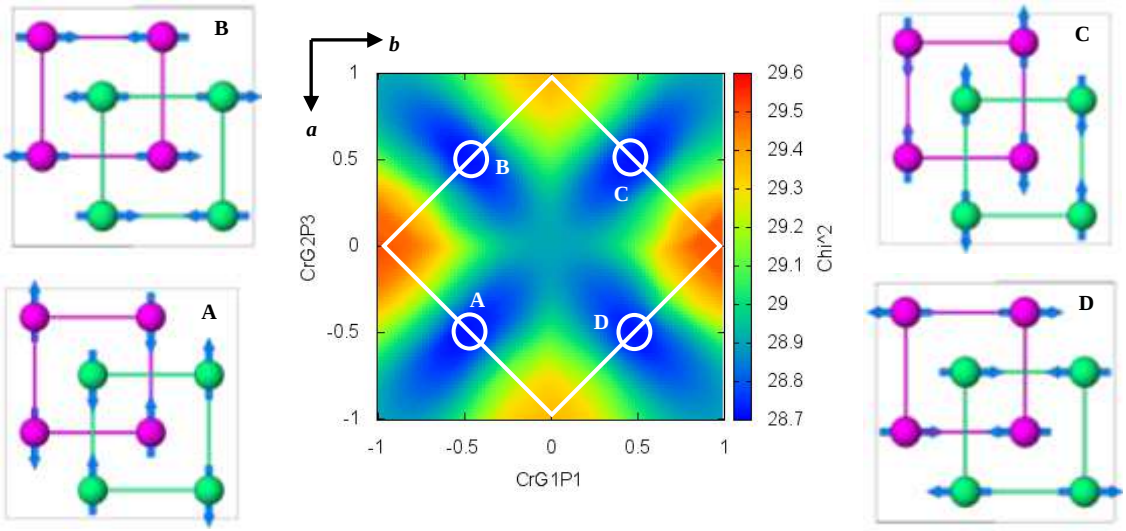

Figure 4.35 Degenerate solutions for the $Sr_2CrO_3Fe_{0.91}Co_{0.09}As$ magnetic structure

The Rietveld fit of the $Sr_2CrO_3Fe_{0.91}Co_{0.09}As$ nuclear and commensurate magnetic phase to 1.5 K WISH data for the 152.9° and 90 ° detector banks are presented in Figure 4.36 and show good agreement between the observed and calculated data. Refined structural parameters are listed in appendix E and instrumental parameters include those to model background, DIFA, scale factors and profile coefficients.

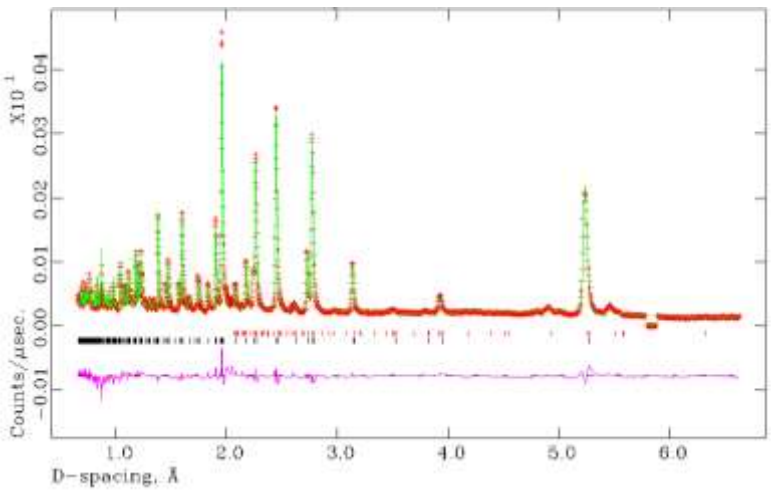

Figure 4.36 Rietveld fit of $Sr_2CrO_3Fe_{0.91}Co_{0.09}As$ to WISH powder neutron diffraction data 90 ° bank

4.8 Discussion

By replacing Sc with Cr at the 2*c* site in the oxide layer of Sr_2ScO_3FeAs the novel iron arsenide oxide Sr_2CrO_3FeAs (*P*4/*nmm*) has been synthesised. The smaller size of the Cr^{3+} (0.615 Å) relative to Sc^{3+} (0.745 Å) leads to a contraction in the *a* and *c* cell parameters and yields $FeAs_4$ tetrahedra that are more regular in geometry (α As-Fe-As = 108.42(3) °). The decrease in the size of the *a* cell parameter also has the effect of decreasing the Fe-Fe distance to 2.76715(2) Å, a value typical for FeAs superconductors Figure 4.37.

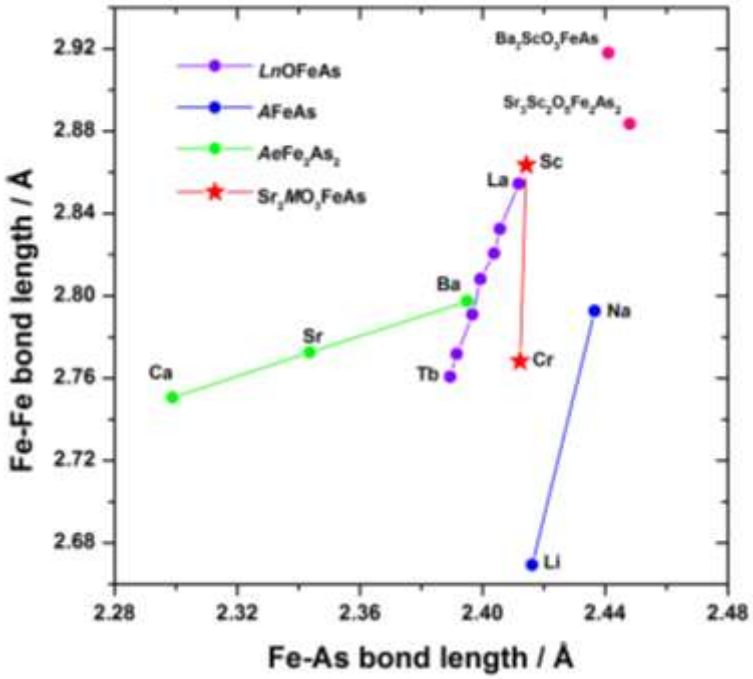

Figure 4.37 Comparison of Fe-Fe and Fe-As bond lengths for selected iron arsenide superconductors.

SQUID magnetometry measurements reveal paramagnetic behaviour at high temperatures and a broad maximum in the susceptibility at approximately 40 K, suggestive of AFM ordering, as seen in the isostructural oxychalcogenide Sr_2CrO_3CuS.[2] The emergence of additional magnetic Bragg reflections in 1.5 K PND data, collected on the WISH ToF diffractometer at ISIS, are consistent with the antiferromagnetic character observed from susceptibility measurements and are described by a $\boldsymbol{k}$ = (½, ½, 0) propagation vector. Analysis of the likely magnetic structure using SARAh Refine suggests that Sr_2CrO_3FeAs adopts a magnetic structure similar to that seen in Pr_2CuO_4 with a checkerboard arrangement of Cr^{3+} spins in the *ab*-plane.[18] However, since there is no net interaction between Cr^{3+} ions in adjacent planes, it is not possible to ascertain their relative spin orientations, such that collinear and non-collinear spin arrangements described in Figure 4.15 give identical magnetic Bragg scattering. In Pr_2CuO_4 a non-collinear arrangement of

Cu^{2+} spins has been established by neutron scattering experiments performed in an applied magnetic field on a single crystal. Similar experiments would be required to confirm if this is also the case in Sr_2CrO_3FeAs.

Additional variable temperature measurements on WISH allow the Neel temperature T_N = 35.9(1) K and critical exponent β = 0.302(9) to be established. These results are in agreement with those reported by Tegel *et al*. and suggest a more gradual transition to long-range order than in the archetypal 2D antiferromagnet K_2NiF_4,[3,19] indicating that significant interlayer coupling exists to give a more 3D-like transition, as seen in Sr_2CoO_3Cl (β = 0.28(3)).[10] No significant evidence for an orthorhombic distortion or striped AFM ordering of Fe moments were observed by comparison of room temperature and 5 K PND data. This is consistent with ^{57}Fe Mossbauer measurements on Sr_2CrO_3FeAs which displays a single signal that broadens below T_N, but shows no evidence for ordering of Fe moments.[20]

The stoichiometry of Sr_2CrO_3FeAs was assessed by Rietveld refinement against room temperature powder neutron diffraction data collected on two separate samples of Sr_2CrO_3FeAs using the POLARIS and WISH ToF instruments at ISIS, with both refinements indicating a mixed occupancy of Cr (2.5 %) and Fe (97.5 %) in the FeAs layers. Such Cr doping is nominally hole doping and in $BaFe_{2-x}Cr_xAs_2$ has been shown to fully suppress the magnetic and structural phase transitions in $BaFe_2As_2$ at x = 0.75, without inducing superconductivity.[21] However, this level of Cr substitution is an order of magnitude greater than that seen in Sr_2CrO_3FeAs and therefore is unlikely to be able account for the absence of an observable orthorhombic distortion and striped AFM order of Fe moments. It is therefore proposed that, as discussed in the previous chapter for Sr_2ScO_3FeAs, the introduction of thick oxide layers between anti-PbO-type FeAs layers is detrimental to the formation of a spin density wave.

$Sr_2CrO_3Fe_{1-x}Co_xAs$ samples were successfully synthesised in the compositional range ($0 \leq x \leq 0.3$) as confirmed by a linear decrease in the c cell parameter with x. SQUID magnetometry measurements reveal the onset of superconductivity below 8 K in $Sr_2CrO_3Fe_{1-x}Co_xAs$ with a nominal x = 0.05. Further Co substitution increases T_c which is maximised at 18 K in $Sr_2CrO_3Fe_{0.92}Co_{0.08}As$. Samples with Co levels greater than 0.11 electrons per iron do not exhibit superconductivity. These observations indicate that electron doping of Sr_2CrO_3FeAs through the partial substitution of Fe^{2+} (d^6) by Co^{2+} (d^7) on the 2*a* site has been successful in inducing superconductivity. The profile of the

$Sr_2CrO_3Fe_{1-x}Co_xAs$ superconducting dome is characteristic of cobalt doped superconducting 122 and 1111 FeAs-based materials.[13,14,16] However, superconducting volume fractions for the most diamagnetic samples are only estimated to be 25 %, indicating that the majority of the sample is not superconducting. It is however suggested that the observed superconductivity is inherent to a $Sr_2CrO_3Fe_{1-x}Co_xAs$ phase since no measurable $SrFe_{2-x}Co_xAs_2$ impurities were observed and the level to which the unidentified impurity phase in PXRD patterns is present does not correlate with the magnitude of the diamagnetic signal. Additional magnetic susceptibility measurements in the temperature range 2 – 300 K reveal that AFM ordering persists in $Sr_2CrO_3Fe_{1-x}Co_xAs$ materials and the Neel temperature (T_N) is raised to between 70 and 80 K.

The strong contrast between Co (2.49 fm) and Fe (9.45 fm) with neutrons allows the fractional occupancies of Fe and Co on the Fe 2*a* site to be determined by refinement against room temperature D2B data, which confirm the successful substitution of Co at the nominal doping level. Low temperature PND measurements on D2B reveal additional reflections which could be indexed to a tetragonal cell according to the propagation vector $\boldsymbol{k}$ = (½, ½, ½). This represents a doubling in the size of the magnetic unit cell along *c*, implying a similar checkerboard in-plane coupling of spins, but with AFM coupling between spins in adjacent oxide slabs. Refinement of trial magnetic structures against D2B data suggests that the moments are aligned along the *c* axis. However the resolution on D2B is 2θ-dependent and some reflections at high *d*-spacings are unfeasibly broad in nature. Additional measurements on a further Co doped sample using the WISH ToF diffractometer at 1.5 K, yielded data with an improved signal to noise ratio at high *d*-spacings. Furthermore the enhanced resolution on this instrument reveals that the broad reflection observed on D2B at 4.95 Å is in fact 3 distinct peaks. In performing systematic Le Bail fits to these additional reflections it was established that the majority magnetic phase could be described by a $\boldsymbol{k}$ = (½, ½, ½) propagation vector, with a further minor phase displaying a (0.530, ½, ½) $\boldsymbol{k}$ vector. This indicates that $Sr_2CrO_3Fe_{1-x}Co_xAs$ materials display both commensurate and incommensurate magnetic order, the latter with a small modulation in the basal plane.

Analysis of the commensurate component to magnetic Bragg scattering using SARAh Refine suggests a collinear arrangement with Cr spins directed along either the (100) or (010) directions. This magnetic structure is therefore similar to that of Ca_2MnO_4 and Sr_2FeO_3F, but in this case the Cr spins are directed towards the nearest-neighbour in-plane

Cr.[22,23] Overall the observed superconducting and magnetic properties of the $Sr_2CrO_3Fe_{1-x}Co_xAs$ system are summarised in the magnetic phase diagram depicted in Figure 4.38.

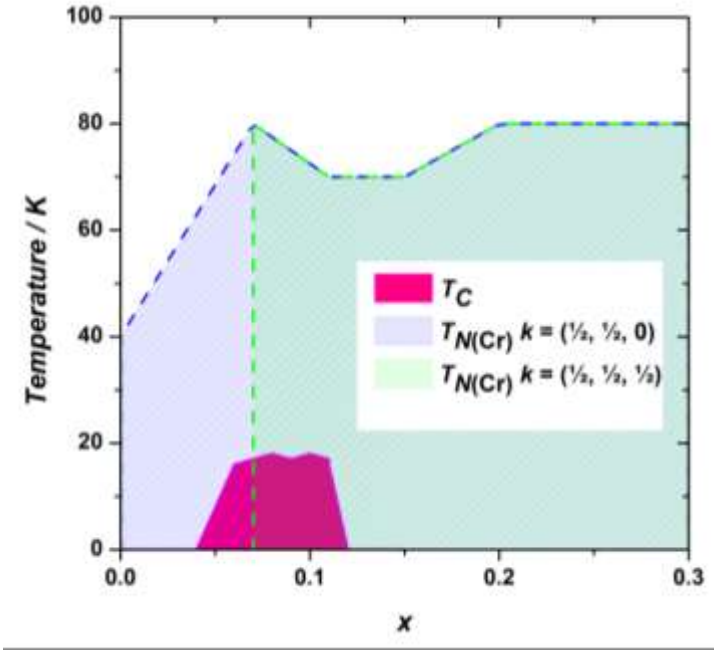

Figure 4.38 Magnetic and superconducting phase diagram of $Sr_2CrO_3Fe_{1-x}Co_xAs$

References

(1) Shannon, R. *Acta Crystallographica Section A* **1976**, *32*, 751-767.
(2) Zhu, W. J.; Hor, P. H. *Journal of Solid State Chemistry* **1997**, *134*, 128-131.
(3) Tegel, M.; Hummel, F.; Su, Y.; Chatterji, T.; Brunelli, M.; Johrendt, D. *EPL (Europhysics Letters)* **2010**, *89*, 37006.
(4) Hubbard, J.; Marshall, W. *Proceedings of the Physical Society* **1965**, *86*, 561.
(5) Aeppli, G.; Buttrey, D. J. *Physical Review Letters* **1988**, *61*, 203-206.
(6) Vaknin, D.; Sinha, S. K.; Moncton, D. E.; Johnston, D. C.; Newsam, J. M.; Safinya, C. R.; King, H. E., Jr. *Physical Review Letters* **1987**, *58*, 2802-2805.
(7) Skanthakumar, S.; Lynn, J. W.; Peng, J. L.; Li, Z. Y. *Physical Review B* **1993**, *47*, 6173-6176.
(8) Bramwell, S. T.; Holdsworth, P. C. W. *Physical Review B* **1994**, *49*, 8811-8814.
(9) Birgeneau, R. J.; Guggenheim, H. J.; Shirane, G. *Physical Review B* **1970**, *1*, 2211-2230.
(10) Knee, C. S.; Price, D. J.; Lees, M. R.; Weller, M. T. *Physical Review B* **2003**, *68*, 174407.
(11) Moor, R. C. *Part II thesis* **2009**, *University of Oxford*.
(12) Leithe-Jasper, A.; Schnelle, W.; Geibel, C.; Rosner, H. *Physical Review Letters* **2008**, *101*, 207004.
(13) Wang, C.; Li, Y. K.; Zhu, Z. W.; Jiang, S.; Lin, X.; Luo, Y. K.; Chi, S.; Li, L. J.; Ren, Z.; He, M.; Chen, H.; Wang, Y. T.; Tao, Q.; Cao, G. H.; Xu, Z. A. *Physical Review B* **2009**, *79*, 9.
(14) Leithe-Jasper, A.; Schnelle, W.; Geibel, C.; Rosner, H. *Physical Review Letters* **2008**, *101*, 207004.
(15) Wang, X. F.; Wu, T.; Wu, G.; Liu, R. H.; Chen, H.; Xie, Y. L.; Chen, X. H. *New Journal of Physics* **2009**, *11*, 045003.
(16) Matsuishi, S.; Inoue, Y.; Nomura, T.; Yanagi, H.; Hirano, M.; Hosono, H. *Journal of the American Chemical Society* **2008**, *130*, 14428.
(17) Cracknell, A. P., Davies, B.L., Miller, S. C., Love, W. F. *Kronecker Product Tables.* **1979**, *1*.
(18) Sumarlin, I. W.; Lynn, J. W.; Chattopadhyay, T.; Barilo, S. N.; Zhigunov, D. I.; Peng, J. L. *Physical Review B* **1995**, *51*, 5824-5839.
(19) Ganguly, P.; Rao, C. N. R. *Journal of Solid State Chemistry* **1984**, *53*, 193-216.
(20) Tegel, M.; Hummel, F.; Lackner, S.; Schellenberg, I.; Pöttgen, R.; Johrendt, D. *Zeitschrift Fur Anorganische Und Allgemeine Chemie* **2009**, *635*, 2242-2248.
(21) Sefat, A. S.; Singh, D. J.; VanBebber, L. H.; Mozharivskyj, Y.; McGuire, M. A.; Jin, R.; Sales, B. C.; Keppens, V.; Mandrus, D. *Physical Review B* **2009**, *79*, 224524.
(22) Hector, A. L.; Knee, C. S.; MacDonald, A. I.; Price, D. J.; Weller, M. T. *Journal of Materials Chemistry* **2005**, *15*, 3093-3103.
(23) Cox, D. E.; Shirane, G.; Birgeneau, R. J.; MacChesney, J. B. *Physical Review* **1969**, *188*, 930-932.

5. Sr_2VO_3FeAs

5.1 Introduction

In the previous chapters it has been shown that Sr_2ScO_3FeAs and Sr_2CrO_3FeAs are somewhat different from other FeAs-based superconducting parent materials in that they do not exhibit any strong evidence for a structural distortion or striped magnetic order. It is proposed that this is a result of the enhanced interplanar separation in this Sr_2MO_3FeAs family which inhibits the development of long range magnetic order. However, it was also shown in the previous chapter that it is possible that in electron doping Sr_2CrO_3FeAs, through the partial substitution of Fe^{2+} (d^6) by Co^{2+} (d^7), it is possible to induce superconductivity with critical temperatures up to 19 K. This suggests that the Sr_2MO_3FeAs family are in some ways not so different from other iron based superconductors.

In April 2009 isostructural Sr_2VO_3FeAs was reported by Wen *et al* and curiously shown to be superconducting without the need for carrier doping, with an onset critical temperature of 37 K from resistivity measurements.[1-3] The only other FeAs-based material to exhibit superconductivity, in the absence of external pressure, and without the need for carrier doping is LiFeAs.[4] In Sr_2VO_3FeAs the observed superconductivity has prompted debate as to whether the V 3*d* derived bands contribute significantly to the Fermi surface, which in other FeAs-based parent materials are dominated by Fe bands.[5,6]

Mazin has argued that the apparent complexity of the Fermi surface is entirely a product of V-derived electronic states and by weighting of the electronic states with Fe character a susceptibility is obtained that supports the existing quasi-nesting model for iron pnictide superconductors.[6] Assuming therefore that Sr_2VO_3FeAs displays the same essential Fermi nesting features as other iron pnictide superconductors, the absence of a SDW anomaly and the presence of superconductivity in the stoichiometric material may suggest intrinsic doping. Since vanadium can easily adopt a range of formal oxidation states from +2 to +5 it could conceivably hole or electron dope the FeAs layer. However, such analysis has been somewhat hampered by the poor quality of samples that have been reported, which typically contain significant proportions of ternary vanadate as well as iron arsenide impurities, the quantification of which has often been less than candid, as noted by Johrendt *et al*.[7]

In this chapter a synthetic route to comparatively clean samples of Sr_2VO_3FeAs is first optimised. The stoichiometry and structure of Sr_2VO_3FeAs is then scrutinised by a combination of synchrotron X-ray and neutron powder diffraction, before further investigations are made into the magnetic properties and the valence states of V and Fe.

5.2 Sr_2VO_3FeAs

5.2.1 Attempted synthesis of phase pure Sr_2VO_3FeAs

The initial report of Sr_2VO_3FeAs by Wen *et al.*[1] used V_2O_5 as a starting material, but this is known to be highly reactive with alumina and other crucible materials. A revised V_2O_5 free synthetic route to Sr_2VO_3FeAs was therefore designed. In a preliminary attempt to synthesise Sr_2VO_3FeAs, stoichiometric amounts of SrO (prepared by the thermal decomposition of $SrCO_3$ (Alfa 99.99 %)), V (Alfa 99.5 %), Fe_2O_3 (Alfa 99.998 %), Fe (Alfa 99.998 %) and As (Alfa, 99.9999 %) were combined in a 2 : 1 : ⅓ : ⅓ : 1 ratio. This sample was then pelletised, placed in an alumina crucible, sealed in a silica ampoule and heated at 1 °C / min to 1100 °C for 48 h. The resultant black crystalline powder was ground and stored in an argon-filled glove box. A powder X-ray diffraction pattern was then collected on the X'pert diffractometer and the Rietveld fit to this data is presented in Figure 5.1. Additional weak reflections are attributed to Sr_2VO_4 and FeAs impurity phases which are found to present at 9.31 and 9.55 wt %, respectively.

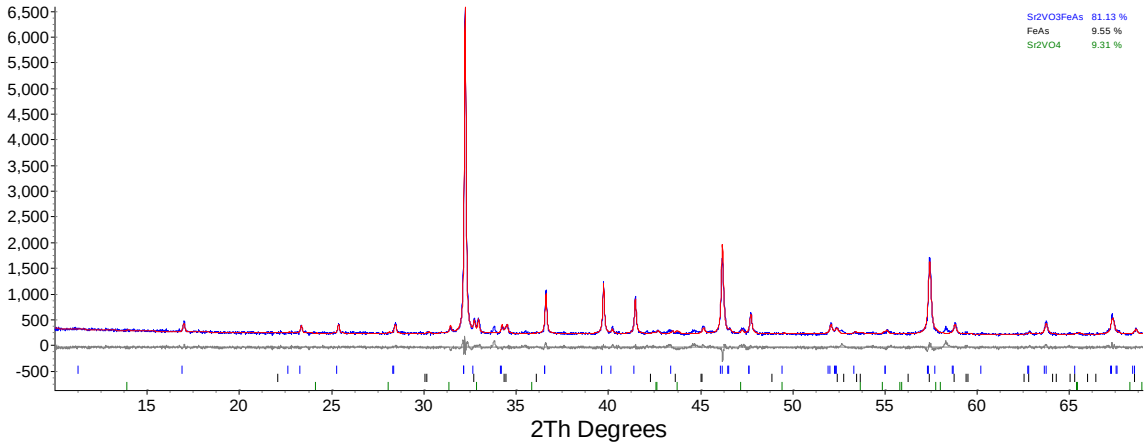

Figure 5.1 Rietveld fit of Sr_2VO_3FeAs (AJC038) to PXRD data

In an attempt to improve the purity of Sr_2VO_3FeAs this sample (AJC038) was reground, pressed in a pellet and annealed at to 1100 °C for a further 48 h. This reheated sample (AJC038a) was assessed by PXRD and is compared to that of the once heated sample in Figure 5.2. It is evident from inspection of these patterns that greater proportions of Sr_2VO_4 and FeAs are present. Rietveld analysis confirms this with weight fractions of

Sr_2VO_4 and FeAs at 14.17 and 21.72 wt %, respectively. This suggests that the formation of strontium vanadate phases is favourable with repeated annealing cycles (Figure 5.2).

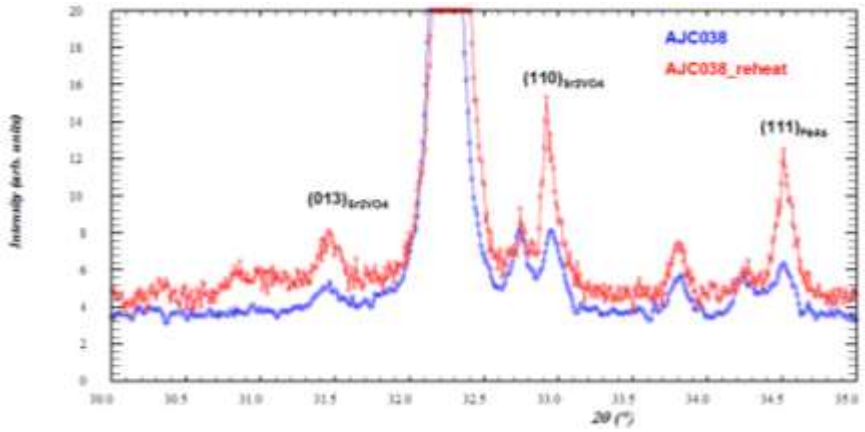

Figure 5.2 Magnification of the 30 – 35 ° 2θ region of Sr_2VO_3FeAs (AJC038) showing the growth of Sr_2VO_4 and FeAs impurity phases upon repeated annealing.

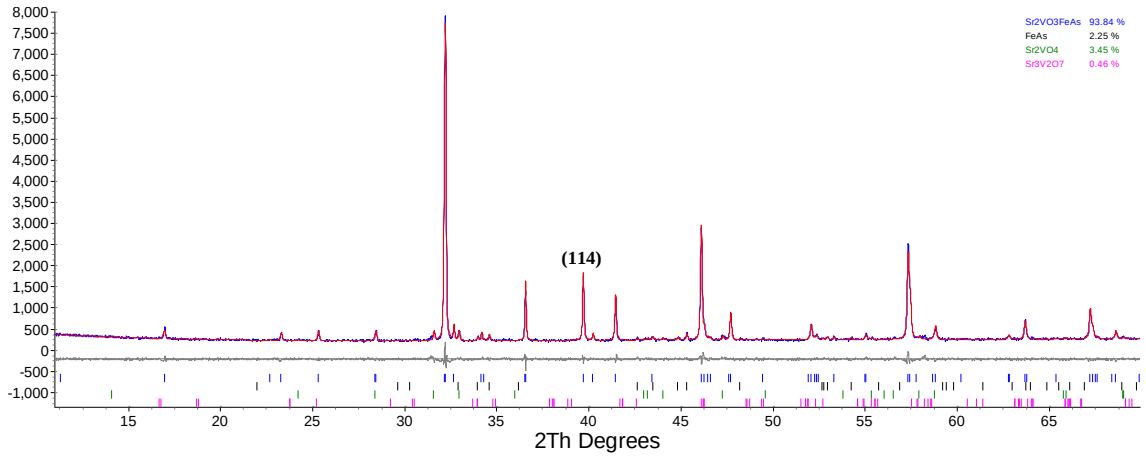

Figure 5.3 Rietveld fit of Sr_2VO_3FeAs (AJC093) to PXRD data.

Extensive investigations were therefore made in an attempt to optimise a synthetic route to a phase pure sample of Sr_2VO_3FeAs. In this improved procedure stoichiometric amounts of SrO (prepared by the thermal decomposition of as discussed in Chapter 2 ($SrCO_3$ (Alfa 99.99 %))), VAs (preparation discussed in Chapter 2), Fe_2O_3 (Alfa 99.998 %) and Fe (Alfa 99.998 %) are mixed together in a 2 : 1 : ⅓ : ⅓ ratio. These reagents were thoroughly ground together using an agate pestle and mortar, pressed into 13 mm diameter pellets at a force of 5 tonnes, placed in alumina crucibles and sealed in silica ampoules under dynamic vacuum. The ampoules were heated to 1100 °C at a rate of 1 °C / min, held at this temperature for 48 h, before being cooled to room temperature. The resultant black crystalline powders were stored in an argon-filled dry box. The Rietveld fit to PXRD data collected on this sample (AJC093) is shown in Figure 5.3.

Unfortunately it was not possible to completely eradicate the iron arsenide and strontium vanadate impurity phases. However, in this sample they are present in considerably lower proportions, with Sr_2VO_4, FeAs and $Sr_3V_2O_7$ at levels of 3.36, 2.28 and 0.42 wt %, respectively. To further characterise this sample (AJC093) variable temperature synchrotron X-ray powder diffraction measurements were performed on the I11 beamline at Diamond, the results of which are discussed in section 5.2.3. The air and moisture sensitivity of Sr_2VO_3FeAs was also investigated by bubbling oxygen through water over a sample (AJC127) for 24 h. This sample was observed to exhibit no obvious air sensitivity, as judged by invariant powder X-ray diffraction pre and post treatment (appendix F).

As stated in the introduction to this chapter the reporting and quantification of impurities phases in Sr_2VO_3FeAs samples has not always been clear. The initial report of Sr_2VO_3FeAs by Wen *et al* noted the presence of Sr_2VO_4 in the sample at a 13 : 1 ratio to the main phase.[1] That a FeAs containing impurity was not also reported either implies that Sr_2VO_3FeAs is inherently deficient in the oxide layer or that the authors did not model such phases. A further study by Awana *et al*,[8] does not identify impurity peaks that are present in their sample to such a level that the most intense reflections are of comparable intensity to that of the (114) reflection of the main phase (labelled in Figure 5.3).[9] Notably, this study does not report superconductivity from resistivity measurements made down to 20 K, but does show evidence for a phase transition at approximately 175 K. These observations imply that the properties of Sr_2VO_3FeAs are very dependent on the synthetic route employed and presumably the resultant stoichiometry. It is encouraging that the samples synthesised here appear to be the purest samples of Sr_2VO_3FeAs synthesised to date with strontium vanadate and iron arsenide impurities present at a level < 4 wt %.

5.2.2 SQUID Magnetometry

The zero-field-cooled and field-cooled magnetic susceptibility of Sr_2VO_3FeAs (AJC093) measured in an applied field of 50 Oe between 2 and 300 K is shown in Figure 5.4. It shows Sr_2VO_3FeAs to be a good superconductor with T_c = 25(1) K and a shielding fraction, estimated from the ZFC susceptibility at 2 K, of 35 %. Whilst this critical temperature is appreciably lower than those reported elsewhere in the literature, it is important to note that T_c as measured by the onset of superconducting transition from resistivity measurements are consistently reported as being higher than those from susceptibility data.

Author	Wen *et al*[1]	Johrendt *et al*[7]
$T_{c\ (onset)}\ \rho$ / K	37	33
$T_{c\ (onset)}\ \chi$ / K	31.5	20 (estimated)

Table 5.1 Comparison of superconducting critical temperatures from resistivity and susceptibility measurements.

The strong diamagnetic signal from this sample at low temperatures dominates the susceptibility of Sr_2VO_3FeAs on preliminary visual inspection. However, in analysing the paramagnetic region of data at appropriate temperature intervals it appears that Sr_2VO_3FeAs undergoes additional magnetic transitions as shown in Figure 5.5.

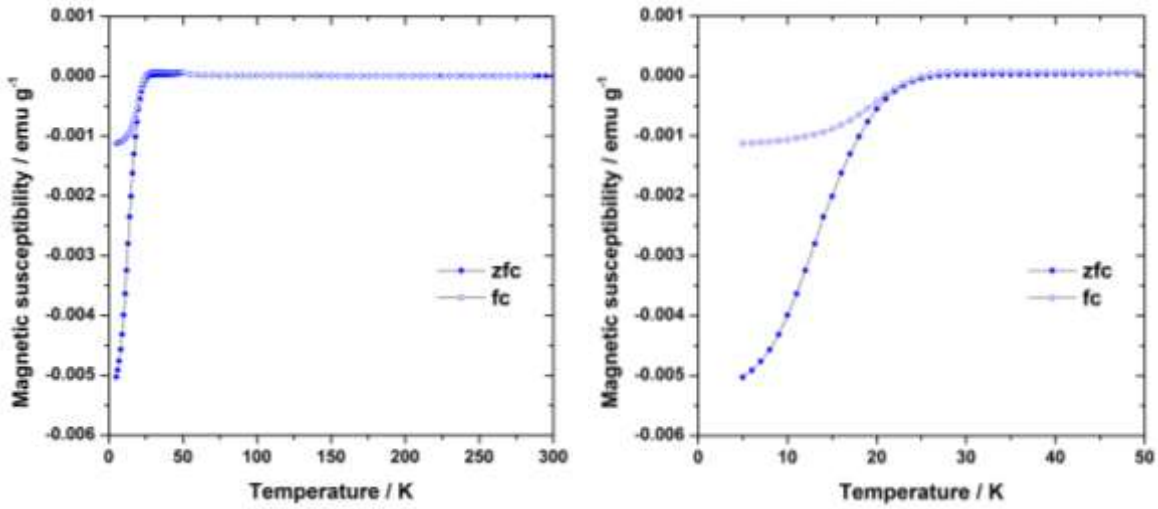

Figure 5.4 Zero-field-cooled and field-cooled magnetic susceptibility measurements performed on a sample of Sr_2VO_3FeAs (AJC093) measured in an applied field of 50 Oe between 2 and 300 K.

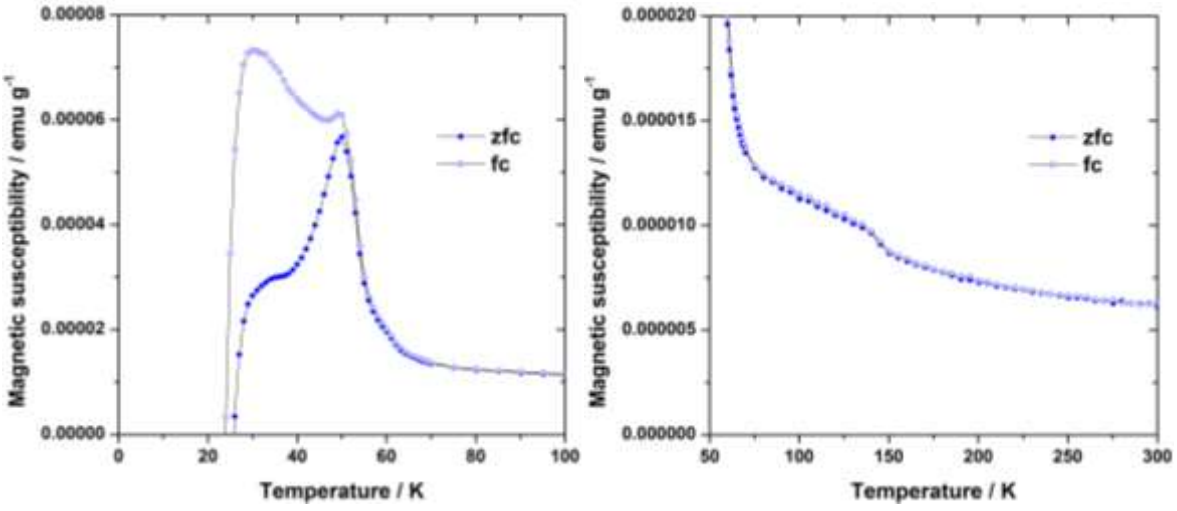

Figure 5.5 Magnetic transitions in Sr_2VO_3FeAs (AJC093).

At 150 K Sr_2VO_3FeAs exhibits a step-like increase in the susceptibility is observed, however this is unlikely to be as a result of a ferromagnetic transition, since a *M* vs *H* loop made at 75 K is approximately linear (Figure 6 A). Further transitions are observed at ~ 70

and 50 K, the latter is concomitant with the divergence of the ZFC and FC susceptibilities. This divergence suggests ferromagnetic or spin glass type behaviour which is supported by the magnetic hysteresis loop measured at 35 K (Figure **5.6**). However, the very small extrapolated residual magnetism suggests a very weak ferromagnetic moment, perhaps due to a small spin canting of magnetic moments. A more detailed discussion of the possible nature of these transitions is made in section 5.3. However, it is important to note that a ^{57}Fe Mössbauer study by Cao *et al* shows no evidence for signal splitting, as would be anticipated for striped AFM Fe ordering.[10] This suggests that the observed transitions are likely a result of ordering on the vanadium sub-lattice.

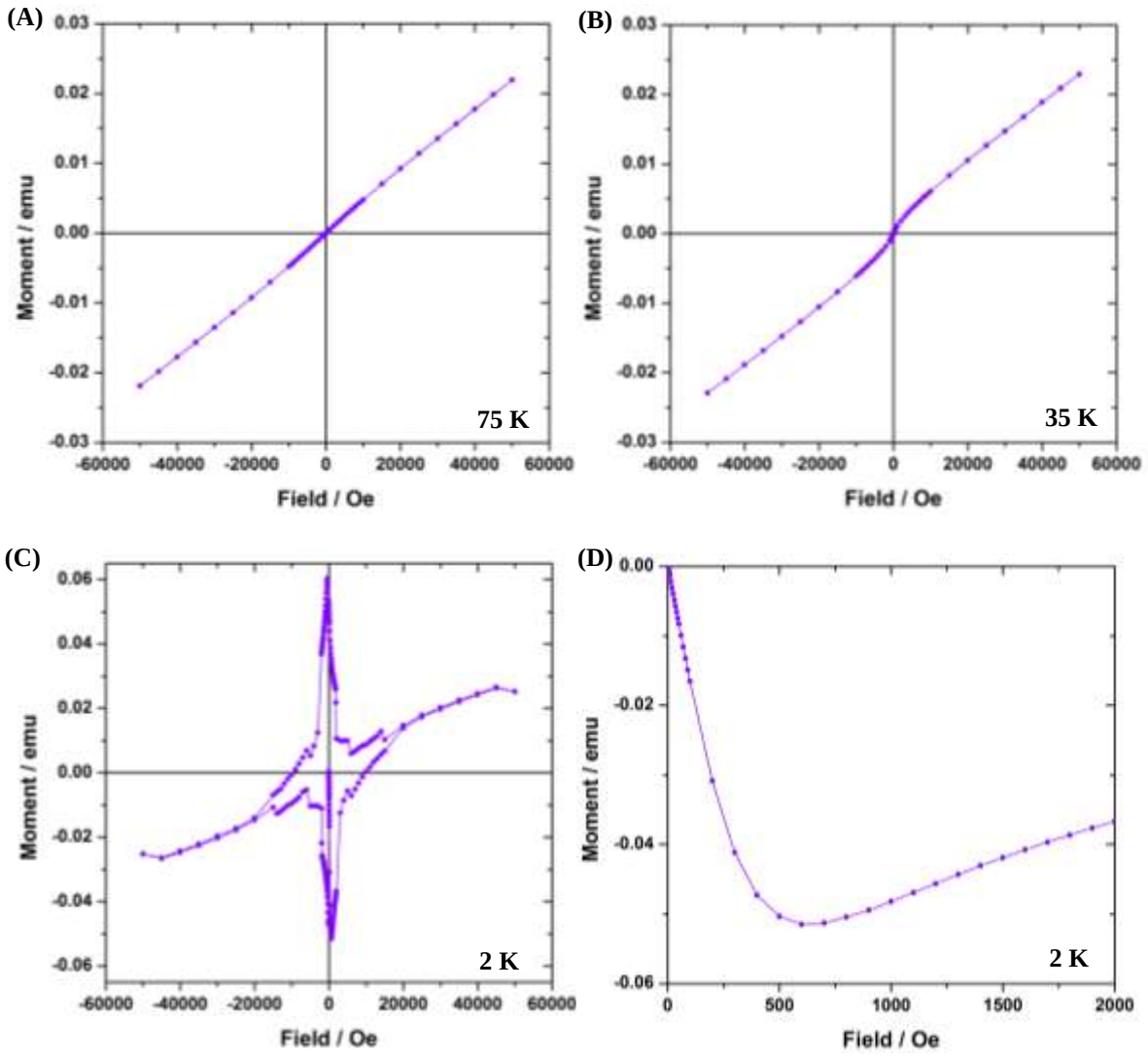

Figure 5.6 Hystersis loops performed at (A) 75 K (B) 35 K (C) 2 K with (D) showing a magnification of the low *H* region.

A comparison of the zero-field-cooled susceptibilities of three different samples of Sr_2VO_3FeAs (AJC093, AJC101, AJC127) that were all synthesised by the same synthetic

route, is made in Figure 5.7. This figure shows the magnetic behaviour of these samples to be reproducible.

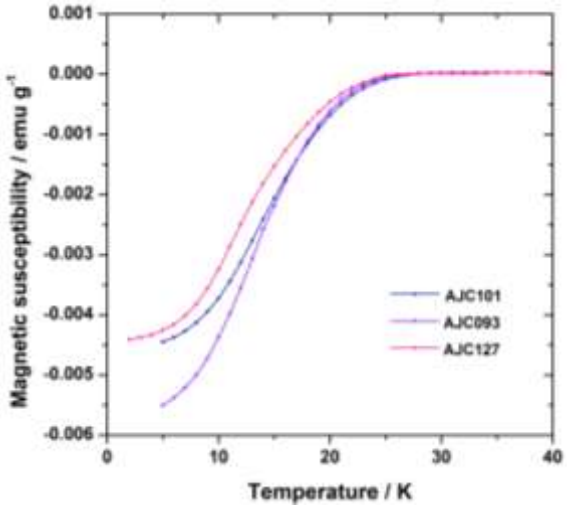

Figure 5.7 Comparison of the superconducting transition in Sr_2VO_3FeAs samples

5.2.3 Synchrotron X-ray powder diffraction measurements

In order to assess the possibility of structural transitions in Sr_2VO_3FeAs (AJC093) variable temperature synchrotron X-ray powder diffraction measurements were performed at Diamond on the I11 beamline. A room temperature data collection was also made on the ID31 instrument at the ESRF to further probe the stoichiometry of Sr_2VO_3FeAs (AJC127).

5.2.3.1 I11 room temperature

In room temperature measurements a sample of Sr_2VO_3FeAs (AJC093) was loaded into a 0.5 mm diameter borosilicate glass capillary. A total of 3 data collections were made in the 5 -145 º 2θ range using 0.601 Å X-rays. The data were then summed into a single histogram and a Rietveld refinement was performed against this data using TOPAS Academic suite in the 2θ range 5-50 °. The Rietveld fit to this data is shown in Figure 5.8.

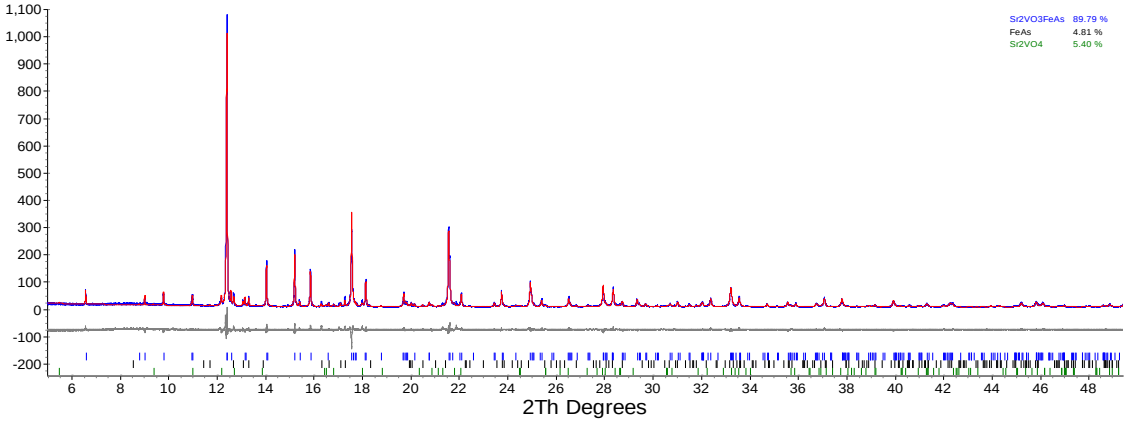

Figure 5.8 Rietveld fit of Sr_2VO_3FeAs (AJC093) to synchrotron X-ray diffraction data

Refined structural parameters are listed in Table 5.2 and instrumental parameters include those to model background, zero error and profile coefficients. FeAs and Sr_2VO_4 impurity phases were also included in these refinements and found to be present at 4.75 and 5.35 wt %, respectively. The occupancies on both the V and Fe crystallographic site were permitted to refine but neither showed any significant vacancies.

5.2.3.2 I11 variable temperature

Variable temperature synchrotron X-ray powder diffraction measurements were also performed in a PheniX cryostat. These measurements were made in order to investigate the possibility of structural distortions associated with the magnetic ordering transitions observed in SQUID magnetometry data. As PheniX cryostats are optimised for flat plate samples, Sr_2VO_3FeAs (AJC093) was contained in a 0.7 mm aluminium capillary to enhance heat exchange with the sample in an attempt to avoid spurious effects of the beam heating the sample. Short data collections (5 mins) were made on cooling from room temperature (293 K) to 12 K (base temperature) at ~ 20 K increments with longer data collections made at 130 K (30 min) and 12 K (3 × 30 mins). Unfortunately the use of an Al capillary, means that Al Bragg reflections dominate the scattering in all of the variable temperature data collections, as illustrated by the 180 K SXRD pattern in Figure 5.9.

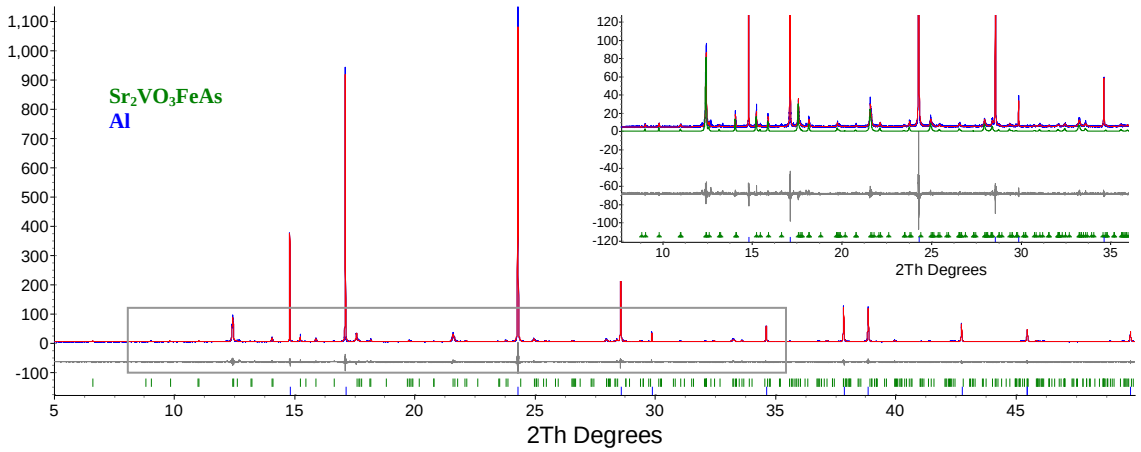

Figure 5.9 Rietveld fit of Sr_2VO_3FeAs and Pawley fit of Al (*Fm*3*m*) to 180 K synchrotron X-ray diffraction data. Inset shows a magnification of reflections from Sr_2VO_3FeAs.

In order to extract some meaningful results from this data, sequential Rietveld refinements of a Sr_2VO_3FeAs phase against variable temperature sets were made in the range 5 – 50 ° 2θ, with a Pawley fit to the Al reflections using the TOPAS academic software. At all temperatures a tetragonal model of Sr_2VO_3FeAs was used to fit the observed Bragg reflections. The variation of the *a* and *c* lattice parameters with temperature are shown in

Figure 5.10. Also included in this figure is the variation of the Pawley fitted Al lattice parameter with temperature, which shows good agreement with that reported by Straumanis *et al.*[11]

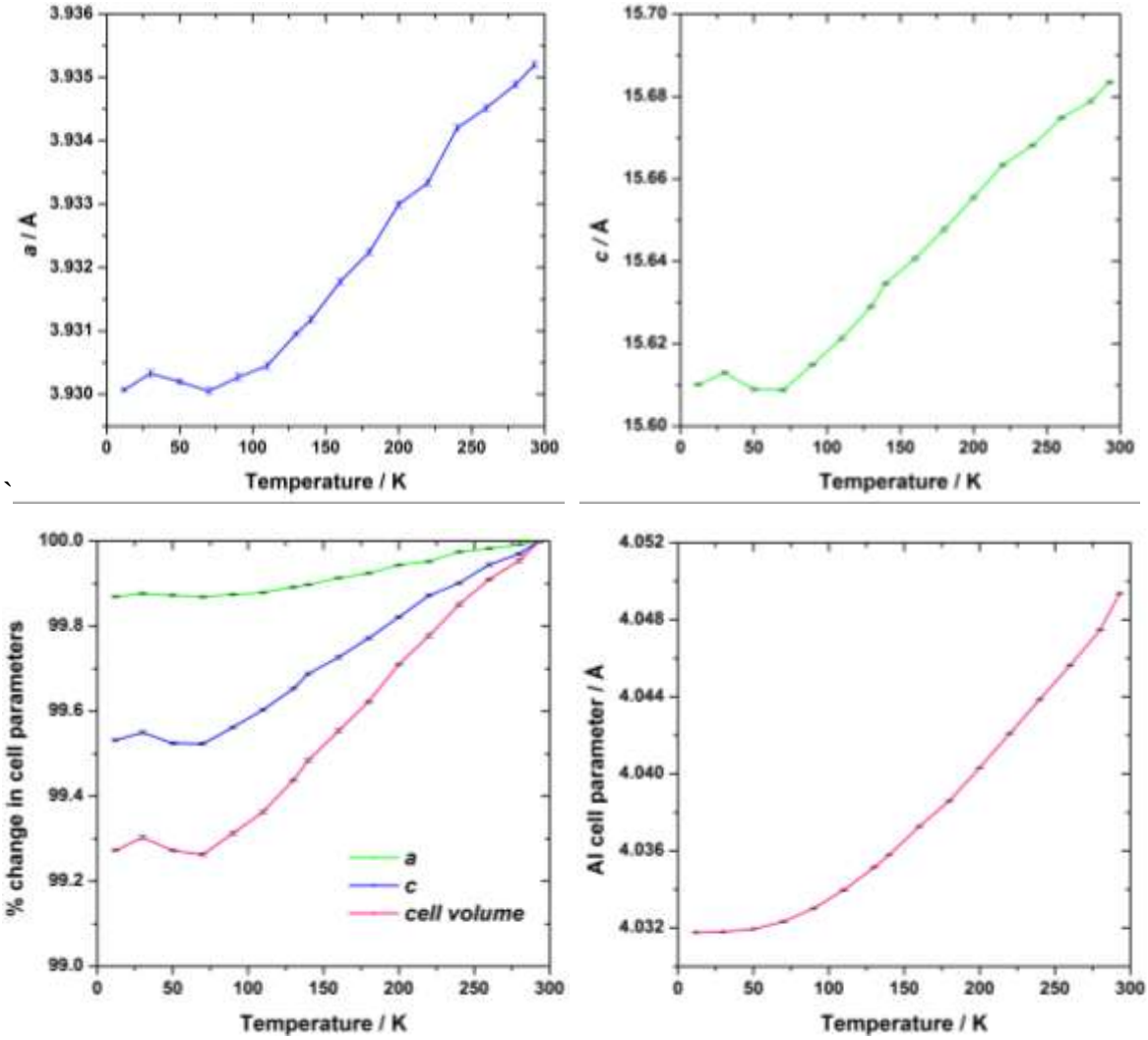

Figure 5.10 Variation of Sr_2VO_3FeAs and Al lattice parameters with temperature

Assuming good thermal contact between capillary and sample, this indicates that the sample temperatures are accurate. Overall the *a* and *c* cell parameters of Sr_2VO_3FeAs decrease by 0.00525 Å (0.13 %) and 0.071 Å (0.45 %), respectively, in cooling Sr_2VO_3FeAs from 293 K to 12 K. There is a small discontinuity in the decrease of both lattice parameters in the 30 K data set, which has lattice parameters that are slightly larger than those seen in the 50 and 70 K data. Unfortunately further investigations into the variations of specific atomic parameters with temperature are hampered by poor signal to noise in the data and absorption effects due to Al capillaries.

Instrument		**ID31**	**I11**	
Temperature / K		**293 K**	**293 K**	**5 K**
Cell parameters and global fitting parameters				
a / Å		3.93723(1)	3.93532(2)	3.93007(3)
c / Å		15.69298(7)	15.6811(1)	15.6101(2)
V / Å^3		243.269(2)	242.849(3)	241.105(5)
R_{wp}		8.49	8.707	8.369
χ^2		1.825	2.839	4.076
Atomic parameters:				
Sr1	[2*c* (¾, ¾, *z*)]	0.19004(5)	0.19013(8)	0.1906(2)
	U_{iso} × 100 / Å^2	0.39(1)	0.34(4)	-0.69(4)
Sr2	[2*c* (¾, ¾, *z*)]	0.41374(5)	0.41333(9)	0.4140(2)
	U_{iso} × 100 / Å^2	0.69(2)	0.45(3)	-0.34(5)
V	[2*c* (¼, ¼, *z*)]	0.30804(9)	0.3074(2)	0.3096(3)
	U_{iso} × 100 / Å^2	0.52(3)	0.34(4)	-0.33(9)
	f_{occ}	1.000(3)		
Fe	[2*a* (¼, ¾, 0)]			
	U_{iso} × 100 / Å^2	0.53(2)	0.45(3)	-0.44(6)
	f_{occ}	1.000(3)		
As	[2*a* (¼, ¼, *z*)]	0.08939(6)	0.0897(1)	0.0903(2)
	U_{iso} × 100 / Å^2	0.47(2)	0.36(3)	-0.74(5)
O1	[4*f* (¼, ¾, *z*)]	0.2945(2)	0.2955(3)	0.2934(6)
	U_{iso} × 100 / Å^2	0.60(7)	0.40(9)	-0.4(2)
	f_{occ}	0.975(5)		
O2	[2*c* (¼, ¼, *z*)]	0.4293(3)	0.4265(4)	0.4283(7)
	U_{iso} × 100 / Å^2	0.9(1)	1.6(2)	-0.9(3)
	f_{occ}	1.00(1)		
Bond lengths and angles:				
Fe-As / Å		2.4179(6)	2.4179(9)	2.418(2)
Fe-Fe / Å		2.78404(1)	2.78269(1)	2.77898(1)
V-O_{ax} / Å		1.903(4)	1.871(7)	1.85(1)
V-O_{eq} / Å		1.9798(3)	1.9759(4)	1.981(1)
α As-Fe-As / °		109.01(4)	108.94(6)	108.7(1)
β As-Fe-As / °		109.70(2)	109.74(3)	109.86(6)

Table 5.2 Results of refinement of Sr_2VO_3FeAs against SXPRD data at 5 K and RT

5.2.3.3 ID31 room temperature

Room temperature synchrotron powder X-ray diffraction data was also collected on the ID31 beamline at the ESRF, on an additional sample of Sr_2VO_3FeAs. The major advantage of the ID31 diffractometer over I11 is that the incident beam has a higher flux at shorter wavelengths than those available to I11, which should allow for more accurate atomic parameters to be determined. This Sr_2VO_3FeAs (AJC127) sample was loaded into a 0.7 mm diameter borosilicate glass capillary and measured at room temperature using 0.39987 Å X-rays. A refinement of Sr_2VO_3FeAs (AJC127) against ID31 data in the range 2-30 ° 2θ was performed using the TOPAS Academic software. Refined structural parameters are listed in Table 5.2 and instrumental parameters include those to model background, scale factors, profile and Stephens' model of asymmetric broadening.[12] Sr_2VO_4, $Sr_3V_2O_7$, $SrFe_2As_2$ and FeAs impurity phases were included in the refinement and found to be present at levels of 5.60, 2.99, 2.82 and 3.85 wt %, respectively. The Rietveld

fit of Sr_2VO_3FeAs to room temperature data is depicted in Figure 5.11 and shows very good agreement between the calculated model and the observed data.

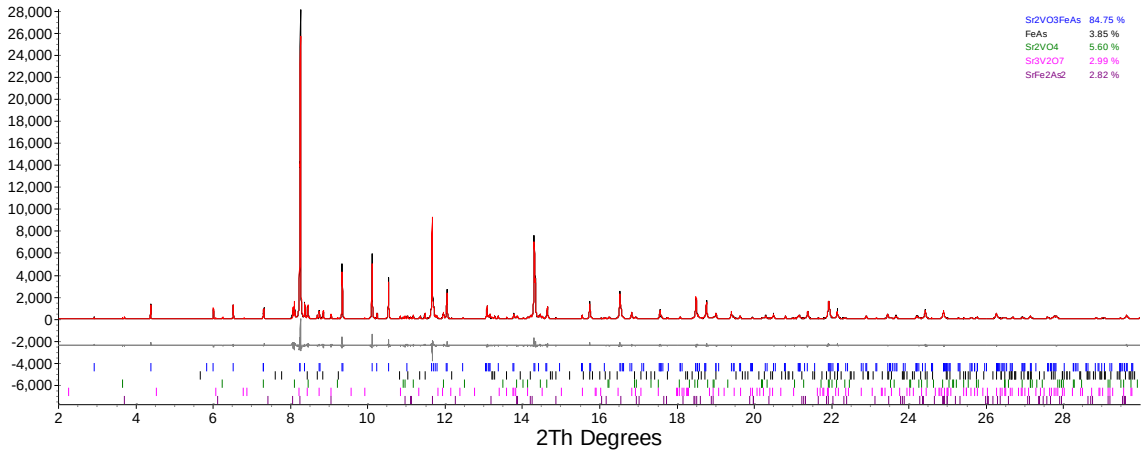

Figure 5.11 Rietveld fit to RT Sr_2VO_3FeAs synchrotron X-ray powder diffraction data

The possibility of non-stoichiometry in Sr_2VO_3FeAs was also addressed by refinement of site occupancies. Refinement of the Fe occupancy on the [2*a* (¼, ¾, 0)] site and V occupancy on the [2*c* (¼, ¼, ~0.308)] site against this data indicate that both sites are fully occupied. However the similarity in the X-ray scattering factors of Fe and V makes assessment of the level of Fe/V mixing difficult to quantify with X-ray data. In the following section room temperature PND measurements on Sr_2VO_3FeAs are made, utilising the large difference in the coherent neutron scattering lengths of V (-0.4 fm) and Fe (9.9 fm), to unequivocally assess the extent of Fe/V mixing.

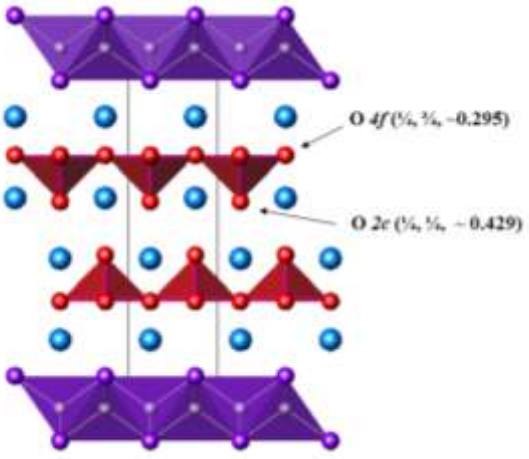

Figure 5.12 Sr_2VO_3FeAs crystal structure with labelled oxide positions.

The possibility of oxygen deficiencies in $Sr_2VO_{3-\delta}FeAs$ have also been suggested by Wen *et al* as an explanation for the observed superconductivity in this "undoped" material. This hypothesis certainly has precedence in Fe-based superconductors with critical temperatures

in *Ln*$FeAsO_{1-y}$ (*Ln* = Nd, Sm, Gd, Tb and Dy) raised as high as 50 K through the nominal electron doping of this 1111 family via the introduction of oxide vacancies.[13] The occupancy on both the [4*f* (¼, ¾, 0.295)] and [2*c* (¼, ¼, 0.429)] oxide sites were therefore refined and found to have fractional occupancies of 0.975(5) and 1.00(1), respectively. This would appear to suggest a small oxygen deficiency on the 4*f* site from refinement against PXRD data, which equates to 0.05(1) oxide vacancies for every iron, implying electron doping.

5.2.4 Powder neutron diffraction measurements

5.2.4.1 HRPD

To further investigate the stoichiometry of Sr_2VO_3FeAs and assess the extent of Fe/V mixing in this material, powder neutron diffraction measurements were performed on the HRPD instrument at ISIS. The high resolution of HRPD over wide *d*-ranges in the 168 ° backscattered bank was also exploited to investigate the possibility of a low temperature structural distortion.

A 3 g sample (AJC160) of Sr_2VO_3FeAs was prepared for this experiment according to the procedure described in 5.2.1. This sample was loaded into a cylindrical vanadium can and sealed with indium wire in an argon filled glove box. A room temperature data collection was made for a total integrated proton current of 94 μAh. The sample was then loaded into a CCR and cooled to 20 K, at which temperature data was collected for a total integrated proton current of 104 μAh. A Rietveld refinement was then performed against room temperature data collected in the backscattered 168 ° and 90 ° banks using the TOPAS academic suite. Refined variables include the atomic parameters described in Table 5.3 and parameters to model the background, absorption, 2θ zero error, ToF calibration in 90 ° bank, scale factors and profile coefficients. $Sr_3V_2O_7$ and FeAs impurity phases were also included and found to be present at 5.5 and 4.5 wt %, respectively. The Rietveld fit of Sr_2VO_3FeAs to the room temperature data collected in the 168 ° and 90 ° banks are depicted in Figure 5.13 and both show good agreement between the observed data and refined model.

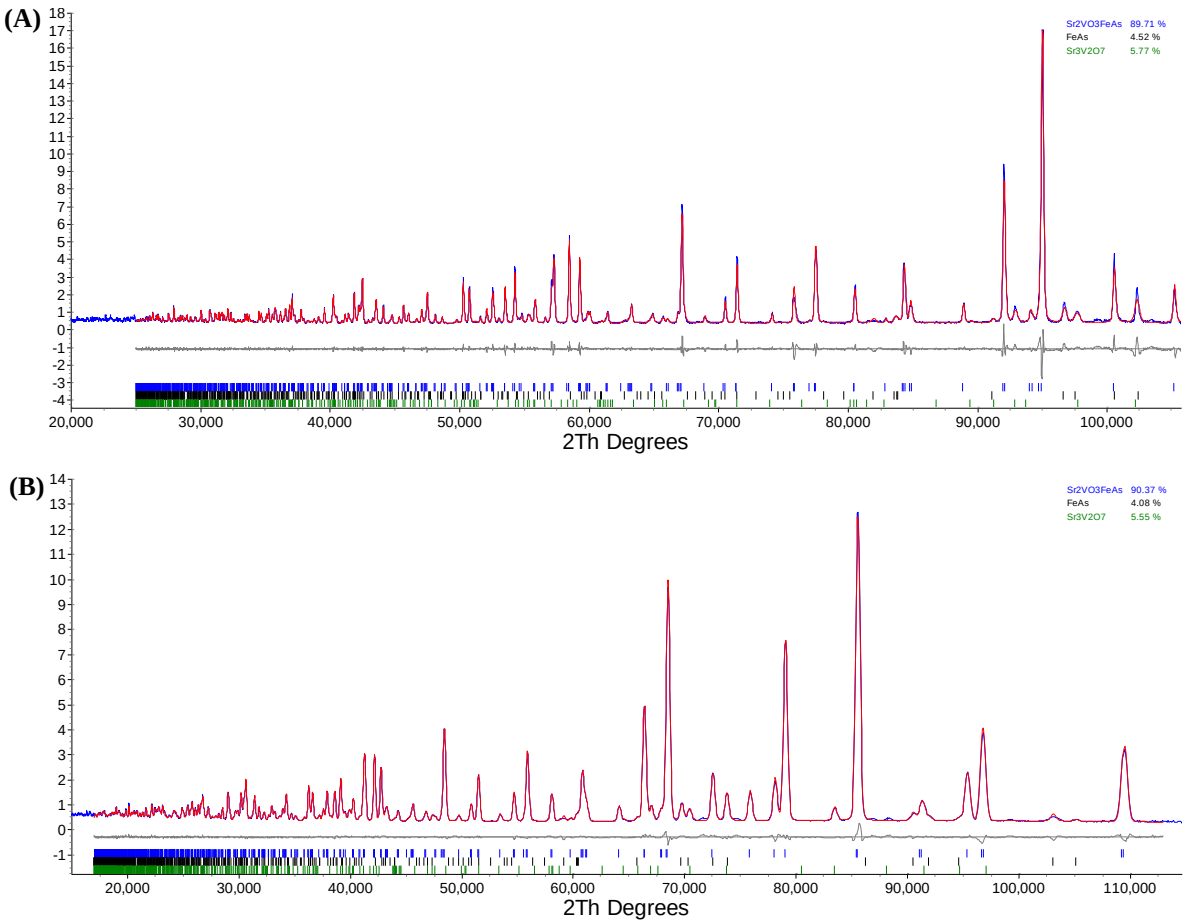

Figure 5.13 Rietveld fit to 168 ° (A) and 90 ° (B) PND data banks for Sr_2VO_3FeAs (AJC160) at RT

As shown in the previous section, refinement of the occupancies of both the Fe [2*a* (¼, ¾, 0)] and V [2*c* (¼, ¼, ~0.308)] sites against synchrotron X-ray powder diffraction data, indicates that both positions are fully occupied. It is assumed that this is also the case in this sample (AJC160), and here the extent to which Fe and V mix is investigated utilising the large difference in the coherent neutron scattering lengths of V (-0.4 fm) and Fe (9.9 fm). Rietveld refinement against PND data, employing a $f_{occV} + f_{occFe} = 1$ constraint on the [2c (¼, ¼, 0.309)] site, does not suggest the presence of any Fe, within the uncertainty of the refinement of about 0.2 %. However, similar analysis on the iron [2*a* (¼, ¾, 0)] site indicates the presence of V 1.8(3) % at this position, implying a small degree of V substitution in the FeAs layers. The effect of extrinsic V substitution in Sr_2VO_3FeAs has been investigated by Johrendt *et al.*[7] They concluded from a combination of PXRD, PND and magnetometry measurements that as little as 7 % V substituted on the Fe site is sufficient to completely suppress superconductivity. Furthermore it was suggested that the scattered reports of T_c in Sr_2VO_3FeAs may be ascribed to varying degrees of intrinsic V doping, which would be very difficult to detect without PND studies. However, this observation does not account for the superconductivity in Sr_2VO_3FeAs. The

occupancies on both the [4*f* (¼, ¾, 0.295)] and [2*c* (¼, ¼, 0.429)] oxide sites were therefore refined to further investigate the possibility of oxide vacancies electron-doping the iron layer. The results of this refinement do not indicate any oxide deficiencies on either site within the uncertainty of the refinement of about 0.5 %. This result is in contrast to that from refinement against ID31 data. However, scattering in X-ray diffraction experiments on Sr_2VO_3FeAs will be dominated by the heavier elements and scattering from the oxide sites will contribute less to the observed Bragg intensity. By contrast the coherent neutron scattering lengths of oxygen is 5.803 fm, comparable to those of Fe and Sr, such that it contributes significantly more to the diffraction pattern. The oxide atomic parameters from refinement against PND data should therefore be more reliable than those from refinement against X-ray diffraction data. Hence it is suggested, from refinement against HRPD data, that no oxide vacancies are present in Sr_2VO_3FeAs.

Temperature		(AJC160) 293 K	(AJC160) 20 K
	a / Å	3.9313(2)	3.9268(4)
	c / Å	15.6895(8)	15.605(2)
	Cell volume / Å	242.49(3)	240.605(2)
	χ^2	4.268	2.787
	$_wR_p$	6.6925	5.4850
Atomic parameters:			
V	[2*c* (¼, ¼, *z*)]	0.304(1)	0.309(1)
	U_{11}, U_{33} × 100 / Å^2	0.0(5), 2(1)	0.0(7), 0(1)
	V_{occ}: Fe_{occ}	1.000(2):0.000(2)	1.000(2):0.000(2)
Fe	[2*a* (¼, ¾, 0)]		
	U_{11}, U_{33} × 100 / Å^2	0.68(3), 0.89(5)	0.34(4), 0.78(7)
	Fe_{occ} : V_{occ}	0.982(3): 0.018(3)	0.982(3): 0.018(3)
Sr(1)	[2*c* (¾,¾, *z*)]	0.19031(7)	0.1897(1)
	U_{11}, U_{33} × 100 / Å^2	0.69(3), 0.89(5)	0.66(4), 0.84(8)
Sr(2)	[2*c* (¾,¾, *z*)]	0.41397(7)	0.4126(1)
	U_{11}, U_{33} × 100 / Å^2	1.14(4), 0.93(6)	0.89(5), 0.75(8)
As	[2*c* (¼, ¼, *z*)]	0.08963(8)	0.0894(1)
	U_{11}, U_{33} × 100 / Å^2	0.70(4), 1.18(7)	0.53(5), 0.93(9)
O(1)	[4*f* (¼, ¾, *z*)]	0.29333(6)	0.29298(7)
	U_{11}, U_{22}, U_{33} × 100 / Å^2	0.77(5), 0.72(4), 1.35(6)	0.71(7), 0.79(6), 0.97(7)
	O_{occ}	1.000(6)	1.000(6)
O(2)	[2*c* (¼, ¼, *z*)]	0.43002(7)	0.43048(9)
	U_{11}, U_{33} × 100 / Å^2	1.40(6), 0.80(8)	1.08(7), 0.4(1)
	O_{occ}	1.000(5)	1.000(5)
Bond lengths and angles:			
	Fe-Fe / Å	2.7799(1)	2.7767(1)
	Fe-As / Å	2.4169(7)	2.409(1)
	α As-Fe-As / °	108.84(5)	109.18(6)
	β As-Fe-As / °	109.79(2)	109.62(3)

Table 5.3 Results of refinement against HRPD data for Sr_2VO_3FeAs at room temperature and 20 K

A Rietveld refinement using a tetragonal model of Sr_2VO_3FeAs was also performed against 20 K data from the 168 ° and 90 ° degree banks. The refined structural parameters were the same as those for the room data and are listed in Table 5.3. The Rietveld fit to

both detector banks are presented in Figure 5.14. Inspection of these fits shows excellent agreement between the observed data and calculated model in the 90 ° bank, slight discrepancies in the backscattered bank are attribute to poor modelling of peak shapes rather than a lowering of the symmetry to an orthorhombic cell.

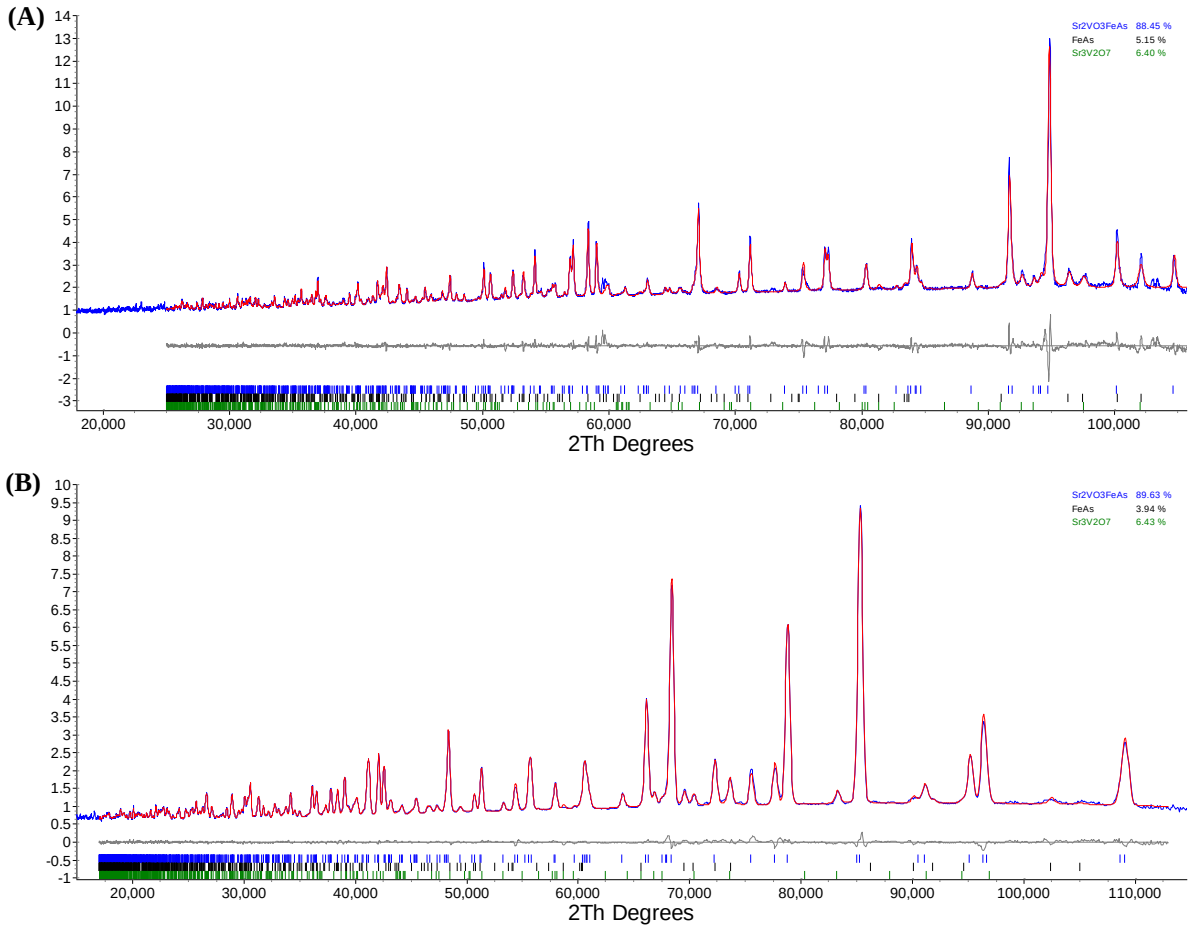

Figure 5.14 Rietveld fit to 168 ° (A) and 90 ° (B) PND data banks for Sr_2VO_3FeAs at 20 K

However, to assess the possibility of peak broadening, that would imply a small degree of orthorhombicity in Sr_2VO_3FeAs, the FWHM of the (200)/(020) reflections were modelled in both the room temperature and 20 K data. This was achieved by performing a Pawley fit to this reflection in the ToF range 94500 – 95500 μsec as shown in Figure 5.15. In the 20 K data set the fitted ToF range had to be reduced slightly to 94600 μsec, such that the entire peak was not being modelled, as the (008) Bragg reflection of Sr_2VO_3FeAs forms a slight shoulder to the (200). However, this is unlikely to have a significant effect on the refined values of the FWHM at 293 and 20 K which are 0.0024(1) and 0.0028(2) Å, respectively. Though the FWHM from the 20 K is slightly greater than that of the room temperature data, these values are equal within 3σ, indicating that this small degree of peak broadening is not statistically significant.

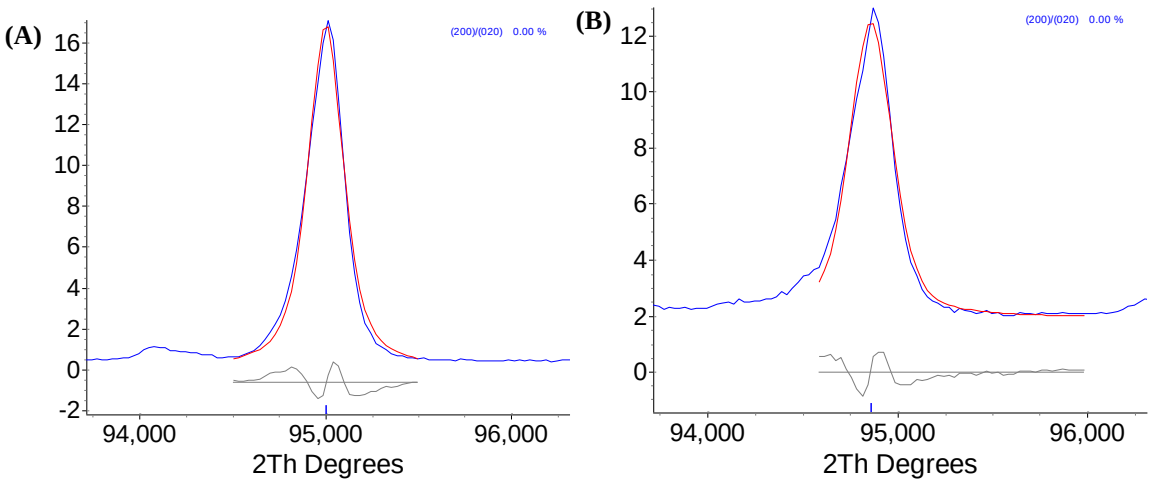

Figure 5.15 Modelling of the FWHM of the (200) reflection by a Pawley fit to HRPD data at (A) 293 and (B) 20 K.

Data from the low angle 30 ° bank was not included in these refinements since the signal to noise ratio in them is quite poor and no additional low temperature magnetic Bragg reflections were observed. However a recent PND study on Sr_2VO_3FeAs has suggested possible incommensurate magnetic ordering on the V sub-lattice with a $\boldsymbol{k}$ = (0, 0, 0.306) propagation vector from very weak reflections in a 4 K powder neutron diffraction measurement. The liquid methane moderator (100 K) used on HRPD means that a lower flux of long wavelength neutrons are received on this instrument. HRPD is therefore not the most suitable powder neutron diffractometer on which to investigate the possibility of low-*Q* magnetic reflections.

5.2.4.2 D2B measurements

The D2B diffractometer at the ILL reactor source, in contrast to HRPD, offers a much higher flux of cold neutrons which means that this instrument is superior for investigating possible long range magnetic ordering. A 3 g sample of Sr_2VO_3FeAs (AJC148) was therefore loaded into a 6 mm diameter cylindrical vanadium can and measured in the range $5\ ° \leq 2\theta \leq 150\ °$ using 1.59 Å neutrons at room temperature (293 K) and 5 K inside an Oxford Instruments cryostat. The full data sets collected on Sr_2VO_3FeAs at 293 K and 5 K are shown in Figure 5.16 along with a magnification of the low angle region.

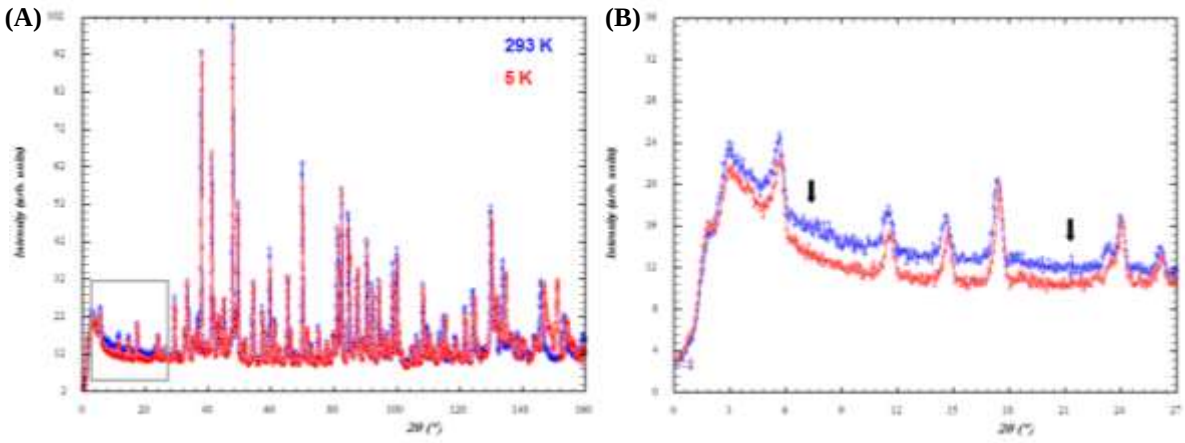

Figure 5.16 (A) Comparison of D2B data collected on Sr_2VO_3FeAs at room temperature and 5 K. (B) Magnification of the low angle region.

From inspection of the low angle region of these diffraction patterns, no additional reflections are observed above background in the 5 K data set. The $\boldsymbol{k}$ = (0, 0, 0.306) propagation vector proposed by Johrendt *et al*, is based on very weak satellites of the (00*l*) reflections and would appear at 7.36 ° and 21.1 ° 2θ in these measurements. The absence of any such magnetic Bragg reflections suggests that long range magnetic order in Sr_2VO_3FeAs is prevented by magnetic frustration or the localised moments on the V or Fe sites are extremely small, indicating that the V and Fe 3*d* electrons are itinerant. Further treatment of this data is discussed chapter 6.

5.2.5 μSR measurements

In order to further probe the magnetic properties of Sr_2VO_3FeAs (AJC101), μSR experiments were conducted by collaborators in the group of Prof. Stephen Blundell at the Paul Scherrer Institut. μSR is used here as a direct local probe of internal fields in Sr_2VO_3FeAs as a function of temperature. In a μSR experiment, a beam of spin-polarized positive muons are implanted into the sample, where they precess in the local field at their stopping sites before decaying into positrons and neutrinos after a mean lifetime of 2.2 μs. Due to parity violation in this weak decay, positrons are emitted preferentially along the instantaneous spin direction at the moment of decay, and this allows the time evolution of the muon spins, which give information about the internal field structure, to be tracked.[14] Figure 5.17 shows the so-called "Asymmetry spectrum" of Sr_2VO_3FeAs obtained in a μSR experiment carried out in zero applied field at 1.5 K. The asymmetry is the normalised difference in positron counts recorded by detectors placed in front of and behind the sample relative to the beam direction.

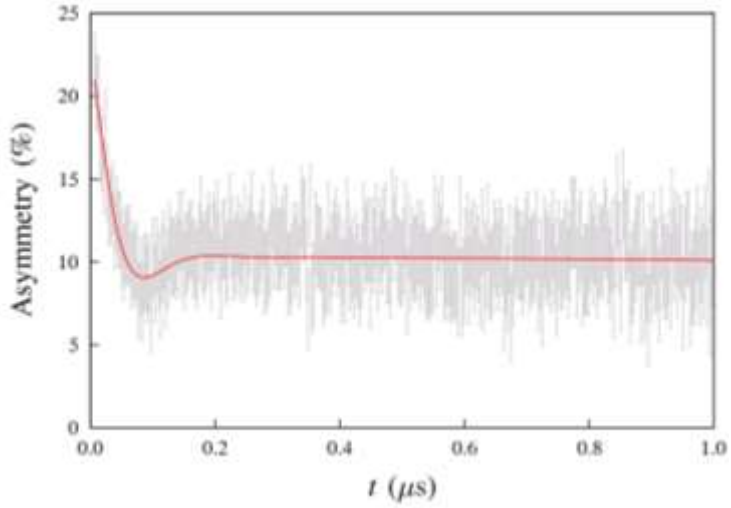

Figure 5.17 Zero-field muon asymmetry spectrum for Sr_2VO_3FeAs at 1.5 K

What can be clearly seen is a heavily damped oscillation at early times superimposed on a slowly varying background. Samples displaying long-range commensurate magnetic order show strong oscillations with minimal damping,[15] as crystallographically equivalent muons experience the same local field. The heavy damping observed here indicates a significantly broader field distribution, possibly due to incommensurate order, as has been suggested elsewhere from neutron scattering experiments.[7] The data has been fitted to the following function

$$A(t) = A_1 \cos(\nu t) e^{-\lambda t} + A_2 G(t) \qquad eqn5.1$$

where A_1 and A_2 are the amplitudes of the damped oscillation (frequency ν, damping factor λ) and a Gaussian background function *G(t)*, due to static nuclear dipole moments. The temperature dependence of the background amplitude A_2 is shown in Figure 5.18, and it is apparent that the magnetic signal is established between 35K and 45K, as the background contribution is reduced. Similar behaviour has been reported by Uemura *et al* to support these findings.[16]

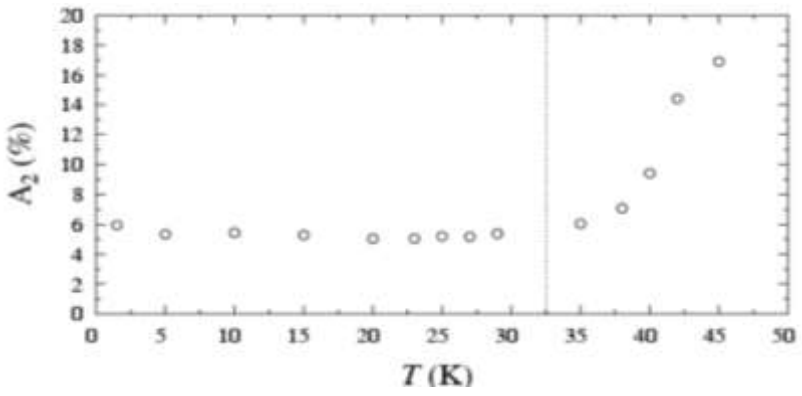

Figure 5.18 Temperature dependence of background amplitude for Sr_2VO_3FeAs.

5.2.6 Structural comparisons

The results of refinement against powder neutron diffraction data discussed in section 5.2.5 do not indicate any significant non-stoichiometry in Sr_2VO_3FeAs. An alternative explanation is therefore sought to rationalise the observed superconductivity in this material. A useful place to start is to compare the structure of Sr_2VO_3FeAs with that of other members of the Sr_2MO_3FeAs family.

The ionic radius of V^{3+} (0.640 Å) is intermediate between that of Sc^{3+} (0.745 Å) and Cr^{3+} (0.615 Å), hence based purely on an argument of steric grounds one would expect the lattice parameters of Sr_2VO_3FeAs to be intermediate between those of Sr_2CrO_3FeAs and Sr_2ScO_3FeAs. Indeed strong positive correlation is seen between the *a* lattice parameter and the ionic radii of M^{3+}, as shown in Figure 5.19. However, no such trend is seen in the variation of the *c* cell parameter of Sr_2MO_3FeAs materials with the ionic radii of M^{3+} and the plot in Figure 5.19 would appear to indicate that either the *c* cell parameter of Sr_2CrO_3FeAs is anomalously large or that the *c* cell parameter of Sr_2VO_3FeAs is anomalously small. Assuming that the latter is the case, one must explain why the interplanar Fe-Fe distance in Sr_2VO_3FeAs has decreased relative to Sr_2CrO_3FeAs, whilst the intra Fe-Fe distance has increased. To rationalise this observation it is instructive to consider how the Fe-As, *M*-As and *M*-O bond distances vary with the ionic radii of M^{3+} in Sr_2MO_3FeAs materials (Figure 5.20).

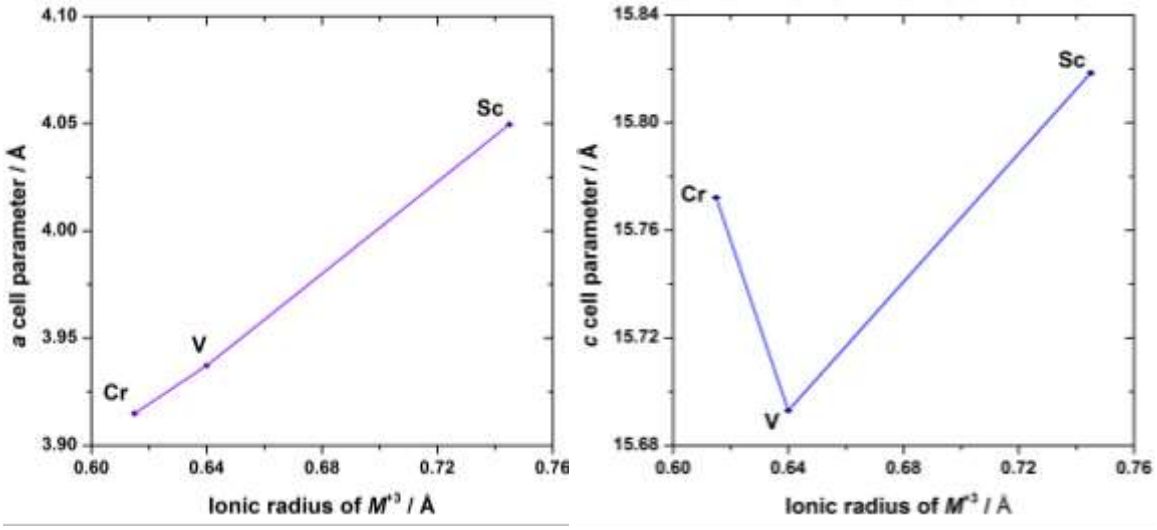

Figure 5.19 Variation in lattice parameters of Sr_2MO_3FeAs materials (*M* = Sc, V, Cr) with the ionic radii of M^{3+}.

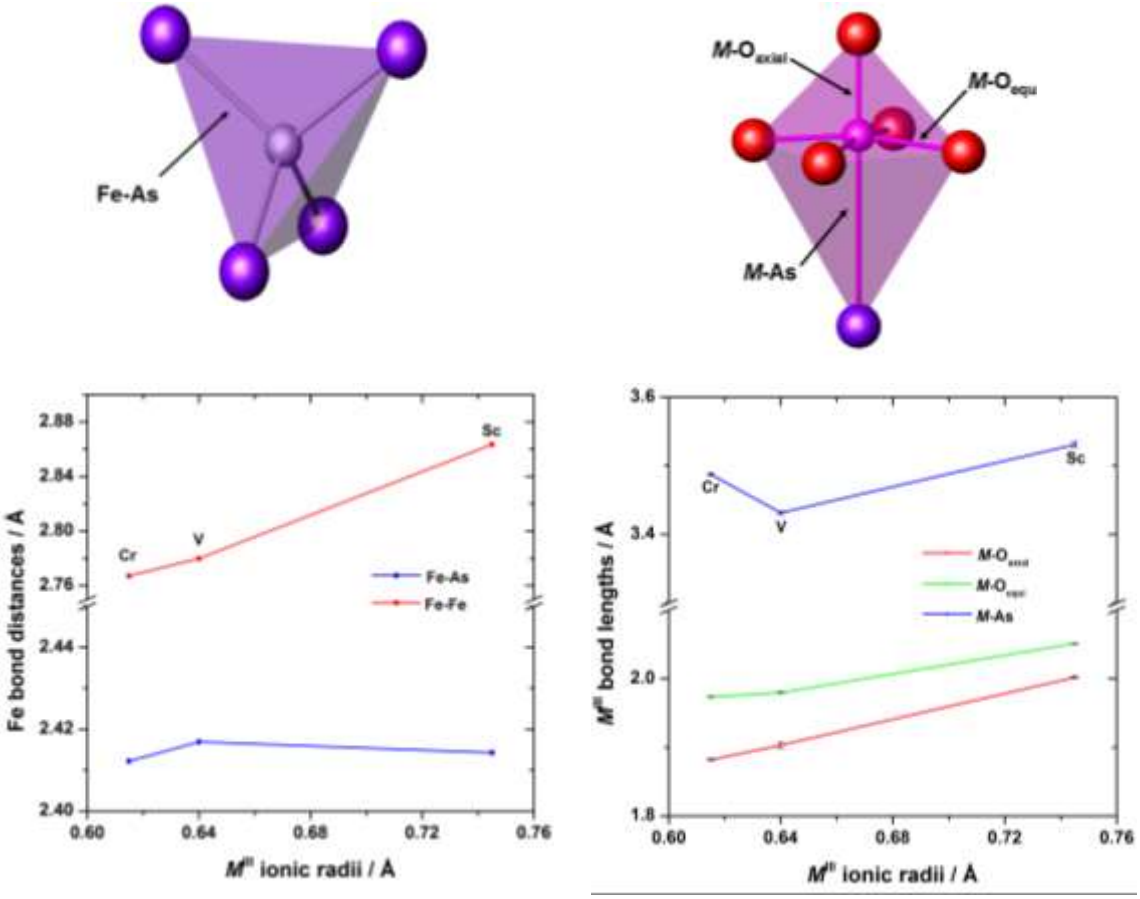

Figure 5.20 Comparison of the Fe-Fe, Fe-As, *M*-As, *M*-O_{ax} and *M*-O_{eq} bond lengths in Sr_2VO_3FeAs

From these plots it is clear that the V-As bond length in Sr_2VO_3FeAs is anomalously short and more surprisingly that the Fe-As bond length is longer than anticipated, relative to those in Sr_2CrO_3FeAs and Sr_2ScO_3FeAs. A plausible explanation that would account for both of these observations can be argued from consideration of mixed valence vanadium. In Sr_2CrO_3FeAs and Sr_2ScO_3FeAs the +3 oxidation is anticipated for both Cr and Sc, however if in Sr_2VO_3FeAs we in fact have a mixture of V^{+3}/V^{+4} this would tend to contract the coordination environment around vanadium, decreasing the V-As distance (Figure 5.20). A mixture of V^{3+} and V^{4+} would also have the effect of donating electrons into antibonding Fe-As and Fe-Fe states,[6] thus leading to the observed elongation of the Fe-As bond length and superconductivity.

Such a theory of intrinsic electron-doping of the FeAs layers from mixed valence V^{3+}/V^{4+} is tested by investigating the valence state of vanadium through bond valence sum (BVS) calculations and XANES measurements on both the Fe and V *K*-edges. BVS calculations allow the estimation of cation oxidation states (V_i) from valence bond parameters (r_0) and cation-anion bond distances (r_{ij}) as shown in equation 5.1, where $B = 0.37$.[17,18]

$$V_i = \sum_j \exp\left(\frac{r_0 - r_{ij}}{B}\right) \qquad \textit{eqn 5.1}$$

Bond valence sum analysis was performed on Sr_2VO_3FeAs using V-O and V-As bond lengths derived from refinement against synchrotron X-ray powder diffraction data collected on the ID31 beamline. The vanadium bond lengths from refinement against HRPD data were not used, since the short coherent neutron scattering length of vanadium (-0.382 fm) leads to a large uncertainty on the V *z* fractional coordinate. By way of comparison the valences of chromium in Sr_2CrO_3FeAs and scandium in Sr_2ScO_3FeAs were also calculated using bond lengths derived from refinement against PND data. The values obtained for the valence state of *M* are plotted against the ionic radii of the trivalent metals in Figure 5.21.

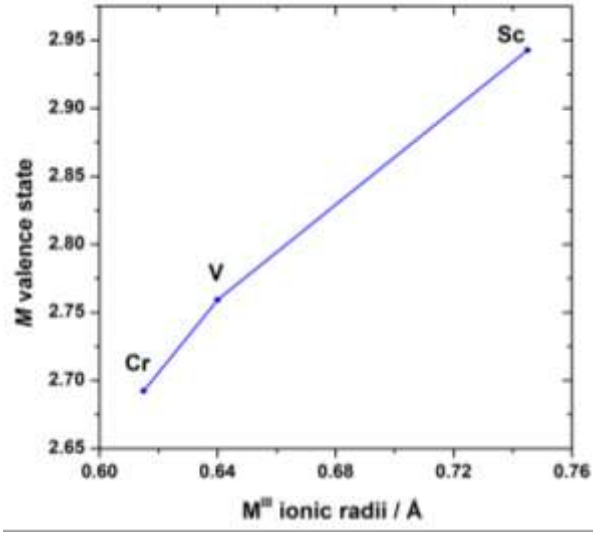

Figure 5.21 Variation of *M* valence and M^{III} ionic radii

These results would appear to indicate that V is not oxidised above the +3 oxidation state and if anything the valence of vanadium is seen to be lower than that of scandium in Sr_2ScO_3FeAs. However, trusting these estimates does require that r_0 values for *M*-O and *M*-As are well established. Furthermore BVS calculations are notoriously unreliable when applied to layered framework materials and systems in which there are few variable crystallographic parameters, as is the case here. In this instance they are far more useful as a relative tool for studying changes of the oxidation state of a given metal across an isostructural series of compounds. Additionally the oxidation of V^{3+} towards V^{4+} and accompanied reduction of Fe^{2+} will tend to exert opposing effects on the crystal structure of Sr_2VO_3FeAs, with vanadium contracting its coordination sphere, whilst the Fe-As bond length increases.

5.2.7 XANES measurements

The X-ray absorption spectra of the vanadium *K*-edge of Sr_2VO_3FeAs as well as those of reference samples $LaVO_3$ and $Sr_3V_2O_7$ were measured on the B18 beamline at the Diamond Light Source. A recent X-ray absorption study by Cao *et al* has estimated the vanadium valence of Sr_2VO_3FeAs to be +3.22 by making comparison of the characteristic absorption thresholds with those of binary vanadium oxides VO, V_2O_3, VO_2 and V_2O_5.[7] Here we use $LaV^{III}O_3$ and $Sr_3V_2{}^{IV}O_7$ as reference samples (synthesis described in appendix B), since they are examples of V^{3+} and V^{4+}, respectively, with coordination environments of vanadium which more closely resemble that of Sr_2VO_3FeAs. Normalized X-ray absorption spectra from the vanadium *K*-edge of Sr_2VO_3FeAs, $LaVO_3$ and $Sr_3V_2O_7$ phases are plotted in Figure 5.22, along with the derivative of the absorption spectra.

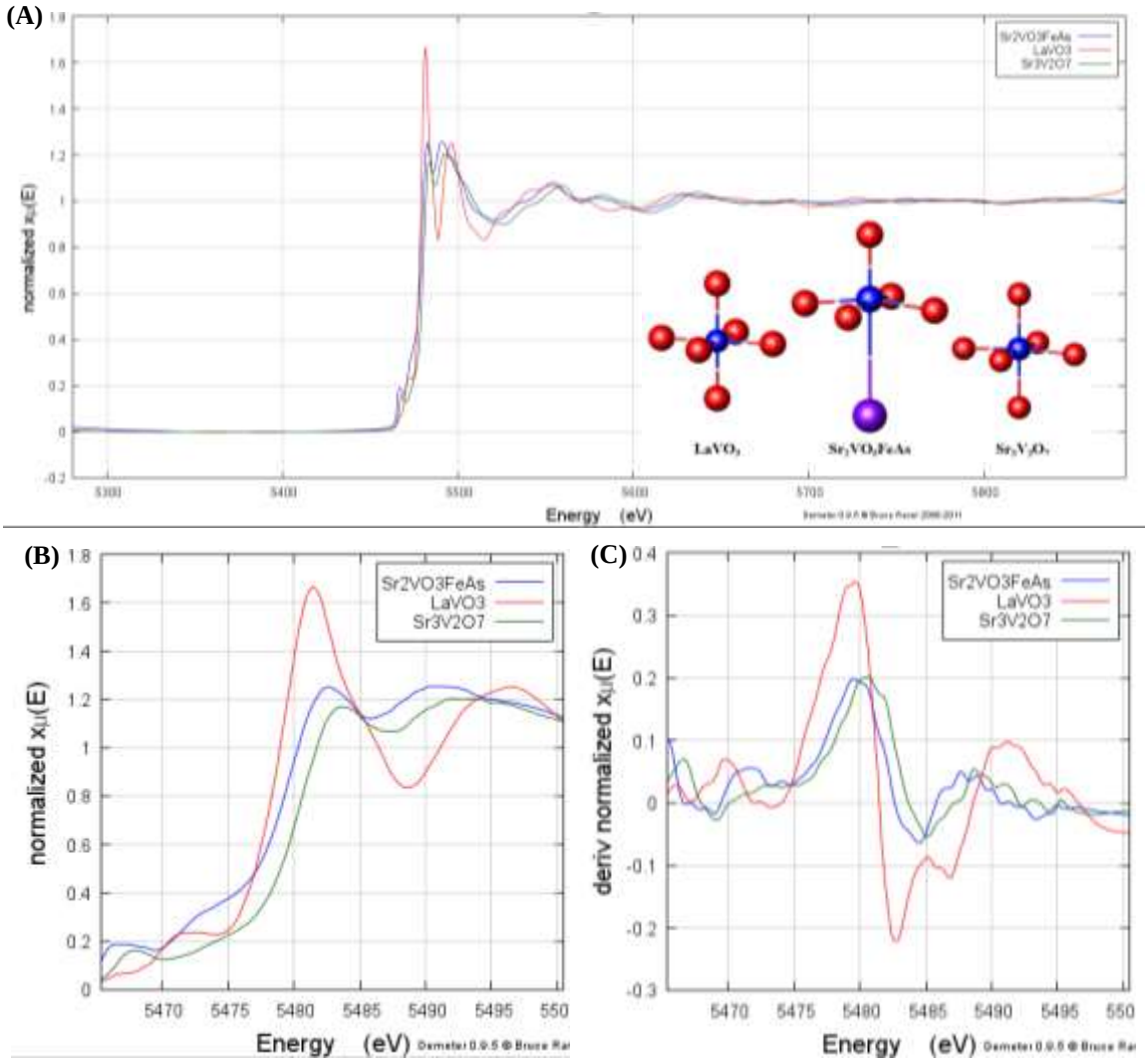

Figure 5.22 (A) Normalised Vanadium *K*-edge of Sr_2VO_3FeAs (blue), $LaVO_3$ (red) and $Sr_3V_2O_7$ (green) Inset shows coordination environments of V in Sr_2VO_3FeAs and reference samples. (B) Magnification of absorption edge. (C) Derivative.

The first obvious feature in the XANES spectra is the appearance of a pre-edge feature at approximately 5467 eV. This absorption feature is assigned to the 1*s* → 3*d* transition, which is strictly dipole forbidden in $LaVO_3$ due to the initial 1*s* gerade state and inversion centre present in the regularly octahedral VO_6 units. Sr_2VO_3FeAs and $Sr_3V_2O_7$ spectra by contrast do show a weak pre-edge feature, since the distortion of the VO_5X environment away from that of a regular octahedron, removes the inversion centre making the transition dipole allowed.

Another point to note is that the pre-edge feature in Sr_2VO_3FeAs is at a slightly lower energy than that in $Sr_3V_2O_7$ which, assuming the validity of Kunzl's law to these systems, indicates that the valence of vanadium in Sr_2VO_3FeAs is less than +4. Additional low energy shoulders are attributed to 1*s* → 4*p* 'shakedown' transitions whilst the main edge feature in all three samples corresponds to the dipole allowed 1*s* → 4*p* transition.[19]

Visual inspection of the V *K*-edge of Sr_2VO_3FeAs shows that it lies intermediate between those of $LaV^{III}O_3$ and $Sr_3V_2^{IV}O_7$, consistent with a mixed valence V as proposed by Cao *et al*.[10] The derivative of the absorption edge confirms this and estimates of the maxima in the derivative allow tentative energies to be estimated for the position absorption edges for $LaVO_3$, Sr_2VO_3FeAs and $Sr_3V_2O_7$ to be made at 5479.37, 5479.56 and 5480.70 eV, respectively. Assuming a linear relationship between the position of the absorption edge and the valence state of vanadium, the oxidation state of vanadium in Sr_2VO_3FeAs can be estimated to be +3.13(5). This indicates mixed valence vanadium V^{3+}/V^{4+}, consistent with the study by Cao *et al*.[10] However, the data are quite noisy, likely due to air scattering of the low energy of the X-rays required to study the vanadium *K*-edge, and the estimates of the position of vanadium are therefore subject to large errors.

Similar measurements were performed on the Fe *K*-edge of Sr_2VO_3FeAs, which are here compared with the Fe *K*-edges of the isostructural oxypnictides Sr_2CrO_3FeAs and Sr_2ScO_3FeAs (Figure 5.23). Both of these materials have been shown to be stoichiometric, with the *TM* metals in the oxide layer in the +3 oxidation state. This gives Fe a formal valence of +2 as in other 'undoped' iron-based superconductors. If Fe in Sr_2VO_3FeAs is intrinsically doped by electron transfer from mixed valence $V^{3+/4+}$, a shift in the Fe *K*-edge to lower energy relative to Sr_2CrO_3FeAs and Sr_2ScO_3FeAs would then be anticipated. Indeed a small shift in the position of the Sr_2VO_3FeAs Fe *K*-edge to lower energies is observed, relative to Sr_2CrO_3FeAs and Sr_2ScO_3FeAs. This indicates that iron is in a lower

oxidation state in Sr_2VO_3FeAs, consistent with electron doping. However, this shift is too small to quantitatively assess the degree of Fe reduction.

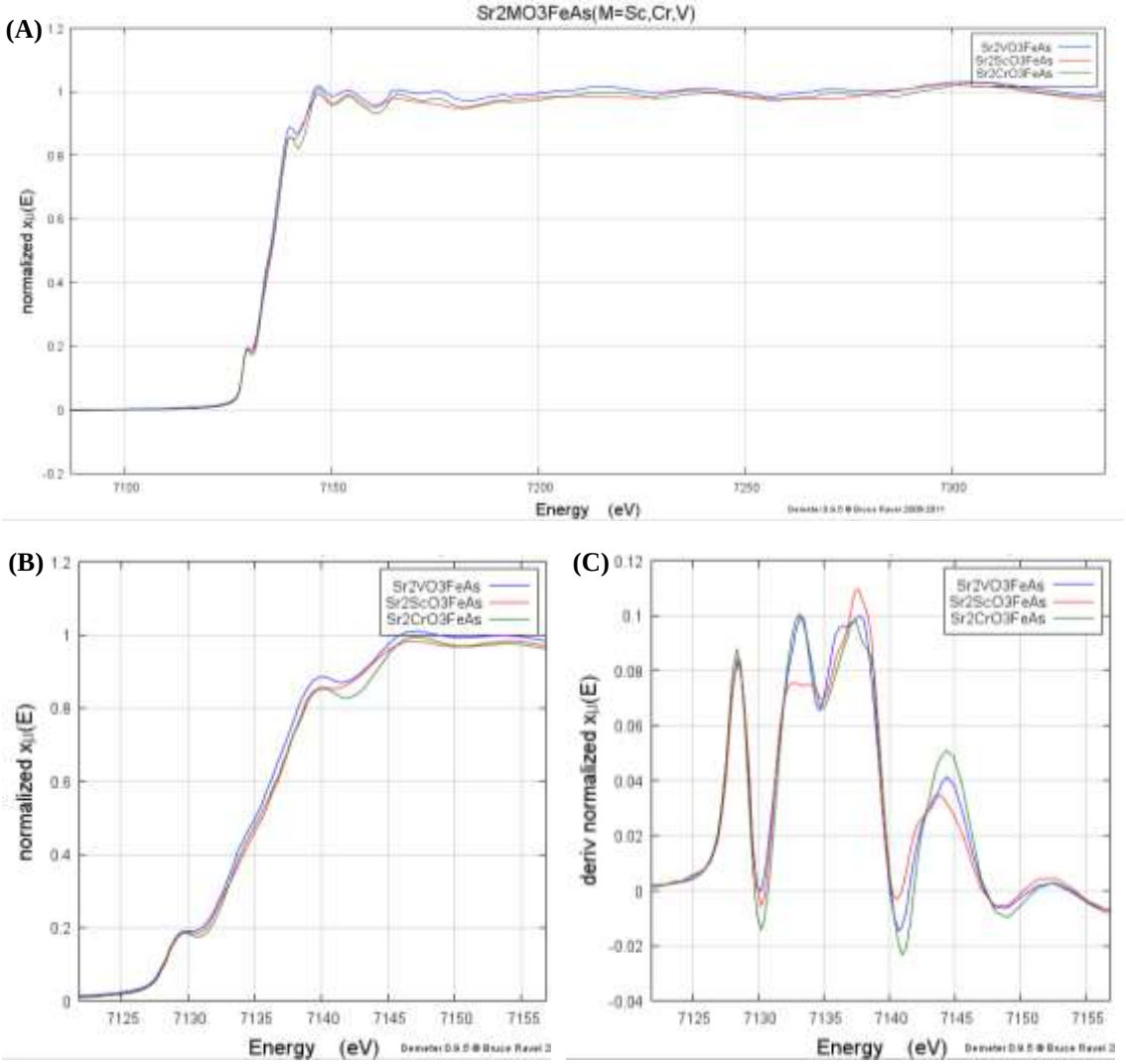

Figure 5.23 (A) Normalised iron *K*-edge of Sr_2VO_3FeAs (blue), Sr_2CrO_3FeAs (red) and Sr_2ScO_3FeAs (green). (B) Magnification of pre-edge and absorption edge. (C) Derivative.

5.3 Discussion

In summary, an improved synthetic route to Sr_2VO_3FeAs has been designed which minimises the levels of iron arsenide and strontium vanadium oxide impurity phases, to a level of less than 5 wt %. The stability of Sr_2VO_3FeAs is perhaps surprising, given that the cuprous sulphide analogue Sr_2VO_3CuS is not known. SQUID magnetometry measurements on 3 separate samples of Sr_2VO_3FeAs show reproducible magnetic properties, with superconducting transition temperatures ~ 25(1) K. Estimated superconducting volume fractions range between 31 – 35 %, values somewhat higher than those seen in Co doped Sr_2CrO_3FeAs, but still far from bulk.

As well as displaying superconductivity at low temperatures, Sr_2VO_3FeAs also exhibits magnetic transitions at ~ 150, 70 and 50 K as seen from magnetic susceptibility measurements. A ^{57}Fe Mössbauer study by Cao *et al* shows no evidence for signal splitting, as would be anticipated for Fe ordering, hence it is proposed that the observed behaviour originates from the V sub-lattice. The absence of even a weak signal from ordered Fe moments, as well as the retention of tetragonal symmetry at the low temperatures, from HRPD measurements at 20 K, is consistent both with the behaviour seen in isostructural Sr_2CrO_3FeAs/Sr_2ScO_3FeAs and the observation of superconductivity.

In order to examine the stoichiometry of Sr_2VO_3FeAs, synchrotron X-ray powder diffraction and powder neutron diffraction measurements were undertaken. The results of refinement against PND and SXPD data suggest a small degree of intrinsic V-doping on the Fe [2*a* (¼, ¾, 0)] site of approximately 1.8(3) %. This is a slightly lower level of mixing than is seen for Cr on the Fe site (2.5(1.1) %) in isostructural Sr_2CrO_3FeAs, which is presumably a result of the more electropositive nature of V giving a greater preference for the oxide layer. However, this is unlikely to account for the observed superconductivity in Sr_2VO_3FeAs since extrinsic V substitutions have been shown, by Johrendt *et al*, to be detrimental to superconductivity. The possibility of oxide deficiencies in $Sr_2VO_{3-\delta}FeAs$ was also explored utilising the large coherent neutron scattering length of O in refinement against PND data to unequivocally show that both oxide sites are fully occupied.

A comparison of the lattice parameters of Sr_2MO_3FeAs materials, shows Sr_2VO_3FeAs to exhibit an anomalously small *c* cell parameter, based on the size of the M^{3+} cations. This observation along with the anomalously long Fe-As bond length and short V-As bond length are rationalised in terms of partial oxidation of V^{3+} towards V^{4+}, which has the additional effect of donating electrons into Fe-As antibonding orbitals. In order to test this hypothesis, XANES measurements were performed on the vanadium and iron *K*-edges using the B18 beamline at the Diamond synchrotron. Measurements on the vanadium *K*-edge show the position of the absorption edge to be intermediate between that of $LaV^{III}O_3$ and $Sr_3V_2^{IV}O_7$. A tentative estimate of the vanadium oxidation state in Sr_2VO_3FeAs is made to be +3.13(5), assuming the validity of Kunzl's law to these systems. This suggests that the FeAs layers in Sr_2VO_3FeAs are internally electron-doped into the superconducting regime by mixed valence $V^{3+/4+}$. Comparative measurements on the Fe *K*-edge of Sr_2VO_3FeAs, Sr_2CrO_3FeAs and Sr_2ScO_3FeAs, show the position of the edge in the vanadium analogue to be at very slightly low energy than those of Sc and Cr

members, consistent with Fe reduction. The nature of the magnetic transitions observed from SQUID magnetometry measurements remain an unresolved issue. However possible ordering schemes have been discussed by Cao *et al*.[10] In the pseudo square pyramidal coordination environment, which V occupies in Sr_2VO_3FeAs, AFM superexchange interactions would be expected for d^2 V^{3+} with the electronic configuration $d_{yz}^{\uparrow}$ $d_{xz}^{\uparrow}$.

However, with mixed valence $V^{+3.13}$ as is proposed for Sr_2VO_3FeAs, double exchange would favour a ferromagnetic in-plane spin arrangement. An *A*-type magnetic structure with AFM coupling of in-plane FM spins was therefore proposed by Cao *et al*,[10] with a small ferromagnetic spin canting of the vanadium moments accounting for the weak ferromagnetism seen below 55 K. However the absence of magnetic Bragg reflections from low temperature PND measurements collected on D2B (5 K) and HRPD (20 K) suggest that the V 3*d* electrons are itinerant. Additionally μSR results show a very weakly damped oscillation below ~ 45 K, perhaps suggestive of incommensurate order, as proposed by Johrendt *et al*.[7] Clearly further variable temperature measurements are required to elucidate the true nature of the magnetic ordering transitions in Sr_2VO_3FeAs.

References

(1) Zhu, X. Y.; Han, F.; Mu, G.; Cheng, P.; Shen, B.; Zeng, B.; Wen, H. H. *Physical Review B* **2009**, *79*, 4.

(2) Ogino, H.; Katsura, Y.; Horii, S.; Kishio, K.; Shimoyama, J. *Superconductor Science & Technology* **2009**, *22*, 5.

(3) Tegel, M.; Hummel, F.; Lackner, S.; Schellenberg, I.; Pöttgen, R.; Johrendt, D. *Zeitschrift Fur Anorganische Und Allgemeine Chemie* **2009**, *635*, 2242-2248.

(4) Pitcher, M. J.; Lancaster, T.; Wright, J. D.; Franke, I.; Steele, A. J.; Baker, P. J.; Pratt, F. L.; Thomas, W. T.; Parker, D. R.; Blundell, S. J.; Clarke, S. J. *Journal of the American Chemical Society* **2010**, *132*, 10467-10476.

(5) Lee, K. W.; Pickett, W. E. *EPL (Europhysics Letters)* **2010**, *89*, 57008.

(6) Mazin, I. I. *Physical Review B* **2010**, *81*, 020507.

(7) Tegel, M.; Schmid, T.; Stürzer, T.; Egawa, M.; Su, Y.; Senyshyn, A.; Johrendt, D. *Physical Review B* **2010**, *82*, 140507.

(8) Pal, A.; Vajpayee, A.; Meena, R.; Kishan, H.; Awana, V. *Journal of Superconductivity and Novel Magnetism* **2009**, *22*, 619-621.

(9) A Pal, A. V., R. S. Meena, H. Kishan, V. P. S. Awana *J. Sup. & Novel Magnetisim* **2009**, *22*, 619.

(10) Cao, G.-H.; Ma, Z.; Wang, C.; Sun, Y.; Bao, J.; Jiang, S.; Luo, Y.; Feng, C.; Zhou, Y.; Xie, Z.; Hu, F.; Wei, S.; Nowik, I.; Felner, I.; Zhang, L.; Xu, Z. a.; Zhang, F.-C. *Physical Review B* **2010**, *82*, 104518.

(11) Straumanis, M. E.; Woodward, C. L. *Acta Crystallographica Section A* **1971**, *27*, 549-551.

(12) Stephens, P. *Journal of Applied Crystallography* **1999**, *32*, 281-289.

(13) Miyazawa, K.; Kihou, K.; Shirage, P. M.; Lee, C.-H.; Kito, H.; Eisaki, H.; Iyo, A. *Journal of the Physical Society of Japan* **2009**, *78*, 034712.

(14) Blundell, S. J. *Contemporary Physics* **1999**, *40*, 175-192.

(15) Wright, J. D.; Lancaster, T.; Franke, I.; Steele, A. J.; Möller, J. S.; Pitcher, M. J.; Corkett, A. J.; Parker, D. R.; Free, D. G.; Pratt, F. L.; Baker, P. J.; Clarke, S. J.; Blundell, S. J. *Physical Review B* **2012**, *85*, 054503.

(16) Munevar, J.; Sánchez, D. R.; Alzamora, M.; Baggio-Saitovitch, E.; Carlo, J. P.; Goko, T.; Aczel, A. A.; Williams, T. J.; Luke, G. M.; Wen, H.-H.; Zhu, X.; Han, F.; Uemura, Y. J. *Physical Review B* **2011**, *84*, 024527.

(17) Brese, N. E.; O'Keeffe, M. *Acta Crystallographica Section B* **1991**, *47*, 192-197.

(18) Brown, I. D.; Altermatt, D. *Acta Crystallographica Section B* **1985**, *41*, 244-247.

(19) Wong, J.; Lytle, F. W.; Messmer, R. P.; Maylotte, D. H. *Physical Review B* **1984**, *30*, 5596-5610.

6. Aliovalent and Isovalent substitutions in Sr_2VO_3FeAs

6.1 Introduction

In chapter 5 it was shown that Sr_2VO_3FeAs appears to be an internally electron-doped superconductor in which mixed valence vanadium (V^{3+}/V^{4+}) in the oxide layer donates electrons to the FeAs layer. In this chapter aliovalent and isovalent substitutions are undertaken on a variety of different crystallographic sites in an attempt to optimise the superconducting properties of this material. The chemical substitutions that will be discussed in this chapter are summarised in Figure 6.1.

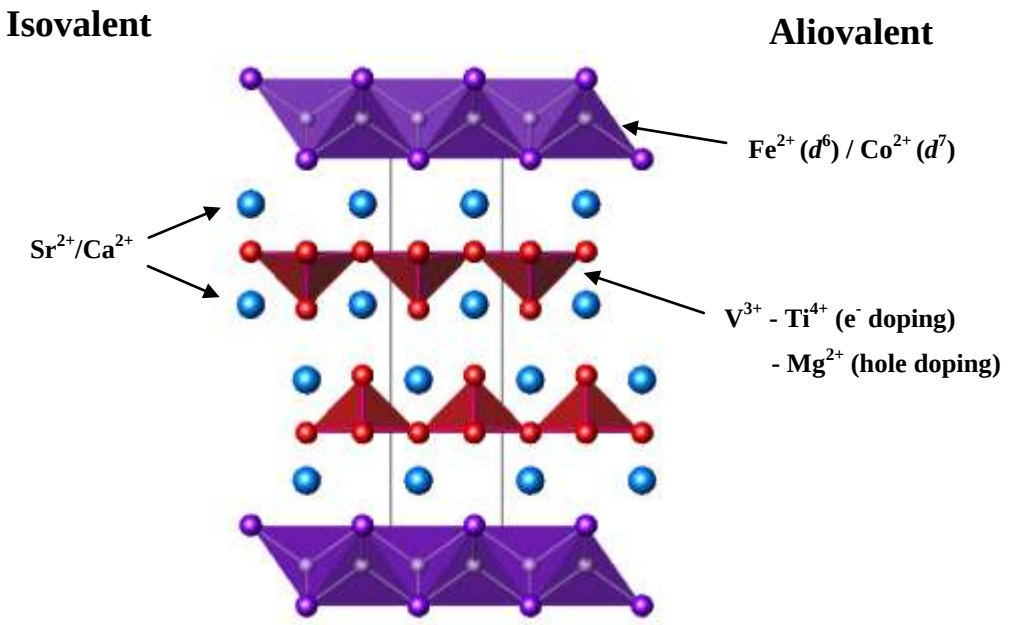

Figure 6.1 Summary of aliovalent and isovalent substitutions in Sr_2VO_3FeAs.

6.2 Aliovalent substitutions

6.2.1 $Sr_2VO_3Fe_{1-x}Co_xAs$ materials

In chapter 4 cobalt substitution on the iron site in Sr_2CrO_3FeAs was shown to be a successful electron-doping strategy. In this chapter it is investigated if similar substitutions in Sr_2VO_3FeAs can be made to influence the superconducting properties of this material.

6.2.1.1 Experimental

$Sr_2VO_3Fe_{1-x}Co_xAs$ with nominal Co doping levels of x = 0.05, 0.1, 0.15, 0.2 were synthesized on a 1 g scale by annealing stoichiometric mixtures of SrO (prepared by the

thermal decomposition of $SrCO_3$), V (Alfa 99.988%), Fe_2O_3 (Alfa 99.998%), Fe (Alfa 99.998%), Co (Alfa 99.998%) and As (Alfa 99.999%) according to *eqn6.1*.

$$2\ SrO + V + \tfrac{1}{3}\ Fe_2O_3 + (\tfrac{1}{3} - x)\ Fe + x\ Co + As \rightarrow Sr_2VO_3Fe_{1-x}Co_xAs \qquad eqn6.1$$

A sample with the nominal composition Sr_2VO_3CoAs was also prepared by the reaction of SrO, V, CoO (Aldrich, 99.99+ %) and As in a stoichiometric 2 : 1 : 1 : 1 ratio. All samples were treated according to the synthetic procedure described in 5.2.1, with a single annealing at 1100 °C for 48 h. The resultant black crystalline powders were stored in an argon-filled dry box.

6.2.1.2 PXRD

$Sr_2VO_3Fe_{1-x}Co_xAs$ samples were characterised by X-ray powder diffraction (XRPD) using the CRL PANalytical X'pert PRO diffractometer. This instrument has no incident beam monochromator so both Cu $K_{\alpha 1}$ and $K_{\alpha 2}$ radiation are observed. Analysis of the PXRD patterns collected on samples of $Sr_2VO_3Fe_{1-x}Co_xAs$ in the range ($0.05 \leq x \leq 0.2$) show these samples to be largely phase pure, with Sr_2VO_4 and FeAs impurity phases identified at less than 5 wt % in all cases. The Rietveld fit of $Sr_2VO_3Fe_{0.9}Co_{0.1}As$ to X-ray powder diffraction data is shown in Figure 6.2.

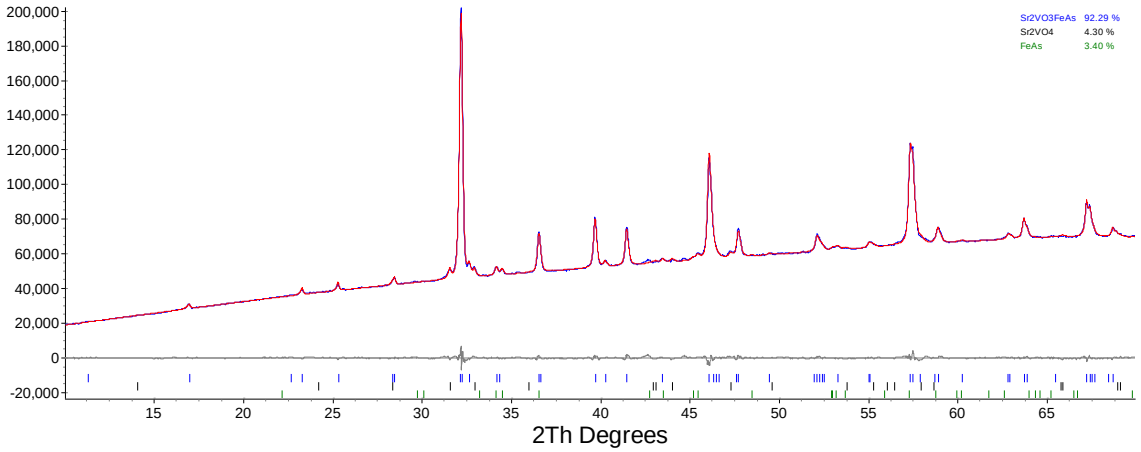

Figure 6.2 Rietveld fit of $Sr_2VO_3Fe_{0.9}Co_{0.1}As$ to powder X-ray diffraction data.

The successful substitution of Co on the Fe site is confirmed by an approximately linear decrease in the size *c* lattice parameter across the $Sr_2VO_3Fe_{1-x}Co_xAs$ series. By contrast the *a* lattice parameter remains relatively invariant upon Co substitution as shown in Figure 6.3. Overall these trends are much the same as those seen in the $Sr_2CrO_3Fe_{1-x}Co_xAs$ family. The Rietveld fit of the sample (AJC106) with the nominal composition Sr_2VO_3CoAs, to PXRD data is presented in Figure 6.4. In this sample the majority phase is Sr_2VO_3CoAs, however a large number of additional reflections are also observed that are attributed to

Sr_2VO_4, SrO, CoAs, VO and $SrVO_3$ impurity phases. Efforts are ongoing to synthesise phase pure samples of Sr_2VO_3CoAs, however the refined structural parameters obtained from Rietveld refinement against PXRD data are compared with those of Sr_2VO_3FeAs in Table 6.1.

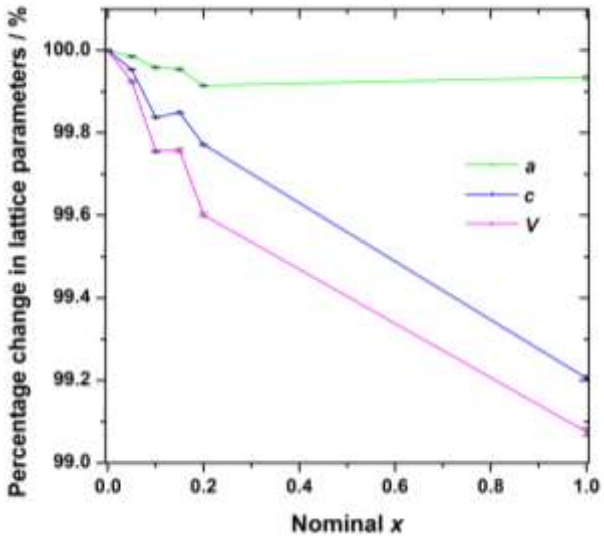

Figure 6.3 Variation of lattice parameters with *x* in $Sr_2VO_3Fe_{1-x}Co_xAs$ materials

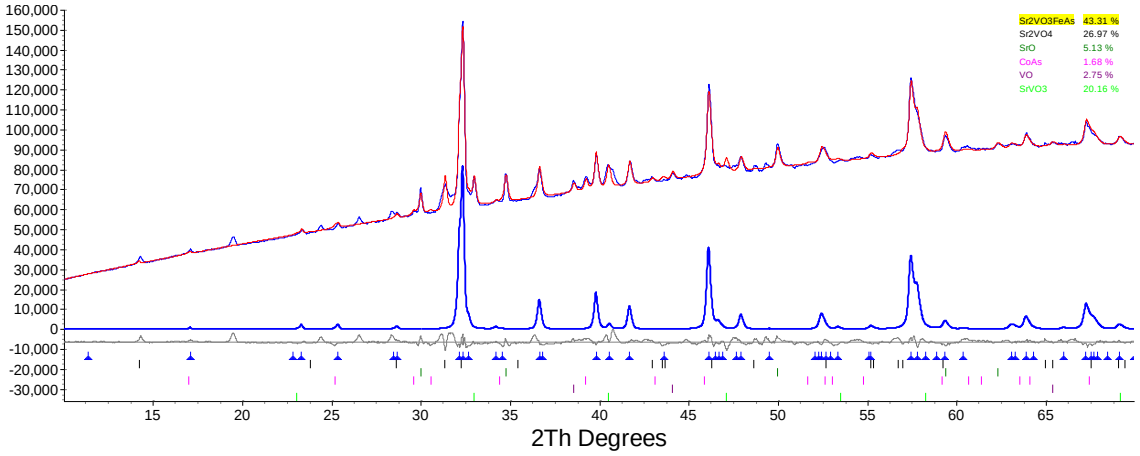

Figure 6.4 Rietveld fit of Sr_2VO_3CoAs to powder X-ray diffraction data, with the contribution from the majority Sr_2VO_3CoAs phase highlighted.

On progression from Sr_2VO_3FeAs to Sr_2VO_3CoAs the replacement of Fe^{2+} (0.63 Å) with the smaller transition metal Co^{2+} (0.58 Å), at the tetrahedral [2*a* (¼, ¾, 0)] crystallographic site in the arsenide layer, causes an overall contraction in both the *a* (0.0625(1) %) and *c* (0.7919(1) %) cell parameters. Accompanying this is a decrease in the Fe(Co)-As bond length of 1.195(3) % and a distortion of the geometry of the $Fe(Co)As_4$ tetrahedra away from being slightly compressed in the basal plane in Sr_2VO_3FeAs (α As-Fe-As = 108.4(1) °) to being slightly compressed along the *c* axis in Sr_2VO_3CoAs (α As-Co-As = 110.3(3) °). Similar structural changes have been described by Chen *et al*. in the isostructural

layered oxypnictides Sr_2ScO_3FeAs and Sr_2ScO_3CoAs.[1] However, the structural parameters of Sr_2VO_3CoAs displayed in Table 6.1 are very much preliminary results and further characterisation will have to wait until issues of sample purity are resolved.

		Sr_2VO_3FeAs (AJC127)	Sr_2VO_3CoAs (AJC106)
Instrument:		ICL X'pert	CRL X'pert
		Space group *P*4/*nmm*: origin choice 2	
Cell parameters and global fitting parameters:			
a / Å		3.93806(4)	3.9356(2)
c / Å		15.6963(2)	15.572(1)
Cell volume / Å^3		243.423(5)	241.19(3)
R_{wp}		5.597	1.971
χ^2		1.118	5.215
Variables refined		28	27
Atomic parameters:			
Sr1	[2*c* (¾, ¾, *z*)]	0.1909(2)	0.1839(4)
Sr2	[2*c* (¾, ¾, *z*)]	0.4144(2)	0.4154(4)
V	[2*c* (¼, ¼, *z*)]	0.3089(3)	0.3023(9)
Fe(Co)	[2*a* (¼, ¾, 0)]		
As	[2*a* (¼, ¼, *z*)]	0.0904(2)	0.0881(6)
O1	[4*f* (¼, ¾, *z*)]	0.2962(6)	0.289(2)
O2	[2*c* (¼, ¼, *z*)]	0.4232(9)	0.434(2)
Bond lengths and angles:			
	Fe(Co)-As / Å	2.427(2)	2.398(5)
	Fe(Co)-Fe(Co) / Å	2.78463	2.7829(1)
	V-O(eq) / Å	1.9792(9)	1.979(3)
	V-O(ax) / Å	1.79(1)	2.05(3)
	α As-Fe(Co)-As / °	108.4(1)	110.3(3)
	β As-Fe(Co)-As / °	109.99(7)	109.1(2)

Table 6.1 Results of refinement against laboratory X-ray powder diffraction data

6.2.1.3 Magnetometry measurements

The magnetic susceptibility of $Sr_2VO_3Fe_{0.95}Co_{0.05}As$ (AJC102) measured in an applied field of 50 Oe between 2 and 300 K is shown in Figure 6.5.

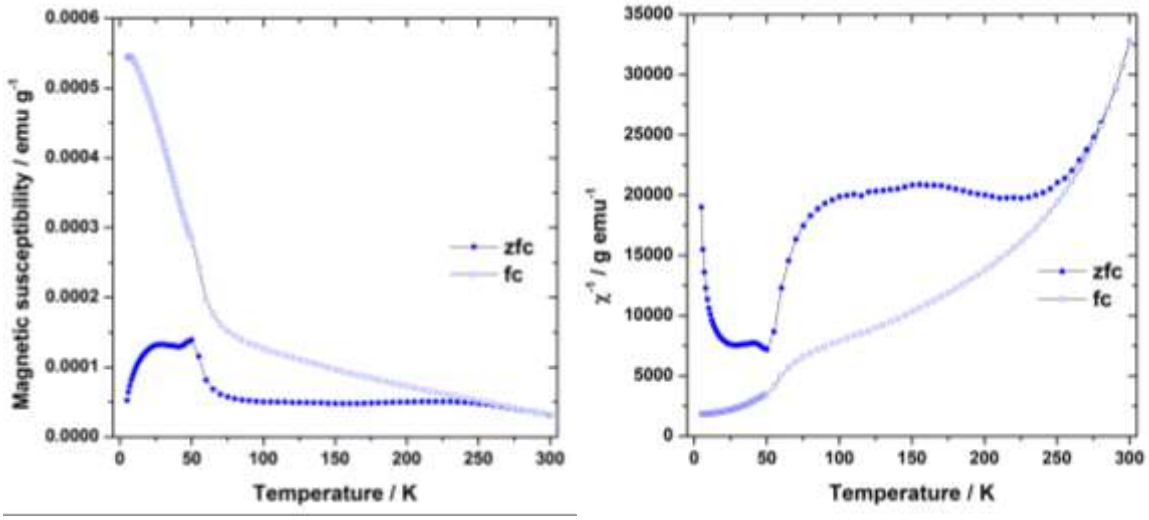

Figure 6.5 Magnetic susceptibility of $Sr_2VO_3Fe_{0.95}Co_{0.05}As$ measured in an applied field of 50 Oe

This sample shows no transition to diamagnetism suggesting that as little as 5 % Co substituted on the Fe crystallographic site is sufficient to electron-dope Sr_2VO_3FeAs away from the superconducting region. Instead this sample shows complex magnetic behaviour with transitions at 270, 70 and 25 K. The divergence of FC and ZFC susceptibilities at 250 K imply that weak ferromagnetic interactions predominate. An abrupt step in the susceptibility is then seen at 70 K, before a further antiferromagnetic transition at 25 K.

Due to the poor sample purity of Sr_2VO_3CoAs, SQUID magnetometry measurements were not performed on this sample. However, *Ln*OCoAs (*Ln* = La, Nd, Ce, Pr, Sm, Gd) materials, with anti-PbO-type CoAs layers, are typically metallic intinerant ferromagnets and therefore one would anticipate an intriguing interplay between magnetism on the oxide and arsenide sublattices in Sr_2VO_3CoAs.[2,3]

6.2.2 Aliovalent doping on the *B* site

In March 2010, the novel iron oxide pnictide $Sr_2Ti_{0.5}Mg_{0.5}O_3FeAs$ was reported by Shinya *et al*.[4] This material is isostructural to the Sr_2MO_3FeAs family that have formed the bulk of this thesis, but with the *B* site in the oxide layer displaying a disordered mixture of Ti^{4+} and Mg^{2+} cations. Magnetometry measurements performed on $Sr_2Ti_{0.5}Mg_{0.5}O_3FeAs$ showed it to be a poor superconductor with $T_{c(\text{onset})}$ = 10 K and superconducting volume of 1.5 %, however in Co-substituted $Sr_2Ti_{0.5}Mg_{0.5}O_3Fe_{1-x}Co_xAs$, and Ti rich materials, strong diamagnetic signals are observed with critical temperatures enhanced to ~ 35 K. Taking inspiration from this report, electron and hole doping strategies are employed in Sr_2VO_3FeAs through the partial aliovalent substitutions of Ti^{4+} and Mg^{2+} on the V^{3+} [2*c* (¼, ¼, 0.309)] site.

6.2.3 $Sr_2V_{1-x}Ti_xO_3FeAs$ materials

The aliovalent substitution of Ti^{4+} on the V^{3+} crystallographic site was anticipated to electron dope the FeAs layers in $Sr_2V_{1-x}Ti_xO_3FeAs$ materials. $Sr_2V_{1-x}Ti_xO_3FeAs$ samples have been synthesised in the compositional range $0 \leq x \leq 0.25$, according to the experimental procedure described in section 5.2.1, by the reaction of stoichiometric quantities of SrO, V (Alfa 99.988%), Ti (Alfa 99.99 %), Fe_2O_3 (Alfa 99.998%), Fe (Alfa 99.998%) and As (Alfa 99.999%) (*eqn6.2*), with a single annealing at 1100 °C for 48 h.

$$2\ SrO + (1 - x)\ V + x\ Ti + \tfrac{1}{3}\ Fe_2O_3 + \tfrac{1}{3}\ Fe + As \rightarrow Sr_2V_{1-x}Ti_xO_3FeAs \qquad \textit{eqn6.2}$$

6.2.3.1 PXRD

The successful substitution of Ti into the oxide layer of Sr_2VO_3FeAs is confirmed by a general decrease in the magnitude of the *a* and *c* lattice parameters as shown in Figure 6.6. Further structural analysis of $Sr_2V_{1-x}Ti_xO_3FeAs$ materials was hampered by the high proportions of strontium vanadate and iron arsenide impurity phases as exemplified by the Rietveld fit of $Sr_2V_{0.85}Ti_{0.15}O_3FeAs$ to PXRD data.

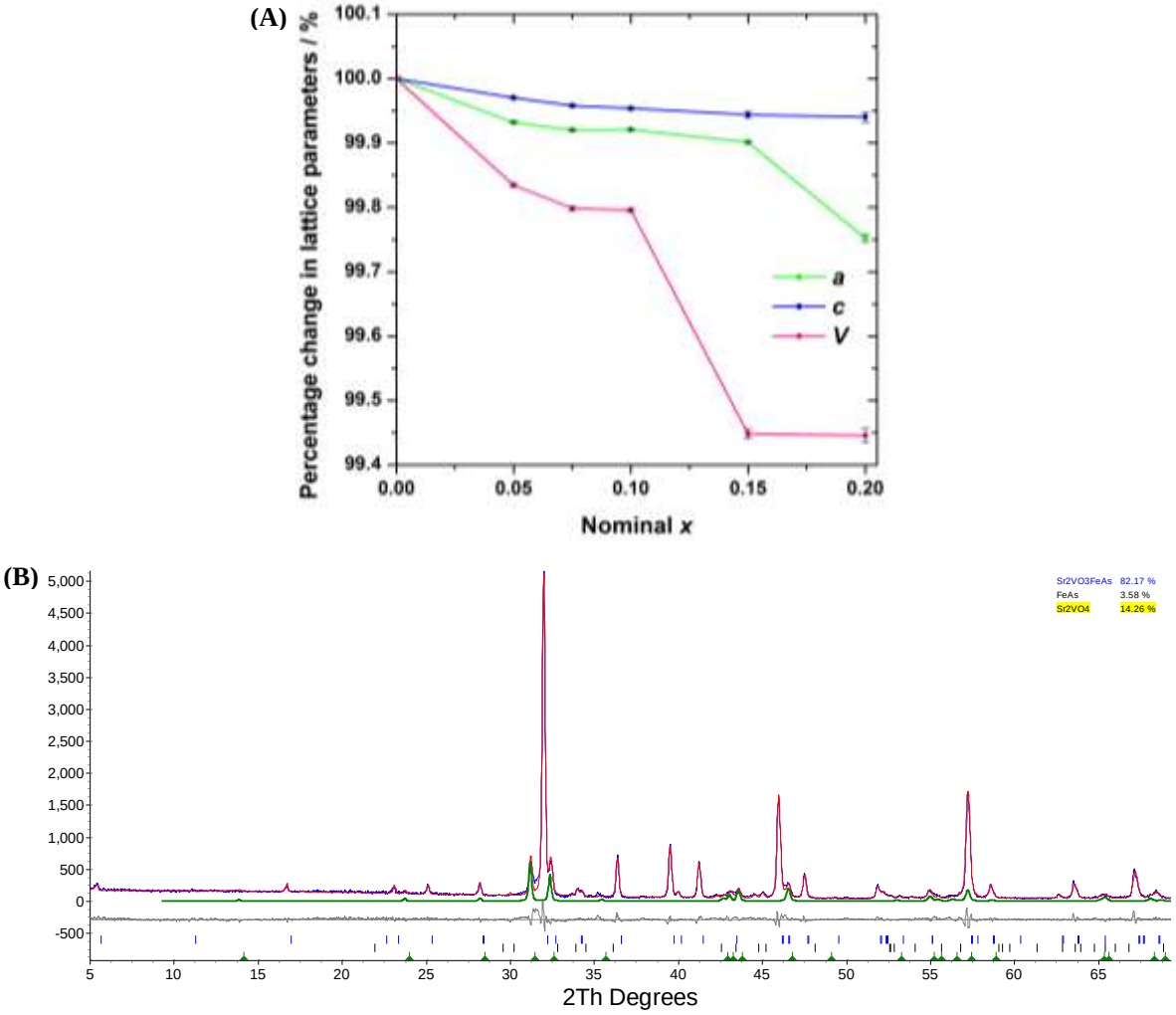

Figure 6.6 (A) Variation of lattice parameters and unit cell volume with *x* in $Sr_2V_{1-x}Ti_xO_3FeAs$ (B) Rietveld fit of $Sr_2V_{0.85}Ti_{0.15}O_3FeAs$ to PXRD data with the contribution from a Sr_2VO_4 impurity phase highlighted.

6.2.3.2 SQUID magnetometry

$Sr_2V_{1-x}Ti_xO_3FeAs$ samples were studied by SQUID magnetometry and the zero-field-cooled susceptibilities of samples in the range $0 \leq x \leq 0.15$ are shown in Figure 6.7 (A). T_c appears to decrease with increasing *x*, this is proposed to be as a result of over electron doping the FeAs layers.

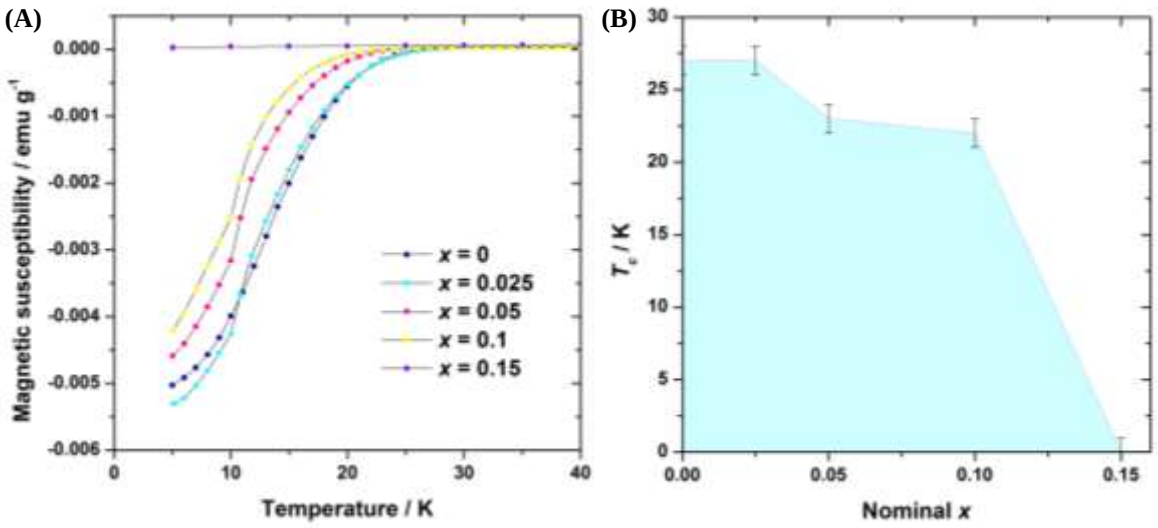

Figure 6.7 (A) Evolution of the zero-field-cooled magnetic susceptibility of $Sr_2V_{1-x}Ti_xO_3FeAs$ samples with *x*. (B) Superconducting phase diagram for $Sr_2V_{1-x}Ti_xO_3FeAs$.

6.2.4 Conclusions on electron doping Sr_2VO_3FeAs

In summary the partial substitution of Ti^{4+} for V^{3+} and Co^{2+} (d^7) for Fe^{2+} (d^6) have been successfully realised in Sr_2VO_3FeAs. However, both of these electron doping strategies have the effect of lowering the superconducting critical temperature in this material and ultimately suppressing superconductivity altogether. It is proposed that this is the result of over electron doping Sr_2VO_3FeAs away from the superconducting region. That a lesser degree of Co^{2+} substitution (5 %), as compared to Ti^{4+} (15 %), is required to suppress superconductivity is consistent with the observation that substitutions on the [2*a* (¼, ¾, 0)] site are more efficient at electron doping FeAs materials through the superconducting regime than aliovalent substitutions at other positions.[5,6]

6.2.5 $Sr_2V_{1-x}Mg_xO_3FeAs$ materials

The effect of hole doping the FeAs layers of Sr_2VO_3FeAs has also been investigated through the partial substitution of the lower valent Mg^{2+} cation on the V^{3+} crystallographic site. 1 g samples of $Sr_2V_{1-x}Mg_xO_3FeAs$ in the compositional range $0 \leq x \leq 0.5$ were prepared from SrO (prepared by the thermal decomposition of $SrCO_3$), MgO (Alfa 99.99%), V (Alfa 99.988%), Fe_2O_3 (Alfa 99.998%), Fe (Alfa 99.998%) and As (Alfa 99.999%) according to *eqn6.3*, using the experimental procedure detailed in section 5.2.1, with a single annealing at 1100 °C for 48 h.

$$2\,SrO + x\,MgO + (1-x)V + (\tfrac{1}{3} - x/2)\,Fe_2O_3 + (\tfrac{1}{3} + \tfrac{2}{3}x)\,Fe + As \rightarrow Sr_2V_{1-x}Mg_xO_3FeAs \quad \textit{eqn6.3}$$

6.2.5.1 PXRD

The changes in the crystal structure of $Sr_2V_{1-x}Mg_xO_3FeAs$ that are brought about by Mg substitution were followed by laboratory X-ray powder diffraction measurements. Rietveld refinement was performed against these data using TOPAS Academic and the variation of the lattice parameters with the nominal Mg doping level (x) are shown in Figure 6.8.

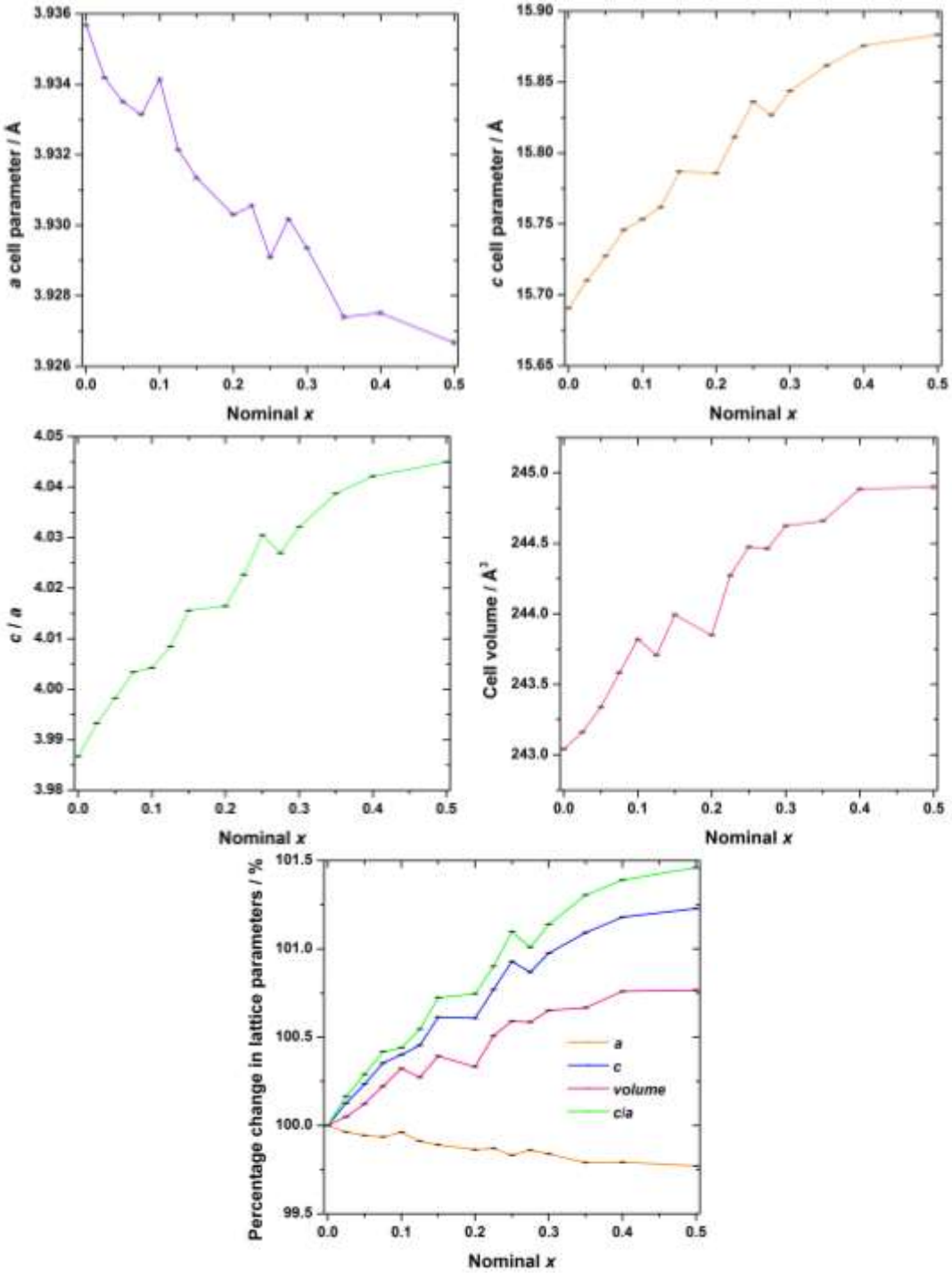

Figure 6.8 Variation of lattice parameters and unit cell volume with the nominal doping level (x) in $Sr_2V_{1-x}Mg_xO_3FeAs$.

In general a decrease in the *a* cell parameter is observed across the full compositional range $0 \leq x \leq 0.5$ in $Sr_2V_{1-x}Mg_xO_3FeAs$. Conversely, the *c* lattice parameter shows a general increase as Mg^{2+} is substituted on the V^{3+} crystallographic site. The differing trends in the *a* and *c* lattice parameters upon Mg^{2+} substitution in $Sr_2V_{1-x}Mg_xO_3FeAs$ are presumably a result of the two competing effects that are brought about by this aliovalent doping strategy. Firstly the substitution of the larger Mg^{2+} cation (0.66 Å) on the V^{3+} (0.64 Å) site would be expected to increase the size of the lattice parameters.[7]

However, the aliovalent doping of Mg^{2+} will also have the effect of oxidising one of the two transition metal cations, decreasing the effective ionic radii of the cation in question. In the $Sr_2V_{1-x}Mg_xO_3FeAs$ system this competition manifests itself in a modest decrease in the size of the basal lattice parameter, with *x*, and a much larger increase in the size of the *c* lattice parameter. Overall this has the effect of increasing the magnitude of both the *c*/*a* ratio and the cell volume, which vary approximately linearly with *x*, until $x = 0.3$, whereupon the rate of the increase slows, indicating that a limiting composition at $x \sim 0.4$.

The Rietveld fit of $Sr_2V_{0.85}Mg_{0.15}O_3FeAs$ (AJC183) to PXRD data is shown in Figure 6.9. Additional phases included in this refinement are FeAs, Sr_2VO_4, $Sr_3V_2O_7$ impurity phases and a reference Si Pawley fitted phase (5.431195 Å). Sr_2VO_4, FeAs and $Sr_3V_2O_7$ impurity phases are observed in all samples but are typically present in proportions lower than those seen in Sr_2VO_3FeAs, however the level to which they are present increases considerably in $Sr_2V_{1-x}Mg_xO_3FeAs$ samples with $x \geq 0.3$.

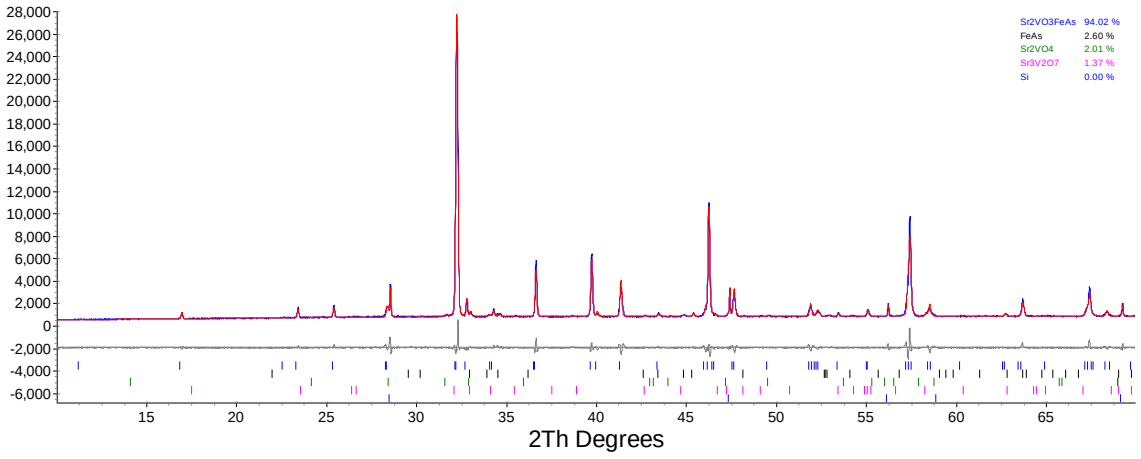

Figure 6.9 Rietveld fit of $Sr_2V_{0.85}Mg_{0.15}O_3FeAs$ to PXRD data

The observed linear changes in the lattice parameters of $Sr_2V_{1-x}Mg_xO_3FeAs$ materials in the compositional range $0 \leq x \leq 0.3$, would appear to imply the successful substitution of Mg. However, given the strong contrast in the X-ray scattering factors of Mg^{2+} and V^{3+},

the fractional occupancies of magnesium (f_{occMg}) and vanadium (f_{occV}) on the [2c (¼, ¼, ~0.309)] site were also refined, employing a $f_{occV} + f_{occMg} = 1$ constraint. A plot of the refined Mg^{2+} occupancy (f_{occMg}) against the nominal Mg level (x) is shown in Figure 6.10. The general increase in the refined Mg^{2+} occupancy with the nominal value of x provides further evidence for successful Mg substitution. However, whilst the values of f_{occMg} and x show good agreement at low doping levels, f_{occMg} does not follow x at higher levels. That said, given the weak X-ray scattering factors of Mg^{2+}/V^{3+} relative to other scatters in the material like Sr^{2+} and As^{3-}, the trends in lattice parameters are perhaps better gauges of the level of Mg substitution.

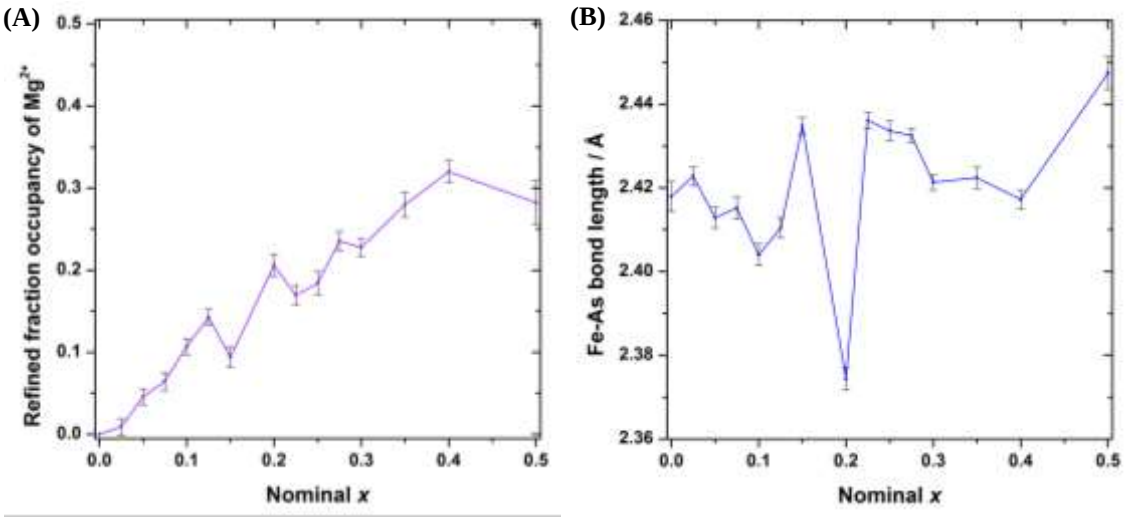

Figure 6.10 (A) Plot of the refined Mg doping level (f_{occMg}) against the nominal Mg^{2+} doping level (x). (B) Variation of Fe-As bond length with x.

In an attempt to identify the nature of the oxidised species in $Sr_2V_{1-x}Mg_xO_3FeAs$ materials, the Fe-As bond length was scrutinised. If the electronic effect of Mg^{2+} substitution is to oxidise Fe, this would likely have the effect contracting the Fe-As bond length. Instead what is seen in Figure 6.10, apart from an anomalously short Fe-As bond length in $Sr_2V_{0.8}Mg_{0.2}O_3FeAs$, is that there are no strong trends in the Fe-As bond length with x. Similar consideration of the valence state of vanadium through changes in the V-O bond lengths with x are not made, owing to the fact that the Mg^{2+} dopant is substituted on the vanadium site.

6.2.5.2 XANES measurements

A better probe of the local changes in the valence states of Fe and V across the $Sr_2V_{1-x}Mg_xO_3FeAs$ series is made through XANES measurements performed on the B18 beamline at the Diamond synchrotron. Upon oxidation one would expect a shift in the

position of the metal *K*-edge to higher energies, as more energy is required to ionise core electrons in higher valent cations (Kunzl's law). Normalized X-ray absorption spectra collected in fluorescence mode on the iron *K*-edge of $Sr_2V_{1-x}Mg_xO_3FeAs$ samples in the compositional range $0 \leq x \leq 0.4$ are plotted in Figure 6.11, along with the derivative of the absorption spectra.

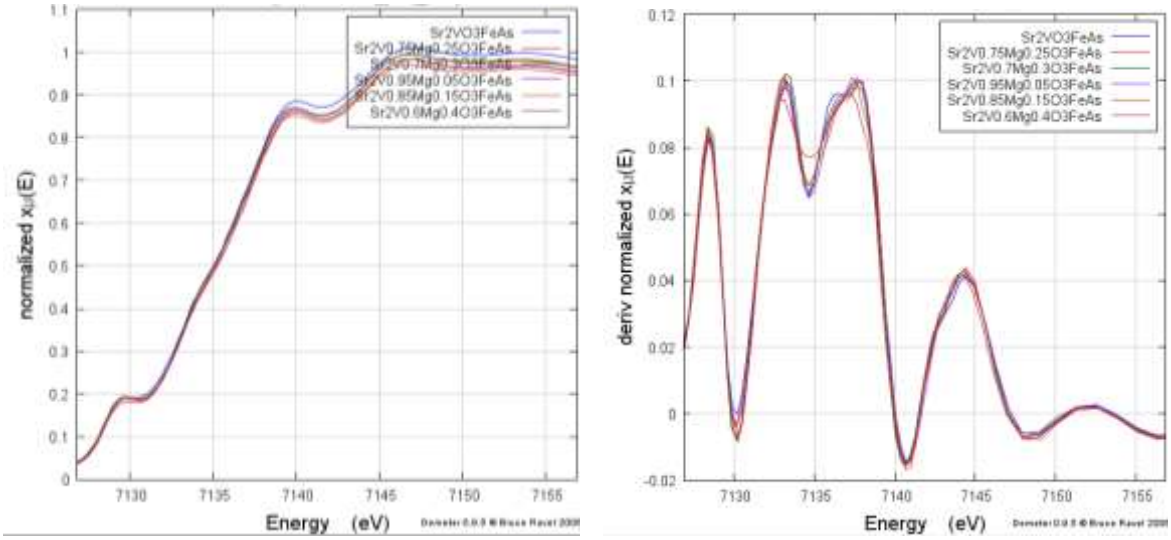

Figure 6.11 (A) Normalised Fe *K*-edge of $Sr_2V_{1-x}Mg_xO_3FeAs$ samples. (B) Derivative of the normalised Fe *K*-edge of $Sr_2V_{1-x}Mg_xO_3FeAs$ samples

No noticeable shift in the position of the Fe *K*-edge is observed away from that of Sr_2VO_3FeAs with increasing *x*. This implies that the oxidation state of Fe does not change with the level of hole-doping in $Sr_2V_{1-x}Mg_xO_3FeAs$ samples. Additional measurements were therefore performed on the V *K*-edge. Shown in Figure 6.12 are the normalised absorption spectra of Sr_2VO_3FeAs, $Sr_2V_{0.8}Mg_{0.2}O_3FeAs$ and $Sr_2V_{0.6}Mg_{0.4}O_3FeAs$. These XANES data clearly show that the position of the vanadium *K*-edge moves to higher energy with increasing *x*, an observation consistent with the oxidation of vanadium. To quantify this shift, the derivative of the absorption edge and the second derivative of these spectra are also presented in Figure 6.12.

Here the position of the absorption edge is taken to be the most rapidly rising part of the absorption spectrum, i.e. the point at which the derivative of the absorption spectrum is maximised, or when the second derivative is equal to zero. The valence state of vanadium (V_V) in $Sr_2V_{1-x}Mg_xO_3FeAs$ samples may then be estimated from the position of the edge relative to those of the $LaV^{III}O_3$ and $Sr_3V^{IV}{}_2O_7$ according to Figure 6.13.

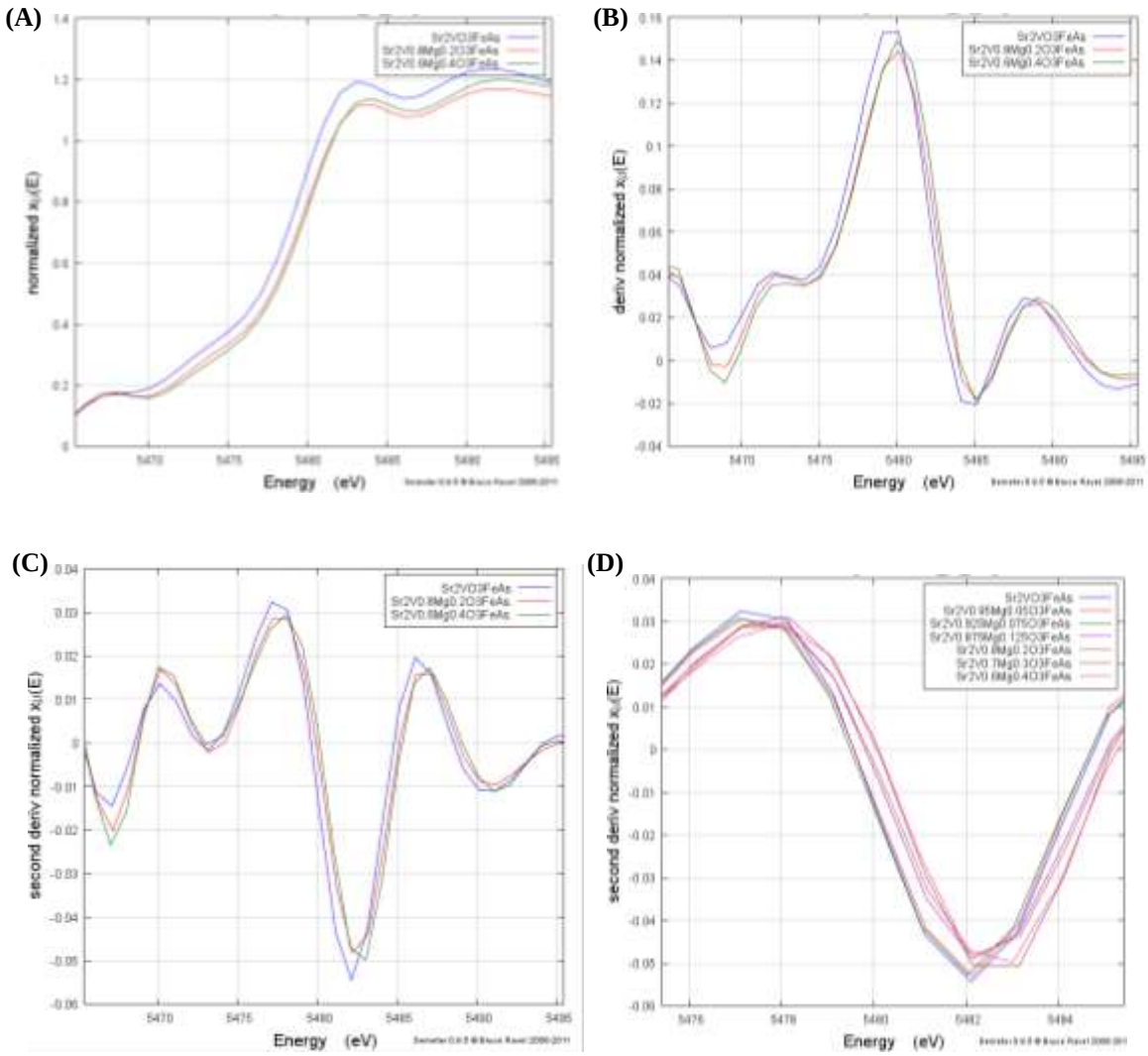

Figure 6.12 (A) Normalised V *K*-edge of Sr_2VO_3FeAs, $Sr_2V_{0.8}Mg_{0.2}O_3FeAs$ and $Sr_2V_{0.6}Mg_{0.4}O_3FeAs$ (B) The derivative of the normalised absorption spectra. (C) Second derivative of normalised absorption spectra. (D) Second derivative of the $Sr_2V_{1-x}Mg_xO_3FeAs$ samples 5 eV either side of the absorption edge.

The variation of V_V with the nominal level of Mg substitution in $Sr_2V_{1-x}Mg_xO_3FeAs$ samples is presented in Figure 6.13. This plot shows a general increase in the oxidation state of vanadium with *x*, which is enhanced from +3.13(5) in Sr_2VO_3FeAs to +3.53(5) in $Sr_2V_{0.6}Mg_{0.4}O_3FeAs$. These XANES measurements strongly suggest that the substitution of the lower valent Mg^{2+} cation on the [2*c* (¼, ¼, ~0.309)] site has the effect of exclusively oxidising $V^{3+} \rightarrow V^{4+}$, since no observable shift in the position of the iron *K*-edge is observed.

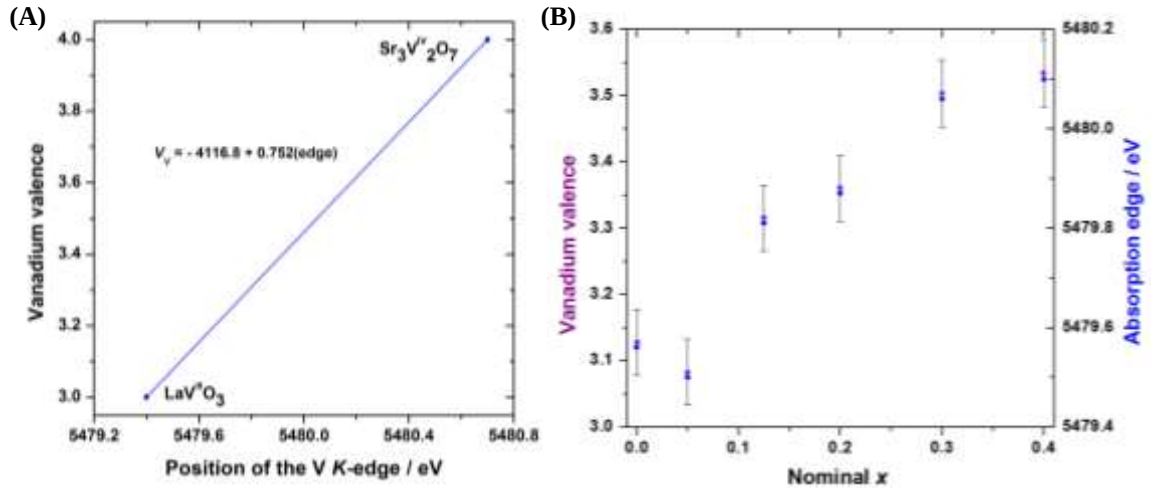

Figure 6.13 (A) Plot describing the linear arrangement between the position of the absorption edge and the oxidation state of vanadium in $LaVO_3$ and $Sr_3V_2O_7$ reference samples. (B) Oxidation states of $Sr_2V_{1-x}Mg_xO_3FeAs$ samples derived from the position of the vanadium absorption edge.

6.2.5.3 SQUID magnetometry

Whilst it has been shown in the previous section that Mg substitution in $Sr_2V_{1-x}Mg_xO_3FeAs$ materials does not have the effect of hole doping the FeAs layers, the significant structural changes which this doping strategy imparts are likely to influence the superconducting properties of these materials. SQUID magnetometry measurements were therefore performed on $Sr_2V_{1-x}Mg_xO_3FeAs$ samples across the compositional range $0 \leq x \leq 0.4$, in applied fields of 50 Oe. The zero-field-cooled susceptibilities of $Sr_2V_{1-x}Mg_xO_3FeAs$ samples with nominal levels of x = 0, 0.075, 0.15, 0.225 and 0.3 are presented in Figure 6.14.

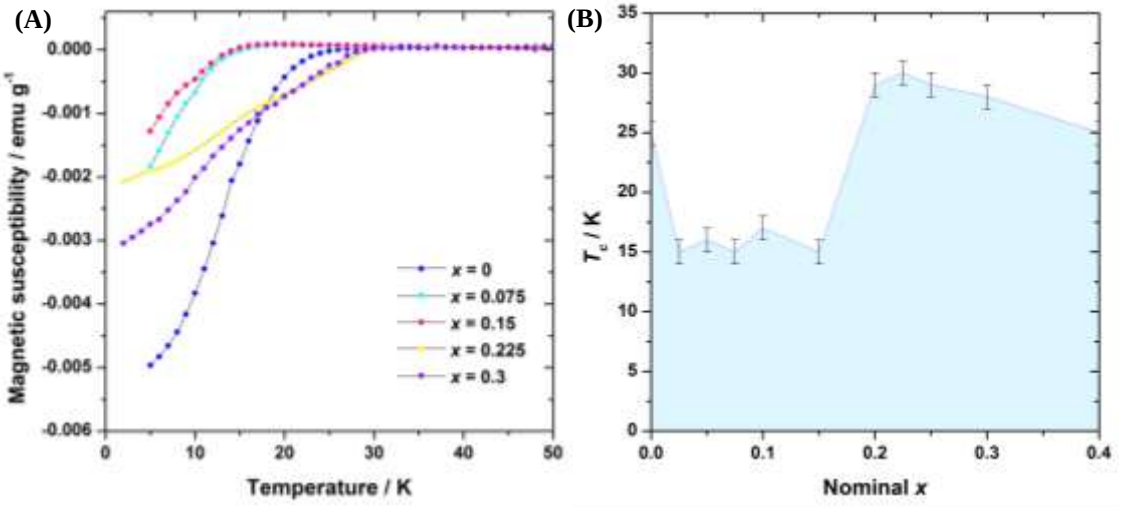

Figure 6.14 (A) Evolution of the zero-field-cooled magnetic susceptibility of selected $Sr_2V_{1-x}Mg_xO_3FeAs$ samples. (B) Superconducting phase diagram for $Sr_2V_{1-x}Mg_xO_3FeAs$.

At low Mg doping levels ($0 \leq x \leq 0.15$) a significant drop in both the superconducting critical temperatures (T_c) and the superconducting volume fraction is observed. In samples with $x \geq 0.2$ superconducting critical temperatures are increased to values above that of stoichiometric Sr_2VO_3FeAs, maximised at 30 K in $Sr_2V_{0.775}Mg_{0.225}O_3FeAs$. The overall superconducting phase diagram of $Sr_2V_{1-x}Mg_xO_3FeAs$ is shown in Figure 6.14. The possible origins of the observed variations of T_c with x are discussed in section 6.2.3.5.

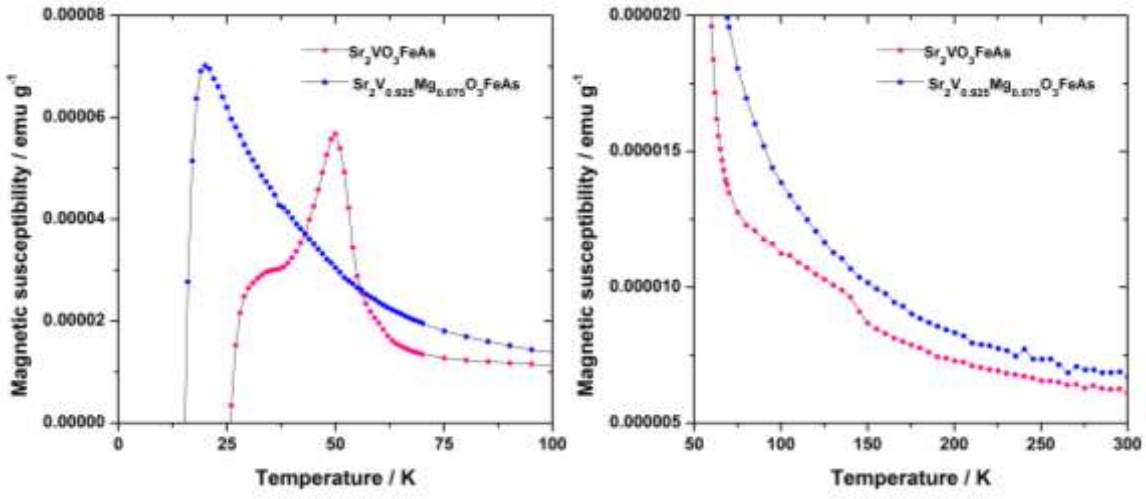

Figure 6.15 Comparison of the zero-field-cooled susceptibilities of $Sr_2V_{0.925}Mg_{0.075}O_3FeAs$ and Sr_2VO_3FeAs.

A further point to address is the effect that Mg substitution on the V site has on the magnetic transitions that are observed in the parent Sr_2VO_3FeAs material. The zero-field-cooled susceptibility of $Sr_2V_{0.925}Mg_{0.075}O_3FeAs$ in the paramagnetic region is compared with that of Sr_2VO_3FeAs in Figure 6.15. From this comparison it would appear that by substituting as little 7.5 % Mg on the V site, all of the magnetic transitions observed in Sr_2VO_3FeAs are suppressed. However, it is also possible that the disorder created on the [2*c* (¼, ¼, ~0.309)] site through the partial substitution of Mg reduces the ordering temperature in $Sr_2V_{1-x}Mg_xO_3FeAs$ samples to below T_c, where the transition would be masked by the strong diamagnetic signal of the superconducting state.

6.2.5.4 TF-μSR measurements

In the previous chapter μSR measurements were performed on Sr_2VO_3FeAs to probe the magnetic order on the vanadium sub-lattice, which exhibits a heavily damped muon signal below ~ 45 K, consistent with an incommensurately ordered phase. Given the apparent suppression of the magnetic transitions in Mg substituted $Sr_2V_{1-x}Mg_xO_3FeAs$ samples, transverse field μSR (TF-μSR) measurements were performed on 3 samples with nominal

Mg levels of x = 0.075, 0.2 and 0.25, by collaborators in the group of Prof. Steve Blundell Oxford Physics Department.

This technique is well established for probing the superconducting state of type-II superconductors and is described in detail in a paper by Sonier *et al.*[8] In a TF-μSR experiment one applies a magnetic field perpendicular to the incident muon polarisation. The muons precess in this field, giving rise to an oscillatory asymmetry signal. In type-II superconductors, the applied field ($H > H_{C1}$) also establishes a vortex lattice and the corresponding field distribution experienced by the muons causes damping in the oscillations. The damping parameter σ then is typically related to the penetration depth. However, what is observed for $Sr_2V_{1-x}Mg_xO_3FeAs$ samples is a strong magnetic contribution to the damping parameter σ, which dominates the signal and is used here to follow the evolution of magnetic order with temperature. The asymmetry signal is fitted to the function given below.

$$Asymmetry = \cos(\omega t)\left(e^{-\sigma^2 t^2/2}\right) + \cos(\omega_{bg} t)\left(e^{-\sigma_{bg}^2 t^2/2}\right) \qquad eqn6.4$$

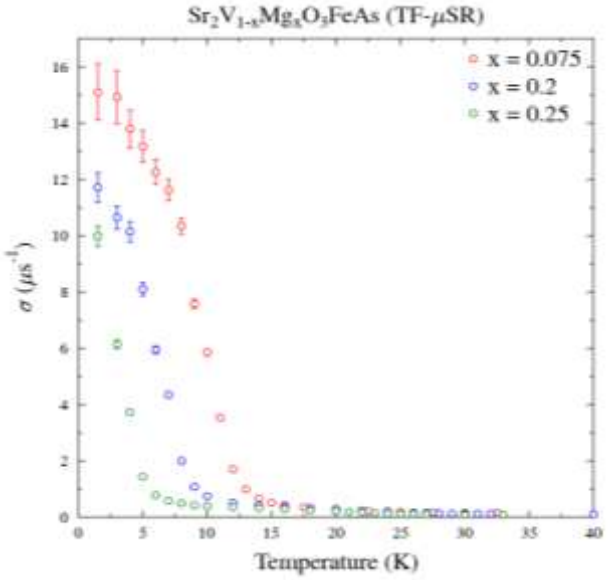

Figure 6.16 Temperature dependence of the σ parameter in $Sr_2V_{1-x}Mg_xO_3FeAs$

The temperature dependence of the σ parameter for all 3 $Sr_2V_{1-x}Mg_xO_3FeAs$ samples is shown in Figure 6.16. It is apparent from these data that the magnetic ordering temperature decreases with x, with onsets of the magnetic signal in $Sr_2V_{1-x}Mg_xO_3FeAs$ samples with x = 0.075, 0.2, 0.25 at ~ 17, 14 and 10 K, respectively. This result suggests that Mg doping on the V site does not completely destroy LRO on the vanadium sub-lattice, but instead lowers the ordering temperature with increasing x.

6.2.5.5 Conclusions on $Sr_2V_{1-x}Mg_xO_3FeAs$

In summary, the substitution of Mg on V site has been successfully realised in $Sr_2V_{1-x}Mg_xO_3FeAs$ samples, within the compositional range $0 \leq x \leq 0.5$. This has the effect of increasing the *c* lattice parameter, but decreasing the *a* lattice parameter as Mg is introduced. XANES measurements show a clear shift in the V *K*-edge to higher energies with increasing *x*, whilst no shift is seen in the Fe *K*-edge, indicating that this aliovalent substitution has the effect of exclusively oxidising V^{3+} to V^{4+}.

SQUID magnetometry measurements reveal curious trends in the superconducting critical temperature with *x*, in which after an initial decrease in T_c at low Mg doping levels ($0.025 \leq x \leq 0.15$), T_c is enhanced in samples with $x \geq 0.2$ and then maximised in $Sr_2V_{0.775}Mg_{0.225}O_3FeAs$ at 31 K. Since there is no apparent change in the oxidation state of Fe upon Mg substitution, as judged by invariant positions of the Fe *K*-edge from XANES measurements, it is likely that the observed variations in T_c with *x* are a result of structural, rather than electronic, changes to the FeAs layers. However, examination of the variation in the As-Fe-As bond angles (appendix G), Fe-Fe distances and the Fe-As bond lengths with *x* shows trends that do not mimic those of T_c.

More detailed structural studies are therefore required to examine the structural and compositional changes brought about by Mg substitution. With respect to composition, it is plausible that the level to which V is present on the Fe site varies with *x* in $Sr_2V_{1-x}Mg_xO_3FeAs$ materials. If this is the case then the reduced critical temperatures observed in samples in the compositional range $0.025 \leq x \leq 0.15$ may possibly be the result of additional V substituted on the Fe position, which has been shown to be detrimental to the superconducting properties of Sr_2VO_3FeAs.[9] This theory could be verified by PND studies.

μSR experiments reveal that, contrary to what is observed from SQUID measurements, the magnetic order on the vanadium sub-lattice is not completely destroyed by Mg substitution, but rather it is suppressed below the superconducting critical temperature and is therefore masked by the strong diamagnetic signal of the superconducting state. By following the evolution of the damping of the muon asymmetry signal with temperature, it is observed that the magnetic ordering temperature decreases with increasing *x*. This is presumably as a result of the disorder created on the [2*c* (¼, ¼, ~0.309)] site having a detrimental effect on the exchange pathways through the vanadium sub-lattice.

6.3 Isovalent substitutions

6.3.1 $Sr_{2-x}Ca_xVO_3FeAs$ materials

A recent high pressure study examining the effect of hydrostatic pressure on the electrical resistivity and crystal structure of Sr_2VO_3FeAs has shown that at pressures above 10 GPa a decrease in the two-fold α As-Fe-As bond angle is observed, as the $FeAs_4$ tetrahedra are deformed away from regularity, with an accompanied decrease in T_c.[10] This empirical observation that T_c is maximised in FeAs-based superconductors with regular $FeAs_4$ tetrahedra was first highlighted by Lee *et al* and has shown to be applicable to the majority of Fe*Pn* systems (Figure 6.17).[11]

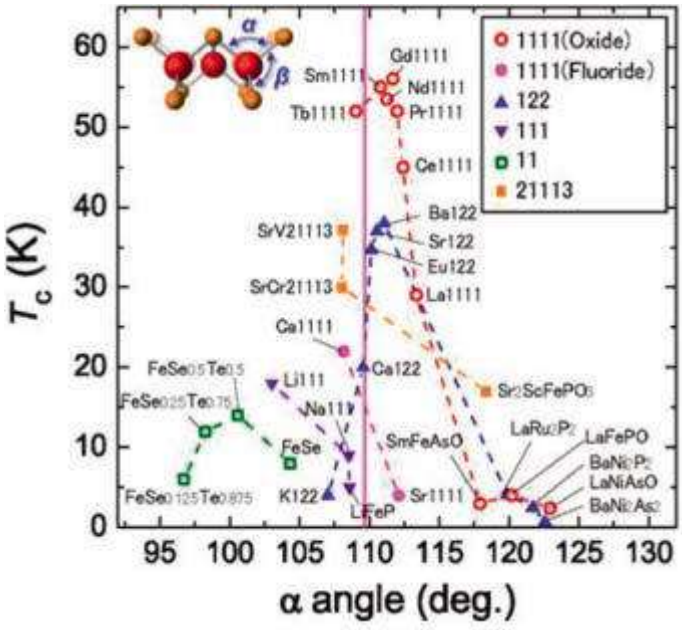

Figure 6.17 Correlation between T_c and the α As-Fe-As bond angle, as described by Johrendt *et al*.[12]

Here a complementary study is made, in which the effect of the application of chemical pressure through the isovalent substitution of Sr by Ca in $Sr_{2-x}Ca_xVO_3FeAs$ is investigated.

6.3.1.1 Experimental

$Sr_{2-x}Ca_xVO_3FeAs$ ($0 < x < 0.5$) samples were synthesized on the 0.5 – 3 g scale by annealing stoichiometric mixtures of SrO (prepared by the thermal decomposition of $SrCO_3$ (Alfa 99.99 %)), CaO (prepared by the thermal decomposition of $CaCO_3$ (99.95 %)), V (Alfa 99.5 %), Fe_2O_3 (Alfa 99.998 %), Fe (Alfa 99.998 %) and As (Alfa 99.999 %) according to *eqn.6.5*.

$$2\text{-}x\ SrO + x\ CaO + V + \tfrac{1}{3}\ Fe_2O_3 + Fe + As \rightarrow Sr_{2-x}Ca_xVO_3FeAs \qquad \textit{eqn.6.5}$$

These samples were annealed according to the synthetic procedure described in 5.2.1, with a single firing at 1100 °C for 48 h. The resultant black crystalline powders were stored in an argon-filled dry box.

6.3.1.2 PXRD

Initial characterisation was carried out by X-ray powder diffraction using a PANalytical X'pert PRO instrument operating in Bragg-Brentano geometry with a Ge(111) monochromator to select Cu $K\alpha_1$ radiation. All $Sr_{2-x}Ca_xVO_3FeAs$ samples crystallize in the *P*4/*nmm* space group and Rietveld refinement against room temperature PXRD data reveals a linear decrease in cell volume with the nominal value of x (Figure 6.18). This confirms the successful substitution of the smaller Ca^{2+} (1.12 Å) cation on the Sr^{2+} sites (1.26 Å).[7]

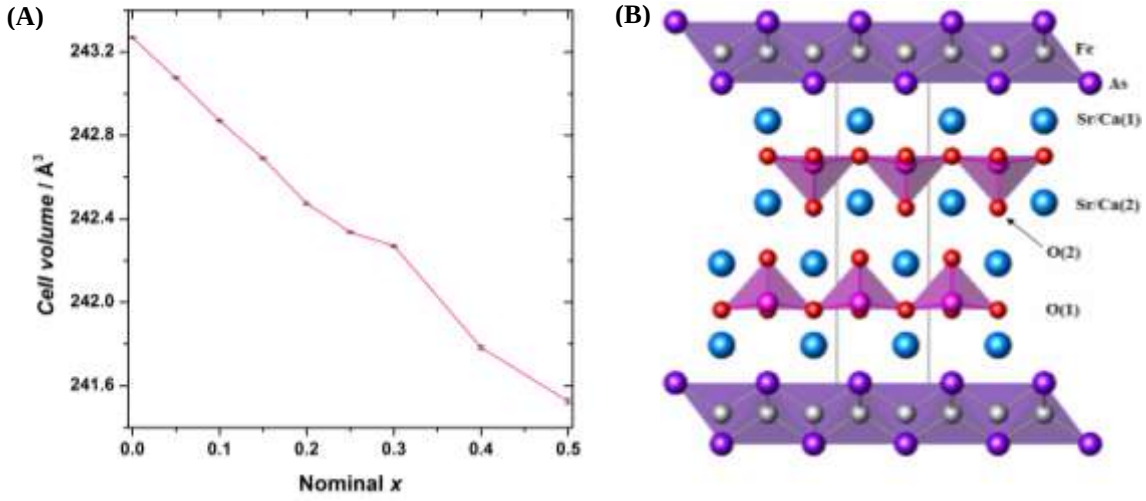

Figure 6.18 (A) Variation of unit cell volume with x in $Sr_{2-x}Ca_xVO_3FeAs$ ($0 \leq x \leq 0.5$) from refinement against SXRD data. (B) Crystal structure of Sr_2VO_3FeAs.

In contrast to the behaviour of the cell volume, the decrease in the a and c cell parameters are not linear over the entire compositional range studied. The decrease in cell volume is initially dominated by the contraction in c, until $x = 0.1$ whereupon the basal cell parameter also begins to decrease in an approximately linear manner (Figure 6.19). This behaviour of the lattice parameters and additional structural parameters is discussed below in the context of the evolution of the superconducting properties of the $Sr_{2-x}Ca_xVO_3FeAs$ samples.

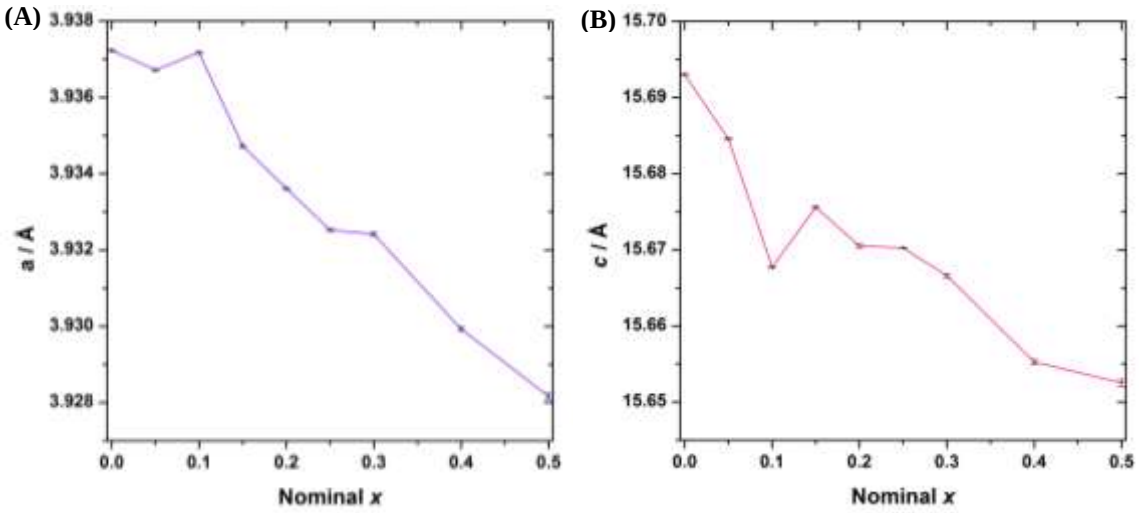

Figure 6.19 Variation of the *a* (A) and *c* (B) lattice parameters with *x*.

As discussed in the previous chapter, the synthesis of phase pure samples of Sr_2VO_3FeAs is made challenging by the competitive formation of various strontium vanadate phases. Ca substituted samples also contained significant levels of these impurity phases which are accounted for quantitatively by Rietveld analysis (Table 6.3). To further characterise these samples, SQUID magnetometry, powder neutron diffraction and synchrotron X-ray diffraction experiments were performed and the results of these measurements are considered here.

6.3.1.3 SQUID magnetometry

As discussed in the previous chapter Sr_2VO_3FeAs is proposed to be an internally electron-doped superconductor, to investigate the effect of chemical pressure on the superconducting properties of $Sr_{2-x}Ca_xVO_3FeAs$ samples, magnetic susceptibility measurements were performed on a SQUID magnetometer. The zero-field-cooled magnetisations of $Sr_{2-x}Ca_xVO_3FeAs$ samples in the range $0 \leq x \leq 0.3$ measured in an applied field of 50 Oe are shown in Figure 6.20. These measurements reveal an initial increase in T_c with x, in which T_c is maximised at 27 K in $Sr_{1.95}Ca_{0.05}VO_3FeAs$. Further Ca doping suppresses T_c in an approximately linear manner, until $x = 0.3$ which shows no transition to diamagnetism. The superconducting phase diagram for $Sr_{2-x}Ca_xVO_3FeAs$ is shown in Figure 6.20. Superconducting volume fractions were also estimated from the magnitude of the ZFC signal at 2 K. $Sr_{2-x}Ca_xVO_3FeAs$ samples in the range $0 \leq x \leq 0.1$ have volume fractions of approximately 30 %, with further Ca doping leading to a decrease in the superconducting volume fractions.

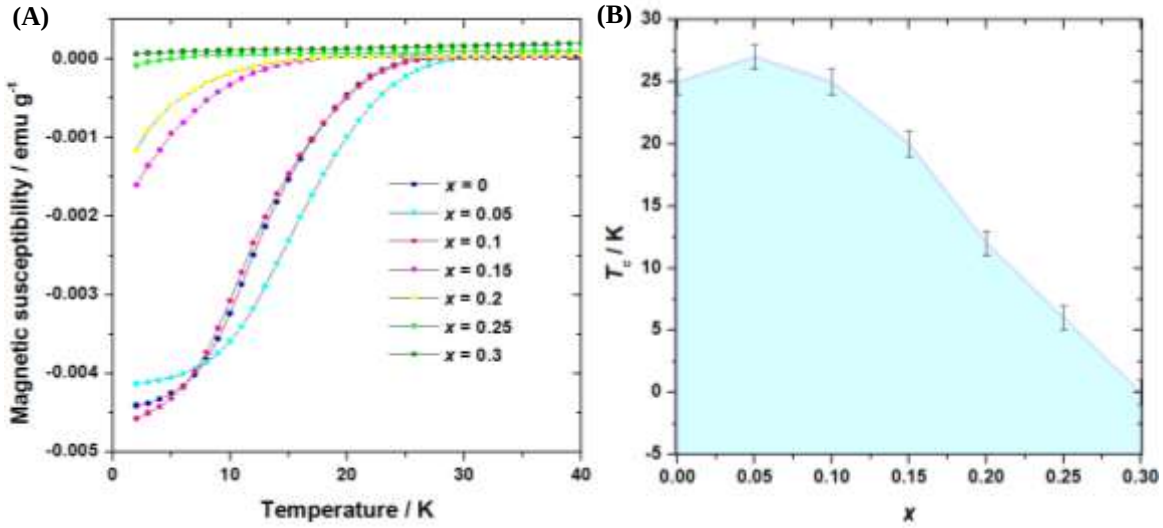

Figure 6.20 (A) Evolution of the zero-field-cooled magnetic susceptibility of $Sr_{2-x}Ca_xVO_3FeAs$ samples with *x*. (B) Superconducting phase diagram of $Sr_{2-x}Ca_xVO_3FeAs$.

A combination of synchrotron X-ray powder diffraction and neutron powder diffraction techniques are now used to rationalise the observed changes in T_c with x, in terms of changes to the structure and stoichiometry of $Sr_{2-x}Ca_xVO_3FeAs$ samples.

6.3.1.4 Powder neutron diffraction (D2B)

Room temperature PND measurements were performed on D2B using 1.59 Å neutrons on 3 g samples of $Sr_{2-x}Ca_xVO_3FeAs$, with x = 0, 0.1, 0.2 and 0.3. These were loaded into 6 mm diameter cylindrical vanadium sample cans and measured in the range 5 ° ≤ 2θ ≤ 150 °. Rietveld refinements were performed against all room temperature data sets using the GSAS software suite. Refined variables include the atomic parameters described in Table 6.2 and parameters to model the background, 2θ zero error, scale factors and profile coefficients. $Sr_3V_2O_7$, Sr_2VO_4, SrO, $SrFe_2As_2$ and FeAs impurity phases were also included, where appropriate, and levels to which they are present are recorded in Table 6.2.

The Rietveld fit of $Sr_{1.8}Ca_{0.2}VO_3FeAs$ to room temperature data is depicted in Figure 6.21 and shows good agreement between the observed data and refined model. The first point to address with regard to stoichiometry is the level to which Ca has been successfully doped into the majority $Sr_{2-x}Ca_xVO_3FeAs$ phase. In performing refinements against PND data both Sr crystallographic sites were subject to a $f_{occ\mathrm{Sr}} + f_{occ\mathrm{Ca}} = 1$ constraint, but the relative amounts of Ca and Sr were allowed to refine freely. The refinement results for $Sr_{2-x}Ca_xVO_3FeAs$ samples, with x = 0, 0.1, 0.2 and 0.3, all give values for the sums of the

refined Ca^{2+} occupancies $f_{occ}Ca(1)$ and $f_{occ}Ca(2)$ that are equal, within error, to the nominal composition (Figure 6.22) and (Table 6.2).

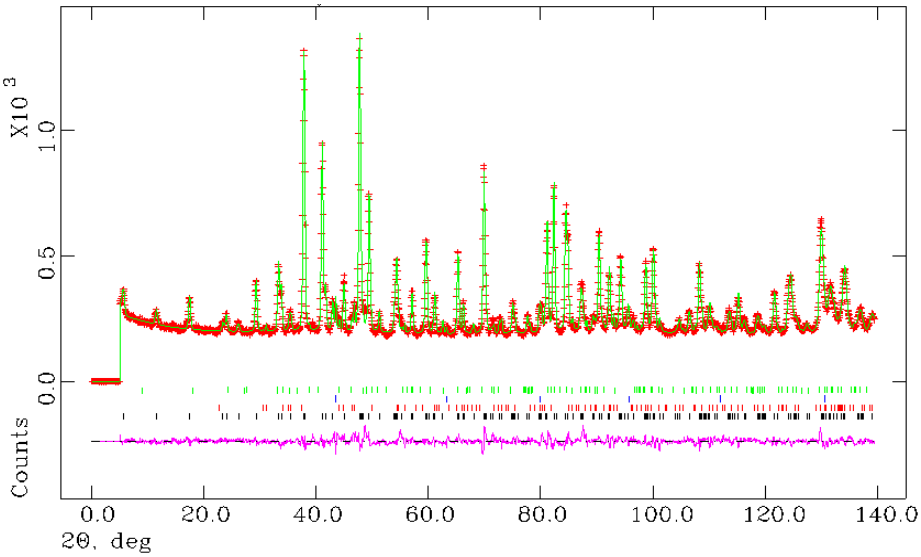

Figure 6.21 Rietveld fit to powder neutron diffraction data for $Sr_{1.8}Ca_{0.2}VO_3FeAs$ at room temperature

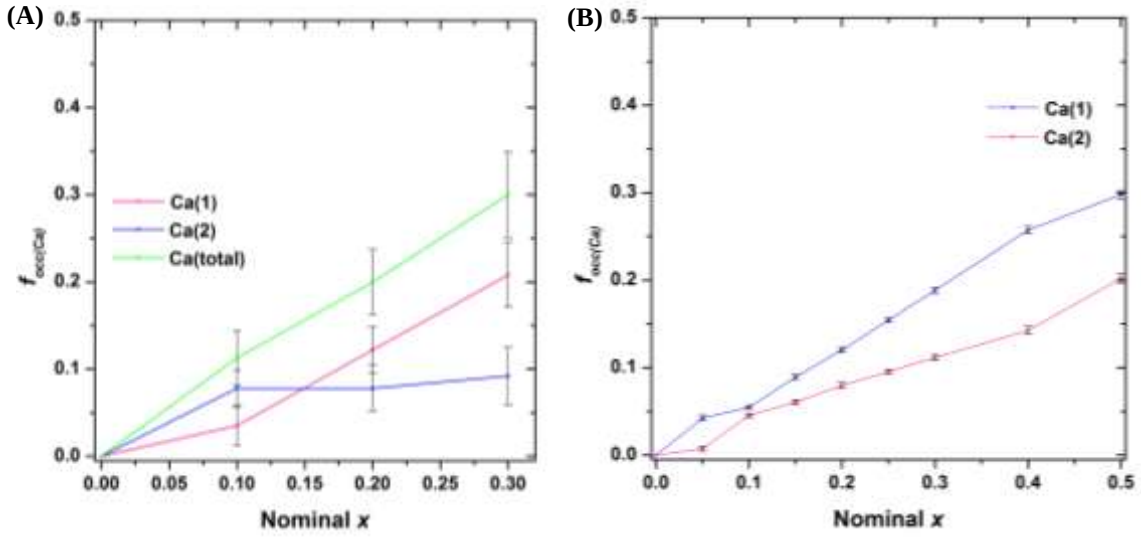

Figure 6.22 Ca occupancies on the Sr1 and Sr2 crystallographic sites from refinement against powder neutron diffraction data (A) and synchrotron X-ray powder diffraction data (B).

Fe/V mixing on the Fe crystallographic site, has been shown to have a very detrimental effect on the superconducting properties of Sr_2VO_3FeAs.[9] The extent of Fe/V mixing is therefore investigated in these samples by refinement against PND data employing a $f_{occ}V + f_{occ}Fe = 1$ constraint for the [2*a* (¼, ¾, 0)] site; it is shown from refinement against synchrotron X-ray powder diffraction data that both the Fe and V sites are fully occupied in all $Sr_{2-x}Ca_xVO_3FeAs$ samples (section 6.3.1.5). The results of these refinements indicate that, within the uncertainty of the refinement of about 0.3 %, there was no occupancy of

the Fe site by V. Furthermore similar analysis on the vanadium [2c (¼, ¼, 0.309)] crystallographic site does not indicate the presence of any Fe at this position.

x		**0**	**0.1**	**0.2**	**0.3**
Cell parameters and global fitting parameters:					
a / Å		3.93695(4)	3.93561(3)	3.93302(6)	3.93098(6)
c / Å		15.7143(3)	15.6711(2)	15.6574(4)	15.6589(5)
V / Å^3		243.565(6)	242.730(4)	242.19(1)	241.974(9)
R_{wp}		4.95	4.69	4.12	5.97
χ^2		4.685	4.158	4.515	7.382
Atomic parameters:					
Sr1/Ca1	[2*c* (¾, ¾, *z*)]	0.1897(1)	0.1900(2)	0.1901(2)	0.1898(3)
	U_{iso} ×100 / Å^2	0.43(4)	0.60(6)	0.19(7)	0.45(9)
	Sr_{occ} : Ca_{occ}		0.97(2) : 0.03(2)	0.88(3) : 0.12(3)	0.79(4) : 0.21(4)
Sr2/Ca2	[2*c* (¾, ¾, *z*)]	0.4138(2)	0.4137(2)	0.4131(2)	0.4126(3)
	U_{iso} ×100 / Å^2	1.09(5)	0.70(7)	0.47(3)	0.93(3)
	Sr_{occ} : Ca_{occ}		0.92(2) : 0.08(2)	0.92(3) : 0.08(3)	0.91(1) : 0.09(1)
Total *Ca occupancy*		0	0.11(3)	0.20(4)	0.30(5)
V	[2*c* (¼, ¼, *z*)]	0.309(1)	0.309(2)	0.309(2)	0.305(2)
	U_{iso} ×100 / Å^2	-2.6(3)	-1.4(5)	-4.1(4)	-5.4(4)
	V_{occ} : Fe_{occ}	1.000 : 0.000(3)			
Fe	[2*a* (¼, ¾, 0)]				
	U_{iso} ×100 / Å^2	0.70(3)	0.71(4)	0.68(6)	0.81(8)
	Fe_{occ} : V_{occ}	1.000 : 0.000(3)			
As	[2*a* (¼, ¼, *z*)]	0.0895(2)	0.0891(2)	0.0891(2)	0.0895(3)
	U_{iso} ×100 / Å^2	0.52(5)	0.77(4)	0.64(7)	0.79(9)
O1	[4*f* (¼, ¾, *z*)]	0.2937(1)	0.2928(1)	0.2924(2)	0.2923(2)
	U_{iso} ×100 / Å^2	0.67(3)	0.77(4)	0.47(5)	0.48(6)
O2	[2*c* (¼, ¼, *z*)]	0.4295(2)	0.4296(2)	0.4303(2)	0.4314(3)
	U_{iso} ×100 / Å^2	0.73(6)	1.01(6)	1.11(8)	1.16(9)
Impurity phases:					
FeAs / wt%		1.9(1)	3.2(1)	3.4(2)	5.4(2)
Sr_2VO_4 / wt%			1.78(5)		
$Sr_3V_2O_7$ / wt%		3.59(9)			1.49(9)
$SrFe_2As_2$ /wt%		9.1(1)		0.79(8)	
SrO / wt%		1.26(5)			

Table 6.2 Results of refinements against room temperature PND data

6.3.1.5 Synchrotron X-ray diffraction powder diffraction (ID31)

In order to more fully characterise the structural changes in $Sr_{2-x}Ca_xVO_3FeAs$ with *x* across the entire doping range, room temperature synchrotron X-ray powder diffraction measurements were performed on the ID31 beamline at the ESRF. Nine $Sr_{2-x}Ca_xVO_3FeAs$ samples, in the compositional range $0 \leq x \leq 0.5$, were loaded into 0.7 mm diameter borosilicate glass capillaries and measured at room temperature using 0.39987 Å X-rays. Data were collected in the 2-30 degrees 2θ range.

Rietveld refinements against these data sets were performed using TOPAS Academic and the Rietveld fit of $Sr_{1.85}Ca_{0.15}VO_3FeAs$ to room temperature X-ray powder diffraction data is shown in Figure 6.23. The refined atomic parameters are detailed in Table 6.3. Additional refined parameters are those to describe: background, 2θ zero error, scale factors, profile coefficients and Stephens model of asymmetric peak broadening.[13] Again

$Sr_3V_2O_7$, Sr_2VO_4 and FeAs impurities are present in all $Sr_{2-x}Ca_xVO_3FeAs$ samples, though typically at a level of less than 10 wt %. Small levels of $SrFe_2As_2$ were also identified, but are present at no greater than 5 wt %. The phase purity of $Sr_{2-x}Ca_xVO_3FeAs$ samples with $x \leq 0.3$ are at least of comparable to those reported elsewhere in the literature.[9,14,15] However samples with doping levels $x \geq 0.3$ become progressively less pure, as CaO, along with greater proportions of FeAs and $Sr_3V_2O_7$ impurity phases, grow in.

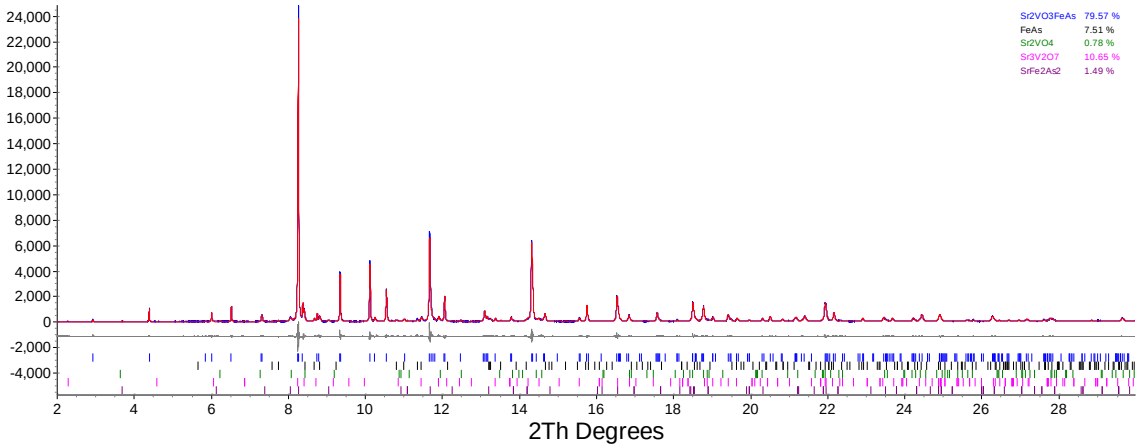

Figure 6.23 Rietveld fit of $Sr_{1.85}Ca_{0.15}VO_3FeAs$ to room temperature SXPRD data

As for refinements against PND data, the occupancy of Ca on the two Sr crystallographic sites was investigated by allowing the fractional occupancy of Ca (f_{occ}Ca) to refine on both Sr sites, with a f_{occ}Sr + f_{occ}Ca = 1 constraint. Given the good contrast in the X-ray scattering factors of Ca^{2+} and Sr^{2+}, one would expect to obtain reliable occupancies from refinement against synchrotron X-ray diffraction data. However, upon refinement, the Ca fractional occupancies frequently refined to values that were inconsistent with the nominal compositions and refined cell volumes. The reason for this is unclear, though it is likely that strong correlation between U_{iso} and f_{occ} parameters combined with those describing asymmetric peak broadening (Stephens model) and peak shape is a contributing factor.

Since the cell parameters derived from refinement against PND and SXRD data show very similar trends with *x*, further refinements against ID31 data were undertaken with a constraint fixing the overall occupancy of Ca^{2+} to that of the nominal composition and the total occupancy of each site to 1, but allowing the distribution of Ca^{2+} to be refined. Important structural parameters from these constrained refinements for the complete series of $Sr_{2-x}Ca_xVO_3FeAs$ samples measured on ID31 are given in Table 6.3. The refined distribution of Ca across the 2 crystallographic sites for both SXRD and PND data agree well and indicate that Ca has a preference for the inter-planar Sr(1) [2*c* (¾, ¾, ~0.190)]

crystallographic site that coordinates both arsenide and oxide in an anti-square prismatic coordination environment.

x (nominal)		0	0.05	0.1	0.15	0.2	0.25	0.3	0.4	0.5
Space group P4/*nmm*: cell setting 2										
Cell parameters and global fitting parameters:										
a / Å		3.93723(1)	3.93672(3)	3.93718(3)	3.93472(4)	3.93361(4)	3.93252(3)	3.93241(5)	3.92992(6)	3.92816(8)
c / Å		15.69298(7)	15.6845(1)	15.6678(1)	15.6755(2)	15.6705(2)	15.6703(2)	15.6669(2)	15.6553(3)	15.6525(5)
V / Å^3		243.269(2)	243.075(4)	242.874(4)	242.689(5)	242.474(2)	242.334(5)	242.270(7)	241.784(9)	241.52(1)
R_{wp}		0.0849	0.11029	0.11002	0.1006	0.01205	0.01414	0.11674	0.1634	0.18410
χ^2		1.825	2.789	5.29	2.72	3.49	3.771	2.599	4.96	5.871
Variables refined		76	79	79	79	84	84	84	84	84
Atomic parameters:										
Sr1/Ca1	[2*c* (¾, ¾, *z*)]	0.18980(7)	0.18982(7)	0.18973(7)	0.19023(6)	0.19038(8)	0.19090(8)	0.1907(1)	0.1910(2)	0.1904(2)
	U_{iso} ×100 / Å^2	0.34(2)	0.36(3)	0.30(2)	0.34(2)	0.39(3)	0.37(2)	0.18(3)	0.06(4)	0.12(5)
	Sr occ.		0.9587(3)	0.917(3)	0.911(3)	0.879(3)	0.846(3)	0.811(3)	0.743(5)	0.702(5)
	Ca occ.		0.0413(3)	0.083(3)	0.089(3)	0.120(3)	0.154(3)	0.189(3)	0.257(5)	0.298(5)
Sr2/Ca2	[2*c* (¾, ¾, *z*)]	0.41374(5)	0.41387(8)	0.41365(7)	0.41393(7)	0.41415(9)	0.41451(8)	0.4141(1)	0.4148(2)	0.4143(2)
	U_{iso} ×100 / Å^2	0.69(2)	0.69(3)	0.84(3)	0.59(2)	0.62(3)	0.62(3)	0.59(3)	0.72(5)	0.57(6)
	Sr occ.		0.9913(7)	0.983(3)	0.939(3)	0.920(3)	0.904(3)	0.889(3)	0.857(5)	0.798(5)
	Ca occ.		0.009(3)	0.017(3)	0.06(3)	0.080(3)	0.096(3)	0.111(3)	0.143(5)	0.202(5)
V	[2*c* (¼, ¼, *z*)]	0.30804(9)	0.3074(1)	0.3075(1)	0.3074(1)	0.3075(2)	0.30791)	0.3078(2)	0.3083(3)	0.3073(3)
	U_{iso} ×100 / Å^2	0.52(3)	0.53(4)	0.61(3)	0.74(4)	0.70(4)	0.80(4)	0.81(5)	0.86(8)	0.96(9)
Fe	[2*a* (¼, ¾, 0)]	0	0	0	0	0	0	0	0	0
	U_{iso} ×100 / Å^2	0.53(2)	0.68(3)	0.56(3)	0.64(3)	0.78(4)	0.89(3)	0.78(5)	0.76(7)	0.71(8)
As	[2*a* (¼, ¼, *z*)]	0.08939(6)	0.08892(9)	0.08921(8)	0.08969(8)	0.0898(1)	0.09012(9)	0.09063(1)	0.0916(2)	0.0919(2)
	U_{iso} ×100 / Å^2	0.47(2)	0.50(3)	0.53(2)	0.58(2)	0.62(3)	0.77(2)	0.63(3)	0.53(4)	0.69(6)
O1	[4*f* (¼, ¾, *z*)]	0.2945(2)	0.2934(3)	0.2928(3)	0.2922(3)	0.2918(3)	0.29139(3)	0.2915(3)	0.2911(5)	0.2914(6)
	U_{iso} ×100 / Å^2	0.60(7)	0.9(1)	0.66(9)	0.40(8)	0.6(1)	0.60(9)	0.8(1)	1.2(2)	2.5(3)
O2	[2*c* (¼, ¼, *z*)]	0.4293(3)	0.4291(3)	0.4290(4)	0.4313(3)	0.4292(4)	0.4324(3)	0.4318(4)	0.4318(5)	0.4344(6)
	U_{iso} ×100 / Å^2	0.9(1)	0.51(2)	0.8(2)	0.3(1)	1.4(2)	1.7(2)	0.4(2)	0.5(3)	1.2(3)
Impurity phases:										
FeAs / wt%		6.65	8.00	11.26	7.51	7.66	9.67	9.56	13.56	14.17
Sr_2VO_4 / wt%		5.75	4.69	6.83	0.78	3.98	2.98	0.25	0.01	0.02
$Sr_3V_2O_7$ / wt%		3.70	8.31	9.96	10.65	5.98	6.48	12.69	19.29	17.63
$SrFe_2As_2$ / wt%		3.87	3.51	4.9	1.49	1.15	1.31	1.25	1.49	1.43
CaO / wt%						1.59	2.03	3.91	2.79	4.48

Table 6.3 Results of PXRD refinements against room temperature synchrotron X-ray diffraction on $Sr_{2-x}Ca_xVO_3FeAs$ samples data measured in the 2θ range 2-30 °

6.3.1.6 Structural changes in $Sr_{2-x}Ca_xVO_3FeAs$ materials

Considering the overall contraction of both the *a* and *c* cell parameters with *x* across the $Sr_{2-x}Ca_xVO_3FeAs$ series, a decrease in the Fe-As bond length with upon Ca substitution might be anticipated. In fact the opposite is observed. After an initial decrease, a 0.998(3) % increase in Fe-As bond length with *x* is observed in the range $0.05 < x < 0.5$ (Figure 6.24). Similar trends are seen in two important and related parameters, namely the height of As above the Fe plane and the As-Fe-As bond angles in the $FeAs_4$ tetrahedra (Figure 6.24).

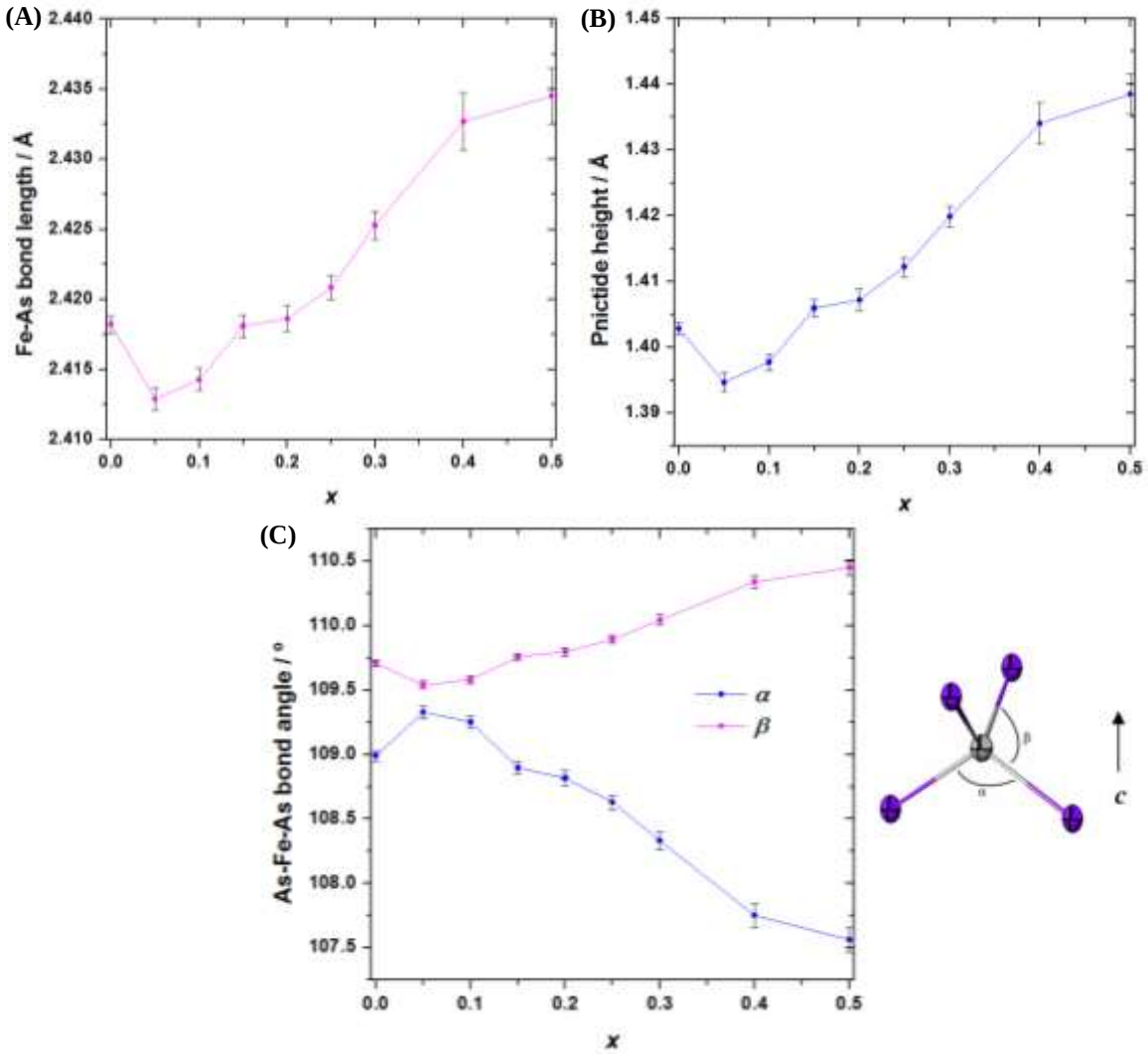

Figure 6.24 Plots of the (A) Fe-As bond length and (B) pnictogen height above the Fe plane against *x* for $Sr_{2-x}Ca_xVO_3FeAs$ samples. Inset shows a definition of the *α* and *β* As-Fe-As bond angles in a $FeAs_4$ tetrahedron.

To rationalise the changes in these important structural parameters it is useful to consider the observation that the Ca^{2+} dopant appears to preferentially occupy the inter-planar Sr(1) site [2*c* (¾, ¾, ~0.190)], which coordinates both oxide and arsenide anions, especially at higher doping levels. The presence of the smaller Ca^{2+} cation at this position has the effect of increasing the value of the *z* fractional coordinate of As, moving arsenic further away from Fe plane, increasing the Fe-As bond length and the four-fold *β* As-Fe-As bond angle. The observation that the Ca^{2+} is not doped exclusively onto either Sr crystallographic site is consistent with the non-linear variations in the lattice parameters.

Another plausible explanation for the observed Fe-As bond length changes can be argued from changes in the valence states of V and Fe. If the decrease in the cell volume across the $Sr_{2-x}Ca_xVO_3FeAs$ series causes a contraction in the coordination environment around

vanadium it is plausible that this could oxidise vanadium to a higher valence, with an accompanied reduction of iron. Since the Fe 3*d* orbitals of Sr_2VO_3FeAs at the Fermi level have been shown to be anti-bonding in nature,[16] one would expect this to lead to an increase in the Fe-As bond length. To test this hypothesis, the valence states of Fe and V were probed as a function of Ca doping through XANES measurements on the Fe and V *K*-edges.

6.3.1.7 XANES measurements (B18)

XANES measurements were performed on V and Fe absorption *K*-edges at the B18 beamline, Diamond Light Source, UK on $Sr_{2-x}Ca_xVO_3FeAs$ samples in the range $0 \leq x \leq 0.4$. One might expect that the chemical pressure exerted through partial replacement of Sr^{2+} with isovalent Ca^{2+} could contract the coordination sphere around V sufficiently to bring about a change in the V oxidation state. However, the normalised XANES spectra of $Sr_{2-x}Ca_xVO_3FeAs$ samples shown in Figure 6.25, exhibit no shift in the energy of the vanadium *K*-edge with *x*, indicating that the vanadium valence does not change. The slight variations in the positions of the V *K*-edge are attributed to poor data normalisation, however this does not effect the position of the maxima in the derivative, from which the edge position is estimated, only its magnitude.

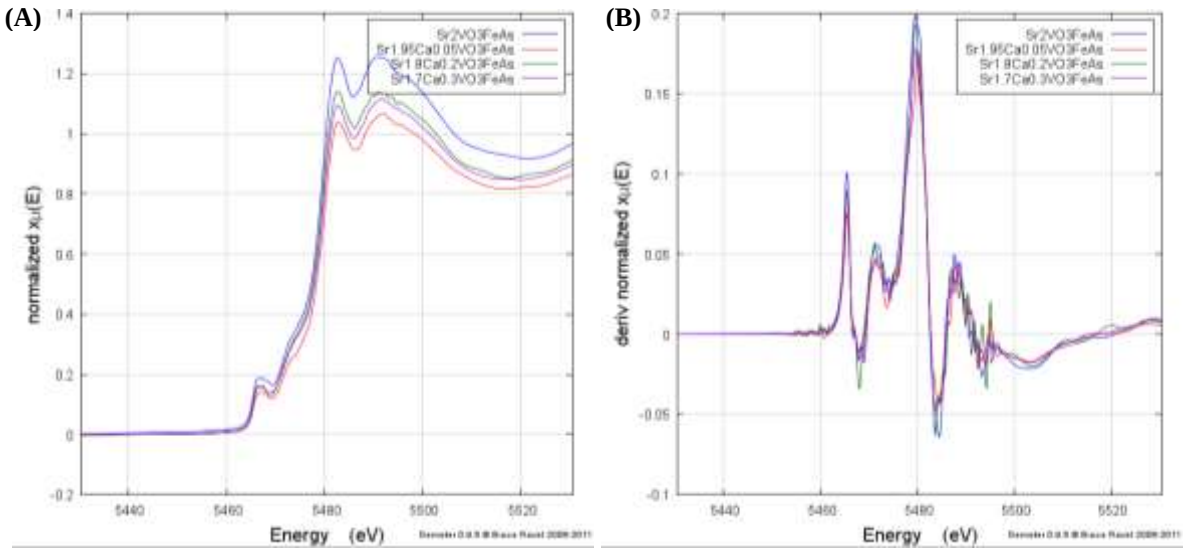

Figure 6.25 (A) Normalised vanadium *K*-edge of $Sr_{2-x}Ca_xVO_3FeAs$ samples. (B) Derivative of the normalised vanadium *K*-edge of $Sr_{2-x}Ca_xVO_3FeAs$ samples.

Measurements performed on the Fe *K*-edge were made in transmission mode and the normalised X-ray absorption spectra for $Sr_{2-x}Ca_xVO_3FeAs$ samples, with $x = 0$, 0.1, 0.2, 0.3 and 0.4 are shown in Figure 6.26.

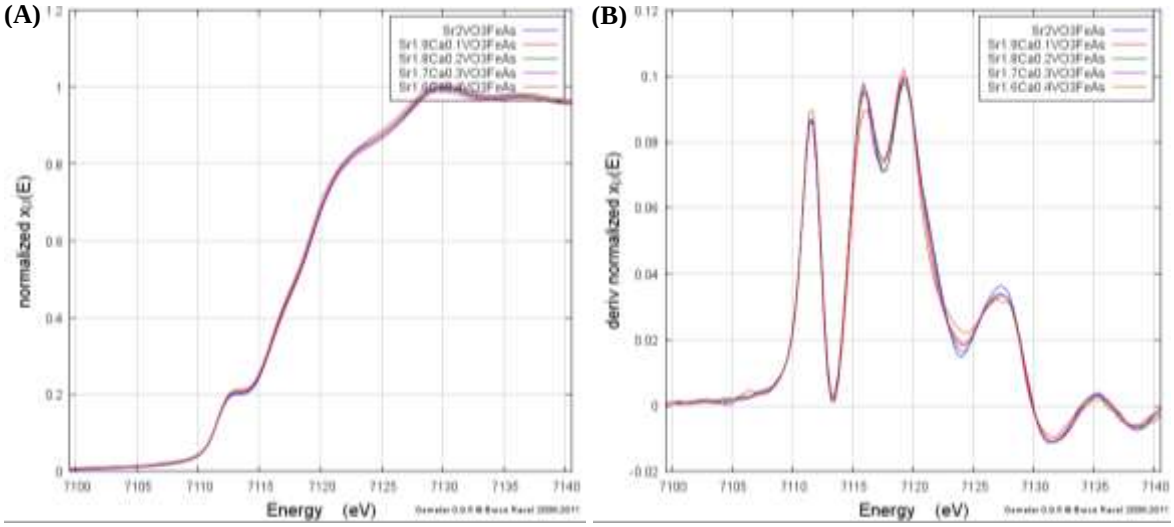

Figure 6.26 (A) Normalised iron *K*-edge of $Sr_{2-x}Ca_xVO_3FeAs$ samples. (B) Derivative of the normalised iron *K*-edge of $Sr_{2-x}Ca_xVO_3FeAs$ samples.

No shift in the position of the absorption edge is observed, indicating that Ca doping does not have an effect on the iron oxidation state and hence it is not a change in electron count that accounts for the dramatic variations in the superconducting properties of $Sr_{2-x}Ca_xVO_3FeAs$ materials.

6.3.2 Discussion

In summary, it is clear that the isovalent substitution of Sr^{2+} by Ca^{2+} in $Sr_{2-x}Ca_xVO_3FeAs$ has been successfully realised in the compositional range $0 < x < 0.5$, as evidenced by the linear decrease in the cell volume with x. This substitution also results in the complete suppression of superconductivity in samples with $x \geq 0.3$.

Investigations into the changes in the crystal structure and stoichiometry of $Sr_{2-x}Ca_xVO_3FeAs$ with x have been undertaken through neutron powder and synchrotron X-ray powder diffraction measurements. Refinement against neutron powder diffraction data collected on the D2B instrument at the ILL on $Sr_{2-x}Ca_xVO_3FeAs$ samples (x = 0, 0.1, 0.2 and 0.3) confirms the successful substitution of Ca from refined occupancies at levels equal within the uncertainty of the refinement to that of the nominal doping level. Furthermore no evidence for Fe/V mixing was observed on either crystallographic site. Synchrotron X-ray diffraction measurements on 9 samples of $Sr_{2-x}Ca_xVO_3FeAs$ were performed across the entire doping range $0 \leq x \leq 0.5$ to more fully characterise the structural changes imparted by this isovalent substitution. Surprisingly refinement results suggest that, despite the contraction in cell volume with x, the Fe-As bond length in

$Sr_{2-x}Ca_xVO_3FeAs$ increases upon Ca substitution. The observation is rationalised by consideration that the Ca dopant preferentially occupies the inter-planar Sr(1) site, which coordinates both oxide and arsenide in an anti-square prismatic environment (Figure 6.27). This has the effect of increasing the value of the *z* fractional coordinate of As, moving arsenic further away from Fe plane, increasing the Fe-As bond length and the four-fold β As-Fe-As bond angle, whilst decreasing the two-fold α As-Fe-As bond angle (Figure 6.28).

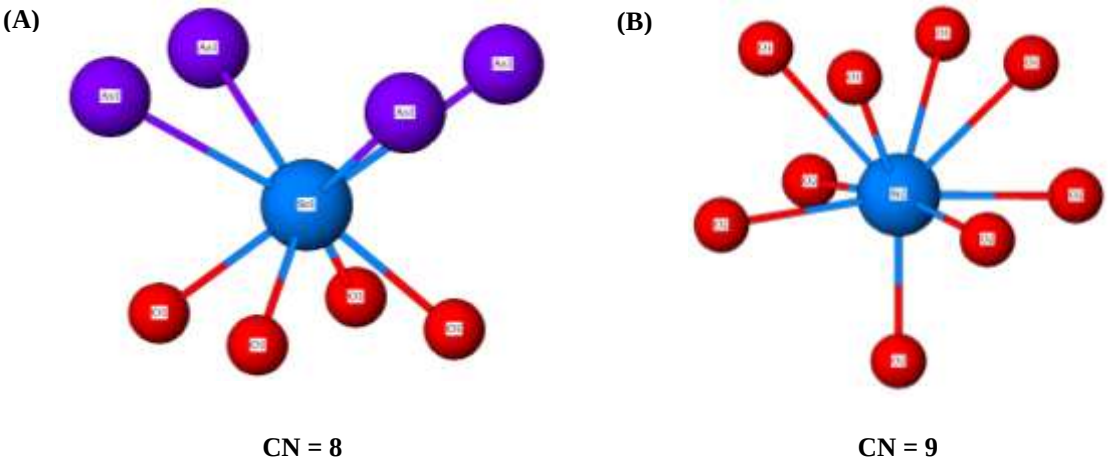

Figure 6.27 Coordination environments of Sr(1) (A) and Sr(2) (B).

XANES measurements performed on the Fe and V *K*-edges of $Sr_{2-x}Ca_xVO_3FeAs$ on the B18 beamline at Diamond were used to investigate any potential electronic changes brought about by this isovalent substitution. The results of these measurements show there to be no measurable shift in the position of either the Fe or V *K*-edges as a function of *x*, indicating that the valence states of iron and vanadium do not change. This result indicates that it is not a change in electron count that accounts for the dramatic variation in superconducting properties across the $Sr_{2-x}Ca_xVO_3FeAs$ series.

Instead the observed variation of T_c with *x* is rationalised by the structural changes brought about by Ca doping. Since the observed variation of T_c with *x* is non-linear a simplistic argument that the application of chemical pressure, as seen in the linear contraction in cell volume with *x*, suppresses superconductivity will not suffice. Lee *et al.* have highlighted a correlation between the *Pn*-Fe-*Pn* bond angles and T_c, demonstrating that T_c is maximised for a given Fe*Pn* based system as the bond angle approaches that of a regular tetrahedron (109.47 °). It was shown in chapter 5 that the $FeAs_4$ tetrahedra in undoped Sr_2VO_3FeAs are already close to regularity (109 °). In this chapter synchrotron X-ray powder diffraction measurements have been used to follow the variation of the As-Fe-As bond angles with *x*. Refinement results show that Ca substitution initially increases the regularity of $FeAs_4$

tetrahedra, before an approximately linear decrease in the α As-Fe-As bond angle is seen for samples with $x > 0.05$. If one compares the variation of the superconducting critical temperature and the α As-Fe-As bond angle with x, strikingly similar trends are observed. The relationship between the α As-Fe-As bond angle and T_c for $Sr_{2-x}Ca_xVO_3FeAs$ samples is presented in Figure 6.28.

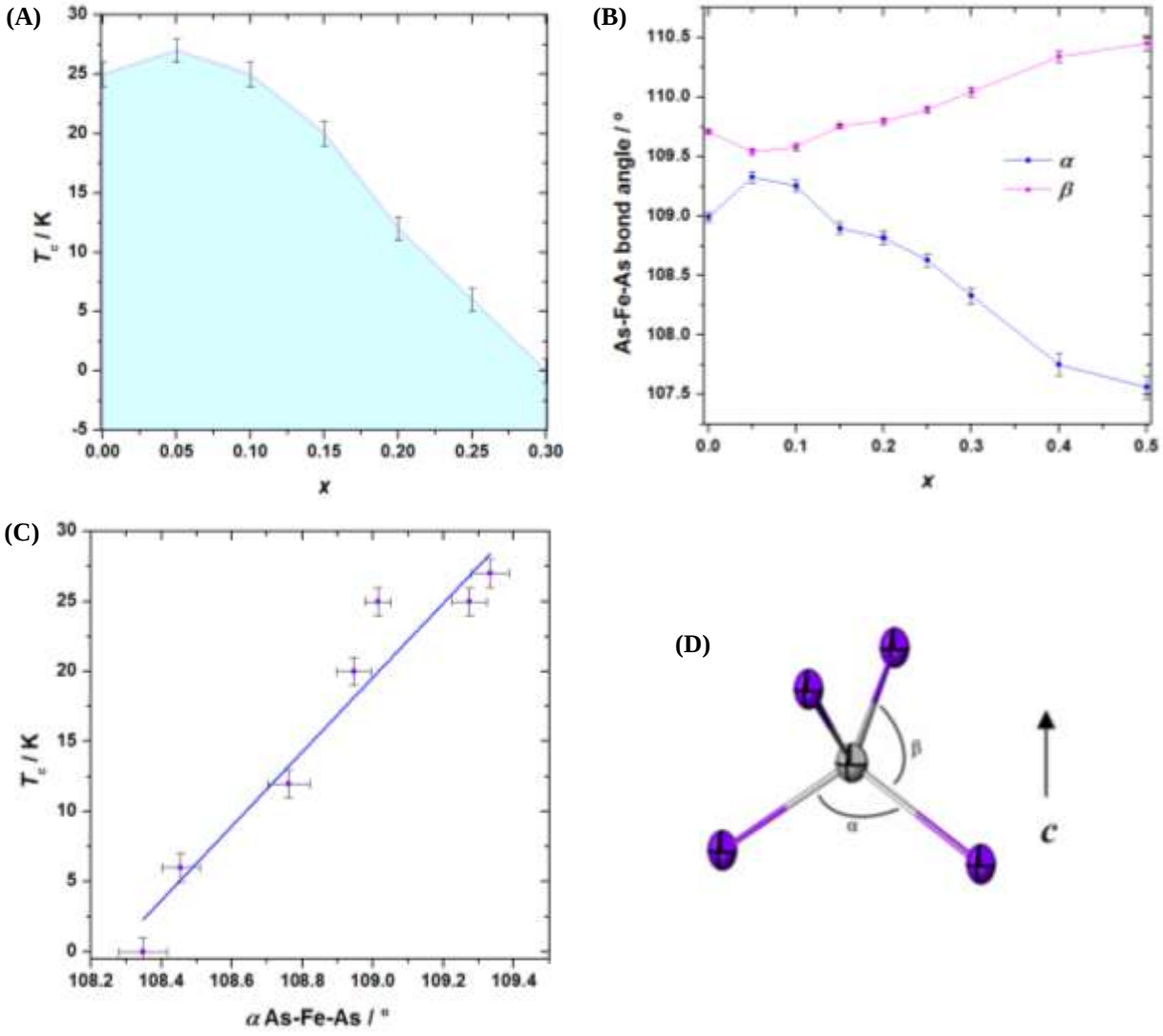

Figure 6.28 (A) Superconducting phase diagram of $Sr_{2-x}Ca_xVO_3FeAs$. (B) α and β As-Fe-As bond angles against x for $Sr_{2-x}Ca_xVO_3FeAs$ samples (C) Correlation between α As-Fe-As bond angle and T_c in Fe*Pn* superconductors. (D) Definition of the α and β As-Fe-As bond angles.

This plot clearly demonstrates a strong correlation between the α As-Fe-As bond angle and the superconducting critical temperature, with T_c maximised at 27 K in $Sr_{1.95}Ca_{0.05}VO_3FeAs$. The evolution of T_c and the shape of the $FeAs_4$ tetrahedron in this $Sr_{2-x}Ca_xVO_3FeAs$ system therefore offer further support to view that superconductivity in the iron-based superconductors is extremely sensitive to the crystal structure.

References

(1) Xie, Y. L.; Liu, R. H.; Wu, T.; Wu, G.; Song, Y. A.; Tan, D.; Wang, X. F.; Chen, H.; Ying, J. J.; Yan, Y. J.; Li, Q. J.; Chen, X. H. *EPL (Europhysics Letters)* **2009**, *86*, 57007.

(2) McGuire, M. A.; Gout, D. J.; Garlea, V. O.; Sefat, A. S.; Sales, B. C.; Mandrus, D. *Physical Review B* **2010**, *81*, 104405.

(3) Ohta, H.; Yoshimura, K. *Physical Review B* **2009**, *79*, 184407.

(4) Shinya, S.; Hiraku, O.; Naoto, K.; Yukari, K.; Kohji, K.; Jun-ichi, S.; Hisashi, K.; Hideki, T. *Superconductor Science and Technology* **2010**, *23*, 045001.

(5) Drew, A. J.; Niedermayer, C.; Baker, P. J.; Pratt, F. L.; Blundell, S. J.; Lancaster, T.; Liu, R. H.; Wu, G.; Chen, X. H.; Watanabe, I.; Malik, V. K.; Dubroka, A.; Rossle, M.; Kim, K. W.; Baines, C.; Bernhard, C. *Nat Mater* **2009**, *8*, 310-314.

(6) Wang, C.; Li, Y. K.; Zhu, Z. W.; Jiang, S.; Lin, X.; Luo, Y. K.; Chi, S.; Li, L. J.; Ren, Z.; He, M.; Chen, H.; Wang, Y. T.; Tao, Q.; Cao, G. H.; Xu, Z. A. *Physical Review B* **2009**, *79*, 9.

(7) Shannon, R. *Acta Crystallographica Section A* **1976**, *32*, 751-767.

(8) Sonier, J. E.; Brewer, J. H.; Kiefl, R. F. *Reviews of Modern Physics* **2000**, *72*, 769-811.

(9) Tegel, M.; Schmid, T.; Stürzer, T.; Egawa, M.; Su, Y.; Senyshyn, A.; Johrendt, D. *Physical Review B* **2010**, *82*, 140507.

(10) Garbarino G.; Weht R.; Sow A.; Lacroix C.; Sulpice A.; Mezouar M.; Zhu X.; Han .; Wen Hai Hu.; Núñez-Regueiro M. *EPL (Europhysics Letters)* **2011**, *96*, 57002.

(11) Lee, C. H.; Iyo, A.; Eisaki, H.; Kito, H.; Fernandez-Diaz, M. T.; Ito, T.; Kihou, K.; Matsuhata, H.; Braden, M.; Yamada, K. *Journal of the Physical Society of Japan* **2008**, *77*, 4.

(12) Johrendt, D.; Hosono, H.; Hoffmann, R.-D.; Poettgen, R. *Zeitschrift für Kristallographie* **2011**, *226*, 435-446.

(13) Stephens, P. *Journal of Applied Crystallography* **1999**, *32*, 281-289.

(14) Pal, A.; Vajpayee, A.; Meena, R.; Kishan, H.; Awana, V. *Journal of Superconductivity and Novel Magnetism* **2009**, *22*, 619-621.

(15) Zhu, X. Y.; Han, F.; Mu, G.; Cheng, P.; Shen, B.; Zeng, B.; Wen, H. H. *Physical Review B* **2009**, *79*, 4.

(16) Mazin, I. I. *Physical Review B* **2010**, *81*, 020507.

7 CeOMnAs

7.1 Introduction

Compounds with the ZrCuSiAs structure (Figure 7.1) show diverse electronic, magnetic and structural properties and of particular interest and relevance to this thesis are the novel class of superconductors containing FeAs anti-PbO-type layers, exemplified by $LaO_{1-x}F_xFeAs$.[1] A wide range of isostructural so-called '1111' iron arsenides derived from *Ln*OFeAs and *Ae*FFeAs materials has been described (*Ln* = La - Dy and *Ae* = Ca, Sr, Ba or Eu).[2,3,4,5] Upon cooling these stoichiometric compounds (and others containing similar FeAs layers and a formal Fe^{II} oxidation state) exhibit an itinerant antiferromagnetic order (often described as a commensurate spin-density wave) with an accompanying orthorhombic distortion of the crystal structure. Chemical doping or the application of hydrostatic pressure suppresses the magnetic order and the associated distortions and induces superconductivity.

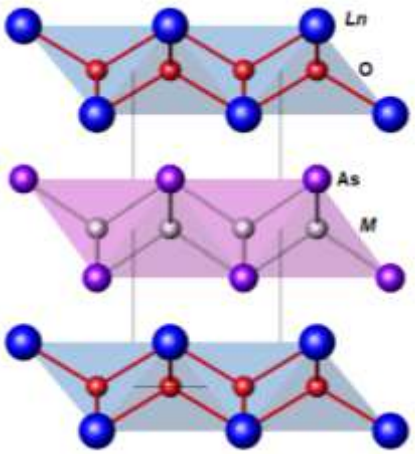

Figure 7.1 *Ln*O*M*As crystal structure

With such exotic phenomena observed in iron based '1111' materials it is of interest to investigate isostructural materials containing other 1st row transition metals in the anti-PbO-type arsenide layers. In *Ln*O*M*As materials (*M* = 1st row transition metal) it appears that the choice of transition metal in the arsenide layer largely dictates the physical properties. Ni analogues exhibit what appears to be conventional phonon-mediated superconductivity with T_c < 4 K and show quite different electronic properties to those seen in Fe-based high T_c superconductors.[6,7] The two extra *d* electrons supplied by Ni^{2+} (d^8) compared to Fe^{2+} (d^6) raise the Fermi level to generate a complex Fermi surface that is

quite unlike that of the Fe*Pn*-based superconductors.[8,9] By contrast *Ln*OCoAs (*Ln* = La, Ce, Pr, Nd, Sm, Gd) materials are metallic and are itinerant ferromagnets (with the exception of GdOCoAs which is ferrimagnetic) with small ordered moments associated with Co^{2+} below 70 – 100 K.[10,11] However, two further antiferromagnetic transitions (T_{N1} and T_{N2}) are observed in the cases of NdOCoAs and SmOCoAs. In NdOCoAs these transitions have been well characterised by powder neutron diffraction. Below T_{N1} NdOCoAs enters an antiferromagnetic state (***k*** = (0, 0, ½)) with small ordered moments on Nd and Co orientated in the *ab*-plane. The additional transition at T_{N2} is the result of an enhancement of the Nd^{3+} ordered moment and no change in the propagation vector is observed.[12] These curious changes in the interplanar ordering from FM to AFM states indicate an intriguing coupling between Co 3*d* and *Ln* 4*f* electrons. A schematic magnetic phase diagram for *Ln*OCoAs materials, along with the magnetic structure of NdOCoAs in its low temperature (***k*** = (0, 0, ½)) antiferromagnetic state are shown in Figure 7.2.

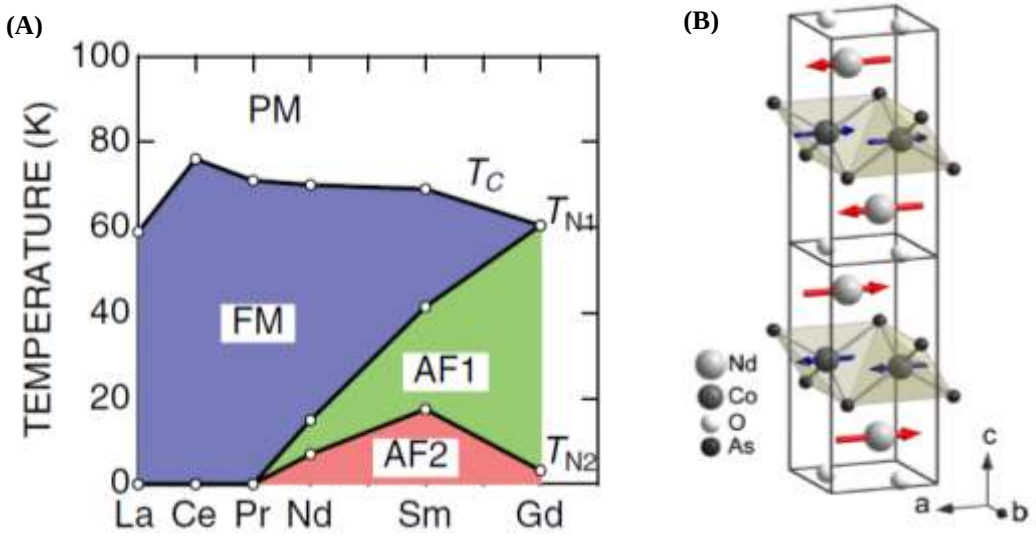

Figure 7.2 (A) Magnetic phase diagram of *Ln*OCoAs materials from *μ*SR experiments. (B) The low temperature AFM structure of NdOCoAs. [10,12]

A series of *Ln*OMnAs (*Ln* = Y, La, Ce, Pr, Nd, Sm, Gd, Tb, Dy, U) materials were first synthesised by Nientiedt *et al* in 1997.[13] Until recently their physical properties have received little attention. Other compounds with anti-PbO-type MnAs layers have been studied in more detail. For example $BaMn_2As_2$ with the $ThCr_2Si_2$ structure,[14] exhibits antiferromagnetic ordering of Mn^{2+} moments below T_N = 625 K with a checkerboard *G*-type magnetic structure and antiferromagnetic coupling between the layers. This indicates much stronger hybridisation between Mn 3*d* and As 4*p* states than seen in isostructural $BaFe_2As_2$, as well as the dominance of nearest-neighbour interactions.[14] More

recently *Ln*OMnAs (*Ln* = La, Nd) materials have been characterised and similarly shown to be semiconducting antiferromagnets.[15,16] The Mn^{2+} moments in these materials order antiferromagnetically above room temperature with a $\boldsymbol{k} = 0$ propagation vector and nearest neighbour Mn moments aligned antiferromagnetically within the layers, with moments directed along the *c* axis. The Mn moments related by the *c* lattice vector are aligned ferromagnetically, unlike $BaMn_2As_2$, presumably as a result of the increased dimensionality of these 1111 materials.

However, upon cooling NdOMnAs undergoes a spin-reorientation of the Mn moments into the *ab* plane, with the accompanied long-range AFM ordering of Nd moments and without a change in the magnetic propagation vector (Figure 7.3). In contrast LaOMnAs with no *f* electrons exhibits no such spin reorientation, indicating that a rare earth magnetic sublattice can influence the orientation of the Mn moments in the plane and is not restricted to altering the relative spin orientation between the planes as in NdOCoAs.

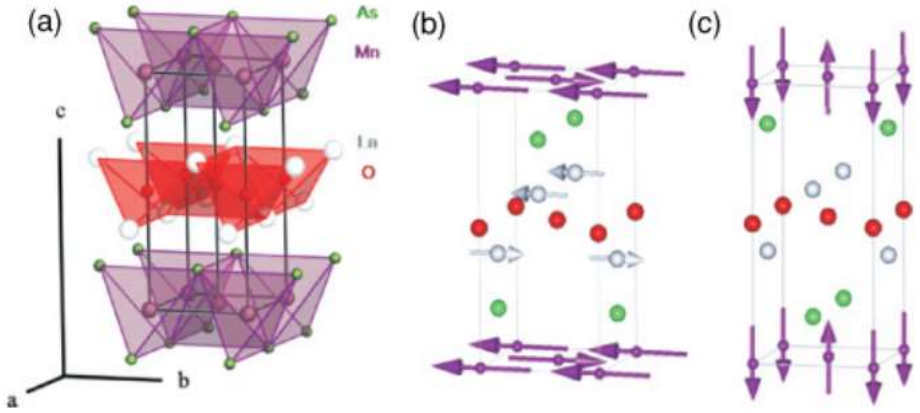

Figure 7.3 (a) Crystal structure, (b) 2 K magnetic structure and (c) 290 K magnetic structure of NdOMnAs, taken from a paper by Emery *et al.*[16]

A recent study of CeOMnAs shows evidence for a first-order phase transition at 34 K from magnetic susceptibility and heat capacity measurements.[17] In this chapter the changes in the magnetic ordering and crystal structure of CeOMnAs are followed through this transition by neutron powder diffraction.

7.2 Experimental

CeOMnAs samples were prepared on the 1 - 3 g scale by the solid state reaction of CeAs (the preparation of which is detailed in chapter 2), CeO_2 (Alfa, 99.99 %), As (Alfa, 99.9999 %) and Mn in a stoichiometric 1:1:1:2 ratio. This mixture was homogenized using an agate pestle and mortar, pressed into a pellet at a force of 5 tonnes, placed in an alumina crucible, then sealed in a silica ampoule under a dynamic vacuum. The sample

was then heated at a rate of 1 °C/min to 1100 °C and held at this temperature for 48 h. The resultant black crystalline powder was stored in an argon dry box.

7.3 Laboratory X-ray powder diffraction data

Initial structural characterisation was carried out by X-ray powder diffraction measurements. The sample was ground with a Si calibrant and measured at room temperature on a PANalytical pro diffractometer. Inspection of the resultant pattern revealed the sample to be largely phase pure with small amounts of CeO_2 (1.8 wt %). Multiple grinding and heating cycles did not lead to an increase in phase purity.

Rietveld analysis of the XRPD data was performed using the TOPAS-Academic software. The variables used to model the data include structural parameters summarised in Table 7.1 and parameters to model background, scale, profile coefficients, zero error and cell parameters for the CeO_2 and MnAs phases. The Rietveld fit to room temperature laboratory X-ray diffraction for CeOMnAs is given in Figure 7.4. The refined values for the cell parameters (Table 7.1) are comparable though slightly smaller than those reported by Nientiedt *et al.*.[13]

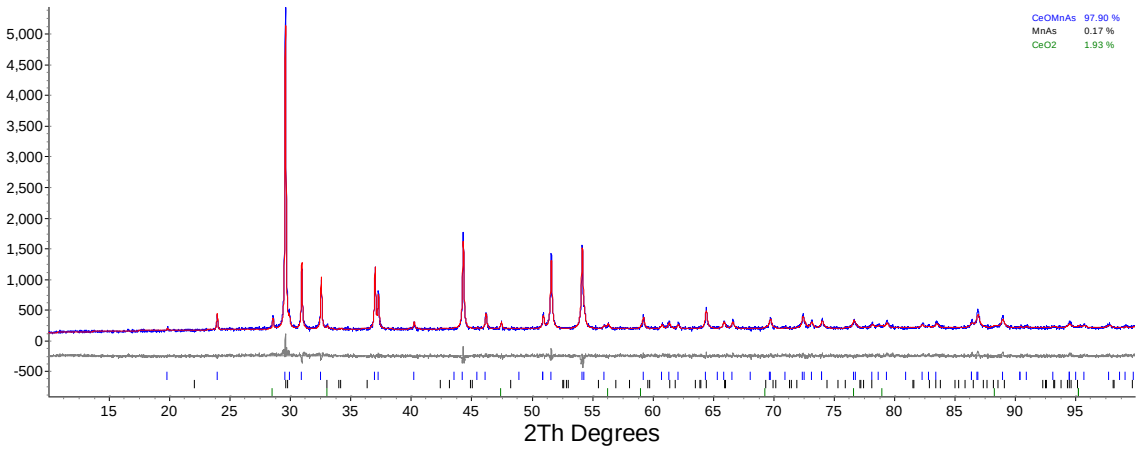

Figure 7.4. Rietveld fit to RT X-ray powder diffraction data CeOMnAs (AJC201)

7.4 SQUID magnetometry

In order to investigate the magnetic properties of CeOMnAs, magnetic susceptibility measurements were performed using a Quantum Design SQUID magnetometer. Firstly the magnetisation of CeOMnAs (AJC207) was measured as a function applied field at room temperature between -5 and 5 T, as shown in Figure 7.5.

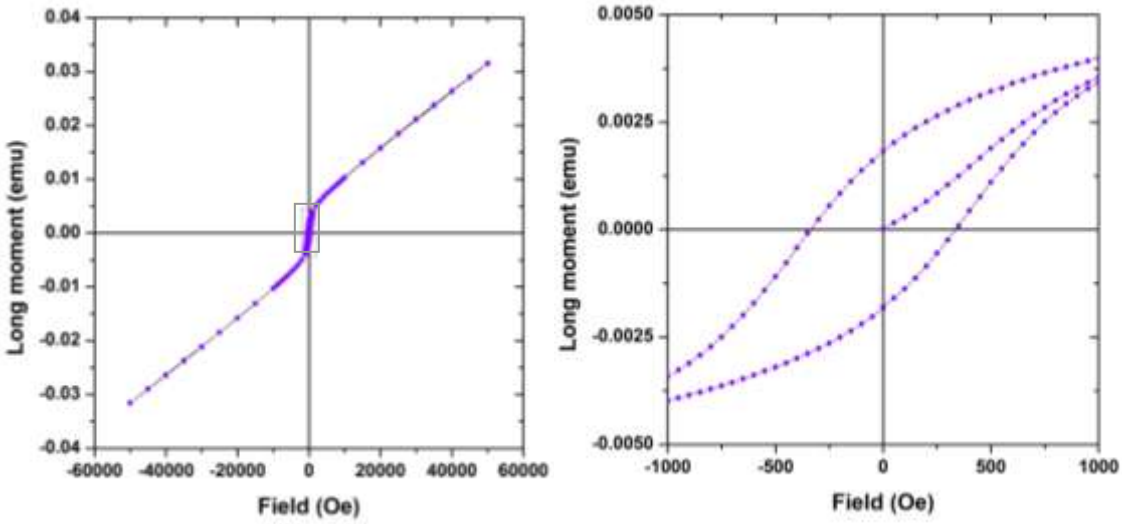

Figure 7.5 Hystersis loop of CeOMnAs at room temperature

These data show a weak hysteresis appearing to indicate ferromagnetism in this sample. This observation is perhaps unexpected for a material with MnAs antifluorite-type layers which typically ordered antiferromagnetically above RT. However, similar evidence for weak ferromagnetism is seen in magnetic susceptibility measurements in a study of LaOMnAs and NdOMnAs by Emery e*t al*.[18] They ascribed such behaviour to a small ferromagnetic spin canting of Mn magnetic moments. However, more recent studies of LaOMnAs and NdOMnAs do not show any evidence for ferromagnetism.[15,16] An alternative explanation for the observed behaviour is the presence of small amounts of a ferromagnetic impurity phase. MnAs, with the hexagonal NiAs-type structure, orders ferromagnetically at 318 K with Mn moments orientated perpendicular to the *c* axis.[19] By extrapolating the M vs H plot to zero field and given the room temperature ordered moment of MnAs (2.7 μ_B), one can calculate the implied mass fraction of MnAs in the sample to be 1.36 %, which although not observed in XRPD data can be clearly resolved in PND studies.

Since the observed data for CeOMnAs (AJC207) are consistent with the presence of a MnAs impurity phase, additional susceptibility measurements were made to extract the true susceptibility of CeOMnAs. As magnetisation has a non-linear dependence on *H* at low fields, measurements were made at two higher applied fields H_2 (4 T) and H_1 (3 T) that lie in the linear region above the ferromagnetic saturation field. *M* values are then converted to χ_{mol} by eqn. 7.1. The resulting plot of χ_{mol} against *T* is shown in Figure 7.6.

$$\chi_{mol} = \frac{M_{H2} - M1}{n(H_2 - H_1)} = \frac{M}{nH} \qquad \text{eqn. 7.1}$$

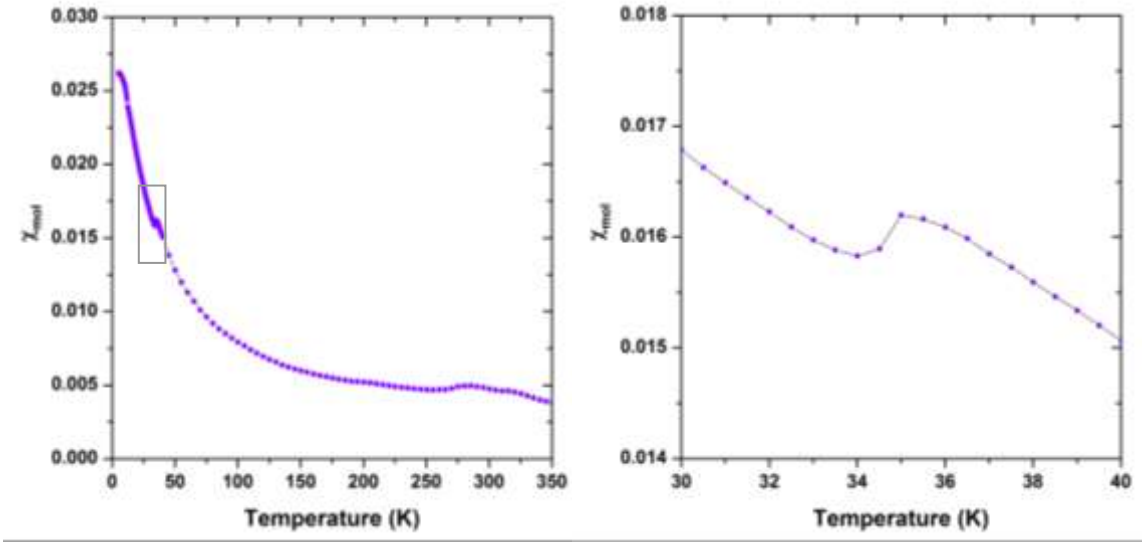

Figure 7.6 ZFC and FC susceptibilities between 350 and 2 K. Magnification of SR transition between 30 and 40 K.

An abrupt maximum is observed in the susceptibility at 35 K which is likely due to a spin reorientation of Mn moments concomitant with the onset of rare earth ordering as observed in NdOMnAs. Supporting these observations are magnetic susceptibility measurements on CeOMnAs samples described by Hiroi *et al*.[17]

7.5 Synchrotron X-ray powder diffraction 5-300 K

Variable temperature synchrotron X-ray diffraction measurements were performed on the ID31 instrument at the ESRF, with a view to identifying any changes in the crystal structure of CeOMnAs upon cooling through the proposed spin reorientation transition at 35 K. A sample of CeOMnAs (AJC201) was loaded into a 0.5 mm borosilicate glass capillary and cooled to 5 K in a liquid-helium-cooled cryostat. The capillary was then spun and data were collected at 5 K intervals on warming up to 50 K, with one further measurement at room temperature. All data collections were made over a 2θ range 0 - 30 ° using X-rays with a wavelength of 0.3499 Å.

Unfortunately the peak shapes in the majority of these data sets have proven difficult to model, and even obtaining a good Pawley fit to some diffraction patterns has been a considerable challenge. Furthermore, the intensities of some Bragg reflections appear to vary quite unsystematically with temperature, making Rietveld refinement against the low temperature data sets of little meaningful value. The reason for these issues is unclear,

though it may be related to poor powder averaging. However, the fit to the room temperature data set was sufficient to merit Rietveld analysis and the Rietveld fit to this data set is shown in Figure 7.7. Important structural parameters are given in Table 7.2 and also included is a CeO_2 impurity phase (2.3 wt %).

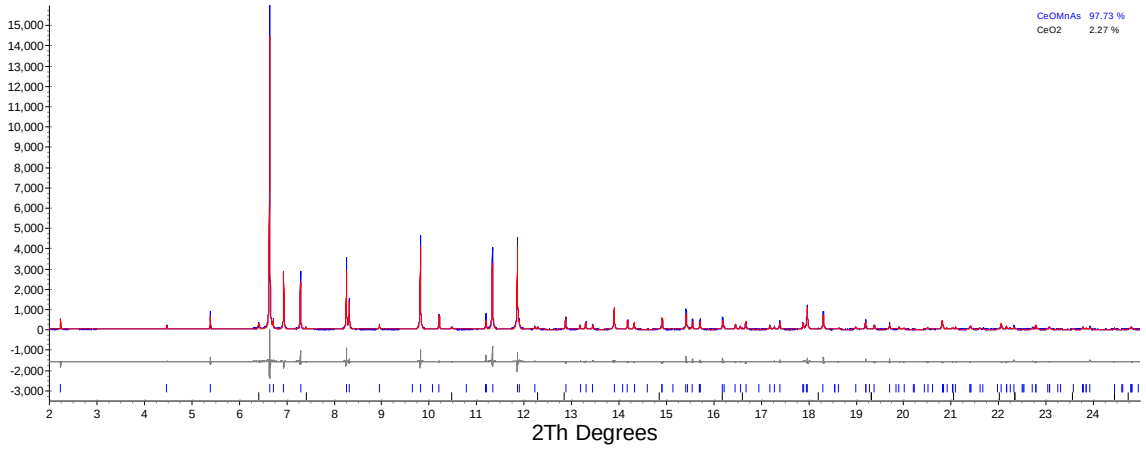

Figure 7.7 Rietveld fit to RT data for CeOMnAs

Space Group		*P*4/*nmm*	
Source	Lab. X-ray, CuK_α	ID31 λ = 0.4 Å	Nientiedt *et al* PXRD.[13]
Temperature / K	298	298	298
a / Å	4.0913(1)	4.09083(3)	4.086(1)
c / Å	8.96791(4)	8.96792(7)	8.956(2)
V / Å	150.11(1)	150.077(2)	149.5(3)

Table 7.1 Refinement results for CeOMnAs against XRPD data

Atom	*site*	*x*	*y*	*z*	*Occ.*	U_{iso} × 100 / Å^2
Ce	2*c*	0.25	0.25	0.1323(3)	1	0.76(2)
O	2*a*	0.75	0.25	0	1	0.33(4)
Mn	2*b*	0.75	0.25	0.5	1	0.63(3)
As	2*c*	0.25	0.25	0.6719(5)	1	1.3(2)

Table 7.2 Fractional coordinates and site occupancies for CeOMnAs from ID31 data

Despite the difficulties in modelling the atypical peak shapes and spurious intensities in the low temperature patterns some valuable information may be extracted from certain data sets by the examination of individual Bragg reflections. Whilst no structural distortions have been reported in *Ln*OMnAs materials to date, PrOMnSb exhibits a tetragonal (*P*4/*nmm*) to orthorhombic (*Pmmn*) transition at 35 K.[20] Interestingly this is a temperature

well below that at which the spin reorientation occurs (80 K) and the reduction in symmetry is thought to be driven by *f*-electron degrees of freedom.

To investigate whether such a transition is present in CeOMnAs, the (200)/(020) reflections were scrutinised. In the room temperature tetragonal unit cell these two reflections are coincident. However when the sample was cooled below 40 K a modest, but clear broadening of the reflection is observed (Figure 7.8) indicating a departure from tetragonal symmetry. The simplest transformation that can account for this observation is a small distortion in the *ab* plane lowering the symmetry of the space group to *Pmmn*. Since this distortion appears to occur between 40 and 35 K it is likely coincident with the anomaly in the magnetic susceptibility.

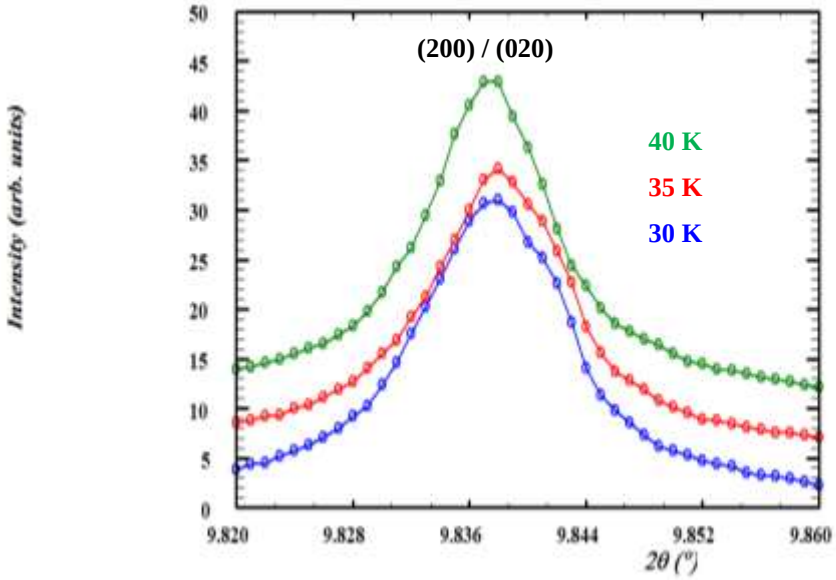

Figure 7.8 Splitting of (200) reflection into (200) and (020) as cell transforms from *P4/nmm* to *Pmmn* between 40 and 30 K.

7.6 Variable Temperature Powder Neutron Diffraction (PND)

In order to characterise the magnetic properties of CeOMnAs, a 3 g sample (AJC207) was prepared using the synthetic method described in section 7.2 and variable temperature powder neutron diffraction experiments were performed on this sample on the OSIRIS instrument at ISIS. Sample purity was assessed by room temperature laboratory X-ray powder diffraction and found to be largely phase pure, with small amounts of an CeO_2 (1.84 %) impurity phase. The OSIRIS diffractometer offers high resolution at high *d*-spacings, thanks to a 'cold' liquid hydrogen moderator, super mirror guide and back scattered detector bank (scattering angles 2θ from 150 – 171 °), making it a good choice

for investigations of magnetic Bragg reflections at high *d*-spacings. A more in-depth description of the instrument is given in chapter 2.

The sample was contained in a thin-walled vanadium cylindrical can and all measurements were performed inside an aluminium cryostat. This choice of cryostat means that aluminium Bragg reflections are observed from neutrons scattered on entry and upon leaving the cryostat. These are however well modelled by two Al Le Bail phases, with different cell parameters and zero shifts, which fortuitously did not overlap to a great extent with reflections from the main phase, at least at higher *d*-spacing where magnetic Bragg reflections were observed.

7.6.1 Room temperature CeOMnAs magnetic structure

Data were collected at 295 K over 5 *d*-spacing ranges, which were selected by adjusting the chopper frequency. Since the neutron flux decreases as the wavelength of the neutron increases, count times were extended at higher *d*-spacings, so that when the data sets are processed into a single file the statistics are comparable across the full *d*-range. Full details of the count times for different *d*-ranges at all temperatures are given in appendix H. One further consideration is the lack of good data at short *d*-ranges due to the curved guide cut-off, this makes accurate structural parameters more difficult to obtain than on other ToF diffractometers like POLARIS and HRPD. Therefore in refining a nuclear model of CeOMnAs against the 295 K data set, the structural model obtained from refinement against synchrotron X-ray powder diffraction data on the ID31 beamline was used as a starting point. An absorption correction for cylindrical samples (Lobanov and Alte de Veiga) was then refined and upon convergence was fixed thereafter and used for all data sets.

Other than the main CeOMnAs nuclear phase and aluminium from the cryostat (*Fm*-3*m*, $a \approx 4.03$ Å), additional phases were added to account for a minor CeO_2 impurity. Further weak reflections were observed at 3.21, 2.8 and 2.14 Å which are consistent with a MnAs impurity phase. Since MnAs orders ferromagnetically above room temperature ($T_C = 318$ K) a single Le Bail phase was used to model both the nuclear and magnetic contributions to the Bragg reflections. A broad peak between 2.25 and 2.31 Å was also observed, but could not be assigned, and since it was also observed in data collected on structurally unrelated materials it was deemed to instrumental in origin and this region was therefore excluded from the refinement.

Additional Bragg intensity which could not be modelled by the nuclear CeOMnAs phase or impurity phases can be seen in the difference plot of the Rietveld fit shown in Figure 7.9. All of these extra reflections could be indexed to a cell with the same dimensions as the CeOMnAs nuclear phase and were therefore assigned to a magnetic unit cell with a propagation vector $\boldsymbol{k}$ = 0. It is assumed that at room temperature only the Mn moments would contribute to the magnetic Bragg scattering. The presence of a strong (100) magnetic reflection (forbidden for the *P*4/*nmm* nuclear phase), implies antiferromagnetic ordering and the apparent absence of a magnetic contribution to the (002) reflection indicates ordering of the Mn moments along the *c* axis.

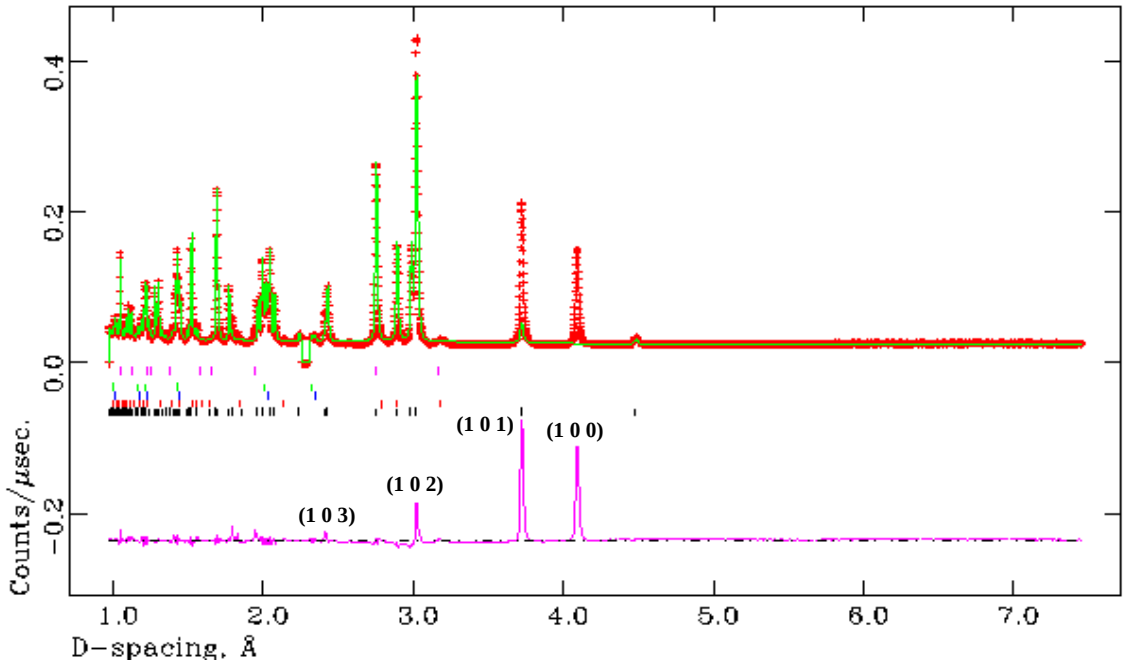

Figure 7.9 Rietveld fit of CeOMnAs nuclear (black), MnAs (red), CeO_2 (pink) and Al (green/blue) phases to room temperature PND data.

To fully investigate this magnetic phase studies in SARAh Representational Analysis and SARAh Refine interfaced with GSAS were undertaken. Four irreducible representations are possible for the arrangement of Mn^{2+} spins in the nuclear space group (*P*4/*nmm*) with the propagation vector $\boldsymbol{k}$ = (0 0 0). Two of these irreducible representations are degenerate so there are 6 basis vectors as shown in Figure 7.10. Γ(3) is a ferromagnetic arrangement of Mn moments along *z*, Γ(6) is an antiferromagnetic arrangement of spins along *z*, the Γ(9) basis vectors correspond to a ferromagnetic ordering along the *x* and *y* axis, whilst the Γ(10) arrangement represent antiferromagnetic ordering of Mn spins along the *x* and *y* axis. SARAh refine interfaced with the GSAS software was used to investigate which basis vector or combination of basic vectors best model the observed Bragg intensity. Initially all

six basis vectors were mixed in an attempt to fit the observed magnetic Bragg intensity. The results are visualised in Figure 7.11 in the form of contour plots, whose preparation is discussed in chapter 2.

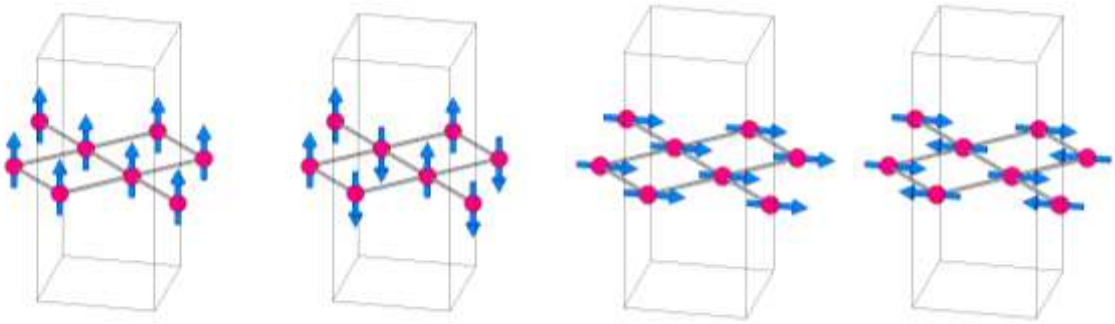

Γ(3)Ψ(1)
FM along *c*

Γ(6)Ψ(2)
AFM along *c*

Γ(9)Ψ(3) / Γ(9)Ψ(4)
FM along *a* and *b*

Γ(10)Ψ(5) & Γ(10)Ψ(6)
AFM along *a* and *b*

Figure 7.10 Basis vectors allowed for Mn ordering in CeOMnAs

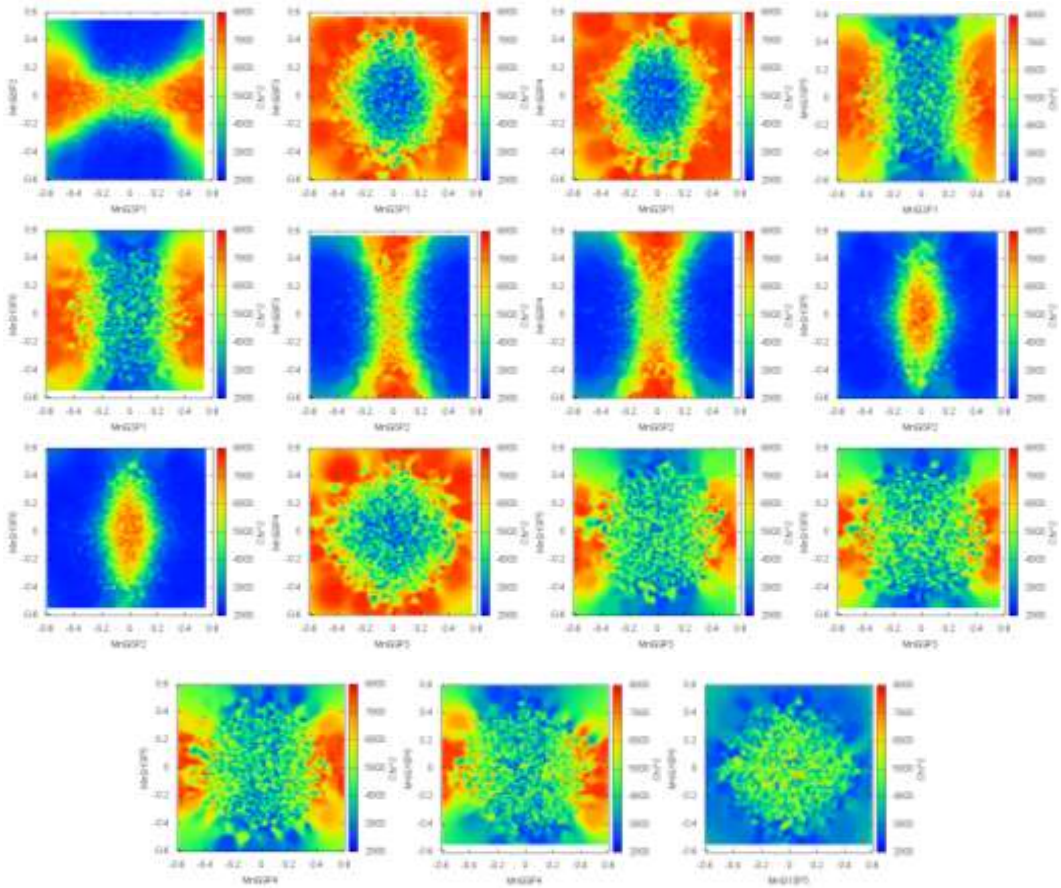

Figure 7.11 Results of reverse Monte Carlo analysis of 6 Mn basis vectors.

These results clearly indicate that values of χ^2 are consistently higher (red) for refinements in which a high proportion of basis vectors describing a ferromagnetic arrangement of Mn

moments were used. Further analysis was therefore carried out excluding the Γ(3)Ψ(1), Γ(9)Ψ(3) and Γ(9)Ψ(4) basis vectors. The resulting contour plots from this analysis are presented in Figure 7.12.

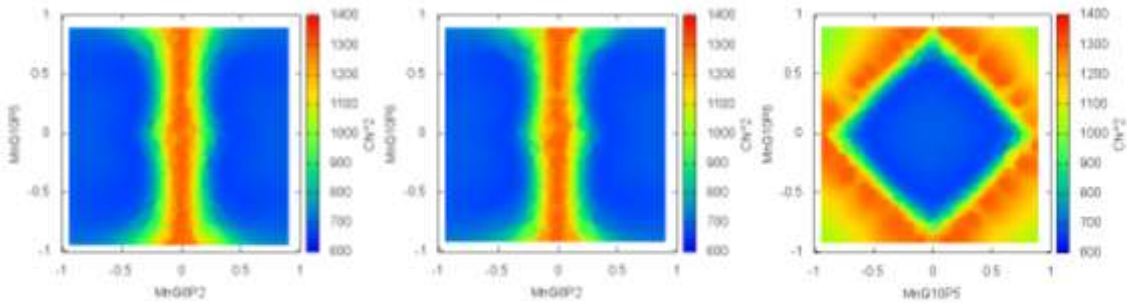

Figure 7.12 Contour plots representing the variation of χ^2 with the coefficients of the 3 antiferromagnetic Mn basis vectors Γ(6)Ψ(2), Γ(10)Ψ(5) & Γ(10)Ψ(6).

These results clearly indicate that the Γ(6)Ψ(2) basis vector in which Mn moments are arranged AFM along *c* gives the best fit to the data and this was therefore deemed to be the likely magnetic structure. However, as previously discussed, magnetisation against field measurements at room temperature suggest weak ferromagnetism. Whilst this is likely accounted for by the presence of a minor ferromagnetic MnAs phase, further analysis was carried out to investigation the possible ferromagnetic canting of Mn moments in the basal plane. This was undertaken by mixing the Γ(6)Ψ(2) basis vector with the Γ(9)Ψ(3) basis vector which describes a ferromagnetic arrangement of Mn spins, with moments orientated along the *a* axis. The results of this analysis are presented in Figure 7.13 and do not suggest any strong evidence for ferromagnetic canting of Mn moments. However neither can one rule out a small degree of canting as whilst χ^2 is minimised in refinements in which Γ(6)Ψ(2) is maximised, it remains invariant as small proportions of Γ(9)Ψ(3) are introduced.

That said, it is suggested that the ferromagnetic character observed from room temperature *M* vs *H* measurements is a result of the minor MnAs phase observed in the sample, as further measurements on additional CeOMnAs samples show a linear dependence of *M* with *H* at room temperature. An antiferromagnetic arrangement of Mn moments is therefore used to model the observed data, with AFM nearest-neighbour coupling in the plane and ferromagnetic stacking of layers i.e Γ(6)Ψ(2). The Rietveld fit including the CeOMnAs magnetic phase to room temperature PND data is shown in Figure 7.14 and important structural parameters and global fitting parameters are detailed in Table 7.3. The refined Mn moment at 295 K of 2.61(1) μ_B is comparable, though slightly larger than that

reported by Emery *et al* in isostructural LaOMnAs (2.43(1) μ_B) and NdOMnAs (2.35(2) μ_B) materials.[16]

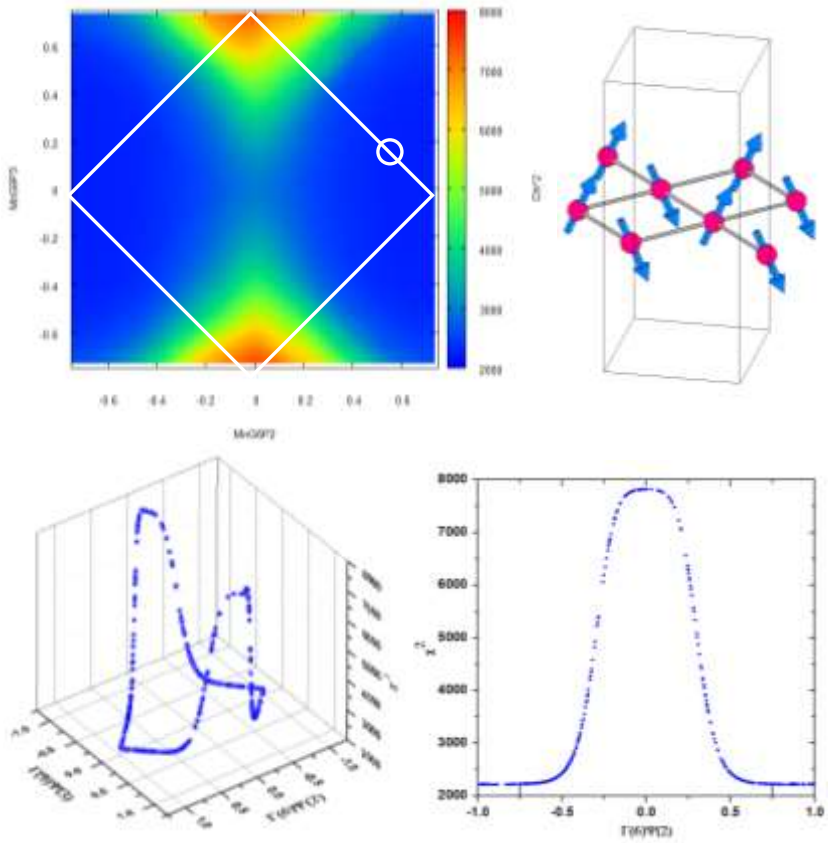

Figure 7.13 Results of combination of Γ(6)Ψ(2) with the Γ(9)Ψ(3) basis vectors describing ferromagnetic canting of Mn moments along the *a* axis.

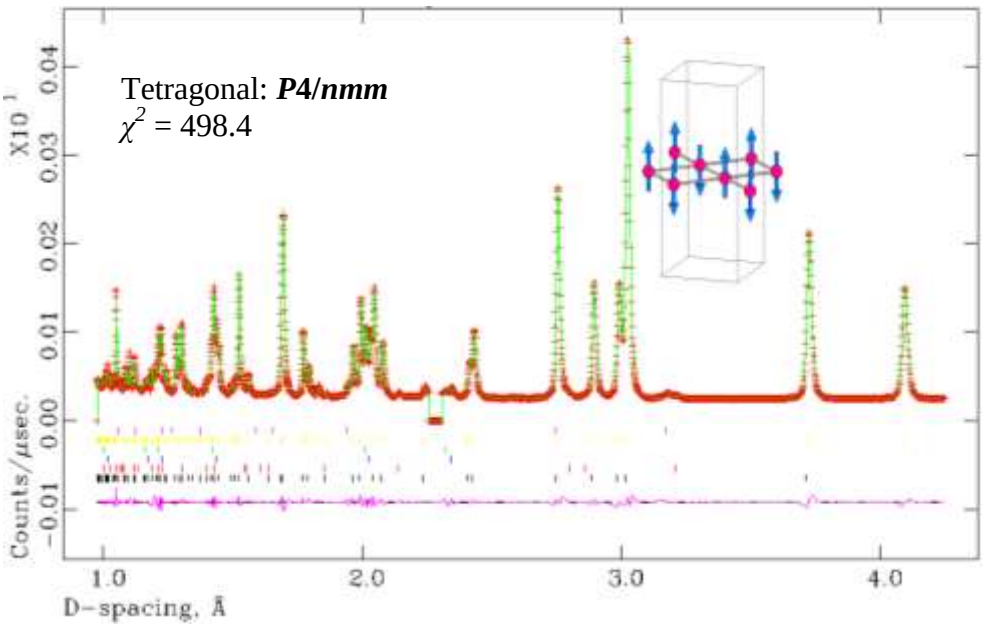

Figure 7.14 Rietveld fit to room temperature OSIRIS data and magnetic unit cell of CeOMnAs.

7.6.2 Determination of the 10 K magnetic structure

A comparison of the PND patterns collected at 295 and 10 K reveals a considerable difference in the relative intensities of reflections with magnetic contributions (Figure 7.15). No additional reflections are observed, however a magnetic contribution to the (002) reflection is observed. Once more all of these magnetic reflections could be indexed on the nuclear cell, implying that a propagation vector of $\boldsymbol{k} = 0$ is still valid.

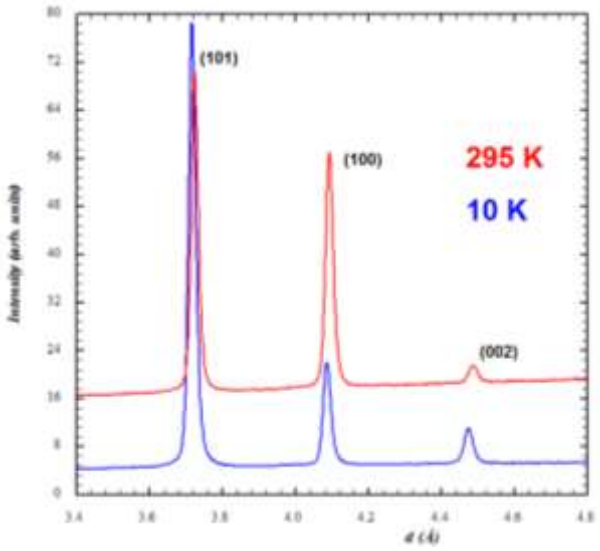

Figure 7.15 Comparison of the normalised PND collected on CeOMnAs at 295 and 10 K

SARAh representational analysis was undertaken in the *P*4/*nmm* space group, with a $\boldsymbol{k} = 0$ propagation vector, including both Ce^{3+} and Mn^{2+} as magnetic atoms. The basis vectors for Mn are identical to those at room temperature (Figure 7.10) and those generated for Ce are similar with 4 irreducible representations (irreps) two of which are degenerate to give the 6 basis vectors described in Figure 7.16. SARAh refine was then used to mix all 12 basis vectors. The results of these refinements are given in appendix H.

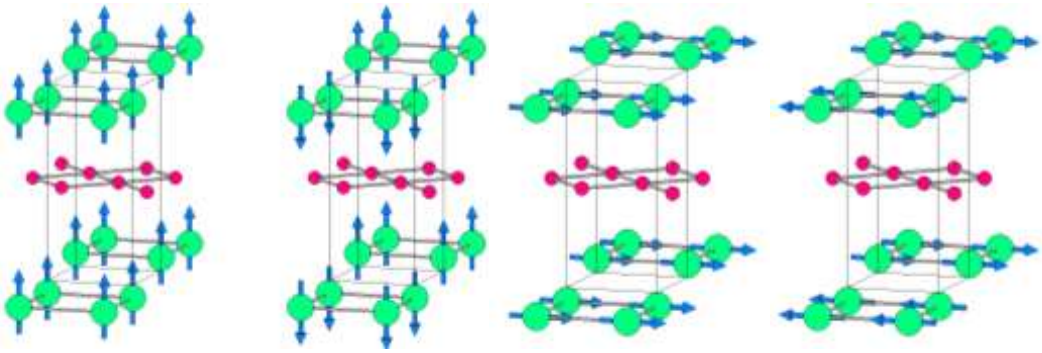

Γ(2)Ψ(1) **Γ(3)Ψ(2)** **Γ(9)Ψ(3) / Γ(9)Ψ(4)** **Γ(10)Ψ(5) & Γ(10)Ψ(6)**

Figure 7.16 Basic vectors describing Ce ordering in CeOMnAs

The results of this analysis suggest that values of χ^2 are consistently higher in refinements which describe a ferromagnetic arrangement of Mn and Ce moments. Further analysis was therefore attempted with the 6 basis vectors that describe antiferromagnetic arrangements of Ce and Mn moments. These results indicate that the presence of Ce $\Gamma(3)\Psi(2)$ and Mn $\Gamma(6)\Psi(2)$ basis vectors, which describe AFM ordering along the *z*-axis do not model the observed magnetic Bragg intensity well. A final set of refinement cycles were then performed mixing just the 2 degenerate $\Gamma(10)\Psi(5)$ and $\Gamma(10)\Psi(6)$ basis vectors for Ce and Mn. These refinement results are visualised in the contour plots shown in Figure 7.17 and clearly indicate that minimum values of χ^2 are obtained when the maximum or null coefficients of Mn $\Psi(5)$ and Ce $\Psi(5)$ or Mn $\Psi(6)$ and Ce $\Psi(6)$ basis vectors are sampled.

This implies a degenerate solution with a collinear arrangement of Mn and Ce moments arranged antiferromagnetically in the basal plane and aligned exclusively along either the *x* or the *y* axes. The magnetic phase was therefore described with Ce and Mn moments aligned along the *x*-axis with nearest neighbour antiferromagnetic interactions and ordered moments of 3.521(1) μ_B for Mn and 0.979(1) μ_B for Ce at 10 K. The Rietveld fit using this tetragonal magnetic and nuclear model of CeOMnAs is shown in Figure 7.19. This plot shows good agreement between the observed data and the calculated model. However, based on the observed broadening of the (200) reflection in low temperature ID31 data, peak modelling was undertaken in TOPAS to investigate the variation in specific peak positions as a function of temperature. Visual inspection of the magnetic (100)/(010) reflection between 40 and 30 K reveals, as well as a considerable decrease in intensity, a small shift in position to higher *d*-spacing. To quantitatively examine the significance of this observation, peak fitting of the (100)/(010), (110) and (004) reflections was carried out. The results of this analysis are displayed graphically in Figure 7.18.

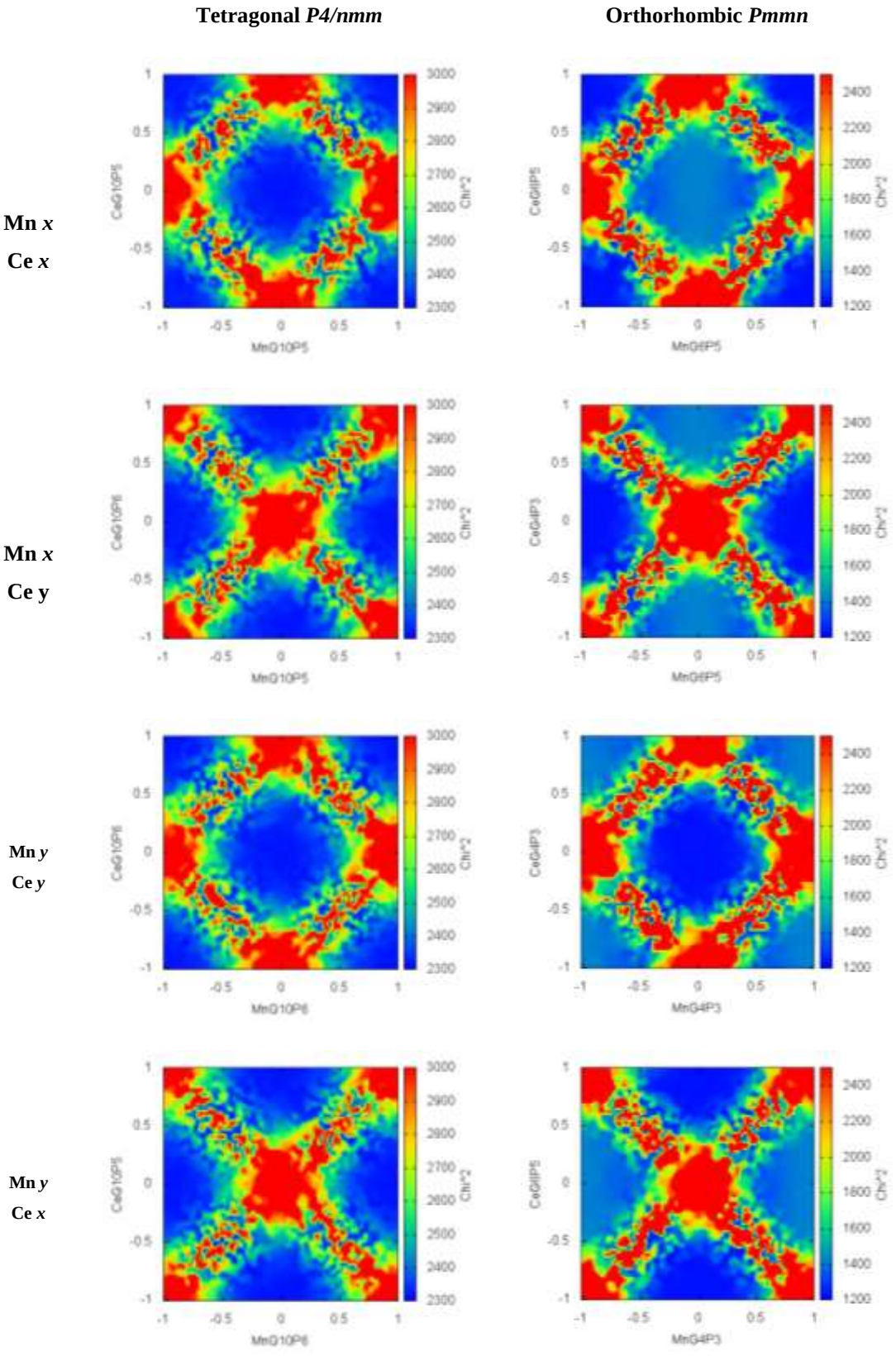

Figure 7.17 Contour plots describing the Γ(10)Ψ(5) & Γ(10)Ψ(6) basis vectors for Ce and Mn.

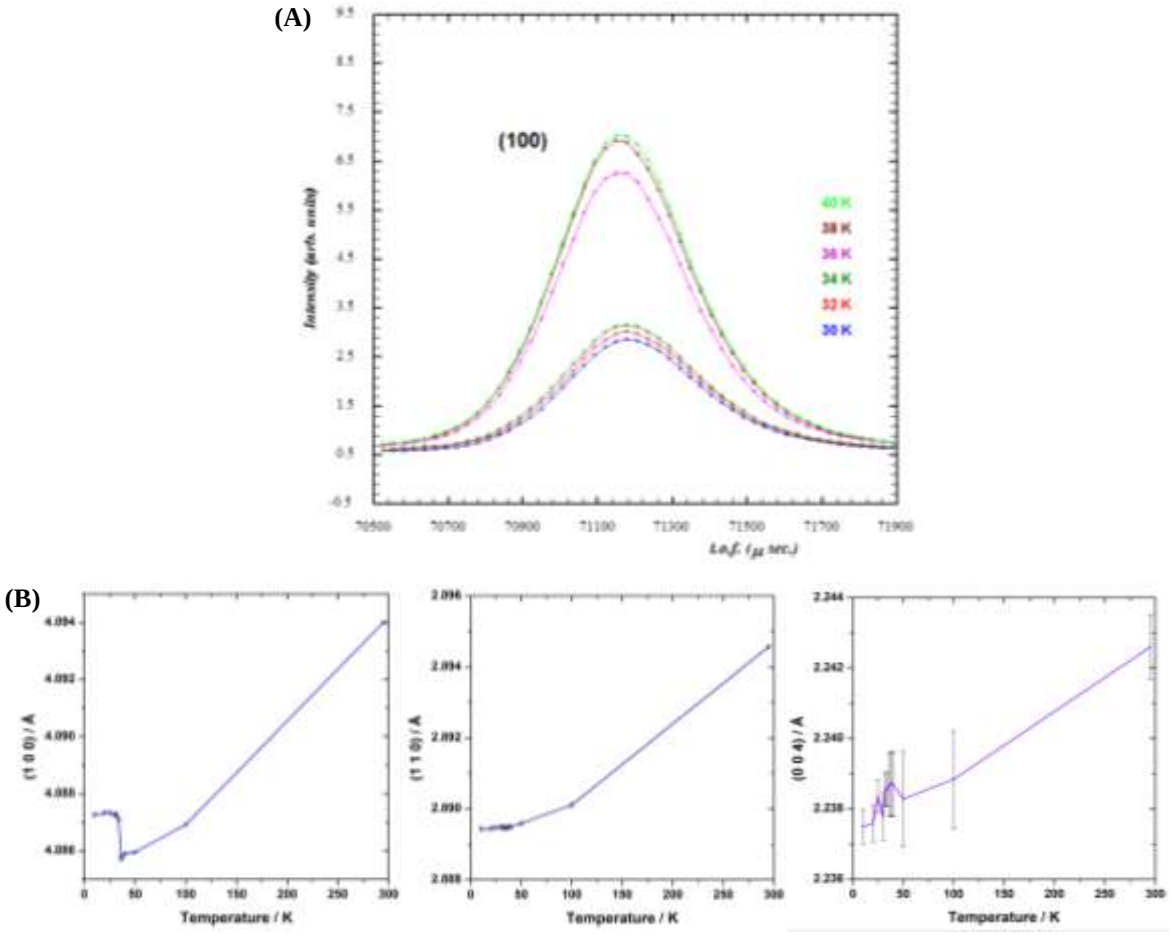

Figure 7.18 (A) Powder neutron diffraction patterns collect between 30 and 40 K in the range. 70500 - 71900 μsec (B) Peak positions of (100)/(010), (110) and (004) reflections as a function of temperature.

The *d*-spacing of the (110) reflection decreases with temperature, tailing off at 50 K with no great changes around the spin reorientation transition at 35 K. By contrast a dramatic increase is seen in the *d*-spacing of the (100)/(010) reflection between 36 and 34 K, though no appreciable change in the FWHM is observed. A naïve interpretation of this result would reason that the absence of an observable broadening/splitting of the (100)/(010) reflection would rule out an orthorhombic distortion in this system. However, one must consider that this reflection is purely magnetic in origin and that neutrons interact only with the projection of a magnetic moment in the plane perpendicular to the vector of that moment. The arbitrary choice of alignment of Mn and Ce moments along *x* therefore means that magnetic Bragg intensity is only observed for the (010) reflection and not the (100). The absence of an increase in the *d*-spacing of the (110) reflection below 35 K therefore implies that $a \neq b$ and that CeOMnAs undergoes a reduction in symmetry, most likely an orthorhombic distortion. The *d*-spacing of the (004) reflection shows an overall decrease upon cooling, and although the data appear to indicate a number of anomalies

below 50 K, the weak intensity of this reflection means that the error on the peak position is much larger than in the other cases and these anomalies were not judged to be significant.

Rietveld refinement against the 10 K data set was therefore repeated using the orthorhombic *Pmmn* subgroup for both the CeOMnAs nuclear and magnetic phases, but starting from a metrically tetragonal cell with $a = b = 4.082285$ Å and both Mn and Ce moment orientated along the x axis. The Rietveld fit to the data is shown in Figure 7.19, and the refined structural and magnetic parameters along with the global fitting statistics are summarised in Table 7.4. The goodness of fit χ^2 shows a significant improvement from 501.3 to 481.3 and refined values for a and b are 4.081097(8) Å and 4.08318(4) Å, respectively.

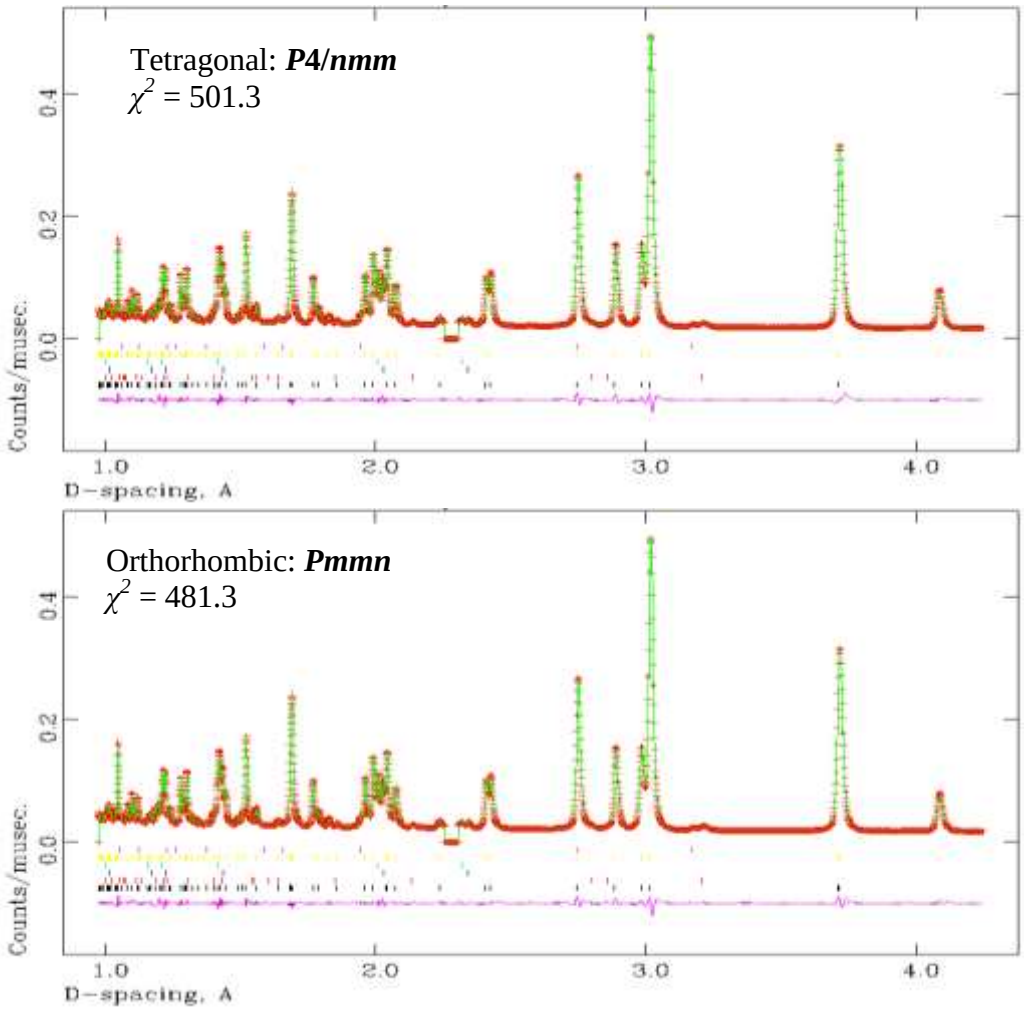

Figure 7.19 Rietveld fits to PND at 10 K using tetragonal and orthorhombic models.

Based on these observations further SARAh analysis was undertaken in the orthorhombic *Pmmn* space group with these new refined cell parameters, mixing the basis vectors that describe the AFM ordering of Mn and Ce moments in the basal plane. The results of this

analysis are compared with those of the tetragonal phase in Figure 7.17. Unsurprisingly these results are similar to those from the tetragonal model, but do clearly indicate that lower values of χ^2 are encountered when both Mn and Ce moments are exclusively aligned along the shorter *x* axis.

An alternative explanation for the observed shift in the position of the (100) reflection could also be as a result of a very small modulation of the magnetic order in the basal plane i.e. incommensurate magnetic order with a propagation vector $\boldsymbol{k}$ = (~0.0003, 0, 0). Further high resolution structural analysis is therefore required to examine whether CeOMnAs undergoes an orthorhombic transition about the spin-reorientation transition at 36 K, or whether CeOMnAs remains tetragonal and the observed shift in the (100) is as a result of incommensurate magnetic order which biases the OSIRIS refinement results towards an orthorhombic cell.

7.6.3 Variable temperature measurements

Rietveld analysis of the PND data collected at intermediate temperatures was then undertaken. For temperatures above and including 36 K a tetragonal *P*4/*nmm* CeOMnAs phase was found to give the best fit to the observed PND data. Below this temperature an orthorhombic *Pmmn* CeOMnAs phase shows an improved fit to the data relative to the tetragonal phase - an outcome consistent with the results of peak fitting to the (010) and (110) reflections. The variation of the lattice parameters of CeOMnAs with temperature are presented in Figure 7.20.

Magnetic Bragg intensity present in data collected in the 100 – 40 K temperature range was well modelled by the room temperature magnetic model with AFM nearest neighbour interactions of Mn moments directed along the *c*-axis and ferromagnetic coupling of the layers. In the proximity of the spin reorientation region, between 38 and 34 K, the data were fitted by refined contributions of the Mn moments m_x and m_z along the *a* and the *c* axes respectively, with a refined Ce moment along the *a*-axis. Below 34 K the 10 K magnetic model with refined Mn and Ce moments described the observed data well. The values of the refined structural parameters and refined Mn m_x m_z and Ce m_x moments across the full temperature are summarised in Table 7.3 and Table 7.4.

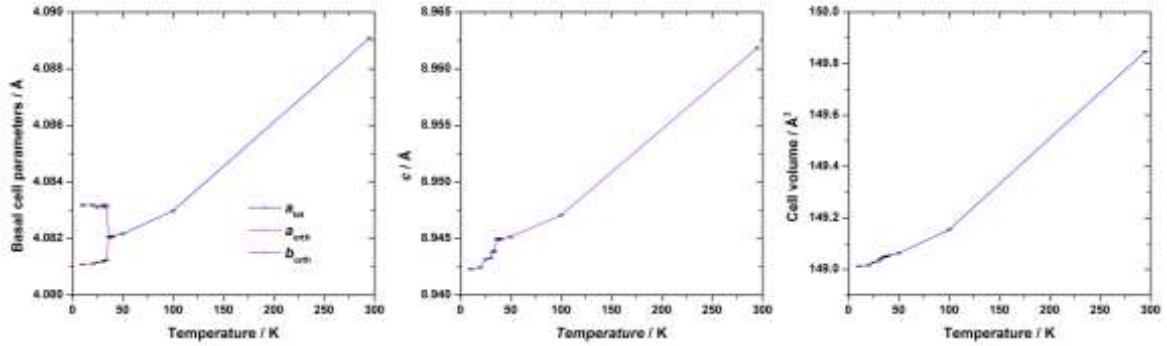

Figure 7.20 Variation in lattice parameters of CeOMnAs with temperature

Temperature / K	295	100	50	40	38	36
	Space group: ***P4/nmm*:2**					
Cell parameters:						
a / Å	4.08908(3)	4.08298(2)	4.08217(3)	4.08208(3)	4.08204(3)	4.08206(3)
b / Å						
c / Å	8.96185(1)	8.94706(1)	8.94517(1)	8.94498(1)	8.94496(1)	8.94488(1)
Cell volume / Å	149.847(2)	149.154(2)	149.063(2)	149.054(2)	149.050(2)	149.051(2)
Atomic parameters:						
Ce [2*c* (¼, ¼, *z*)]	0.1319(1)	0.1326(1)	0.1323(1)	0.1325(1)	0.13252(9)	0.13227(9)
U_{iso} × 100 / Å^2	1.39(4)	0.71(4)	0.91(3)	0.80(3)	0.90(3)	0.87(2)
m_x	0	0	0	0	0(0)	0.42(5)
Mn [2*c* (¼, ¼, 0.5)]						
U_{iso} × 100 / Å^2	1.05(4)	0.79(4)	0.85(3)	0.76(3)	0.83(3)	0.90(3)
m_x / μ_B	0	0	0	0	0(0)	1.03(2)
m_z/ μ_B	2.61(1)	3.477(6)	3.498(8)	3.480(8)	3.439(6)	3.219(6)
m_{total} / μ_B	2.61(1)	3.477(6)	3.498(8)	3.480(8)	3.439(6)	3.380(9)
As [2*c* (¼, ¼, *z*)]	0.67097(8)	0.67091(9)	0.67100(7)	0.67123(8)	0.67131(7)	0.67151(7)
U_{iso} × 100 / Å^2	1.15(3)	0.69(2)	0.70(3)	0.68(2)	0.68(2)	0.72(1)
O [2*c* (¼, ¼, 0)]						
U_{iso} × 100 / Å^2	1.17(3)	0.70(3)	0.81(2)	0.78(3)	0.81(2)	0.89(2)
Global fitting parameters:						
X^2	498.4	434.3	461.0	462.9	470.8	482.5
$_wR_p$	0.0339	0.0319	0.033	0.0331	0.0333	0.0338
Variables refined	44	44	44	44	47	47

Table 7.3 Results of refinement against variable temperature powder neutron diffraction data in the range (1.00 – 4.25 Å) on tetragonal CeOMnAs

Temperature / K	34	32	30	25	20	10
	Space group: ***Pmmn***					
Cell parameters:						
a / Å	4.081246(9)	4.081237(8)	4.081183(9)	4.081171(8)	4.081110(8)	4.081097(8)
b / Å	4.08316(5)	4.08312(5)	4.08317(5)	4.08312(5)	4.08318(4)	4.08318(4)
c / Å	8.94393(9)	8.94381(9)	8.94326(9)	8.94314(9)	8.94246(9)	8.94231(9)
Cell volume / Å	149.045(2)	149.041(2)	149.032(2)	149.028(2)	149.016(2)	149.013(2)

Atomic parameters:							
Ce	[2*b* (¼, ¾, *z*)]	0.8676(1)	0.8673(1)	0.8673(1)	0.8672(1)	0.8672(1)	0.8671(1)
	U_{iso} × 100 / Å^2	0.71(3)	0.79(3)	0.76(3)	0.74(3)	0.74(3)	0.79(3)
	m_x	0.55(1)	0.50(1)	0.61(1)	0.68(1)	0.95(1)	1.0(1)
Mn	[2*a* (¼, ¼, *z*)]	0.5033(2)	0.5017(2)	0.5002(2)	0.5008(1)	0.4995(2)	0.4995(3)
	U_{iso} × 100 / Å^2	0.66(3)	0.51(3)	0.56(3)	0.54(3)	0.48(3)	0.55(3)
	m_x / μ_B	3.216(9)	3.505(7)	3.518(7)	3.521(7)	3.562(7)	3.562(7)
	m_z/ μ_B	1.20(2)	0	0	0	0	0
	m_{total} / μ_B	3.434(9)	3.505(7)	3.518(7)	3.521(7)	3.562(7)	3.562(7)
As	[2*b* (¼, ¾, *z*)]	0.32885(9)	0.32929(9)	0.32922(9)	0.32920(9)	0.32925(8)	0.32931(9)
	U_{iso} × 100 / Å^2	0.69(2)	0.65(2)	0.67(2)	0.64(2)	0.61(2)	0.63(2)
O	[2*a* (¼, ¼, *z*)]	-0.0029(2)	-0.0010(1)	-0.0014(1)	-0.0012(1)	0.0013(1)	0.0004(1)
	U_{iso} × 100 / Å^2	0.71(2)	0.64(2)	0.66(2)	0.66(2)	0.62(2)	0.72(2)
Global fitting parameters:							
χ^2		478.9	483.9	480.2	485.8	483.6	481.3
$_wR_p$		0.0338	0.0339	0.0339	0.0341	0.0341	0.0341
Variables refined		50	48	48	48	48	48

Table 7.4 Results of refinement against variable temperature powder neutron diffraction data in the range (1.00 – 4.25 Å) on tetragonal CeOMnAs

7.7 Discussion

At room temperature CeOMnAs crystallises in the *P*4/*nmm* space group with lattice parameters from refinement against synchrotron X-ray powder diffraction of a = 4.09083(3) Å, c = 8.96792(7) Å and a cell volume of 150.077(2) Å^3. This unit cell volume is anomalously large when one considers a simple extrapolation of cell volumes for other CeO*M*As materials based on the transition metal ionic radii (Figure 7.21).

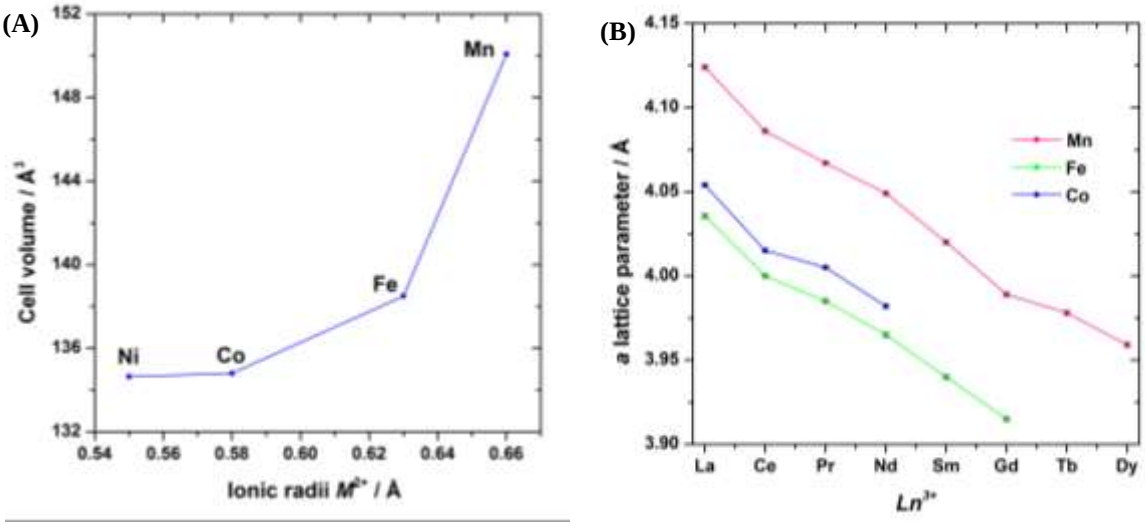

Figure 7.21 (A) Variation of cell volume with the ionic radii of M^{2+} in CeO*M*As. (B) Variation of the *a* cell parameter with rare earth metal for *Ln*OMnAs, *Ln*OFeAs and *Ln*OCoAs.

This is consistent with the localisation of electrons on the tetrahedral Mn ions and accounts for the large localised moment found for Mn in these compounds in contrast with the much smaller localised moments in the largely itinerant Fe and Co analogues. The Mn moments of CeOMnAs order above room temperature with a checkerboard nearest-neighbour antiferromagnetic arrangement in the basal plane. The ordered Mn moments are aligned along the *c* axis and the Mn planes are aligned ferromagnetically. At 295 K the ordered moment of Mn is 2.61(1) μ_B and on cooling to 100 K the moment saturates at a value of ~ 3.477(6) μ_B, a value significantly lower than that expected for free ion Mn^{2+} (5 μ_B). The value is similar to the saturation moment of the Mn^{2+} ions in similar Mn*Pn* (*Pn* = As, Sb) layers in the oxide pnictides $Sr_2Mn_2Pn_2O_3$ where the saturation moments (also reached below 100 K) are 3.5(1) μ_B and 3.4(1) μ_B for *Pn* = Sb and As, respectively.[21] The values of the saturation moments are also comparable to those for $BaMn_2P_2$ (4.2(1) μ_B)[22] and NaMnAs (4.01(5) μ_B)[23] and suggest a very significant reduction in the ordered moment as a consequence of covalency in the Mn-*Pn* bonding and the direct Mn-Mn interactions across shared tetrahedral edges. While the values of the saturated moments are all much reduced by around 1 μ_B compared with the value of 5 μ_B expected for Mn^{2+} there seems to be no clear correlation between the values and the interatomic distances in the Mn*Pn* layers. Brock *et al.* discuss the rather better dependence of the bond lengths with the antiferromagnetic ordering temperature. It is also noted that the ratio of μ/μ_{free} for Mn in CeOMnAs (0.6) is far greater than that of Fe in CeOFeAs (0.16).[24] The iron analogue – a parent of the high temperature iron-based superconductors behaves as an itinerant antiferromagnet and the striped magnetic structure which is very different from that adopted in the Mn analogues is understood by considering Fermi surface nesting and is not as predicted on the basis of superexchange interactions.

The spin reorientation transition occurs over a very narrow temperature range, of approximately 4 K, in which magnetic Bragg intensity is well modelled by Mn moments with contributions from both m_x and m_z. The cerium ions form two planes displaced by the vector (½*a* + ½*b*) in the basal plane and separated by oxide ions, forming a slab of Ce_4O tetrahedra each of which shares four edges with neighbouring tetrahedra. The cerium moments are aligned as ferromagnetic planes that are coupled antiferromagnetically along the *c* axis. The ordered moments of Ce and Mn from refinement against PND data between 100 and 10 K are shown in Figure 7.22.

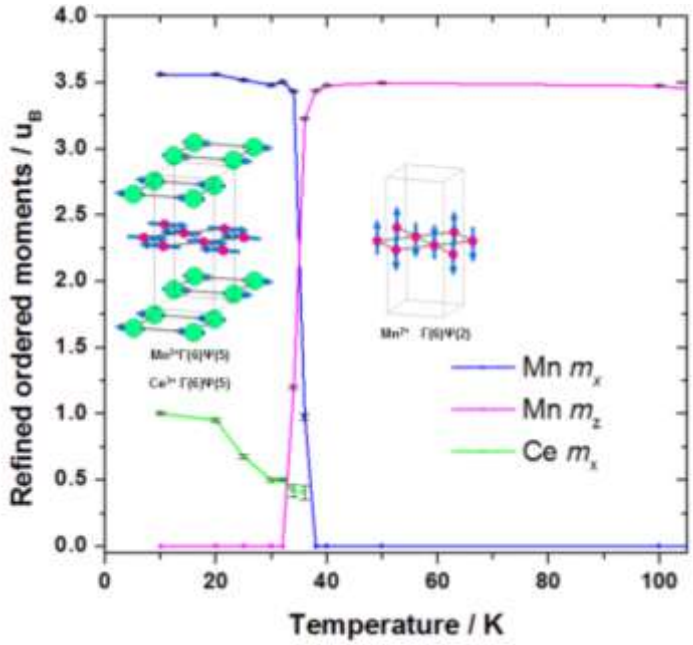

Figure 7.22 Refined values for Mn and Ce moments in CeOMnAs between 10 and 100 K

The ordered Ce moment is first evident with a value of 0.42(1) μ_B at 36 K and then increases reaching a value of 1.0(1) μ_B at 10 K which seems, from the temperature dependence, to be close to the saturation value. It seems likely that, as in the case of NdOMnAs, the spin reorientation of the Mn moments originates from the single-ion anisotropy of the rare earth moment. Above the SR transition only the Mn^{2+} (S = 5/2, L = 0) moments are ordered and these preferentially orientate along the c axis. The Ce^{3+} and Mn^{2+} moments are evidently not independent. The relatively high ordering temperature for the Ce sub-lattice suggests that the Ce order is driven by the interaction with the already-ordered Mn^{2+} moments. The single ion anisotropy of Ce^{3+} (S = ½, L = 3) dictates that the ordered Ce^{3+} moments lie in the basal plane and the relatively isotropic Mn moment follows the Ce moment leading to the observed spin reorientation.

The origin of the proposed orthorhombic distortion in CeOMnAs is undoubtedly different to that observed in CeOFeAs and other iron pnictides, which are itinerant antiferromagnets and the magnetic ordering is driven by Fermi-surface nesting leading to "striped" antiferromagnetic transition metal ordering. The distortion in CeOMnAs does not lead to an enlarged cell, but instead only a slight distortion in the basal plane and a reduction in symmetry from the *P*4/*nmm* tetragonal cell to the orthorhombic subgroup *Pmmn*.

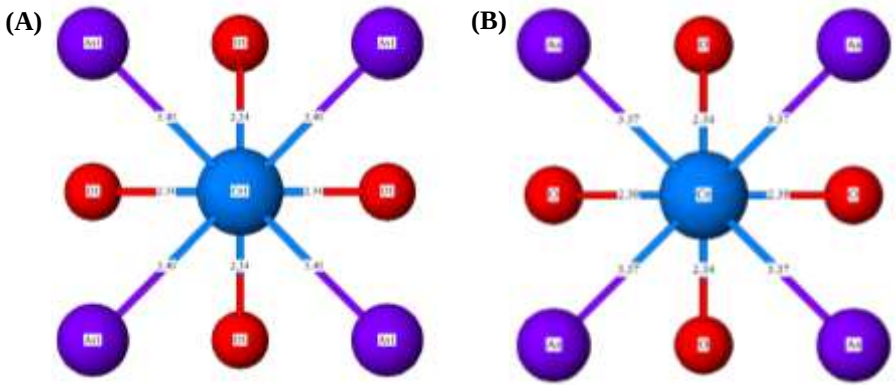

Temperature:	50 K	10 K
Space group:	*P*4/*nmm*	*Pmmn*
Ce site symmetry:	4*mm*	2*m*

Figure 7.23 Coordination environment of Ce (blue), viewed along *z*, to As (purple) and O (red) in CeOMnAs at 50 K (A) and 10 K (B) the spin reorientation temperature.

This distortion does not however have any effect on the Mn-Mn nearest neighbour distances ($\sqrt{2}(a + b)$), although the Mn–Mn–Mn angles deviate very slightly from 90 °. Furthermore it is of interest to note the absence of such a transition in recent studies of NdOMnAs, a material that also exhibits a spin reorientation transition of Mn moments concomitant with the ordering of the rare earth Nd moments. Whilst no structural distortions have been documented in *Ln*OMnAs materials to date, isostructural PrOMnSb exhibits a tetragonal (*P*4/*nmm*) to orthorhombic (*Pmmn*) transition at 35 K.[20] Interestingly the magnitude of the distortion in PrOMnSb ($(a - b)$ = 0.014 Å) is significantly greater than that seen in CeOMnAs ($(a - b)$ = 0.002 Å) and at a temperature well below that at which the spin reorientation occurs (80 K). In PrOMnSb the reduction in symmetry is thought to be driven by *f*-electron degrees of freedom and it is proposed that this is also the situation in CeOMnAs. Consistent with this hypothesis is a small crystallographic distortion of the Ce site (Figure 7.23) below 36 K (T_{SR}) with a split in the Ce-O distance. However further investigations are clearly required to confirm the existence and examine the origins of this distortion.

References

(1) Kamihara, Y.; Watanabe, T.; Hirano, M.; Hosono, H. *Journal of the American Chemical Society* **2008**, *130*, 3296.
(2) Matsuishi, S.; Inoue, Y.; Nomura, T.; Kamihara, Y.; Hirano, M.; Hosono, H. *New Journal of Physics* **2009**, *11*, 9.
(3) Han, F.; Zhu, X.; Mu, G.; Cheng, P.; Wen, H.-H. *Physical Review B* **2008**, *78*, 180503-4.
(4) Baker, P. J.; Franke, I.; Lancaster, T.; Blundell, S. J.; Kerslake, L.; Clarke, S. J. *Physical Review B* **2009**, *79*, 4.
(5) Bos, J. W. G.; Penny, G. B. S.; Rodgers, J. A.; Sokolov, D. A.; Huxley, A. D.; Attfield, J. P. *Chemical Communications* **2008**, 3634-3635.
(6) Watanabe, T.; Yanagi, H.; Kamihara, Y.; Kamiya, T.; Hirano, M.; Hosono, H. *Journal of Solid State Chemistry* **2008**, *181*, 2117-2120.
(7) Subedi, A.; Singh, D. J.; Du, M.-H. *Physical Review B* **2008**, *78*, 060506.
(8) Kurita, N.; Ronning, F.; Miclea, C. F.; Bauer, E. D.; Gofryk, K.; Thompson, J. D.; Movshovich, R. *Physical Review B* **2011**, *83*, 094527.
(9) Subedi, A.; Singh, D. J. *Physical Review B* **2008**, *78*, 132511.
(10) Sarkar, R.; Jesche, A.; Krellner, C.; Baenitz, M.; Geibel, C.; Mazumdar, C.; Poddar, A. *Physical Review B* **2010**, *82*, 054423.
(11) Yanagi, H.; Kawamura, R.; Kamiya, T.; Kamihara, Y.; Hirano, M.; Nakamura, T.; Osawa, H.; Hosono, H. *Physical Review B* **2008**, *77*, 224431.
(12) McGuire, M. A.; Gout, D. J.; Garlea, V. O.; Sefat, A. S.; Sales, B. C.; Mandrus, D. *Physical Review B* **2010**, *81*, 104405.
(13) Nientiedt, A. T.; Jeitschko, W.; Pollmeier, P. G.; Brylak, M. *Z. Naturforsch.* **1997**, *52b*, 560.
(14) An, J.; Sefat, A. S.; Singh, D. J.; Du, M.-H. *Physical Review B* **2009**, *79*, 075120.
(15) Marcinkova, A.; Hansen, T. C.; Curfs, C.; Margadonna, S.; Bos, J. W. G. *Physical Review B* **2010**, *82*, 174438.
(16) Emery, N.; Wildman, E. J.; Skakle, J. M. S.; McLaughlin, A. C.; Smith, R. I.; Fitch, A. N. *Physical Review B* **2011**, *83*, 144429.
(17) Tsukamoto, Y.; Okamoto, Y.; Matsuhira, K.; Whangbo, M.-H.; Hiroi, Z. *Journal of the Physical Society of Japan* **2011**, *80*, 094708.
(18) Emery, N.; Wildman, E. J.; Skakle, J. M. S.; Giriat, G.; Smith, R. I.; McLaughlin, A. C. *Chemical Communications* **2011**, *46*, 6777-6779.
(19) Bean, C. P.; Rodbell, D. S. *Physical Review* **1962**, *126*, 104-115.
(20) Kimber, S. A. J.; Hill, A. H.; Zhang, Y.-Z.; Jeschke, H. O.; Valentí, R.; Ritter, C.; Schellenberg, I.; Hermes, W.; Pöttgen, R.; Argyriou, D. N. *Physical Review B* **2010**, *82*, 100412.
(21) Brock, S. L.; Raju, N. P.; Greedan, J. E.; Kauzlarich, S. M. *Journal of Alloys and Compounds* **1996**, *237*, 9-19.
(22) Brock, S. L.; Greedan, J. E.; Kauzlarich, S. M. *Journal of Solid State Chemistry* **1994**, *113*, 303-311.
(23) Bronger, W.; Mueller, P.; Hoppner, R.; Schuster, H. U. *Z. Anorg. Allg. Chem.* **1986**, *539*, 175-182.
(24) Zhao, J.; Huang, Q.; de la Cruz, C.; Li, S.; Lynn, J. W.; Chen, Y.; Green, M. A.; Chen, G. F.; Li, G.; Li, Z.; Luo, J. L.; Wang, N. L.; Dai, P. *Nat Mater* **2008**, *7*, 953-959.

8 Summary and Conclusions

In this thesis the structure and properties of the layered oxide arsenides Sr_2MO_3FeAs (*M* = Sc, V and Cr) and CeOMnAs have been scrutinised. The physical properties of these materials are largely dictated by the choice of the transition metal cation at the tetrahedral site in the arsenide layers. However, it has also been demonstrated that the nature of the metal, or metals, present in the oxide fragments can strongly influence the character of these layered materials.

The majority of the work discussed in this thesis has focussed on the design and optimisation of the superconducting properties of new iron pnictide superconductors with anti-PbO-type FeAs layers. In Chapter 3 a new FeAs-containing structure type has been realised in the discovery, at a time simultaneous with other groups, of Sr_2ScO_3FeAs. This material crystallises in the *P*4/*nmm* space group with the Sr_2GaO_3CuS structure type, in which FeAs layers are separated by insulating $[Sr_2ScO_3]^+$ oxide fragments that resemble a portion of the K_2NiF_4 structure. In Sr_2ScO_3FeAs both the interplanar and intraplanar Fe-Fe distances are considerably greater than those seen in any ternary or quaternary iron arsenides. Another notable characteristic of Sr_2ScO_3FeAs is the absence of an observable structural distortion and long range ordering of Fe moments. This is despite a Fermi surface that appears to display the same essential features as those of other superconducting FeAs parent materials and would therefore be expected to support Fermi-surface nesting.[1] It is proposed that the absence of structural and magnetic transitions in Sr_2ScO_3FeAs is a result of the decreased dimensionality of this material, with the introduction of thick oxide layers proving detrimental to the formation of long range magnetic order. Furthermore attempts to electron and hole dope Sr_2ScO_3FeAs into the superconducting regime have not borne fruit. However, superconductivity has since been reported in materials with comparable interplanar Fe-Fe distances, such as Sr_2VO_3FeAs (37 K)[2] and $Sr_2Ti_{1-x}Mg_xO_3FeAs$ (35 K),[3] suggesting that the absence of superconductivity in Sr_2ScO_3FeAs is not the result of a decreased dimensionality.

In replacing Sc^{3+} by Cr^{3+} at the 2*c* site in Sr_2ScO_3FeAs, the range of materials with this structure type has been extended, as described in chapter 4. Sr_2CrO_3FeAs has considerably shorter *a* and *c* lattice parameters than the Sc analogue, and also features an intraplanar Fe-Fe distance and As-Fe-As bond angles that are much more typical for superconducting FeAs parent materials. However, as in the case of Sr_2ScO_3FeAs, Sr_2CrO_3FeAs exhibits no

evidence of structural or magnetic anomalies associated with ordering on the Fe sub-lattice.

Magnetometry measurements on Sr_2CrO_3FeAs do reveal a broad maximum in the susceptibility at 40 K, similar to that seen in the isostructural oxychalcogenide Sr_2CrO_3CuS,[4] which is attributed to long-range AFM ordering of Cr^{3+} (S = 3/2) moments. Powder neutron diffraction data collected on WISH at 1.5 K reveals additional magnetic Bragg reflections that are consistent with AFM order, and are described by a $\boldsymbol{k}$ = (½, ½, 0) propagation vector. Magnetic structure analysis in SARAh Refine unearths ordering in Sr_2CrO_3FeAs which is analogous to that seen in Pr_2CuO_4 with a checkerboard arrangement of Cr^{3+} spins in the *ab*-plane (Figure 8.1). However, since collinear and non-collinear arrangements of Cr^{3+} spins in adjacent layers give identical magnetic Bragg scattering it is not possible to ascertain the relative spin orientations from these measurements.[5]

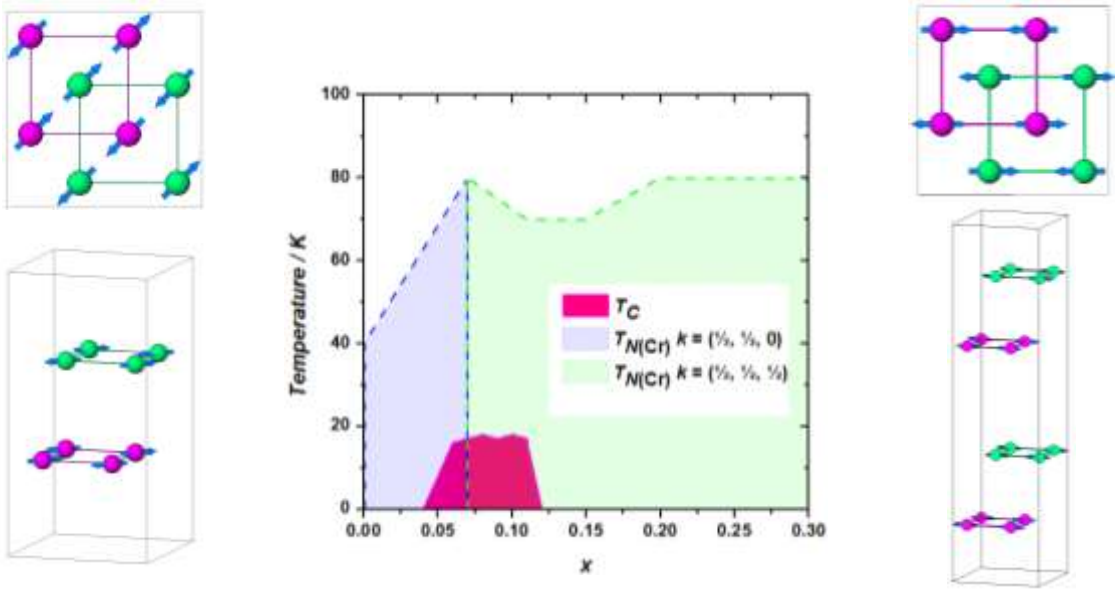

Sr_2CrO_3FeAs
$\boldsymbol{k}$ = (½, ½, 0)

$Sr_2CrO_3Fe_{1-x}Co_xAs$ phase diagram

$Sr_2CrO_3Fe_{1-x}Co_xAs$
$\boldsymbol{k}$ = (½, ½, ½)

Figure 8.1 Summary of magnetic and superconducting properties of $Sr_2CrO_3Fe_{1-x}Co_xAs$

Additionally, the partial substitution of Fe^{2+} (d^6) by Co^{2+} (d^7) in $Sr_2CrO_3Fe_{1-x}Co_xAs$ has been shown to be a successful electron-doping strategy for inducing superconductivity in the compositional range $0.05 \leq x \leq 0.11$, with T_c maximised at 18 K in $Sr_2CrO_3Fe_{0.92}Co_{0.08}As$. Low temperature PND measurements performed on $Sr_2CrO_3Fe_{1-x}Co_xAs$ samples reveal both commensurate and incommensurate components to magnetic order that are described by $\boldsymbol{k}$ = (½, ½, ½) and $\boldsymbol{k}$ = (0.53, ½, ½) propagation vectors, respectively. The commensurate component to magnetic Bragg scattering was

found to be best described by a magnetic structure similar to that of the parent Sr_2CrO_3FeAs phase, but with an AFM coupling of Cr^{3+} spins between adjacent oxide fragments and a checkerboard in-plane arrangement with spins directed along either the (100) or (010) directions (Figure 8.1). These two magnetic structures presumably have very similar energies, since the nearest-neighbour interactions are similar in both, and it is the likely that the subtle changes in the electronic structure of the arsenide layer influence the interactions between adjacent oxide slabs.

In chapter 5 an improved synthetic route was established to Sr_2VO_3FeAs, a rare example of an "undoped" iron arsenide superconductor. To examine the likely origins of superconductivity in Sr_2VO_3FeAs, investigations were made into its stoichiometry, and the valence states of vanadium and iron in this material. Rietveld refinement against a combination of synchrotron X-ray and neutron powder diffraction data does not suggest any significant departure from the nominal composition, though a small degree of Fe/V mixing (1.8(3) %) is suggested on the Fe site. XANES measurements were then performed on the vanadium and iron *K*-edges. The position of the V *K*-edge in Sr_2VO_3FeAs was found to be intermediate between that of the $LaV^{III}O_3$ and $Sr_3V_2{}^{IV}O_7$ reference samples, and a tentative estimate of the vanadium oxidation state was made at +3.13(5). Similar analysis on the Fe *K*-edge shows its position in Sr_2VO_3FeAs to be at marginally lower energy than that in Sr_2ScO_3FeAs and Sr_2CrO_3FeAs, a result consistent with partial reduction of Fe^{2+} which is electron-doped by mixed valence V^{3+}/V^{4+}.

As well as displaying a transition to strong diamagnetism below ~25 K, additional magnetic transitions were also observed in susceptibility measurements. Since a ^{57}Fe Mössbauer study of Sr_2VO_3FeAs showed no evidence for signal splitting, these transitions are attributed to ordering on the V sub-lattice.[6] However, the absence of discernable magnetic Bragg reflections in low temperature powder neutron diffraction data and the very weakly damped μSR signal suggest that the system is some way from commensurate long range order, likely due to the itinerant nature of V 3*d* electrons.

In chapter 6 efforts were made to optimise the superconducting properties of Sr_2VO_3FeAs through aliovalent and isovalent substitutions on a variety of crystallographic sites. Electron doping of the anti-PbO-type FeAs layers in Sr_2VO_3FeAs has been successfully realised through the partial substitution of Ti^{4+} for V^{3+} and Co^{2+} (d^7) for Fe^{2+} (d^6). However, both of these electron-doping strategies have the effect of lowering the superconducting critical temperature of Sr_2VO_3FeAs and ultimately suppressing

superconductivity entirely, suggesting that Sr_2VO_3FeAs is being over electron-doped. A hole-doping scheme of partial Mg^{2+} substitution on the V^{3+} site was also attempted. XANES measurements reveal that, rather than this substitution hole-doping the iron layer, vanadium is preferentially oxidised towards V^{4+} with increasing x. However, this substitution does have a considerable influence on the superconducting properties of $Sr_2V_{1-x}Mg_xO_3FeAs$, where, after an initial decrease, T_c is raised as high as 31 K in $Sr_2V_{0.775}Mg_{0.225}O_3FeAs$. These curious trends brought about by Mg substitution have yet to be rationalised, but are likely a result of subtle structural and compositional changes.

The isovalent substitution of Sr^{2+} by Ca^{2+} in $Sr_{2-x}Ca_xVO_3FeAs$ has also been demonstrated to impart significant changes to the structure and superconductivity of this material. XANES measurements show no evidence for measurable changes in the electron distribution in the system on isovalent substitution, but there is a clear correlation between the evolution of T_c and the shape of the $FeAs_4$ tetrahedron. This offers further support that superconductivity in the iron-based superconductors is extremely sensitive to the crystal structure.

The differing structural and physical properties in the Sr_2MO_3FeAs family are now considered as a whole and compared to those of other iron based superconductors. A linear increase is seen in the size of the a lattice parameter with the increasing ionic radii of the M^{3+} cation in going from Sr_2CrO_3FeAs to Sr_2ScO_3FeAs. The trends in the intraplanar Fe-Fe bond distance mirror those of the basal lattice parameter, since Fe-Fe = $a/\sqrt{2}$. In Figure 8.2 the Fe-Fe and Fe-As bond lengths are compared with those of other iron arsenide superconductors.

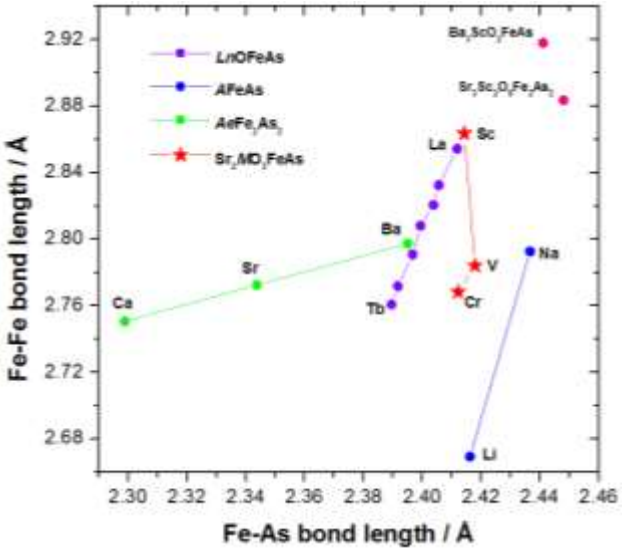

Figure 8.2 Comparison of Fe-Fe and Fe-As bond lengths in iron arsenide superconductors.

This plot demonstrates the anomalously large intraplanar Fe-Fe distance found in Sr_2ScO_3FeAs, which is smaller only than those seen in isostructural Ba_2ScO_3FeAs and the related material $Sr_3Sc_2O_5Fe_2As_2$.[7,8] It is also notable that there have been no reports of superconductivity in any of these scandium oxide arsenide materials. The Fe-Fe bond lengths in Sr_2CrO_3FeAs and Sr_2VO_3FeAs are by contrast comparable to those in FeAs parent materials that support superconductivity. Sr_2VO_3FeAs does, however, feature an unexpectedly long Fe-As bond length, based on the size of the metal in the oxide layer. This and the observed superconductivity in Sr_2VO_3FeAs are understood in terms of electron-doping of the FeAs layers from mixed valence vanadium.

No member of the Sr_2MO_3FeAs family shows any strong evidence for magnetic ordering on the Fe lattice, which is believed to be a consequence of the decreased dimensionality in this structure type inhibiting the development of long range magnetic order. The observation of a nematic ordering transition in 1111 materials at temperatures (T_S) well above that of T_N suggests that short range correlations can drive a structural distortion. However, the absence of significant peak broadening/splitting in high resolution PND measurements implies that the drastically decreased dimensionality in Sr_2MO_3FeAs materials inhibits this ordering.

Despite the absence of these transitions in this novel FeAs family, superconductivity has been realised and controlled by a variety of isovalent and aliovalent substitutions in both Sr_2VO_3FeAs and Sr_2CrO_3FeAs. This indicates that the introduction of thick blocking layers in these materials is no barrier to superconductivity and offers further support to the view that the superconductivity in the iron-based superconductors is extremely sensitive to both the carrier doping level and crystal structure.

With a view to future progress in the field, the development of further structure types should aid in the understanding of structure property relationships, leading to an improved understanding of the fundamentals of superconductivity in this Fe-based class of superconductor and ultimately a "recipe" for a room temperature superconductor. There is certainly still scope for the development of further iron based superconductors. The recent reports of high temperature superconductivity in the iron arsenides $(Ca_{n+1}(Sc,Ti)_nO_y)Fe_2As_2$ (n = 3, 4, 5) and $(CaFe_{1-x}Pt_xAs)_{10}Pt_{4-y}As_8$ demonstrate that the "iron-rush" is still in full flow (Figure 8.3).[9,10] Additionally the intercalation of Li^+, NH_3 and NH_2^- between FeSe layers in $Li_x(NH_2)_y(NH_3)_{1-y}Fe_2Se_2$ ($x \sim 0.6$; $y \sim 0.2$) has recently

been shown to increase the superconducting critical temperature of FeSe from 8.5 to 43 K.[11] This offers a new synthetic route to a potential treasure trove of molecular intercalates, which may help to optimize the superconducting properties in this family.

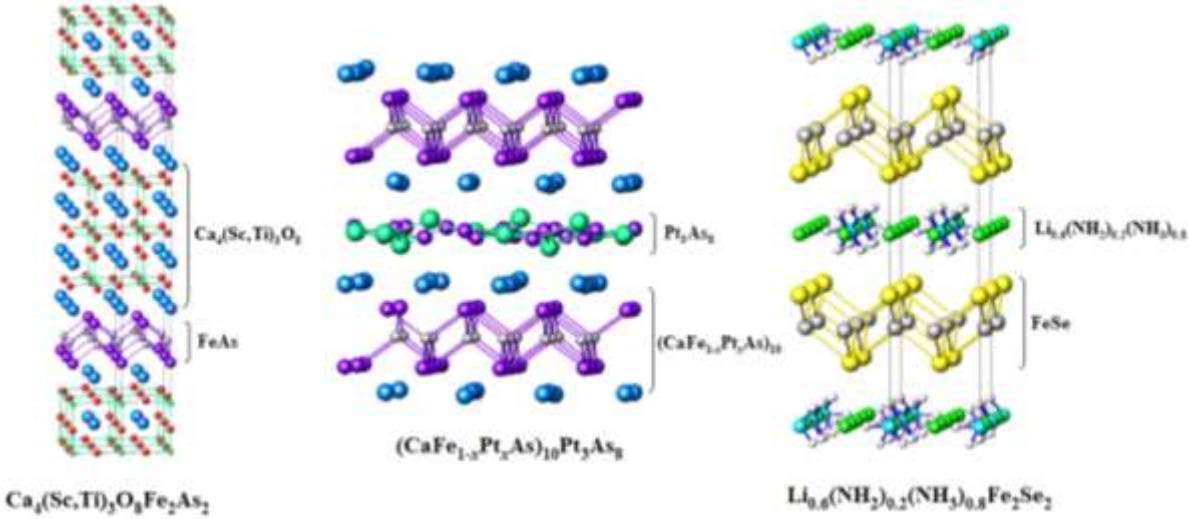

Figure 8.3 Novel structure types of Fe-based superconductors

Whilst the blockbuster iron pnictide and chalcogenide superconductors have rightly received a good deal of attention and formed the bulk of this thesis, they have also kick-started investigations into related materials with different 1st row transition metals coordinated in the arsenide layers. Studies into manganese oxide arsenides with the general formulae *Ln*OMnAs reveal intriguing magnetic transitions. In chapter 8 the magnetic properties of CeOMnAs were examined by powder neutron diffraction. These measurements reveal a spin reorientation of Mn moments at 36 K concomitant with Ce ordering and an apparent weak structural distortion, demonstrating that *f* electrons are able to dictate the orientation of Mn moments.

To conclude, these results illustrate the wealth of exciting magnetic and electronic properties expressed by layered oxide pnictide materials and what is clear from the lesson of the iron-based superconductors is that both design and serendipity have a role to play in the search for exotic phenomena in the solid state.

References

(1) Shein, I. R.; Ivanovskii, A. L. *Physical Review B* **2009**, *79*, 7.
(2) Zhu, X. Y.; Han, F.; Mu, G.; Cheng, P.; Shen, B.; Zeng, B.; Wen, H. H. *Physical Review B* **2009**, *79*, 4.
(3) Shinya, S.; Hiraku, O.; Naoto, K.; Yukari, K.; Kohji, K.; Jun-ichi, S.; Hisashi, K.; Hideki, T. *Superconductor Science and Technology* **2010**, *23*, 045001.
(4) Zhu, W. J.; Hor, P. H. *Journal of Solid State Chemistry* **1997**, *134*, 128-131.
(5) Sumarlin, I. W.; Lynn, J. W.; Chattopadhyay, T.; Barilo, S. N.; Zhigunov, D. I.; Peng, J. L. *Physical Review B* **1995**, *51*, 5824-5839.
(6) Cao, G.-H.; Ma, Z.; Wang, C.; Sun, Y.; Bao, J.; Jiang, S.; Luo, Y.; Feng, C.; Zhou, Y.; Xie, Z.; Hu, F.; Wei, S.; Nowik, I.; Felner, I.; Zhang, L.; Xu, Z. a.; Zhang, F.-C. *Physical Review B* **2010**, *82*, 104518.
(7) Zhu, X. Y.; Han, F.; Mu, G.; Zeng, B.; Cheng, P.; Shen, B.; Wen, H. H. *Physical Review B* **2009**, *79*, 5.
(8) Tegel, M.; Hummel, F.; Lackner, S.; Schellenberg, I.; Pöttgen, R.; Johrendt, D. *Zeitschrift Fur Anorganische Und Allgemeine Chemie* **2009**, *635*, 2242-2248.
(9) Ogino, H.; Sato, S.; Kishio, K.; Shimoyama, J.; Tohei, T.; Ikuhara, Y. *Applied Physics Letters* **2010**, *97*, 3.
(10) Löhnert, C.; Stürzer, T.; Tegel, M.; Frankovsky, R.; Friederichs, G.; Johrendt, D. *Angewandte Chemie International Edition* **2011**, *50*, 9195-9199.
(11) Burrard-Lucas, M.; Free, D. G.; Sedlmaier, S.; Wright, J. D.; Cassidy, S. J.; Hara, Y.; Corkett, A. J.; Lancaster, T.; Baker, P. J.; Blundell, S. J.; Clarke, S. J. **2012**, *arXiv:1203.5046v2*.

Appendix A: Exchange mechanisms

Superexchange

The indirect superexchange interaction occurs via an intermediate non-magnetic ion and typically leads to antiferromagnetic ordering.[1,2] This is illustrated in Figure A.1 which describes superexchange in a linear *M*-O-*M* array in which the coupled metal centres (*M*) each have a single electron in a *d* (e_g) orbital which overlap with the filled oxygen 2*p*(σ) orbital, to give partial covalent character. It follows that if the unpaired electron on metal centre *M*(1) are spin 'up' the Pauli exclusion principle dictates that the e^- density transferred from the oxygen *p*-orbital must be spin 'down'. Furthermore if the same oxygen *p*-orbital is to simultaneously bond to *M*(2) then the unpaired electron in the metal *d* orbital is necessarily spin down, generating an antiferromagnetic interaction.

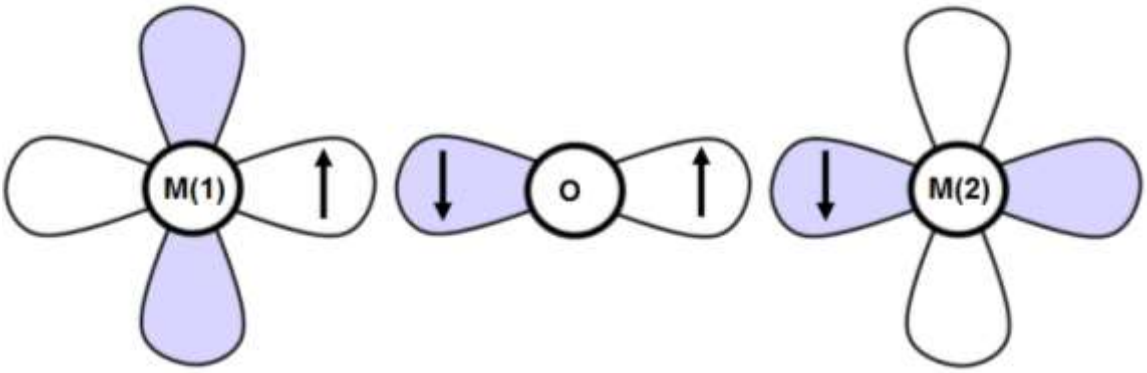

Figure A.1 Schematic representation of the superexchange interaction between two metals centres *M*(1) and *M*(2) through an intermediary O 2*p* orbital

Since the mechanism is reliant on orbital overlap the strength of the interaction is dependent on the degree of covalency. This is well seen in the increase in the Neel temperature of binary 1st row transition metal oxides as one moves across the period, due to an increase in the degree of *M*-O mixing as a result of a lowering of the energies of the metal *d*-orbitals.

In certain circumstances the superexchange mechanism can also bring about ferromagnetic ordering.[3] This is anticipated for the linear *M*-*L*-*M* array, in which a partially filled metal *d* orbital on *M*(1) orbital has a vacant *d* orbital orthogonal to it on *M*(2). This is the case in Rb_2CrCl_4 which takes the K_2NiF_4 structure but with $CrCl_2$ planes which are Jahn-Teller distorted away from tetragonal symmetry. This causes orbital ordering which means that occupied orbitals on adjacent Cr^{2+} sites are orthogonal to one another, generating

ferromagnetic layers. Since the superexchange interaction is driven by orbital overlap, it is very sensitive to changes in bond angle. However, a set of semi empirical rules have been developed by J. B. Goodenough and J. Kanamori which attempt to predict the magnetic ordering schemes on a qualitative level.[4] These rules often work well for simple systems but run into problems when bond angles deviate from 180°, direct exchange and superexchange compete and when spin orbit coupling becomes a factor.[2,5]

Double exchange

Double exchange is another important magnetic exchange mechanism that may arise between magnetic ions in different oxidation states. In the $Ln_{1-x}A_xMnO_3$ family of rare earth manganates, doping of a divalent alkaline earth cation on the rare earth *Ln* site, oxidises some Mn^{3+} to Mn^{4+} to give a mixed valence system on the octahedral transition metal sites. Here the Mn^{3+} is high spin and has 1 e_g electron, whilst Mn^{4+} e_g orbitals are vacant and the delocalisation of e_g electrons in the partially filled band produces ferromagnetic exchange to conform with Hund's rules, which overcome the AFM superexchange coupling of t_{2g} electrons. However, such a mechanism requires that sufficient proportions of Mn^{3+} and Mn^{4+} are present, so that continuous pathways for double exchange are present. The onset of this double exchange 'hopping' of e_g electrons also brings about a metal to insulator transition coincident with the onset of ferromagnetic ordering. At temperatures just above the ferromagnetic ordering temperature T_C it is possible to induce the metal to insulator transitions by the application of an applied magnetic field, in a phenomenon known as colossal magnetoresistance(CMR). CMR is observed in $La_{0.67}Ca_{0.33}MnO_3$ as well in the layered Ruddlesden-Popper phases $Sr_{2-x}Ln_{1+x}Mn_2O_7$ and $Ca_{2-x}Ln_xMnO_4$.[6-8]

There are also situations where the superexchange and double exchange interactions can coexist in a single material. This is the case with magnetite, Fe_3O_4, in which double exchange between octahedral Fe^{3+} and Fe^{2+} promotes ferromagnetism, whilst superexchange interactions between tetrahedral Fe^{3+} and the octahedral sites causes AFM alignments. This results in oppositely aligned arrays of magnetic ions a net moment due to the Fe^{2+} bringing about Ferrimagnetism.

RKKY interaction

The Ruderman-Kittel-Kasuya-Yosida (RKKY) interaction describes how exchange coupling between localised magnetic moments in metallic materials is mediated by conduction electrons.[9-11] The mechanism relies on the localised magnetic moments to spin polarise conduction electrons which subsequently couple with another magnetic centre some distance away. The RKKY exchange coefficient oscillates from positive to negative as the separation of magnetic ions changes, such that the exchange can bring about antiferromagnetic or ferromagnetic coupling depending on the separation of the magnetic ions. Such interactions are particularly important in the magnetism of rare-earth metals whose valence 4*f* electrons are shielded by 5*s* and 5*p* electrons such that direct exchange is weak.

References

(1) Anderson, P. W. *Physical Review* **1950**, *79*, 350-356.
(2) Kanamori, J. *Journal of Physics and Chemistry of Solids* **1959**, *10*, 87-98.
(3) Anderson, P. W.; Hasegawa, H. *Physical Review* **1955**, *100*, 675-681.
(4) Goodenough, J. B. *Physical Review* **1955**, *100*, 564-573.
(5) Zhou, J. S.; Goodenough, J. B.; Yan, J. Q.; Ren, Y. *Physical Review Letters* **2007**, *99*, 156401.
(6) Maignan, A.; Simon, C.; Caignaert, V.; Raveau, B. *Solid State Communications* **1995**, *96*, 623-625.
(7) Coldea, A. I.; Spring, L. E.; Blundell, S. J.; Singleton, J.; Hayes, W. *Journal of Physics: Condensed Matter* **1999**, *11*, 9053.
(8) Battle, P. D.; Rosseinsky*, M. J. *Current Opinion in Solid State and Materials Science* **1999**, *4*, 163-170.
(9) Ruderman, M. A.; Kittel, C. *Physical Review* **1954**, *96*, 99-102.
(10) Kasuya, T. *Progress of Theoretical Physics*, *16*, 45.
(11) Yosida, K. *Physical Review* **1957**, *106*, 893-898.

Appendix B: Vanadium reference samples

Synthesis of $LaVO_3$

In chapter 6, $LaV^{(III)}O_3$ and $Sr_3V_2{}^{(IV)}O_7$ are used as reference samples in X-ray absorption spectra measurements performed on the vanadium *K*-edge, being examples of V^{3+} and V^{4+}, respectively.

$LaVO_3$ (*Pnma*) was prepared by the reduction of a sample of $LaVO_4$, by heating at 950 °C for 24 h under an atmosphere of 5 % H_2 / 95 % N_2.[2] $LaVO_4$ was prepared by calcining stoichiometric amounts of La_2O_3 (Alfa, 99.99 %) and V_2O_5 (Sigma 99.99 %) powders at 950 °C in air for 6 h. The X-ray powder diffraction pattern of the phase pure $LaVO_3$ sample is shown in Figure B.1.

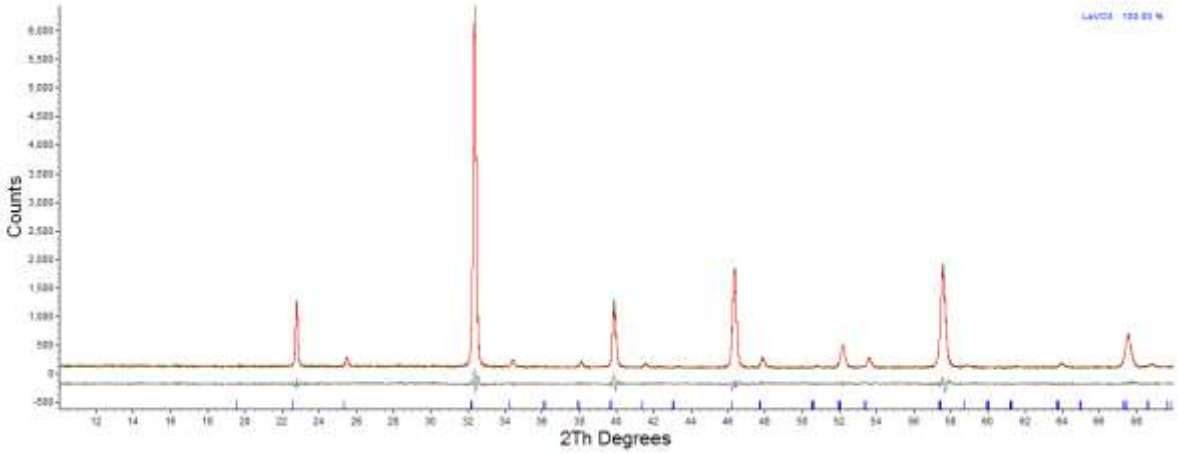

Figure B.1 Rietveld fit to PXRD data for $LaVO_3$

Synthesis of $Sr_3V_2O_7$

In a similar manner $Sr_3V_2O_7$ was prepared by twice annealing a sample of $Sr_3V_2O_8$ in a reducing H_2 flow (5 % H_2 / 95 % N_2) at 1050°C for 12 h, with an intermediate grinding. The precursor $Sr_3V_2O_8$ was synthesised by calcining a mixture of V_2O_5 (Sigma 99.99 %) and $SrCO_3$ (Alfa 99.99 %) in air.[3] Rietveld analysis of the PXRD pattern in Figure B.2 reveals that whilst the majority of the sample is $Sr_3V_2O_7$ (85 wt. %), small amounts of Sr_2VO_4 (10 wt. %) and $Sr_4V_3O_{10}$ (5 wt. %). However, since this sample is being used as a standard for the vanadium +4 oxidation state and given that the formal valence of vanadium in all of these materials is +4 this was not considered to be a major issue.

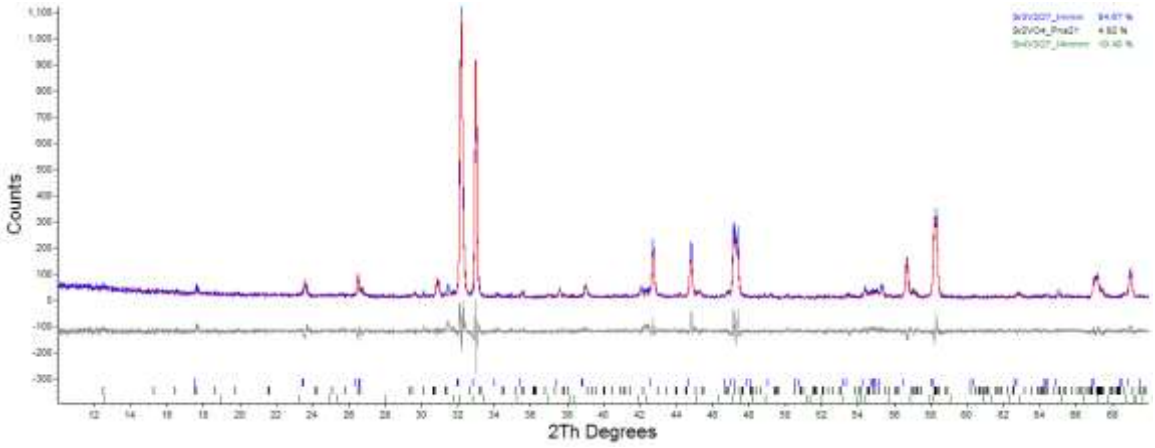

Figure B.2 Rietveld fit to PXRD data for $Sr_3V_2O_7$

Appendix C: Magnetic structure determination

Analysis of neutron diffraction data can yield information on the magnetic structure of a magnetically ordered material. Firstly a propagation vector is determined by indexing the magnetic Bragg reflections in the diffraction pattern, before magnetic structure determination is undertaken using the SARAh program, interfaced with the GSAS and Fullprof refinement suites. SARAh Representational Analysis is then performed, which uses the nuclear symmetry, along with the fractional coordinates of the magnetic atoms and the propagation vector to generate a list of irreducible representations. These so called 'irreps' describe the possible arrangements of magnetic moments in the magnetic unit cell. Since magnetic symmetry definitions are limited in GSAS, no ***k***-vector is used, instead SARAh reduces the symmetry of the cell to *P*1 and includes additional atoms. This reduction of symmetry means that the moments are not restricted by the nuclear symmetry and the details of all possible irreps are saved in a *.mat file. SARAh refine is then implemented to solve the magnetic structure by investigating which basis vectors can best model the additional Bragg intensity. To achieve this, first the nuclear phase is refined in GSAS to a global minimum. All parameters are then fixed and SARAh Refine is used to introduce a magnetic phase into the input file using information from the .mat file.

Basis vectors are then selected and SARAh refine loads this information into the input file whereupon GSAS refines the fractional occupancies of the magnetic atoms, until the refinement converges. This process is repeated for all possible basis vectors, and a comparison of the goodness of fit of these results is used to suggest a likely magnetic structure. A more rigorous treatment can be made by mixing a combination of different basis vectors, through reverse Monte Carlo cycles, to access a whole array of magnetic structures. The results of such refinements are visualised using contours plots generated in *gnuplot* 4.0, utilizing the *dgrid* and *pm3d* functions. The contour plots take the form of a grid *x* columns wide by *y* rows high which represent the coefficients of different basis vectors, over which is laid a coloured surface that describes χ^2, where blue and red points describe the regions of lowest and highest χ^2, respectively. Data points are weighted such that the closer a point is to a position on the grid the more highly it is weighted.

If the basis vectors (Ψ(1) & Ψ(3)) of a single magnetic ion are combined, as is shown in (A), then there will be regions of the contour plot which are outside the physical bounds of the magnetic structures that can been sampled i.e. where |Ψ(1) | + |Ψ(3) | > 1. This is emphasised in the contour plot in Figure 1 (A) by the white diamond, outside of which the data are extrapolated to the 'corners'. However, if the basis vectors of two different magnetic ions are combined, as in Figure C.1 (B), then the entire surface of the plot represents spin arrangements that may have been sampled. The power of SARAh Refine lies in its ability to mix different coefficients of all possible basis vectors to generate an exhaustive array of trial magnetic structures, the merit of which may then considered by scrutinising contour plots such as those shown below.

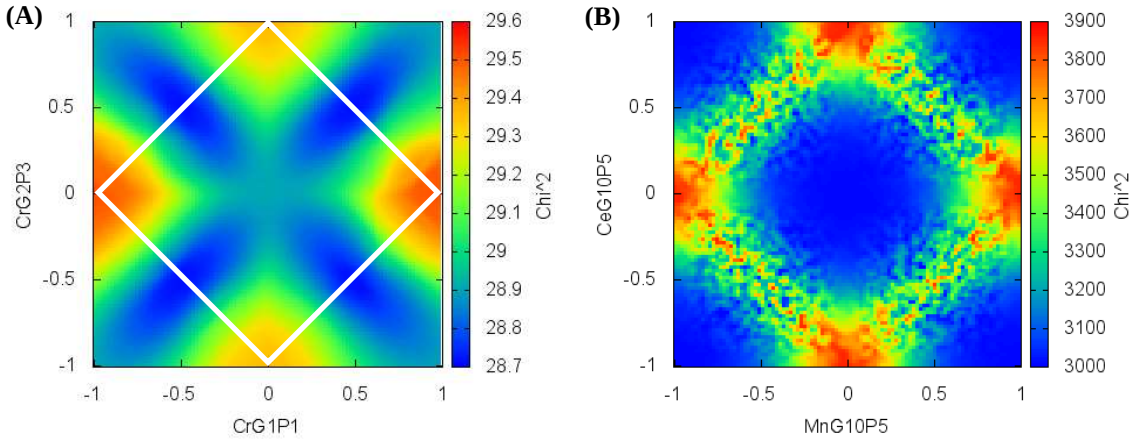

Figure C.1 Contour plots generated using GNUPLOT representing the combination of Cr basis vectors in Sr_2CrO_3FeAs (A) and the combination of Ce and Mn basis vectors in CeOMnAs (B).

Appendix D: Aliovalent substitutions in Sr_2ScO_3FeAs

$Sr_2Sc_{1-x}Mg_xO_3FeAs$ samples were synthesised in the compositional range $0 \leq x \leq 0.3$ according to the equation below:

$$(2\text{-}x)\ SrO + (½\text{-}x/2)\ Sc_2O_3 + x\ Mg + x\ SrAs + (1\text{-}x)As + Fe \rightarrow Sr_2Sc_{1-x}Mg_xO_3FeAs$$

The phase purity of these samples was assessed my PXRD and the Rietveld fit of $Sr_2Sc_{0.9}Mg_{0.1}O_3FeAs$ is shown in Figure D.1.

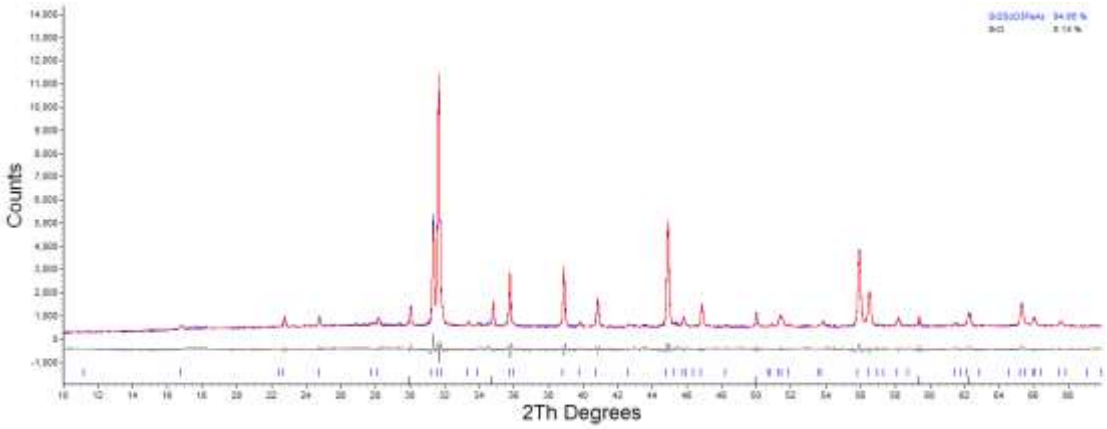

Figure D.1 Rietveld fit of $Sr_2Sc_{0.9}Mg_{0.1}O_3FeAs$ to PXRD data

The refined lattice parameters and occupancies of Sc and Mg on the 2*c* (¼, ¼, 0.31) site are a = 4.04240(6) Å, c = 15.6838(3) Å, $f_{occ(Sc)}$ = 0.90(3) and $f_{occ(Mg)}$ = 0.10(3), respectively, confirming the successful replacement of Sc^{3+} with the lower valent Mg^{2+} cation. The magnetic properties of $Sr_2Sc_{1-x}Mg_xO_3FeAs$ samples were characterised by ZFC and FC magnetisation measurements using a SQUID magnetometer. The magnetic susceptibility of $Sr_2Sc_{0.9}Mg_{0.1}O_3FeAs$ is shown in Figure D.2 and remains paramagnetic down to 2 K.

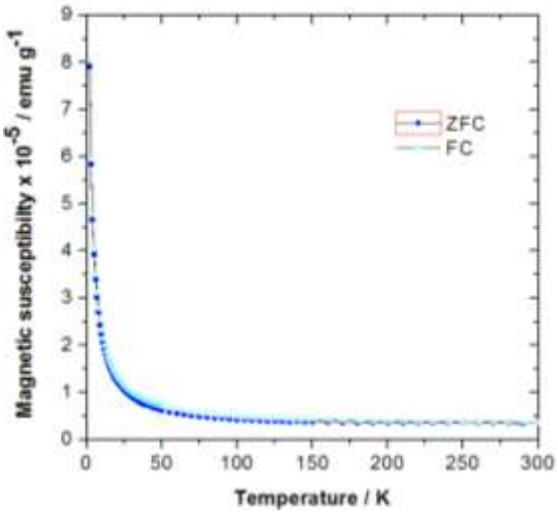

Figure D.2 Magnetic susceptibility $Sr_2Sc_{0.9}Mg_{0.1}O_3FeAs$ applied field of 50 Oe

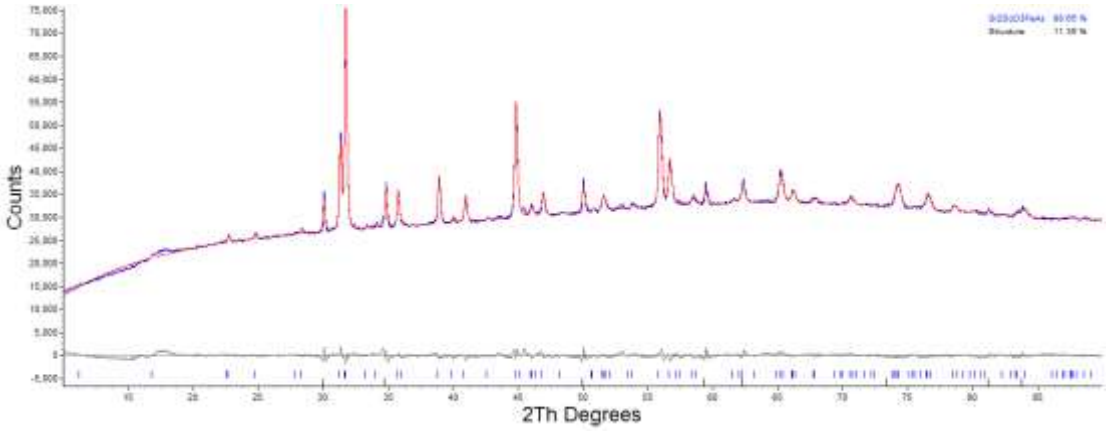

Figure D.3 Rietveld fit of $Sr_{1.95}La_{0.05}ScO_3FeAs$ to PXRD data

a = 4.0489(1) Å
c = 15.7955(6) Å

Appendix E: Refinement results for Sr_2CrO_3FeAs

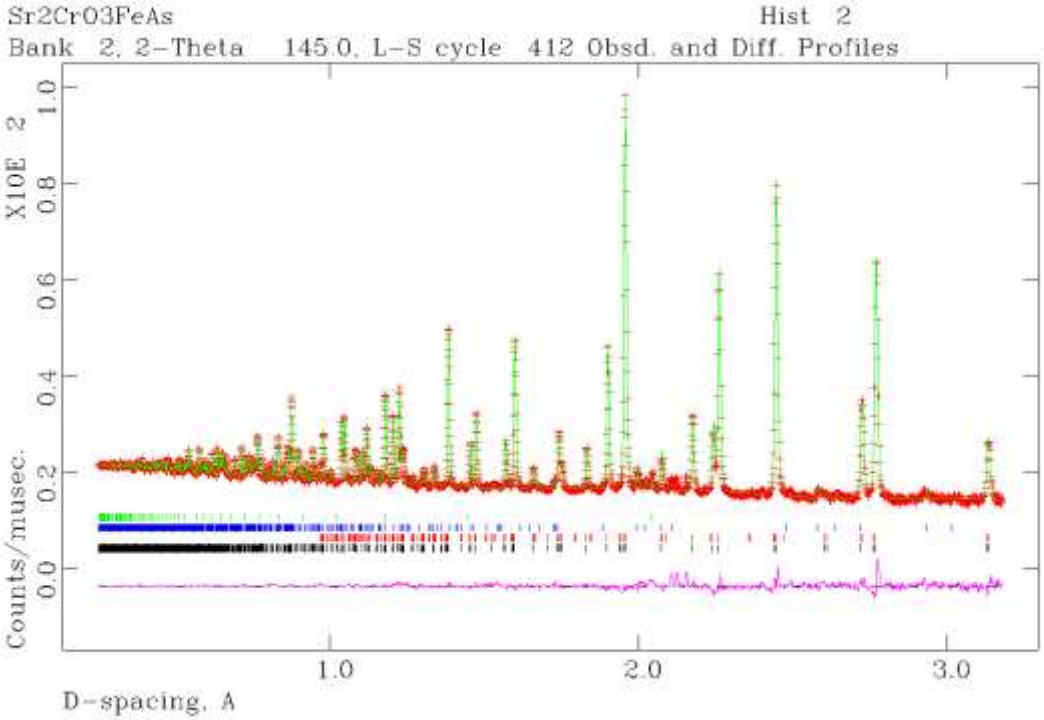

Figure 1 Rietveld fit of Sr_2CrO_3FeAs to POLARIS PND data collected in the 145 ° detector bank at 5 K

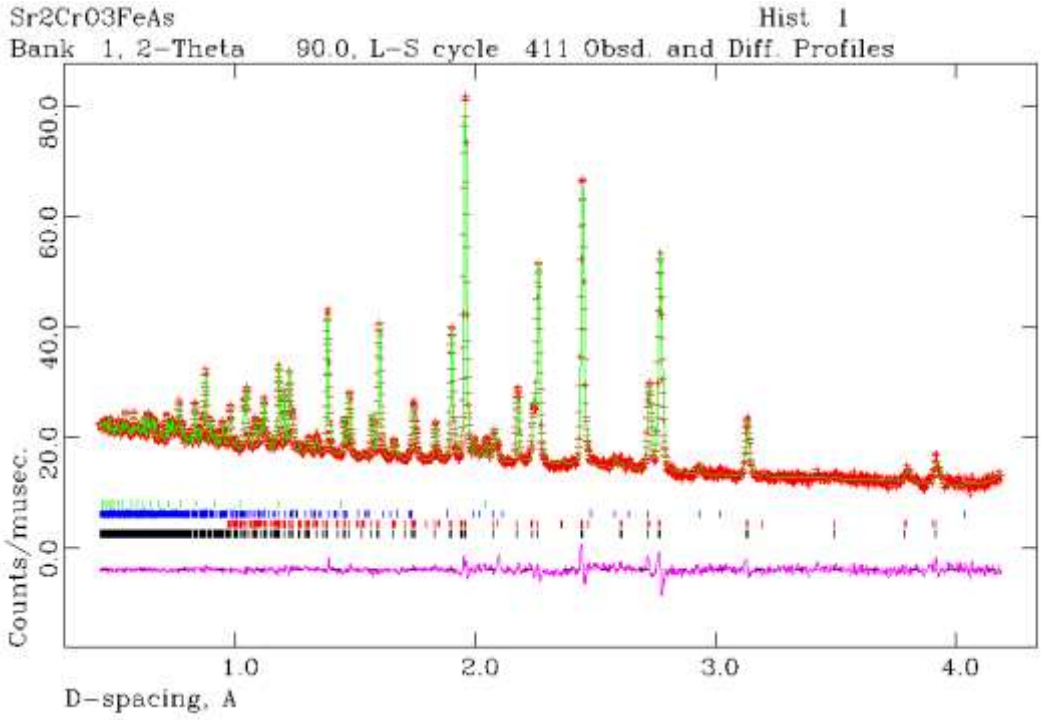

Figure 2 Rietveld fit of Sr_2CrO_3FeAs to POLARIS PND data collected in the 90 ° detector bank at 5 K

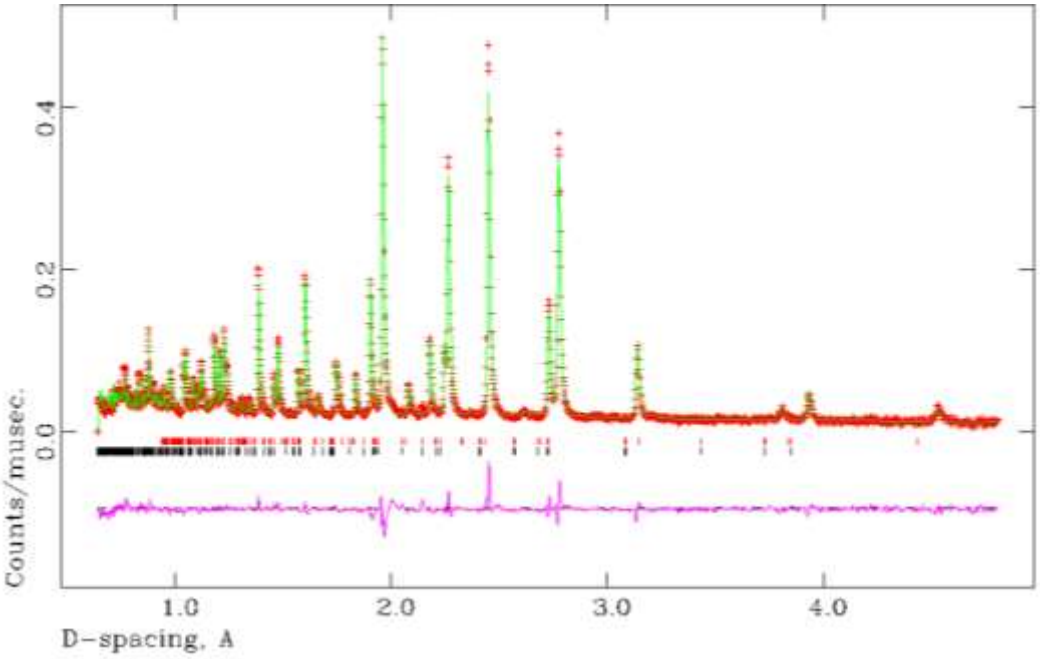

Figure 2 Rietveld fit of Sr_2CrO_3FeAs to WISH PND data collected in the 153 ° detector bank at 1.5 K

Temperature:		Sr_2CrO_3FeAs (100 K)	Sr_2CrO_3FeAs (1.5 K)
		Space group *P*4/*nmm*: 2	
Cell parameters and global fitting parameters:			
a / Å		3.91416(4)	3.913486(3)
c / Å		15.7357(3)	15.7097(1)
Cell volume / Å^3		241.081(5)	240.60(2)
R_{wp} 90° bank		0.0685	0.0730
145° bank		0.0673	0.0714
χ^2		5.667	7.468
Atomic parameters:			
Sr1	[2*c* (¾, ¾, *z*)]	0.1955(2)	0.1948(2)
	$U \times 100$ / Å^2	0.7(1)	0.64(7)
Sr2	[2*c* (¾, ¾, *z*)]	0.4159(2)	0.4162(2)
	$U \times 100$ / Å^2	0.5(1)	0.85(9)
Cr	[2*c* (¼, ¼, *z*)]	0.3103(4)	0.3114(3)
	$U \times 100$ / Å^2	1.7(2)	0.9(1)
	m_x / μ_B		1.97(5)
Fe	[2*a* (¼, ¾, 0)]		
	$U \times 100$ / Å^2	0.8(1)	1.15(8)
As	[2*a* (¼, ¼, *z*)]	0.0909(2)	0.0906(2)
	$U \times 100$ / Å^2	1.4(2)	1.19(9)
O1	[4*f* (¼, ¾, *z*)]	0.2937(1)	0.2943(1)
	$U \times 100$ / Å^2	0.8(2)	0.89(6)
O2	[2*c* (¼, ¼, *z*)]	0.4285(2)	0.4291(2)
	$U \times 100$ / Å^2	1.7(2)	1.10(1)

Table 1 Results of refinement against WISH data for Sr_2CrO_3FeAs at 100 and 1.5 K

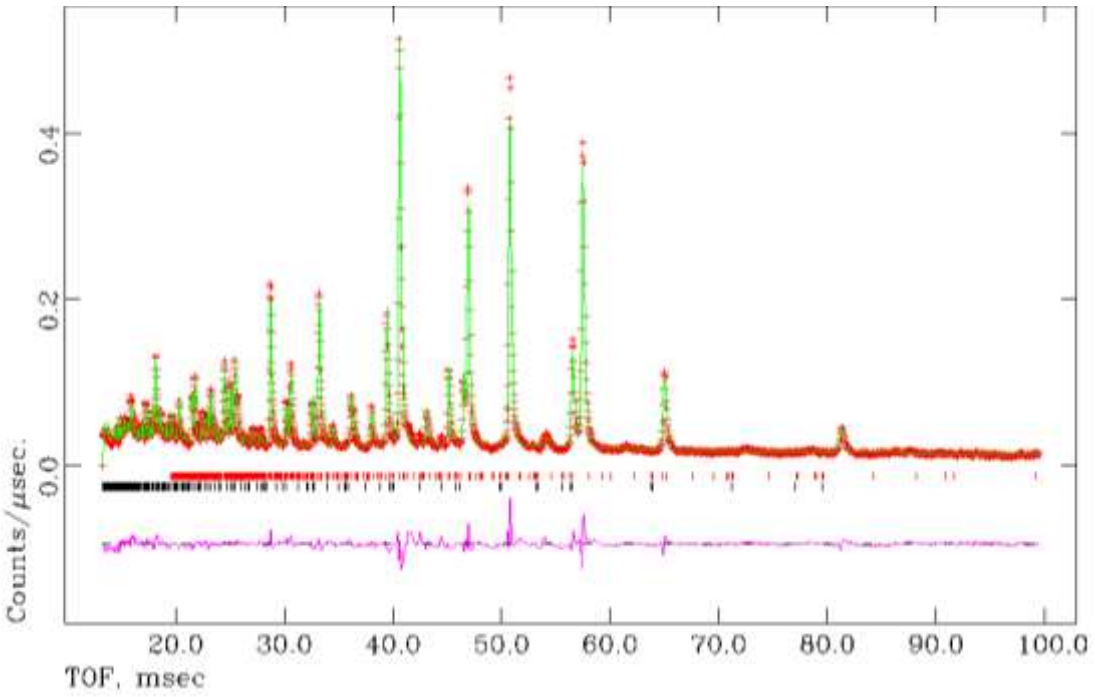

Figure 2 Rietveld fit of $Sr_2CrO_3Fe_{0.91}Co_{0.09}As$ to WISH PND data collected in the 153 ° detector bank at 1.5 K

		$Sr_2CrO_3Fe_{0.91}Co_{0.09}As$ (AJC069)	
Temperature / K		100	1.5
Cell parameters and global fitting parameters:			
a / Å		3.91315(4)	3.91310(8)
c / Å		15.7091(3)	15.6892(5)
Cell volume / Å^3		240.550(5)	240.24(2)
R_{wp} 153 ° bank		0.077	0.0737
90 ° bank		0.0761	0.0772
χ^2		11.95	46.17
Atomic parameters:			
Sr1	[2*c* (¾, ¾, *z*)]	0.1943(2)	0.1943(2)
	U × 100 / Å^2	0.68(7)	0.64(7)
Sr2	[2*c* (¾, ¾, *z*)]	0.4163(2)	0.4160(2)
	U × 100 / Å^2	0.69(9)	0.65(9)
Cr	[2*c* (¼, ¼, *z*)]	0.3119(3)	0.3112(3)
	U × 100 / Å^2	1.1(1)	1.3(1)
	Cr moment / u_B		1.20(6)
Fe	[2*a* (¼, ¾, 0)]		
	Fe : Co	0.869(8):0.131(8)	0.870(8):0.130(8)
	U × 100 / Å^2	0.92(9)	0.91(9)
As	[2*a* (¼, ¼, *z*)]	0.0903(2)	0.0902(2)
	U × 100 / Å^2	1.4(1)	1.33(9)
O1	[4*f* (¼, ¾, *z*)]	0.2939(1)	0.2940(1)
	U × 100 / Å^2	0.89(7)	0.95(6)
O2	[2*c* (¼, ¼, *z*)]	0.4294(2)	0.4295(2)
	U × 100 / Å^2	1.1(1)	1.03(9)

Table 2 Results of refinement against PND data for $Sr_2CrO_3Fe_{0.91}Co_{0.09}As$ at 100 and 1.5 K

Appendix F: Sr_2VO_3FeAs

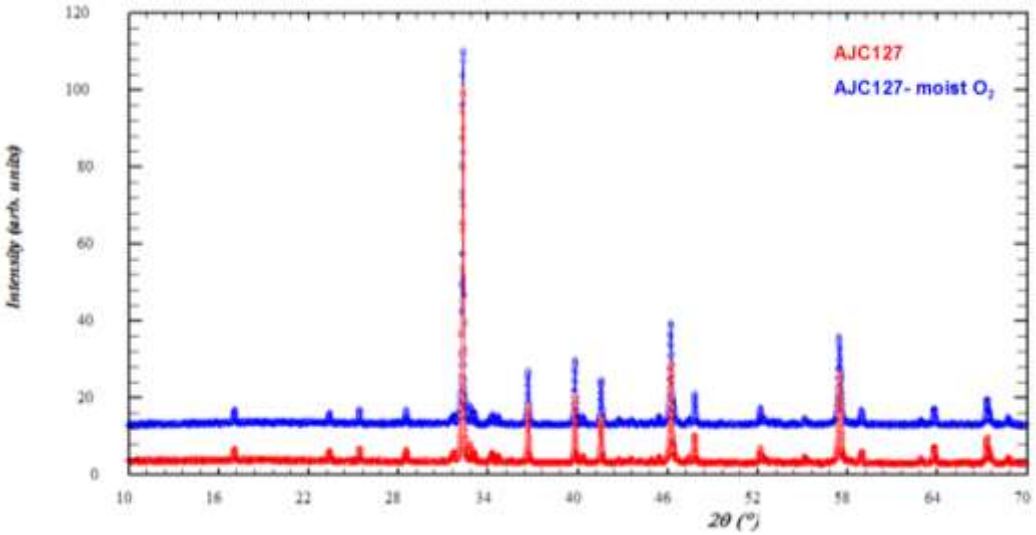

Figure 1 PXRD patterns of Sr_2VO_3FeAs collected before and after treatment with moist O_2

Appendix G: Sr_2VO_3FeAs doping studies

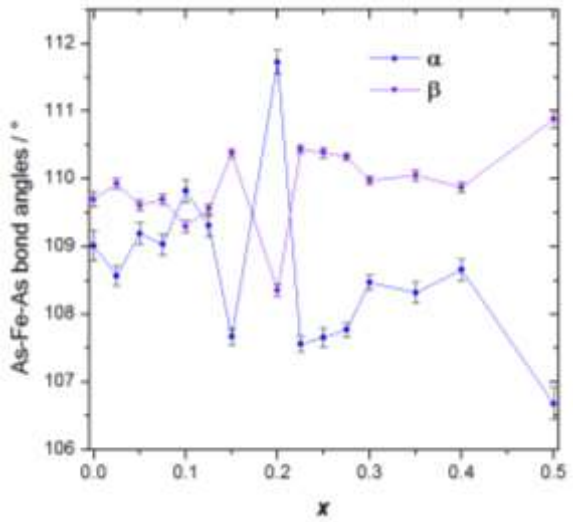

Figure 1 Variation of As-Fe-As bond angle in $Sr_2V_{1-x}Mg_xO_3FeAs$ with *x*

$Sr_{2-x}Ca_xVO_3FeAs$ bond lengths and angles derived from refinement against synchrotron X-ray powder diffraction data

x (nominal)	V-O short / Å	V-O long / Å	V-As / Å	V oxidation state	Fe- As / Å	Fe-Fe / Å	*α* As-Fe-As / °	*β* As-Fe-As / °
0	1.9799(3)	1.90494)	3.428(2)	2.816(6)	2.4182(6)	2.7840	108.99(4)	109.71(2)
0.05	1.9807(5)	1.901(6)	3.428(3)	2.817(9)	2.4129(8)	2.7837	109.33(5)	109.54(3)
0.1	1.9818(5)	1.904(6)	3.419(2)	2.807(9)	2.4139(8)	2.7840	109.28(5)	109.57(3)
0.15	1.9804(4)	1.927(5)	3.413(2)	2.777(9)	2.4174(8)	2.7823	108.95(5)	109.73(2)
0.2	1.9805(6)	1.904(7)	3.413(3)	2.815(9)	2.4195(9)	2.7815	108.76(6)	109.83(3)
0.25	1.9807(5)	1.914(6)	3.416(3)	2.796(9)	2.4231(9)	2.7807	108.48(5)	109.97(3)
0.3	1.9802(6)	1.909(7)	3.406(3)	2.81(1)	2.427(1)	2.7806	108.23(7)	110.09(4)
0.4	1.9792(9)	1.888(9)	3.399(5)	2.85(1)	2.435(2)	2.779	107.61(9)	110.41(5)
0.5	1.9748(9)	1.914(1)	3.381(6)	2.84(2)	2.437(2)	2.777	107.4(1)	110.51(6)

Table 2. Derived bond lengths, angles and bond valence sum calculations from refinement against synchrotron X-ray radiation.

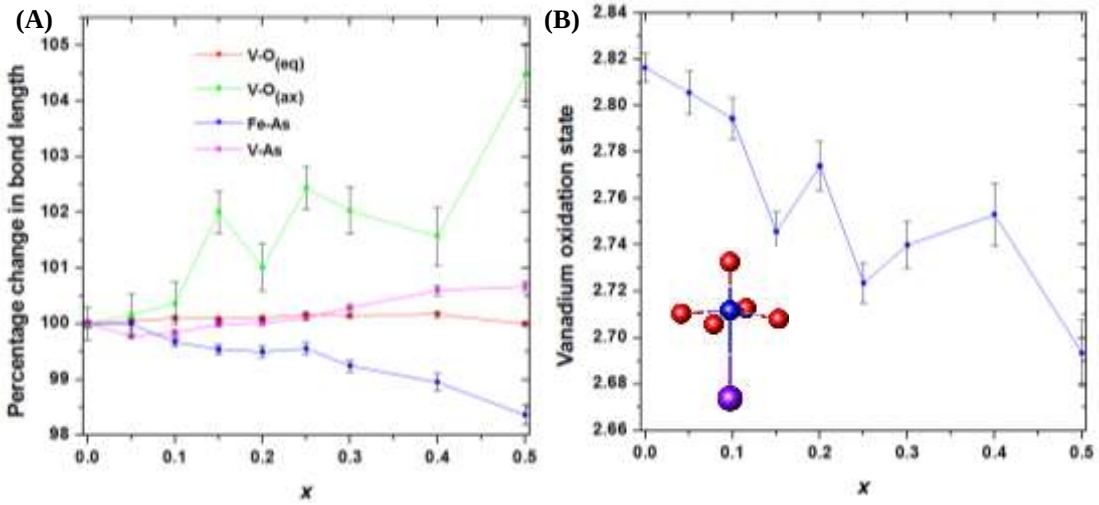

Figure 2. Plots of nominal Ca doping level against the percentage change in Fe-As, V-O and V-As bond lengths (A) and V oxidation state based on bond valence sum calculations (B) derived from refinement against ID31 data. Inset shows the coordination environment of vanadium in Sr_2VO_3FeAs.

Appendix H: CeOMnAs PND measurements

OSIRIS room temperature and 10 K collection times and *d*-ranges:

"*d*-range"	1	2	3	4	5
d (Å)	0.7-2.5	2.1-3.3	3.1-4.3	4.1-5.3	5.2-6.2
μA	10	10	20	20	20

Variable temperature data collections:

"*d*-range"	2	3
d (Å)	2.1-3.3	3.1-4.3
μA	10	20

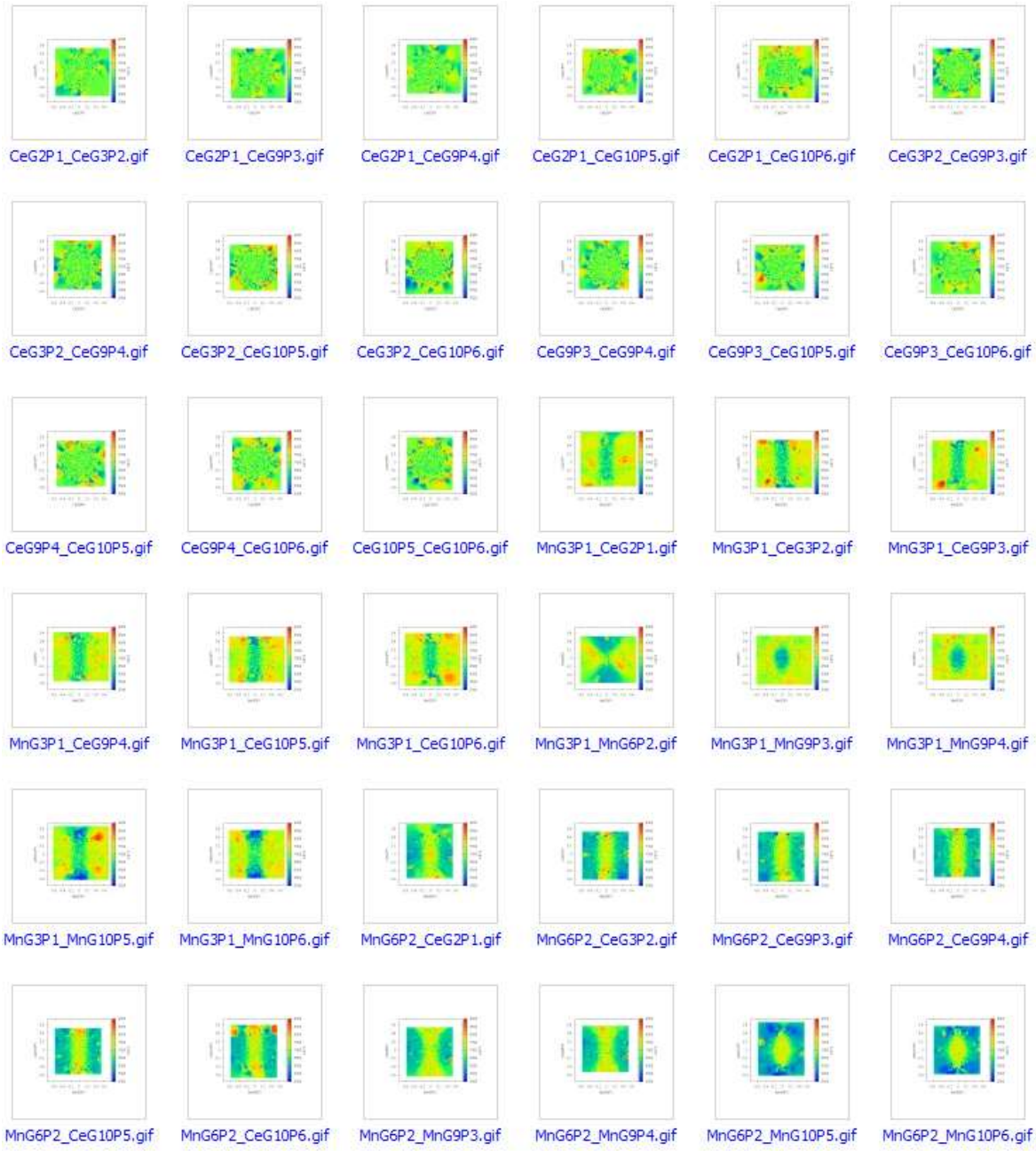

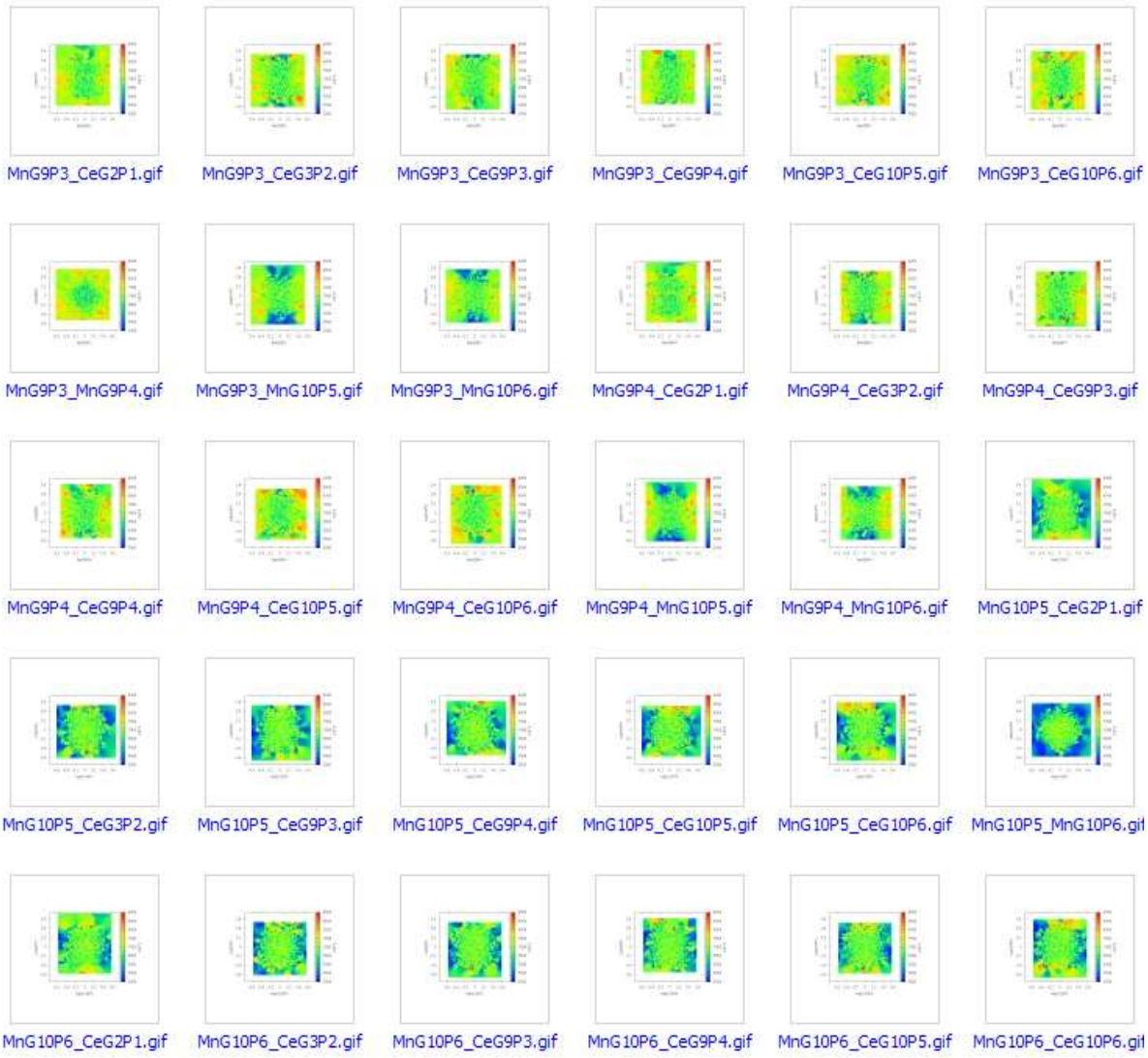

Figure 1 Results of reverse Monte Carlo analysis of 6 Mn and 6 Ce basis vectors.